UNIVERSITY OF CALIFORNIA
RIVERSIDE

Quantum Simulation of the Abelian Higgs Lattice Gauge Theory and Quantum Thermalization in Ultracold-Atom Systems

A Dissertation submitted in partial satisfaction
of the requirements for the degree of

Doctor of Philosophy

in

Physics

by

Jin Zhang

September 2019

Dissertation Committee:

Dr. Shan-Wen Tsai, Chairperson
Dr. Leonid Pryadko
Dr. Hai Bo Yu

The Dissertation of Jin Zhang is approved:

Committee Chairperson

University of California, Riverside

Acknowledgments

I would like to thank the admission committee of Department of Physics & Astronomy at University of California, Riverside in year 2013 for offering me an opportunity to pursue my Ph.D. in physics, Derek Beving and other staff in the department for the help with all kinds of questions related to work and life in US, and the Graduate Division for the financial support during my dissertation year.

I am really grateful to my advisor, Shan-Wen Tsai, without whose help, I would not have been here. In the beginning of my life in US, I was very shy with stage fright, weak in English and afraid to talk to people. She is really a kind person and I can talk to her very relaxed. She is always patient and helpful with my questions in both physics and life. She is always available to discuss our research, including the technical details and conceptual understanding of physics. She encourages me to travel, give presentations and attending summer schools, after which I become more confident talking to people. She also cares about my health. I will not forget that she drove me to doctors many times and drove me to campus every day when I had disease and cannot walk. She is both a good advisor and one of my best friends in my life. I thank her and other people in the department who helped me get through the year of medical leave. I would also like to express my sincere gratitude to Professor Leonid Pryadko, and Professor Haibo Yu for their willingness to serve on the evaluation committee for this thesis as well as my defense on May 31, 2019.

I would like to thank my second advisor Prof. Yannick Meurice for helping me understand the high energy part of our project. I thank Judah Unmuth-Yockey for discussing physics with me often until late at night, and Alexei Bazavov, Johannes Zeiher, Liping

Yang and Philipp Preiss for the collaboration in our project. I thank Miles Stoudenmire for helping me learn and start the calculation with Tensor Network algorithm using ITensor Library. I want to thank Shan-Wen Tsai, Yannick Meurice and Kirill Shtengel for preparing recommendation letters for my application for postdoc positions. I thank my postdoc advisor Tigran Sedrakyan for offering me an opportunity to continue my academic career in Physics.

I thank my parents for the efforts and sacrifices to give me better life and better education when I was a child, for always listening to my pains and happiness, and for always respecting and supporting my decisions in life after I grew up; I love you both forever.

I wanted to thank Hua Wei and Yang Li for helping me settle down in the beginning of the first year in US. I thank my friends in Riverside, including, to name a few, Di Chen, Shi Che, Shane Kelly, Rui Lv, Siyu Li, Zhongdong Qi, Jon Spalding, Chenwei Tian, Nan Zhang, Yuchen Xiao, Kuan Zhou, Zhenhai Zhang, Wenyu Wang, Yuanzhi Wang, etc. for lots of help and sharing plenty of happy time during my Ph.D.. I am thankful to my new hiking group Yawen Liu, Yinan Dong and Xi Huang for bringing me more beautiful memories of sunny California in the last few months. I thank my old friends Kangfu Chen, Xunjie Yu and Yujie Zhang who also pursue Ph.D. in different places for sharing joys and complaints in life to each other and encouraging and comforting each other these years. I finally thank all the people who have spent time with me in my life.

Most of the content in Chapters 2-4 of this thesis is reorganized, rewritten or reprint from the material published in Physical Review A [214], Physical Review D [12, 213] and Physical Review Letters [241] of American Physical Society.

To my parents for all the support.

ABSTRACT OF THE DISSERTATION

Quantum Simulation of the Abelian Higgs Lattice Gauge Theory and Quantum Thermalization in Ultracold-Atom Systems

by

Jin Zhang

Doctor of Philosophy, Graduate Program in Physics
University of California, Riverside, September 2019
Dr. Shan-Wen Tsai, Chairperson

This thesis presents our recent studies on quantum simulation of the Abelian Higgs lattice gauge theory with quantum systems engineered with ultracold atoms in optical lattices and quantum equilibration and thermalization dynamics in the context of Joule expansion in cold atom systems.

In the first part, we give proposals for the analog quantum simulation of lattice gauge theories with cold atoms in optical lattices with current experimental techniques, aiming at maximal simplicity on both the theoretical and experimental side. We search for the suitable platform for quantum simulation of the (1+1)-dimensional Abelian Higgs model, which is the scalar quantum electrodynamics replacing the fermionic fields by complex scalar fields. We use a discrete tensor reformulation to smoothly connect the space-time isotropic version used in most numerical lattice simulations to the continuous-time limit corresponding to the Hamiltonian formulation. We propose to use the Bose Hubbard model as a quantum simulator to probe the conformal Calabrese-Cardy scaling of its O(2) limit with a chemical potential. We also propose to use a physical multileg ladder of atoms

trapped in optical lattices and interacting with Rydberg-dressed interactions to quantum simulate the model and measure the Polyakov loop. Numeric results from the Monte Carlo, the tensor renormalization group and the density matrix renormalization group techniques are cross-checked to support our proposals.

In the second part of this thesis, we investigate the Joule expansion of nonintegrable quantum systems that contain bosons or spinless fermions in one-dimensional lattices. Initially a barrier confines the particles to be in half of the system in a thermal state described by the canonical ensemble and is removed at time $t = 0$. We study the properties of the time-evolved density matrix, the diagonal ensemble density matrix and the corresponding canonical ensemble density matrix with an effective temperature determined by the total energy conservation. We discuss the equilibration and thermalization for the Rényi entropy of subsystems, few-body observables and reduced density matrices in subsystems. We finally discuss the difference between bosons and fermions in finite size scaling of the effective temperature. We propose the Joule expansion as a way to dynamically create negative temperature states for fermion systems with repulsive interactions.

Contents

List of Figures **xii**

List of Tables **xviii**

1 Introduction **1**
1.1 General remarks 1
1.2 The lattice regularization of scalar compact QED 4
1.3 Transfer matrix and Hamiltonian 9
1.4 Numerical methods: TRG and DMRG 14
1.5 Cold atoms in optical lattices 17
1.6 Equilibration and thermalization in quantum systems 19

2 Gauge-invariant reformulation for the Abelian-Higgs model **25**
2.1 Introduction 25
2.2 The Abelian Higgs model and the Polyakov loop 28
2.2.1 The model and its gauge-invariant reformulation 28
2.2.2 The large λ limit and the transfer matrix 32
2.2.3 The Polyakov loop 35
2.2.4 The energy gap and the conjectured finite size scaling 38
2.3 The time coninuum limit 40
2.3.1 The spin-S Hamiltonian 41
2.3.2 H with the Polyakov loop 43
2.3.3 The charge representation 44
2.4 Spin truncation and finite-size scaling 47
2.4.1 The O(2) limit 47
2.4.2 Finite size scaling of energy gap 49
2.5 Replacing the Polyakov loop by special boundary conditions 54
2.5.1 Isotropic coupling 54
2.5.2 Continuous-time limit 55
2.6 Conclusions 56

3 Quantum simulation of Abelian Higgs model in optical lattices 59
3.1 Introduction . . . 59
3.2 The two-species Bose-Hubbard model . . . 61
3.2.1 The O(2) model . . . 62
3.2.2 The $1 \ll \beta_{pl} \ll \kappa_\tau$ limit of the Abelian Higgs model . . . 64
3.3 The multi-leg ladder with a single atom along a rung . . . 65
3.4 Experimental implementation for the multi-leg ladder . . . 70
3.4.1 Quadratic interactions in a ladder . . . 70
3.4.2 Imperfections due to decoherence . . . 74
3.4.3 Measurement of the energy gap . . . 75
3.4.4 Experimental numbers . . . 76
3.5 Conclusions . . . 78

4 Probing the conformal Calabrese-Cardy scaling with cold atoms 79
4.1 Introduction . . . 79
4.2 The model and the quantum simulator . . . 82
4.3 The second order Rényi entropy . . . 83
4.3.1 The dependence of fitting parameters on J/U . . . 85
4.3.2 Finite temperature effects . . . 86
4.3.3 $\mathbf{J/U = 0.1}$ . . . 87
4.4 Experimental setup . . . 89
4.5 Conclusion . . . 93

5 Quantum Joule Expansion of One-dimensional Systems 96
5.1 Introduction . . . 96
5.2 The Models . . . 98
5.3 Weights in Ensembles . . . 101
5.4 Entropy For Ensembles . . . 104
5.4.1 Von Neumann Entropy . . . 105
5.4.2 The second order Rényi entropy . . . 109
5.5 Reduced Density Matrices . . . 115
5.6 Momentum Distribution Function . . . 126
5.7 The Effective Temperature . . . 131
5.8 Conclusion . . . 132

6 Conclusions 136

Bibliography 139

A Experimental implementations for the two-species Bose-Hubbard model 157
A.1 ^{87}Rb - ^{41}K mixtures on an optical lattice . . . 158
A.2 Bosons in two hyperfine states . . . 160
A.3 Ladder systems with double-well potentials . . . 162

B Perturbation theory for the two-species Bose-Hubbard model **165**
B.1 Some preliminaries 165
B.2 Two-species Bose-Hubbard model under strong coupling expansion 167

C Finite temperature effects in entanglement entropy of the Bose-Hubbard model **175**
C.1 BH with OBC, $J/U = 0.05, 0.2, T = 0.02, 0.04$ 176
C.2 $J/U = 0.1$ 180
C.3 Scaling Dimension Δ 182

D The Abelian Higgs model with a topological term **187**

List of Figures

1.1 The structure of square lattice. The matter fields are on vertices and the gauge fields are on links. A plaquette term is a product of gauge fields around a plaquette anticlockwise. 8

2.1 The configurations of 2-connected plaquettes, 3-connected plaquettes and 4-connected plaquettes in Eq. (2.18). 31
2.2 The basic B and A tensors (in brown and green, respectively, colors online). The $A^{(s)}$ are attached to the horizontal (spatial) links of the lattice. The $A^{(\tau)}$ are attached the vertical (temporal) links. The product of the tensors in yellow shaded area form a $\mathbb{B}$ tensor. The product of the tensors in blue shaded area form a $\mathbb{A}$ tensor. [12] 34
2.3 (color online) The Polyakov loop (arrows pointing up) and the matter loop (arrows pointing down) composed of matter charges and plaquette quantum numbers for a) 00BC and b) 10BC without the Polyakov loop. Additional columns of zeros or ones are implicit. The dotted line indicates the wrapping in the Euclidean time direction. [241] 37
2.4 (Color online) Energy gaps of O(2) Hamiltonian with spin truncations 1 - 4 in the thermodynamic limit, as a function of Y. 46
2.5 The enegy gap in the O(2) limit with $N_s = 32$ in field representation as a function of X. [213] 48
2.6 The enegy gap in the O(2) limit with $X = 2$ in plaquette quantum number representation as a function of $1/N_s$ for different spin-truncations. [213] . . 49
2.7 The enegy gap in the O(2) limit with a spin-6 truncation in the plaquette quantum number representation and link quantum number representation as a function of $1/N_s$. Here $N_s = 8, 16, ..., 64$ with $X = 2$ fixed. [213] 50
2.8 (color online) $N_s\Delta E$ versus $g^2N_s^2$ for the gap ΔE created by the insertion of the Polaykov loop (lower set) or an external electric field (10 boundary conditions, upper set). Open (filled) markers represent Lagrangian (Hamiltonian) data. The choices of parameters, units and methods for both of the 24 datasets are explained in the text. The black line represents the function $\Delta E N_s = \sqrt{(gN_s/4)^2 + 0.25}$. [241] 51

2.9 (color online) The same as Fig. 2.8, but plot $N_s\Delta E$ versus gN_s, only with Hamiltonian data for $X = 2$ (top). The same data as top figure, but plot ΔE versus g only for OBC (bottom). 52

3.1 $O(2)$ with $\tilde{J}/\tilde{U} = 0.1$ and Bose-Hubbard spectra for $L = 2$ with $\tilde{\mu} = 0.02$ (left) and $L = 4$ with $\tilde{\mu} = 0$ (right). [12] 63
3.2 Abelian-Higgs model with $\tilde{X}/\tilde{U} = 0.1$, $\tilde{Y}/\tilde{U} = 0.1$ and the corresponding Bose-Hubbard spectra for $L = 2$ (left) and $L = 4$ (right). [12] 64
3.3 (color online) Multi-leg ladder implementation for spin-2. The upper part shows the possible m_z-projections. Below, we show the corresponding realization in a ladder within an optical lattice. The atoms (green disks) are allowed to hop within a rung with a strength J, while no hopping is allowed along the legs. The lattice constants along rungs and legs are a_r and a_l respectively. Coupling between atoms in different rungs is implemented via an isotropic Rydberg-dressed interaction V with a cutoff distance R_c (marked by blue shading). [241] 66
3.4 (color online) Quadratic interactions on an asymmetric ladder for $s = 2$. The isotropic Rydberg-dressed potential (dashed blue line) is sampled at different distances occurring in the ladder (blue points). Interactions between atoms in different rungs separated by $\Delta i = |i - i'|$ occur in groups. The inset shows the approximate quadratic dependence for $\Delta i = 1$ versus distance $\Delta m = |m - m'|$ within a rung compared to a true quadratic interaction (red solid line). The parameters used are $R_c = a_l = 7\,a_r$. [241] 68
3.5 (color online) Data collapse for the quantum magnetic susceptibility of the quantum Ising chain with the known rescaling $\chi^{quant.\prime} = \chi^{quant.} N_s^{-(1-\eta)}$ versus $\lambda' = N_s^{1/\nu}(\lambda - 1)$. The reduced magnetic field $h' = hN_s^{15/8} = 1$ for all three system sizes. [241] 69
3.6 (color online) $N_s\Delta E$ obtained from the ladder Hamiltonians with NNNRI 1.5% of NNRI (open markers). When mapping from the spin Hamiltonians to the ladder systems, the energy gap between 10BC and 00BC systems (left) is more robust to NNNRI than the energy gap between PL+00BC and 00BC systems (right). We can correct the ground state energy by subtracting the ground state expectation value of NNNRI from it (filled markers). The solid lines are the collapse lines from the spin Hamiltonians. [241] 74

4.1 S_2 for $O(2)$ with $N_s = 16$ and OBC. Laid over top are the BH boundaries between particle number sectors. [214] 83
4.2 The A values from fits to S_2 with open boundary conditions for Bose-Hubbard data (green triangles online) and $O(2)$ spin model data with a spin-1 truncation (blue circles online) at half-filling. The horizontal line is the conformal field theory prediction. The A values were extracted from a fit to Eq. (4.3) with a correction term proportional to $1/\ln^2(N_s)$. The farthest point to the left is at $J = 0.005$, and the lines through the data are meant to guide the eye. [214] 85

4.3 The second order Rényi entropy, S_2, as a function of the logarithm of system size with a finite temperature and $l = N_s/2$. Here $U = 1$ and $T = 0.04$ is shown. The lines through the data points are fits using Eq. (4.3) with one addition term linear in the system size. The $J = 0.05$ data used sampling methods however the errors are smaller than the markers. [214] 87
4.4 (top) S_2 at half-filling with OBC for $O(2)$ and BH with $J/U = 0.1$. The solid lines are the fits for BH and $O(2)$. (bottom) Values of A as a function of the maximal value of N_s used in the fit, the band represents a positive departure of 5 percent from the expected value 0.125. [214] 88
4.5 Measuring entanglement entropy in optical lattices. a) Two copies of a quantum state $|\Psi\rangle$ interfere under a beamsplitter operation, and site-resolved number measurements reveal the local parity $\hat{P}$ and entanglement entropy. b) Proposed state preparation for BH systems at half-filling, here for 4 atoms on 8 sites. Particles indicated by wavefunctions (blue online) are initialized in a deep optical lattice, where the local environment can be shaped via harmonic confinement and sharp features projected with a spatial light modulator. As the lattice depth is reduced, the particles delocalize but are confined by repulsive walls. [214] 90
4.6 S_2 at half-filling for BH with $J/U = 0.1$ (triangles, orange online) and SGD with random Gaussian fluctuations with $\sigma_{S_2} = 0.02$ (circles, blue online). (left): vs. $\ln(N_s)$ for a subsystem of size $N_s/2$ with the solid line corresponding to a fit of the SGD from Eq. (4.3). (right): vs. the subsystem size ℓ for $N_s = 8$; the solid line corresponds to a fit of the SGD using the formulas of Ref. [232]. Same quantities for $T = 0.2J$ (squares, red online) and $T = 0.4J$ (diamonds, cyan online). [214] 93

5.1 (Color online) Two-dimensional histograms for the weights of eigenstates in the DE, W_n^d (a,c,e) and those in the corresponding CE, W_n^c (b,d,f). Results are for spinless fermions with initial inverse temperatures $\beta_0 = 0.1$ (a), $\beta_0 = 0.4$ (c) and $\beta_0 = 1$ (e). The corresponding CE with effective inverse temperatures are shown in (b,d,f). The color scale represents the number of states per unit area. The dashed lines in the left column are translations of the lines from the right column, indicating the slopes in the right column. 101
5.2 (Color online) Same as Fig. 5.1, but for bosons with 20 sites, 5 particles and $U = 3$. 102
5.3 (Color online) The von Neumann entropy of the reduced density matrix containing left l_A sites for the initial thermal state (blue circle), the state at long time $tJ = 6000$ (orange cross), the diagonal ensemble (green square) and the canonical ensemble (red inverted triangle). Results are for spinless fermions with initial inverse temperatures $\beta_0 = 0.1$ (a), $\beta_0 = 0.4$ (b), $\beta_0 = 1$ (c) and $\beta_0 = 10$ (d). The green dashed lines are linear fits of the first 3 subsystems for the initial states. The black dotted lines are linear fits of the first 3 subsystems for the canonical ensemble density matrices. 105
5.4 (Color online) Same as Fig. 5.3 but for bosons with initial inverse temperatures $\beta_0 = 0.01$ (a), $\beta_0 = 0.1$ (b), $\beta_0 = 1$ (c) and $\beta_0 = 10$ (d). 106

5.5 (Color online) Same as Fig. 5.3, but for the second order Rényi entropy. . 109
5.6 (Color online) The difference between time-averaged Rényi entropy $\bar{S}_{2A}$ and the DE Rényi entropy S^d_{2A} as a function of initial second order Rényi entropy. The results are for spinless fermions, three subsystems with $l_A = 9, 10, 11$. The inset shows the initial second order Rényi entropy as a function of initial temperature T_0. The yellow markers depict the results for $tJ = 6000$. . . . 112
5.7 (Color online) The difference between time-averaged Rényi entropy $\bar{S}_{2A}$ and the DE Rényi entropy S^d_{2A} for $l_A/L = 1/2$ as a function of the system size. The results are for spinless fermions, three initial inverse temperatures $\beta_0 = 0.1, 0.4, 1.0$. The insets show the initial second order Rényi entropy (a) and the diagonal second order Rényi entropy (b) as a function of the system size. The yellow markers depict the results for $tJ = 6000$. 114
5.8 (Color online) Variance of S^t_{2A} in time for $tJ = 81, 82, ..., 200$, as a function of $S_2^{\beta_0}$. The results are for spinless fermions, subsystems with $l_A = 9, 10, 11$. The inset shows the same quantity with $l_A = 10$ but as a function of system size at temperatures $\beta_0 = 0.1, 0.4, 1.0$. 115
5.9 (Color online) Logarithm of eigenvalues of reduced density matrices for the canonical ensemble, the diagonal ensemble and the time-evolved state at $tJ = 6000$, compared with the weights in the canonical ensemble constructed by the Hamiltonian for the subsystem $\hat{H}_A$. The subsystem contains the left six sites of the lattice. The results are for spinless fermions with the initial temperature $\beta_0 = 0.1$ (a) and bosons with the initial temperature $\beta_0 = 0.01$ (b). In each subplot, from top to bottom, the linearly arranged points represent zero, one, two, three, four and five particle states respectively. . . 116
5.10 (Color online) The same with Fig. 5.9 but only for spinless fermions. The subsystem contains the left ten sites of the lattice. The initial temperatures are $\beta_0 = 0.1$ (a) and $\beta_0 = 0.4$ (b). Note that in (b), the point for the zero-particle state is very close to the one-particle states line. 117
5.11 (Color online) The same with Fig. 5.10, but for bosons with initial temperatures $\beta_0 = 0.01$ (a), $\beta_0 = 1$ (b). In (b), those points for zero, one, two, three and four particle states are shifted up by constants for better view. The inset shows the actual eigenvalues for the reduced density matrix of canonical ensemble without shift. 118
5.12 (Color online) Overlaps between eigenstates of reduced density matrices of $\hat{\rho}^t$ (a, d, g, j), $\hat{\rho}^d$ (b, e, h, k), $\hat{\rho}^c$ (c, f, i, l) and those of $\hat{H}_A$. The subsystem contains the left six sites in (a-c, g-i) and ten sites in (d-f, j-l). The results are for spinless fermions with initial inverse temperature $\beta_0 = 0.1$ (a-f) and $\beta_0 = 0.4$ (g-l). 119
5.13 (Color online) MDFs of the initial state, the time-evolved state at $tJ = 6000$, the DE and the corresponding CE as a function of momentum $k \in (-\pi, \pi)$. The results are for spinless fermions, with different initial inverse temperatures $\beta_0 = 0.1$ (a), $\beta_0 = 0.4$ (b), $\beta_0 = 1$ (c) and $\beta_0 = 10$ (d). 126
5.14 The same with Fig. 5.13 but for bosons. The initial inverse temperatures are $\beta_0 = 0.01$ (a), $\beta_0 = 0.1$ (b), $\beta_0 = 1$ (c) and $\beta_0 = 10$ (d). 127

5.15 The finite size scaling of the effective inverse temperature for spinless fermions. The lines from top to bottom, the initial inverse temperatures are $\beta_0 = 0.2, 0.1, 0, -0.1, -0.2$ respectively. The system sizes used are $L = 12, 16, 20, 24, 28$. The inset shows the effective inverse temperature as a function of the initial inverse temperature extrapolated to the thermodynamic limit. 130
5.16 The same plot with Fig. 5.15 for bosons. The system sizes used are $L = 8, 12, 16, 20, 24$. 131

A.1 (Color Online) Two-species (green and red) of bosons on species-dependent optical lattices (with the same color), taken from [248]. 159

C.1 S_2 at half-filling for BH with $J/U = 0.05$ (left) and $J/U = 0.2$ (right) v.s. $\ln(N_s)$. The solid lines corresponding to the fits with Eq. (C.1) plus a term linear with N_s. 177
C.2 δS_2 at half-filling for BH with $J/U = 0.05$ (left) and $J/U = 0.2$ (right) v.s. $\ln(N_s)$. The solid lines corresponding to the fits with Eq. (C.3). 178
C.3 δS_2 at half-filling for BH with $J/U = 0.05$ (left) and $J/U = 0.2$ (right) v.s. N_s. The thermal corrections of entanglement entropy for $J/U = 0.05$ is approximately linear with N_s, but not for $J/U = 0.2$. 179
C.4 $S_2(T = 0) + \delta S_2$ at half-filling for BH with $J/U = 0.05$ (left) and $J/U = 0.2$ (right) v.s. $\ln(N_s)$. Fits with Eq. (C.1) plus a term linear with N_s are also plotted. 180
C.5 S_2 at half-filling for BH with $J/U = 0.1$, pbc(left) and obc (right) v.s. $\ln(N_s)$. The solid lines corresponding to the fits with Eq. (C.1) plus a term linear with N_s. 181
C.6 δS_2 at half-filling for BH with $J/U = 0.1$, PBC (left) and OBC (right) v.s. $\ln(N_s)$. 181
C.7 $S_2(T = 0) + \delta S_2$ at half-filling for BH with $J/U = 0.1$, PBC (left) and OBC (right) v.s. $\ln(N_s)$. Fits with Eq. (C.1) plus a term linear with N_s are also plotted. 182
C.8 Linear fit on $\ln(\delta S_2)$ at half-filling for BH with $J/U = 0.1$, PBC (left) and OBC (right) v.s. $\frac{1}{N_s}$. The results from previous sections are $\Delta = 0.212711$ $(T = 0.02, PBC)$, $\Delta = 0.197151$ $(T = 0.04, PBC)$, $\Delta = 0.105331$ $(T = 0.02, OBC)$, $\Delta = 0.141869$ $(T = 0.04, OBC)$ 183
C.9 Linear fit on $\ln(\delta S_2)$ at half-filling for BH with $J/U = 0.1$, PBC (left) and OBC (right) v.s. $\frac{1}{N_s}$. The results from previous sections are $\Delta = 0.078691$ $(T = 0.02, J/U = 0.05, OBC)$, $\Delta = 0.132599$ $(T = 0.04, J/U = 0.05, OBC)$, $\Delta = 0.168277$ $(T = 0.02, J/U = 0.2, OBC)$, $\Delta = 0.221495$ $(T = 0.04, J/U = 0.2, OBC)$ 184
C.10 (Left) Energy gaps of Bose Hubbard chain with $J/U = 0.05$, OBC. (Right) The fit parameter As as a function of the number of fitting points. The last value of A_s is 0.309644, which gives $\Delta = 0.04928$. 184
C.11 (Left) Energy gaps of Bose Hubbard chain with $J/U = 0.1$, OBC. (Right) The fit parameter As as a function of the number of fitting points. The last value of A_s is 0.595647, which gives $\Delta = 0.09480$. 185

C.12 (Left) Energy gaps of Bose Hubbard chain with $J/U = 0.2$, PBC. (Right) The fit parameter As as a function of the number of fitting points. The last value of A_s is 0.840813, which gives $\Delta = 0.13382$. 185
C.13 (Left) Energy gaps of Bose Hubbard chain with $J/U = 0.2$, OBC. (Right) The fit parameter As as a function of the number of fitting points. The last value of A_s is 1.062028, which gives $\Delta = 0.16903$. 186

List of Tables

C.1 Values of scaling dimension Δ from fits of δS_2 v.s. $\ln(N_s)$, $\ln(\delta S_2)$ v.s. $1/N_s$ and m_{gap} v.s. $1/N_s$ 186

Chapter 1

Introduction

1.1 General remarks

Quantum Field Theory (QFT) is one of the most powerful tools to study modern physics. For small interactions, perturbative approaches are very successful with the help of Feynman diagrams. Because of the smallness of the fine structure constant, quantum electrodynamics (QED) can be treated perturbatively in almost all cases. Perturbative approaches also work for quantum chromodynamics (QCD), which is a non-Abelian gauge theory in the Standard Model of Particle Physics describing the strong interactions between quarks and gluons, at small distances due to the asymptotic freedom [148]. However, QCD enters the strong coupling regime at long distances, where the quarks are confined. A non-perturbative method is needed to tackle the problems in this regime. Lattice gauge theory (LGT) is the most well established non-perturbative approach to QCD, which can be traced back to K. Wilson's seminal work in 1974 on confinement of quarks [230]. It formulates gauge theories on a discretized spacetime where space and time are treated symmetrically

(Euclidean space-time), then field theories in d spatial and one time dimensions correspond to statistical mechanics in $d+1$ dimensions. Most importantly, it makes it possible to perform non-perturbative numeric Monte-Carlo (MC) simulations and then extrapolate the results to the continuum case. More details about LGT can be found in reviews [126, 127] and books [162, 53, 201, 186].

However, due to the exponential growth of Hilbert space, the size of the system that can be dealt with numerics on classical computer is very limited. And the sign problem in MC [143] prevents us from studying the most interesting part of QCD at high background density and finite temperature. To overcome this difficulty, there have been proposals to use ultra-cold atoms in optical lattices to quantum simulate LGTs. As Richard Feynman pointed out [72], we can use quantum systems as quantum simulators to simulate quantum physics. Although the universal quantum computer is still far away from us, it is not difficult to build analog quantum simulators in lab. With the remarkable advances in experimental techniques, experimentalists are able to accurately control atoms trapped in optical lattices and fine tune interactions between them. So artificial quantum systems engineered in optical lattices are good candidates for quantum simulators of LGTs. The goal of my work in this thesis is to design experimental setups that can be used to learn about the phase diagrams of LGT models and their real time evolution, which are difficult to study using conventional methods. But quantum simulation has its challenges too. The gauge theories in the Standard Model uses gauge bosons as force carriers to explain interactions between matter particles. When two matter particles exchange gauge bosons, the overall effect is a force influencing both of them. The gauge theories contain both matter fields and

gauge fields and satisfy the local gauge invariance. Most proposals [229, 245, 207, 247, 243, 116, 134, 135, 87] try to quantum simulate both matter fields and gauge fields on optical lattices, where both fermions on the vertices and bosons on the links are required. And approximations and mappings are needed to reproduce the local gauge invariance, which are often big challenges given current experimental techniques. Our approach is to directly work with a gauge-invariant formulation with only matter fields or only gauge fields where Gausss law is inherently fulfilled, derive the Hamiltonian by taking the time-continuum limit and design the quantum simulator with the simplest artificial model.

Another benefit brought by the remarkable advances in cold atom experiments is the theoretical and experimental study of the nonequilibrium dynamics in recent years. Quantum thermalization is one of the most important topics in this area. In 1929, the classical theory of statistical mechanics was reformulated quantum-mechanically by von Neumann [223], which openned the door to the study of quantum thermalization through the unitary dynamics of quantum systems. Later studies [109, 61, 86] show that quantum thermalization is closely related to random matrix theory [156, 93] and the eigenstate thermalization hypothesis (ETH) [206, 184] was proposed to understand it in finite quantum systems. For nonintegrable quantum systems with Wigner-Dyson level spacing distribution [191], ETH asserts that every eigenstate is thermal and, as a result, few-body observables thermalize [121, 237]. ETH has been verified for a variety of nonintegrable quantum systems [179, 178, 190, 20, 83, 120, 165, 119, 105, 121, 17, 203, 18, 159, 160, 237, 102], with exceptions when little entanglement in the eigenbasis results in equilibration without

thermalization[85]. A modified version of ETH for subdiffusive thermalization [147] and strong forms of ETH for reduced density matrix [81, 66] have been formulated recently.

The quantum quench protocol is often used in studies of nonequilibrium dynamics, where an initial state of the system is prepared at time $t = 0$, some parameters are then suddenly changed and the state is let to evolve under the new Hamiltonian. This operation involves a global quench [31, 33, 204, 178, 180, 96, 97, 203, 38], local quench [32, 68] or sudden expansion [181, 158, 182, 183, 36, 98, 113, 219, 185, 203, 233, 37, 220, 221, 222, 235, 101, 167, 196]. The initial states can be either pure states or any mixed state. The dynamics of sudden expansion has rich results including dynamical fermionization in the expansion of a Tonks-Girardeau gas [158, 222], hard-core bosons [182, 183, 235] or a Bose gas [37], quasi-condensation at finite momentum in hard-core bosons [181, 182, 183, 219, 220, 235], ballistic and diffusive expansion for bosons and fermions in one and two dimensions [113, 185, 219] and quantum distillation of singlons and doublons during the expansion [98, 233, 101, 196]. A time-dependent emergent local Hamiltonian can be constructed to analytically describe these nonequilibrium states as its eigenstates [221, 222, 235]. In this thesis, we discuss the equilibration and thermalization in the sudden expansion of an initially prepared thermal state of fermions or bosons confined in the half of the system, which is the quantum version of the Joule expansion.

1.2 The lattice regularization of scalar compact QED

Our first goal is to provide a proof of principle for analog quantum simulation of LGT. To choose the prime candidate for an experimental quantum simulation of a lattice

gauge theory, we want the model to be simple and at the same time have typical nonperturbative phenomena such as confinement of charges. The scalar QED (sQED) or the Abelian Higgs model satisfies these requirements. The phase structure is studied in [108], where they found phase transitions between confinement, Higgs and Coulomb phase. Before we proceed, please note that all of our discussions will be in Euclidean space-time, where time is purely imaginary by letting $t = -i\tau$. The real time physics can be restored by rotating $\pi/2$ anticlockwise in the complex time plane (Wick rotation) [162]. Following the notation in Ref. [108, 99], the action of sQED in Euclidean space-time is

$$\begin{aligned} S &= \int d^d x \Big\{ \frac{1}{4} F_{\mu\nu}(x) F^{\mu\nu}(x) + (D^\mu \phi^c(x))^\dagger D_\mu \phi^c(x) \\ &+ m_c^2 (\phi^c(x))^\dagger \phi^c(x) + \lambda_c \left[(\phi^c(x))^\dagger \phi^c(x) \right]^2 \Big\}, \end{aligned} \tag{1.1}$$

where $F_{\mu\nu}$ is the electromagnetic tensor, $D_\mu = \partial_\mu + igA_\mu$ is the covariant derivative with minimal coupling matter to the electromagnetic field, the index c on ϕ^c means "continuum". To obtain the lattice version of sQED, we should consider the d-dimensional position vector x as discrete on, for example, a square lattice, and do the following the steps,

$$\begin{aligned} \int d^d x &\rightarrow a^d \sum_x, \\ \phi^c(x) &\rightarrow \phi^c_x \equiv \phi^c(x), \\ \partial_\mu \phi^c(x) &\rightarrow \frac{1}{a} \left(\phi^c_{x+\hat{\mu}} - \phi^c_x \right), \\ 1 + iagA_{x,\hat{\mu}} &\rightarrow U_{x,\hat{\mu}} = e^{iagA_{x,\hat{\mu}}}, \\ D_\mu \phi^c(x) &\rightarrow \frac{1}{a} \left(U_{x,\hat{\mu}} \phi^c_{x+\hat{\mu}} - \phi^c_x \right), \\ F_{\mu\nu} F^{\mu\nu} &\rightarrow \frac{2}{a^4 g^2} \left(1 - Re \left(U_{x,\hat{\mu}} U_{x+\hat{\mu},\hat{\nu}} U^\dagger_{x+\hat{\nu},\hat{\mu}} U^\dagger_{x,\hat{\nu}} \right) \right), \end{aligned} \tag{1.2}$$

where a is the lattice spacing. The parameter g in Eq. (1.1) is the gauge coupling of the theory, which has the physical meaning of charge. The indices $\hat{\mu}, \hat{\nu}$ are components of the unit vectors in d-dimensional space-time. The gauge part of the continuum theory produces the plaquette term on a lattice,

$$S_g = \int d^d x \left\{ \frac{1}{4} F_{\mu\nu}(x) F^{\mu\nu}(x) \to \frac{\beta}{2} \sum_{x,\mu\nu} \left(1 - Re \left(U_{x,\hat{\mu}} U_{x+\hat{\mu},\hat{\nu}} U^{\dagger}_{x+\hat{\nu},\hat{\mu}} U^{\dagger}_{x,\hat{\nu}} \right) \right), \tag{1.3}$$

where $\beta = a^{d-4}/g^2$. The Higgs part of the action is

$$\begin{aligned} S_H &= a^d \sum_x \left\{ \sum_{\mu=0}^{d-1} \frac{1}{a^2} \left[U_{x,\hat{\mu}} \phi^c_{x+\hat{\mu}} - \phi^c_x \right]^{\dagger} \left[U_{x,\hat{\mu}} \phi^c_{x+\hat{\mu}} - \phi^c_x \right] + m_c^2 \phi^{c\dagger}_x \phi^c_x + \lambda_c \left[\phi^{c\dagger}_x \phi^c_x \right]^2 \right\} \\ &= a^{d-2} \sum_{x,\mu} \left[\phi^{c\dagger}_{x+\hat{\mu}} \phi^c_{x+\hat{\mu}} + \phi^{c\dagger}_x \phi^c_x - \phi^{c\dagger}_{x+\hat{\mu}} U^{\dagger}_{x,\hat{\mu}} \phi^c_x - \phi^{c\dagger}_x U_{x,\hat{\mu}} \phi^c_{x+\hat{\mu}} \right] \\ &\quad + a^d \sum_x \left[m_c^2 \phi^{c\dagger}_x \phi^c_x + \lambda_c \left[\phi^{c\dagger}_x \phi^c_x \right]^2 \right] \end{aligned} \tag{1.4}$$

We define the lattice version of the field as

$$a^{\frac{d}{2}-1} \phi^c_x = \sqrt{\kappa} \phi_x. \tag{1.5}$$

Note that the dimension of the continuous field is $[\phi^c] = [a]^{1-d/2}$, the left hand side of Eq. (1.5) is dimensionless, if κ is dimensionless, the lattice field is also dimensionless. Then Eq. (1.4) becomes

$$\begin{aligned} S_H &= -\kappa \sum_{x,\mu} \left[\phi^{\dagger}_{x+\hat{\mu}} U^{\dagger}_{x,\hat{\mu}} \phi_x + \phi^{\dagger}_x U_{x,\hat{\mu}} \phi_{x+\hat{\mu}} \right] \\ &\quad + \sum_x \left[(2d\kappa + a^2 m_c^2 \kappa) \phi^{\dagger}_x \phi_x + \lambda_c \kappa^2 a^{4-d} \left(\phi^{\dagger}_x \phi_x \right)^2 \right] \end{aligned} \tag{1.6}$$

Also note that the dimesion of λ_c is $[a]^{d-4}$, then the coefficients are all dimensionless. To simplify further, we define $\lambda = \lambda_c \kappa^2 a^{4-d}$, and complete a square like $\left(\phi^{\dagger}_x \phi_x - 1 \right)^2$. Note that Eq. (1.5) does not determine κ and ϕ_x, we can let the coefficient of $\phi^{\dagger}_x \phi_x$ be 1, which

is $\kappa(2d + a^2 m_c^2) + 2\lambda = 1$. These steps are just to rescale the radial length of the lattice field. Then for given m_c^2, λ_c, g and lattice spacing a, the lattice coupling constants β, κ, λ are unique. Finally by dropping irrelevant constants, we obtain the lattice version of sQED

$$\begin{aligned} S &= S_g + S_h + S_\lambda \\ &= -\beta \sum_{x,\mu<\nu} Re\left(U_{x,\hat{\mu}} U_{x+\hat{\mu},\hat{\nu}} U^\dagger_{x+\hat{\nu},\hat{\mu}} U^\dagger_{x,\hat{\nu}}\right) - \kappa \sum_{x,\mu} \left[\phi^\dagger_{x+\hat{\mu}} U^\dagger_{x,\hat{\mu}} \phi_x + \phi^\dagger_x U_{x,\hat{\mu}} \phi_{x+\hat{\mu}}\right] \\ &\quad + \sum_x \left[\lambda\left(\phi^\dagger_x \phi_x - 1\right)^2 + \phi^\dagger_x \phi_x\right] \end{aligned} \tag{1.7}$$

where S_g denotes the gauge part (the first summation), S_h the hopping part (the second summation), S_λ the self-interaction part (the third summation). Note that for $(3+1)$-dimensional Euclidean space-time, $\beta = 1/g^2$. And for $(1+1)$-dimensional Euclidean lattice, $\beta = 1/a^2 g^2$, with which we will deal in the following chapters.

For anisotropic space-time, we can repeat the same calculation. Note that the lattice spacing in imaginary time direction a_τ and that in spatial direction a are different. The differences between this and Eq. (1.2) are

$$\begin{aligned} \int d^d x &\rightarrow a_\tau a^{d-1} \sum_x, \\ \partial_\tau \phi^c(x) &\rightarrow \frac{1}{a_\tau}\left(\phi^c_{x+\hat{\tau}} - \phi^c_x\right), \\ 1 + i a_\tau g A_{x,\hat{\tau}} &\rightarrow U_{x,\hat{\tau}} = e^{i a_\tau g A_{x,\hat{\tau}}}, \\ D_\tau \phi^c(x) &\rightarrow \frac{1}{a_\tau}\left(U_{x,\hat{\tau}} \phi^c_{x+\hat{\tau}} - \phi^c_x\right), \\ F_{\tau\nu} F^{\tau\nu} &\rightarrow \frac{2}{a^2 a_\tau^2 g^2}\left(1 - Re\left(U_{x,\hat{\tau}} U_{x+\hat{\tau},\hat{\nu}} U^\dagger_{x+\hat{\nu},\hat{\tau}} U^\dagger_{x,\hat{\nu}}\right)\right). \end{aligned} \tag{1.8}$$

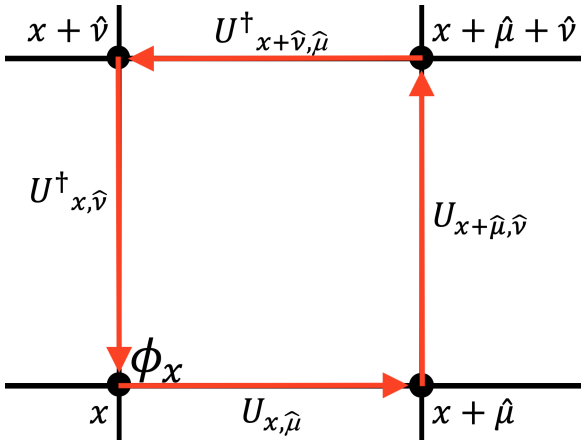

Figure 1.1: The structure of square lattice. The matter fields are on vertices and the gauge fields are on links. A plaquette term is a product of gauge fields around a plaquette anticlockwise.

And let

$$\begin{aligned}\sqrt{a_\tau a^{d-3}}\phi^c_x &= \sqrt{\kappa_s}\phi_x,\\ \sqrt{a^{d-1}/a_\tau}\phi^c_x &= \sqrt{\kappa_\tau}\phi_x.\end{aligned} \tag{1.9}$$

Then the action of sQED in anisotropic Euclidean space-time is

$$\begin{aligned}S &= S_g + S_h + S_\lambda\\ &= -\beta_s \sum_{x,0<\mu<\nu} Re\left(U_{x,\hat{\mu}}U_{x+\hat{\mu},\hat{\nu}}U^\dagger_{x+\hat{\nu},\hat{\mu}}U^\dagger_{x,\hat{\nu}}\right) - \beta_\tau \sum_{x,\nu>0} Re\left(U_{x,\hat{\tau}}U_{x+\hat{\tau},\hat{\nu}}U^\dagger_{x+\hat{\nu},\hat{\tau}}U^\dagger_{x,\hat{\nu}}\right)\\ &\quad -\kappa_s \sum_{x,\mu>0}\left[\phi^\dagger_{x+\hat{\mu}}U^\dagger_{x,\hat{\mu}}\phi_x + \phi^\dagger_x U_{x,\hat{\mu}}\phi_{x+\hat{\mu}}\right] - \kappa_\tau \sum_x \left[\phi^\dagger_{x+\hat{\tau}}U^\dagger_{x,\hat{\tau}}\phi_x + \phi^\dagger_x U_{x,\hat{\tau}}\phi_{x+\hat{\tau}}\right]\\ &\quad + \sum_x \left[\lambda\left(\phi^\dagger_x\phi_x - 1\right)^2 + \phi^\dagger_x\phi_x\right],\end{aligned} \tag{1.10}$$

where $\beta_s = a_\tau a^{d-5}/g^2$, $\beta_\tau = a^{d-3}/a_\tau g^2$, $\lambda = \lambda_c\kappa_s^2 a^{5-d}/a_\tau$, $2(d-1)\kappa_s + 2\kappa_\tau + a^2\kappa_s m_c^2 + 2\lambda = 1$ and $\kappa_s/\kappa_\tau = a_\tau^2/a^2$.

Fig. 1.1 is a visualization of the lattice version of the action. The matter fields ϕ_x are on the vertices and the gauge fields $U_{x,\hat{\mu}}$ are on the links. The plaquette term is a

product of four gauge fields on the links anticlockwise around a plaquette. The hopping terms are vertex-link-vertex interactions, which explicitly exhibits the key idea of gauge theory that matter particles interact with each other via gauge fields. Note that in $(1+1)$-dimensional space-time, there is no spatial plaquette term, we only have $\beta_\tau = 1/aa_\tau g^2$. Finally, the path integral quantization is

$$Z = \int D\phi^\dagger D\phi DU e^{-S}. \tag{1.11}$$

1.3 Transfer matrix and Hamiltonian

We discuss how to obtain the Hamiltonian formulation for sQED in this section. We indeed need the Hamiltonian of the theory because the experimentally engineered quantum systems are in spatial lattices but continuous in real time. We need to take the time continuum limit for Eq. (1.10) and find the Hamiltonian before thinking about how to quantum simulate it. We can also directly canonically quantize the theory, but we will use the method of transfer matrix in the following chapters. This method is closely related to the Feynman path integral formulation.

The Feynman path integral was initially formulated to represent the transition amplitude from an initial state to a final state as a weighted sum of all possible histories of the system. The Lagrangian enters in the weight $e^{iS/\hbar}$ naturally. In the classical limit $\hbar \to 0$, a unique classical path is singled out. In field theory, the same formulation can be obtained by functional integrals of the weighted paths with respect to classical fields. The transition amplitude calculated by the path integral is equivalent to the result from canonical quantization of the field. See text books [148, 162, 53] for details about the path

integral quantization. Eq. (1.11) is the total weight for lattice gauge theories in Euclidean space-time, which contains functional integrals for both matter fields and gauge fields. The path integral can also be expressed in terms of the transfer matrix. Similar to what we do in path integrals of quantum mechanics, for two field configurations on nearest two time slices, $(\Psi_{na_\tau}, \mathcal{U}_{na_\tau})$ and $(\Psi_{(n+1)a_\tau}, \mathcal{U}_{(n+1)a_\tau})$, let

$$S = \sum_n S\left[(\Psi_{na_\tau}, \mathcal{U}_{na_\tau}), (\Psi_{(n+1)a_\tau}, \mathcal{U}_{(n+1)a_\tau})\right], \tag{1.12}$$

where the summation is only over the imaginary time direction. The elements of the transfer matrix are defined by

$$\mathbf{T}\left[(\Psi_{na_\tau}, \mathcal{U}_{na_\tau}), (\Psi_{(n+1)a_\tau}, \mathcal{U}_{(n+1)a_\tau})\right] = e^{-S\left[(\Psi_{na_\tau}, \mathcal{U}_{na_\tau}), (\Psi_{(n+1)a_\tau}, \mathcal{U}_{(n+1)a_\tau})\right]}, \tag{1.13}$$

If periodic boundary condition (PBC) is applied in time and the size of the lattice in time is N_τ, Eq. (1.11) can be rewritten as

$$Z = \mathrm{Tr}(\mathbf{T}^{N_\tau}) \tag{1.14}$$

The transfer matrix is a time evolution operator in Euclidean space-time. The Hamiltonian is then defined by

$$\mathbf{T} = e^{-a_\tau H}, \tag{1.15}$$

Then

$$Z = \mathrm{Tr}(e^{-H/T}), \tag{1.16}$$

is equivalent to the partition function in statistical mechanics with $1/T = a_\tau N_\tau$ the inverse temperature.

If we found the operator expression for the transfer matrix, then the quantum Hamiltonian in the time continuum limit can be found by

$$H = -\lim_{a_\tau \to 0} \frac{1}{a_\tau} \ln \mathbf{T}. \tag{1.17}$$

This is equivalent to canonical quantization for the action, but it is convenient to find the Hamiltonian when the transfer matrix is easy to obtain and canonical quantization is difficult. We will use the method of transfer matrix to find the Hamiltonian when we apply the duality method to find the discrete tensor reformulation of sQED, see Chapter 2.

Let us first see what the Hamiltonian from canonical quantization looks like. We only consider the limit $\lambda \to \infty$, where the radial length of the matter field is fixed to 1. Let $\phi_x = e^{i\theta_x}$ and use temporal gauge $A_\tau = 0$ or $U_{x,\hat{\tau}} = 1$. By squeezing lattice spacing in time, the terms containing time derivative in the action are

$$\begin{aligned}
& -\beta_\tau \sum_{x,\nu>0} Re\left(U_{x,\hat{\tau}} U_{x+\hat{\tau},\hat{\nu}} U^\dagger_{x+\hat{\nu},\hat{\tau}} U^\dagger_{x,\hat{\nu}}\right) - \kappa_\tau \sum_x \left[\phi^\dagger_{x+\hat{\tau}} U^\dagger_{x,\hat{\tau}} \phi_x + \phi^\dagger_x U_{x,\hat{\tau}} \phi_{x+\hat{\tau}}\right] \\
= \quad & -\beta_\tau \sum_{x,\nu>0} cos(agA_{x+\hat{\tau},\hat{\nu}} - agA_{x,\hat{\nu}}) - 2\kappa_\tau \sum_x cos(\theta_{x+\hat{\tau}} - \theta_x) \\
= \quad & \frac{1}{2}\beta_\tau \sum_{x,\nu>0} (agA_{x+\hat{\tau},\hat{\nu}} - agA_{x,\hat{\nu}})^2 + \kappa_\tau \sum_x (\theta_{x+\hat{\tau}} - \theta_x)^2 \\
\to \quad & \int d\tau \left[\frac{1}{2}\beta_\tau a_\tau \sum_{r,\nu>0} (ag\dot{A}_{x,\hat{\nu}})^2 + \kappa_\tau a_\tau \sum_r (\dot{\theta}_x)^2\right],
\end{aligned} \tag{1.18}$$

where $x = (\tau, r)$ and r means spatial coordinates. The conjugate momentum for dimensionless angular variables $agA_{x,\hat{\nu}}$ and θ_x are $E_{x,\hat{\nu}} = \beta_\tau a_\tau ag\dot{A}_{x,\hat{\nu}}$ and $Q_x = 2\kappa_\tau a_\tau \dot{\theta}_x$ respectively. So Eq. (1.18) becomes

$$\int d\tau \left[\frac{1}{2\beta_\tau a_\tau} \sum_{r,\nu>0} (E_{x,\hat{\nu}})^2 + \frac{1}{4\kappa_\tau a_\tau} \sum_r (Q_x)^2\right] \tag{1.19}$$

Finally, the dimensionless Hamiltonian of sQED is

$$\begin{aligned} a\hat{H} &= \frac{D}{2}\sum_{r,\nu>0}(\hat{E}_{r,\hat{\nu}})^2 - \frac{W}{2}\sum_{r,0<\mu<\nu}\left(\hat{U}_{r,\hat{\mu}}\hat{U}_{r+\hat{\mu},\hat{\nu}}\hat{U}^{\dagger}_{r+\hat{\nu},\hat{\mu}}\hat{U}^{\dagger}_{r,\hat{\nu}} + h.c.\right) \\ &+ \frac{Y}{2}\sum_{r}(\hat{Q}_r)^2 - \frac{X}{2}\sum_{r,\mu>0}\left[\hat{\phi}^{\dagger}_{r+\hat{\mu}}\hat{U}^{\dagger}_{r,\hat{\mu}}\hat{\phi}_r + \hat{\phi}^{\dagger}_{r}\hat{U}_{r,\hat{\mu}}\hat{\phi}_{r+\hat{\mu}}\right], \end{aligned} \tag{1.20}$$

where $D = a/\beta_\tau a_\tau, W = a\beta_s/a_\tau, Y = a/2\kappa_\tau a_\tau, X = 2a\kappa_s/a_\tau$. In $(3+1)$-dimensional space-time, $D = g^2$, $W = 1/g^2$. Then the first row of Eq. (1.20) is the pure gauge Kogut-Susskind Hamiltonian [125]. In $(1+1)$-dimensional space-time, $D = a^2g^2$, $W = 1/a^2g^2$, but there is no plaquette interaction in spatial direction. Eq. (1.9) means $\kappa_s = R^2 a_\tau a^{d-3}, \kappa_\tau = R^2 a^{d-1}/a_\tau$ where R is some constant making κ_τ and κ_s dimensionless. So in Eq. (1.20), $Y = 1/2a^{d-2}R^2, X = 2R^2a^{d-2}$. Note that we now have $DW = YX = 1$.

The eigenstates of operators $\hat{E}$ and $\hat{Q}$ are

$$\begin{aligned} \hat{E}\,|m\rangle &= m\,|m\rangle\,, \\ \hat{Q}\,|n\rangle &= n\,|n\rangle\,, \end{aligned} \tag{1.21}$$

where the eigenvalues have physical meaning of electric field and charge, respectively. Note that the plaquette terms in the Hamiltonian is the magnetic field in the space continuum limit. The commutation relation between operators are

$$\begin{aligned} \left[\hat{E}, \hat{U}\right] &= \hat{U}, \\ \left[\hat{Q}, \hat{\phi}\right] &= \hat{\phi} \end{aligned} \tag{1.22}$$

Then $\hat{U}$ is the raising operator of electric field $\hat{U}\,|m\rangle = |m+1\rangle$, $\hat{\phi}$ is the raising operator of charge $\hat{\phi}\,|n\rangle = |n+1\rangle$.

The Hamiltonian is locally gauge invariant. Under the local gauge transformation $\hat{\phi}_r \to \hat{V}_r\hat{\phi}_r, \hat{U}_{r,\hat{\mu}} \to \hat{V}_r\hat{U}_{r,\hat{\mu}}\hat{V}^{\dagger}_{r+\hat{\mu}}$, Eq. (1.20) obviously does not change. There must be local

operators that commute with the Hamiltonian. They are the generators of the local gauge transformation

$$\hat{G}_r = \sum_{\mu>0} \left(\hat{E}_r - \hat{E}_{r-\hat{\mu}} \right) - \hat{Q}_r \tag{1.23}$$

The eigenvalues of $\hat{G}_r$ are conserved quantum numbers, which correspond to the Gauss's Law. More comprehensive discussions for general LGTs can be found in [245, 242].

Although it is standard, the method of canonical quantization to find the Hamiltonian needs a lot of physical reasoning. We will use a different method, named the duality method, to find the transfer matrix and then the Hamiltonian. According to Pontryagin duality theorem [175], as the variables in the action of sQED are all compact, we can do Fourier transform to express the integral Eq. (1.11) in terms of discrete dual variables. The Gauss's Law will emerge naturally by integrating out the compact fields. For a comprehensive introduction of the duality method applied to LGTs, please see our collaborator's thesis [216]. But it is easy to understand when you go to Chapter 2 where there are explicit calculations with the duality method for sQED.

To conclude this section, let us briefly explain how confinement of charges emerges in the Hamiltonian (1.20). In the strong coupling regime $g^2 \gg 1$, the ground state of the Hamiltonian is approximately the state with zero electric field everywhere. Now consider creating a charge pair with distance R, this operation must at least create a string of nonzero electric field with length R by the constraint of Gauss's Law. Then there must be a energy cost proportional to the distance between the two charges. Therefore the charges are confined.

1.4 Numerical methods: TRG and DMRG

To give support to our experimental proposals, we perform numerical calculations, both for the lattice action in Euclidean space-time and for the time-continuum Hamiltonian, to verify the mapping and predict possible measurement outcomes. The calculations with Euclidean action are performed by the tensor renormalization group (TRG) algorithm. And the calculations with Hamiltonian are performed by the density matrix renormalization group (DMRG) algorithm.

The TRG calculations are done by our collaborator. I will not give much introduction to it. But I mention it here because the numerical results from TRG are compared to my DMRG results everywhere in this project. There are detailed introductions in our collaborator's thesis [216], I recommend that readers refer to it and its references. The basic idea is that if the path integral formulation can be expressed in terms of variables with discrete values, we can define tensors with those discrete variables as indices, attached to vertices and links (or links and plaquettes in the dual lattice). Then the path integral can be written as a trace of a product of all these tensors. The contraction of tensors can be done with position space renormalization group, by coarse graining the lattice. For example, we can define new tensors by contracting two nearest-neighbor tensors and attach them to the sites of the new coarse grained lattice. Of course the rank of the tensors will increase exponentially with the number of times of coarse graining we do. But we can truncate them to lower rank tensors by singular value decomposition (SVD) or higher order singular value decomposition (HOSVD) [58]. We can do this accompanied by a global optimization scheme to further decrease the truncation error.

DMRG is a very powerful tool to tackle low energy problems for one-dimensional systems or any other problems with low entanglement entropy. It was first invented by Steven R. White in [226, 227] and was quickly proven to be very successful in 1-d systems. In most cases the accuracy of the results can reach machine precision. But it was then found to be much more difficult to deal with two-dimensional systems. Later on, it was pointed out [138, 218] that the numerical resources needed in DMRG is related to the scaling of the entanglement entropy

$$S = -\mathrm{Tr}\rho_A \ln \rho_A \tag{1.24}$$

where ρ_A is the reduced density matrix of the subsystem A. A state with a dimension bigger than e^S is needed to represent the subsystem. According to the area law [67] of entanglement entropy for a gapped system, $S \sim L^{d-1}$, the dimension needed for 1-d systems would be very small, but it would be exponentially big for 2-d systems. For 1-d critical system, the entanglement entropy scales as $\frac{c}{6} \ln L$ (c is the central charge of the conformal field theory) [103, 218, 110, 30, 34] for open boundary condition (OBC), the dimension increases as $L^{c/6}$, we can still go to very big systems with laptop computers. The DMRG reformulated by the language of the matrix product state (MPS) was first presented in [169, 65]. Although its formalism seems to be more complicated, it provides more elegant graphical notations for beginners to understand quickly and the manipulation of MPS in programming is convenient. The basic idea of finite DMRG algorithm is that we parametrize the initial state with an arbitrary MPS, represent the Hamiltonian with a matrix product operator (MPO) [153, 76, 54], and minimize the expectation of energy by sequentially optimizing the two nearest-neighbor matrices from left to right and then right to left. After

each optimization, we do SVD for the two-site matrix, compress the rank of matrices by keeping the largest M singular values, renormalize the singular matrix and restore the form of MPS. The entanglement entropy can be calculated each time as a byproduct. This is called the two-site optimization and is stable. We can also do single-site optimization which is faster, but it is unstable and often stuck at local minima. In practice, we need to add a noise term to help the single-site optimization algorithm to jump out the local minima [228]. Every time we go back, we finish one sweep. Usually only a few sweeps are needed to reach high accuracy for gapped 1-d systems. More sweeps are needed for critical systems. Note that it doesn't work well if there is true degeneracy in the ground state of a finite system. The algorithm will not know which state to converge because they have the same energy. Near the degeneracy, maybe thousands of sweeps are needed.

For details of the algorithm and other algorithms including time evolving a MPS, finite temperature DMRG, infinite MPS, etc, please refer to the review [197]. I also recommend the documentation website of ITensor Library [1]. There are detailed explanations and sample codes about how to manipulate MPS and MPO. It also has the full DMRG layer with MPS optimization. Our DMRG calculations are performed with ITensor Library. In finite DMRG for ground states, we keep as many Schmidt states as possible to make sure the truncation error is less than 10^{-10}. In most cases, especially with OBC, we do enough sweeps until the energy difference between the last two sweeps is less than 10^{-12} and entropy difference less than 10^{-10}. The typical error is 10^{-8} in energy and 10^{-7} in entropy. For other hard cases like big systems with PBC, we make sure the last two sweeps have energy difference less than 10^{-9} and entropy difference less than 10^{-7}. In finite temperature

[1] https://itensor.org

DMRG calculation, we also set the truncation error in each SVD during the imaginary time evolution to less than 10^{-10}. These settings ensure that the error that comes from DMRG is negligible compared with other source of errors.

1.5 Cold atoms in optical lattices

Atoms can be maintained at temperatures very close to 0 (very low average velocities) by combinations of several experimental cooling techniques, and trapped in the locations of potential minima on optical lattices formed by the ac Stark effect of the interfering laser beams. The interaction parameters can be easily controlled and tuned in these artificial quantum systems. With the remarkable advances in experimental techniques, several lattice models studied in condensed matter physics for their relevance to complex materials have been engineered on optical lattices and tested in regimes where conventional computational methods are reliable. One well-known example of the high level of agreement between theory and experiment is the one-species Bose-Hubbard model, which describes quantum systems with spinless bosons on optical lattices, where details of the experimental time-of-flight pictures can be obtained with Quantum Monte Carlo worm algorithm calculations [212].

For more information on experimental physics of cold atoms, readers can refer to the good reviews [22, 48, 140, 92, 205, 52]. Among them, [22] reviews both theoretical and experimental progress of many-body physics in ultracold gases until 2008, focusing on strong-interaction regime realized by Feshbach resonances. And the phenomenon of Feshbach resonances in ultracold gases and their applcations can be found in [48]. [140, 92]

also review how optical lattice systems can be used to quantum simulate the physics in condensed matter as well as high energy physics. [205] reviews recent theoretical and experimental progress on one-dimensional systems with several ultracold atoms. [52] is a recent review on realizing topological band structures with cold atomic gases.

In particular, in our proposals for quantum simulation of sQED, we map the Hamiltonian to the Bose-Hubbard models or multi-leg ladder systems with atoms trapped in optical lattices and interacting with Rydberg-dressed interactions. The one species Bose-Hubbard model can be realized in optical lattices and its quantum phase transition from the superfluid phase to Mott insulator phase has been studied experimentally [107, 90]. Also see [152, 8] for the extended Bose-Hubbard model. The two-species Bose-Hubbard model can be realized with ^{87}Rb and ^{41}K Bose-Bose mixture [41, 209], where the interspecies interactions can be controlled by Feshbach resonances. The ladder systems have been realized experimentally [198, 46, 89, 6]. Identical copies of Bose-Hubbard chains can be prepared and the entanglement entropy and dynamics can be measured experimentally [106, 118]. The experimental scheme to measure arbitrary order of Rényi entropy, by measuring the parity of on-site occupation in states after a beam splitter operation between two copies of initial states, was proposed in [57]. Finally, the laser-excited Rydberg atoms can serve as a universal quantum simulator for systems with n-body interactions [224] and Rydberg-dressed atoms (a superposition of the ground state and the excited Rydberg state with small probability to be excited) can be used to generate nonlocal, long range interactions [111, 100, 176, 84, 239, 92]. A good review for Rydberg atoms could be [188].

1.6 Equilibration and thermalization in quantum systems

The general language describing the time evolution of a quantum system is the following. Let $\{|i\rangle\}$ be the eigenstates of the initial Hamiltonian, $\hat{H}_0 |i\rangle = e_i |i\rangle$ [$\hat{H}_0$ is the Hamiltonian before expansion in Chapter 5. An arbitrary initial state (pure or mixed) in this eigenbasis is given by

$$\hat{\rho}^0 = \sum_{i,j} \rho^0_{ij} |i\rangle \langle j| . \tag{1.25}$$

If it is a thermal state with an inverse temperature β_0, $\rho^0_{ij} = \delta_{ij}\rho^0_i$ with $\rho^0_i = e^{-\beta_0 e_i}/Z_0(\beta_0)$, and $Z_0(\beta_0) = \mathrm{Tr}\left(e^{-\beta_0 \hat{H}_0}\right)$ is the partition function.

Let $\{|m\rangle\}$ be the eigenstates of the final Hamiltonian $\hat{H}_F$ that drives the time evolution after a quantum quench, that is, $\hat{H}_F |m\rangle = E_m |m\rangle$. The initial state, written in this eigenbasis, is given by,

$$\begin{aligned} \hat{\rho}^0 &= \sum_{m,n} \rho^0_{mn} |m\rangle \langle n| \\ &= \sum_{m,n} \left(\sum_i \rho^0_{ij} \langle m|i\rangle \langle j|n\rangle \right) |m\rangle \langle n| \ , \end{aligned} \tag{1.26}$$

and contains diagonal ($m = n$) and off-diagonal ($m \neq n$) terms. The time-dependent density operator at time t during the expansion is

$$\hat{\rho}^t = \sum_{m,n} \rho^0_{mn} \exp[-it(E_m - E_n)] |m\rangle \langle n| . \tag{1.27}$$

If there is no degeneracy in the spectrum, which is generally true for nonintegrable systems [24], the long-time average of the density operator above will give the diagonal ensemble

(DE) [179] density matrix

$$\begin{aligned}\hat{\bar{\rho}} = \hat{\rho}^d &= \lim_{\tau\to\infty}\frac{1}{\tau}\int_0^\tau d\tau\hat{\rho}^t \\ &= \sum_m \rho^0_{mm}\left|m\right\rangle\left\langle m\right| \\ &= \sum_m W^d_m\left|m\right\rangle\left\langle m\right|. \end{aligned} \tag{1.28}$$

where ρ^0_{mm} is the weight W^d_m that the projector $\hat{P}_m = \left|m\right\rangle\left\langle m\right|$ has in the DE.

For an arbitrary observable $\hat{O} = O_{m'n'}\left|m'\right\rangle\left\langle n'\right|$, the time-dependent expectation value is,

$$\begin{aligned}\langle\hat{O}\rangle_t &= Tr(\hat{O}\hat{\rho}^t) \\ &= \sum_{m,n} O_{mn}\rho^0_{nm}\exp[-it(E_n - E_m)] \\ &= \langle\hat{O}\rangle_d + \sum_{m\neq n} O_{mn}\rho^0_{nm}\exp[-it(E_n - E_m)], \end{aligned} \tag{1.29}$$

where the first term $\langle\hat{O}\rangle_d = \sum_m O_{mm}\rho^0_{mm}$ is the expectation value in the diagonal ensemble, or the long-time average value. The second term, for nonintegrable systems, is expected to be very small at long times for two reasons: firstly, according to ETH, the off-diagonal matrix elements for a few-body observable $\hat{O}$ is exponentially small in the size of the system [61, 206], secondly the long time temporal dephasing [179] guarantees the canceling of oscillations at long enough times. It seems problematic at first that one may need to wait an exponentially long time for the cancellation due to dephasing to occur because of the exponentially small level spacings. It was however pointed out [55] that since the off-diagonal matrix elements of $\hat{O}$ are exponentially small, the phase coherence between only a finite fraction of the eigenstates with a significant contribution to the expectation value needs to be destroyed. If the observable $\hat{O}$ thermalizes, the expectation in the diagonal

ensemble must agree with the expectation value obtained in statistical mechanics. We use the canonical ensemble (CE) to describe this thermalized state. We find the effective inverse temperature β_{eff} of this CE by matching the total energy of the system, which is a time-independent conserved quantity,

$$\begin{aligned} \langle \hat{H}_F \rangle &= \mathrm{Tr}\Big(\hat{H}_F \hat{\rho}^t\Big) \\ &= \sum_m E_m W_m^d \\ &= \mathrm{Tr}\Big[\hat{H}_F \exp\Big(-\beta_{eff}\hat{H}_F\Big)/Z(\beta_{eff})\Big] \end{aligned} \tag{1.30}$$

where $Z(\beta_{eff}) = \mathrm{Tr}\Big(e^{-\beta_{eff}\hat{H}_F}\Big)$ is the partition function for the CE at temperature $T_{eff} = 1/\beta_{eff}$. The function $E(\beta) = \mathrm{Tr}\Big(\hat{H}e^{-\beta\hat{H}}\Big)/Z(\beta)$ is monotonically decreasing with β because

$$\frac{dE(\beta)}{d\beta} = \sum_{m,n} -\frac{e^{-\beta(E_n+E_m)}(E_n - E_m)^2}{2Z^2} < 0, \tag{1.31}$$

and therefore there is only one solution for the effective temperature. For the CE we then have

$$\hat{\rho}^c = \sum_m \frac{e^{-\beta_{eff}E_m}}{Z(\beta_{eff})} |m\rangle \langle m| = \sum_m W_m^c |m\rangle \langle m| . \tag{1.32}$$

Like in a classical gas, the average energy of the initial Hamiltonian H_0 (particles confined to $L/2$) with *repulsive* interactions at a certain temperature is higher than that of the final Hamiltonian H_F (system size L) with the same temperature. So a higher effective temperature is needed for Eq. (1.30) to be satisfied. Conversely, for attractive interactions (such as in the classical van der Waals gas), the system is expected to cool down upon expansion. For repulsive interactions, such as the systems studied here, an interesting possibility can occur. If the initial average energy is higher than the infinite-temperature

energy for the final Hamiltonian, a negative temperature is needed to compensate for the difference. It is convenient to describe this in terms of inverse temperature: the system is prepared in some positive inverse temperature that decreases upon expansion for repulsive interactions. There will be some initial positive inverse temperature for which it decreases to zero (infinite temperature) after expansion. Any positive initial inverse temperature that is smaller than that will then lead to even smaller final inverse temperatures, leading to negative values.

We have the initial thermal state $\hat{\rho}^0$, the time-evolved state $\hat{\rho}^t$, the DE density matrix $\hat{\rho}^d$ and the corresponding CE density matrix $\hat{\rho}^c$. To better compare these states, we can investigate their reduced density matrices. Note that for an arbitrary density operator $\hat{\rho}$, if the observable $\hat{O}$ only resides on a subsystem A, whose complement is denoted as B, the expectation value only depends on the reduced density operator of the subsystem $\hat{\rho}_A = \mathrm{Tr}_B\, \hat{\rho}$ by

$$\langle \hat{O} \rangle = \mathrm{Tr}_A \left(\hat{O} \hat{\rho}_A \right). \tag{1.33}$$

If the reduced density matrix is similar to the CE reduced density matrix, every observable that resides in subsystem A has the same expectation value as in the canonical ensemble.

Another characterization of the reduced density matrix is the Rényi entropy. The p-th order bipartite Rényi entropy for $\hat{\rho}_A$ is defined as

$$S_{pA} = \frac{1}{1-p} \ln \mathrm{Tr}_A \left(\hat{\rho}_A \right)^p. \tag{1.34}$$

The von Neumann entanglement entropy $S_{1A} = -\mathrm{Tr}\{(\hat{\rho}_A \ln \hat{\rho}_A)\}$ is obtained by taking the limit $p \to 1^+$. For pure states, the Rényi entropy probes the entanglement between

subsystems A and B, and $S_{pA} = S_{pB}$. In particular, the conformal field theory (CFT) prediction for the ground state of critical one-dimensional systems with open boundary conditions has the form [103, 218, 110, 30, 34]

$$S_{pA}^{C} = \frac{c}{12}\left(1+\frac{1}{p}\right)\ln\left[\frac{2L}{\pi a}\sin\left(\frac{\pi l_A}{L}\right)\right] + c'_p, \tag{1.35}$$

where c is the central charge of the CFT, a is the lattice spacing, l_A is the size of the subsystem and c'_p is a nonuniversal constant. The states we are dealing with here are mixed states, and generally $S_{pA} \neq S_{pB}$, unless the partition is in the middle. For thermal states, the Rényi entropy for subsystem A contains contributions from both entanglement and thermal mixture. In an infinitely long system at temperature β^{-1}, the Rényi entropy has the form [129, 30, 34]

$$S_{pA}^{\beta} = \frac{c}{12}\left(1+\frac{1}{p}\right)\ln\left[\frac{\beta}{\pi a}\sinh\left(\frac{2\pi l_A}{\beta}\right)\right] + c'_p, \tag{1.36}$$

from where we can see that, for low temperatures and $l_A/\beta \ll 1$, the Rényi entropy scales logarithmically with the size of the subsystem, $S_{pA}^{\beta} \sim \ln l_A$, while for high temperatures and $l_A/\beta \gg 1$, the Rényi entropy recovers the volume law $S_{pA}^{\beta} \sim l_A$. This finite temperature behavior can place an additional challenge in the preparation of ground states of cold atom systems in optical lattices [214]. If A equals the whole system, S_{pA} is the diagonal (thermal) Rényi entropy for the DE (CE). In particular, for the time-evolved density matrix $\hat{\rho}^t$, taking the second order Rényi entropy as an example, it can be expressed by

$$\begin{aligned} S_{2A}^{t} = \quad & -\ln\Bigg[\sum_{\{m,n,i\}} \rho^0_{mn}\rho^0_{m'n'} e^{-it(E_m - E_n + E_{m'} - E_{n'})} \\ & \langle n|i_B\rangle \left\langle i'_B\middle|m'\right\rangle \left\langle n'\middle|i'_B\right\rangle \langle i_B|m\rangle\Bigg], \end{aligned} \tag{1.37}$$

where $\sum_{\{m,n,i\}}$ is a sum over m, m', n, n', i_B, and i'_B, and where i_B and i'_B run over all the states of a basis for subsystem B. If A is the whole system (size L), then B has size zero, and $n = m'$ and $n' = m$, and the phase is therefore always zero. The same argument holds for all orders of the Rényi entropy. The Rényi entropy for the whole system is therefore conserved during the time evolution.

Chapter 2

Gauge-invariant reformulation for the Abelian-Higgs model

2.1 Introduction

Two-dimensional gauge models have played an important role in our understanding of four-dimensional quantum chromodynamics (QCD). They appear prominently in several of the Coleman's Erice lectures [51] and provide non-trivial model calculations for questions related to confinement, topology and symmetry breaking. For these reasons, they are often the first targets when new methods are developed. There has been a recent interest in using controlled quantum systems to perform calculations in lattice gauge theories. The methods used include cold atoms in optical lattices, trapped ions, and state of the art quantum computers. Recent efforts have been focused on the Schwinger model [150, 9, 117, 123] and its scalar counterpart the two-dimensional Abelian Higgs model [134, 135, 87].

In recent years, the tensor renormalization group method (TRG) has been used to reformulate spin and gauge models with compact field variables into models of discrete integer (or half-integer) fields [234, 157, 142, 60, 238]. This reformulation uses discrete character expansions which are suitable for quantum computations and can also be used for sampling purposes [82]. The computation of the tensors involves integration over the field variables and is manifestly gauge invariant. The TRG has been used to reformulate the 2D Abelian Higgs model and find approximations suitable to implement the model on optical lattices [12]. Recently developed experimental methods involving Rydberg atoms [239] have been exploited to propose realistic implementations of the model on a physical ladder [241]. A key aspect of the proposal in Ref. [241] is that gauge invariance is maintained exactly, and the Gauss law constraint need not be enforced "by hand". This differs from other quantum simulation approaches [246, 134, 123, 135, 87, 9, 117, 80].

In order to test the ladder implementation, my collaborators and I have proposed to measure the Polyakov loop [241] for the 2D Abelian Higgs model. In this process we found remarkable finite-size scaling (FSS) properties that to the best of our knowledge have never been reported. In this chapter, we describe these calculations and the interpretation of the results.

This chapter is structured as follows: In Sec. 2.2, we derive the reformulation of the well-known Abelian Higgs model (scalar electrodynamics) [193, 112] with a chemical potential μ on a 1+1 dimensional lattice, in terms of the discrete field-quantum-number variables using the duality method. Strong coupling expansions can be done easily with this formulation. In the limit of arbitrarily large λ where the Brout-Englert-Higgs mode is

infinitely massive and we are left with the compact Nambu-Goldstone modes and compact gauge fields, we use TRG methods to write the partition function as a traced product of local tensors with discrete indices. We can write exact blocking formula for numerical purposes. Truncations must be done in practical implementation, but there is no sign problem for arbitrary chemical potential μ. The transfer matrix can be found by multiplying all tensors along a time slice. And the Polyakov loop is introduced in terms of the reformulated variables.

In Sec. 2.3 we obtain the continuous-time limit of the blocked transfer matrix and derive the Hamiltonian in the field-quantum-number representation and the charge-quantum-number representation. This can also be done numerically. The continuous-time limit of the Polyakov loop can also be obtained by repeating the same procedure. The new Hamiltonian is just the original Hamiltonian with a local modification. We can also write down the Hamiltonian by noting that the insertion of a Polyakov loop creating a static charge in the system without repeating the derivations.

In Sec. 2.4 we check the effect of spin truncation on the energy gap induced by the Polyakov loop in the limit of zero gauge coupling where the model reduces to that of the O(2) spin model, and we give justification for the accuracy of our results. We then report on the FSS of this energy gap and present results across a range of spatial sizes and gauge couplings.

In Sec. 2.5 we relate a special choice of boundary conditions in this model to the inclusion of the Polyakov loop into the system. We find this special boundary condition allows us to probe the non-zero charge sectors of the theory. It is discovered that the energy

gap extracted from this special choice of boundary conditions exhibits similar FSS compared to the energy gap extracted from the Polyakov loop. Again, this FSS is found to persist into the continuous-time limit.

Finally in Sec. 2.6 we give a summary and concluding remarks about the pertinence of this study to the possibility of quantum simulating the 2D Abelian Higgs model using cold atoms in optical lattices.

2.2 The Abelian Higgs model and the Polyakov loop

2.2.1 The model and its gauge-invariant reformulation

We consider the Abelian Higgs model with a chemical potential μ on a 1+1 space-time lattice of size $N_s \times N_\tau$. Let the gauge fields $U_{x,\hat{\nu}} = \exp\{iA_{x,\hat{\nu}}\}$, the matter fields $\phi_x = |\phi_x| \exp(i\theta_x)$, and the plaquette term $U_{pl,x} = U_{x,\hat{s}} U_{x+\hat{s},\hat{\tau}} U^\dagger_{x+\hat{\tau},\hat{s}} U^\dagger_{x,\hat{\tau}}$. As we discussed in Sec. 1.2, the action reads:

$$S = S_g + S_h + S_\lambda, \tag{2.1}$$

where the gauge part is

$$S_g = -\beta_{pl} \sum_x \mathrm{Re}\left[U_{pl,x}\right], \tag{2.2}$$

the hopping

$$\begin{aligned} S_h &= -\kappa_\tau \sum_x \left[\mathrm{e}^{\mu} \phi^\dagger_x U_{x,\hat{\tau}} \phi_{x+\hat{\tau}} + \mathrm{e}^{-\mu} \phi^\dagger_{x+\hat{\tau}} U^\dagger_{x,\hat{\tau}} \phi_x \right] \\ &- \kappa_s \sum_x \left[\phi^\dagger_x U_{x,\hat{s}} \phi_{x+\hat{s}} + \phi^\dagger_{x+\hat{s}} U^\dagger_{x,\hat{s}} \phi_x \right] \end{aligned} \tag{2.3}$$

and the self-interaction

$$S_\lambda = \lambda \sum_x \left(\phi^\dagger_x \phi_x - 1 \right)^2 + \sum_x \phi^\dagger_x \phi_x. \tag{2.4}$$

Note that the chemical potential only enters in the $\hat{\tau}$ links in Eq. (2.3). Because in the continuum limit, the chemical potential is only coupled to the charge density $\phi\dot{\phi}^\dagger - \phi^\dagger\dot{\phi}$. The partition function can then be written as

$$Z = \int D\phi^\dagger D\phi DU e^{-S}. \tag{2.5}$$

The compact and non-compact variables can be separated in the hopping part,

$$\begin{aligned} S_h = & - 2\kappa_\tau |\phi_x||\phi_{x+\hat{\tau}}| \sum_x \cos(\theta_{x+\hat{\tau}} - \theta_x + A_{x,\hat{\tau}} - i\mu) \\ & - 2\kappa_s |\phi_x||\phi_{x+\hat{s}}| \sum_x \cos(\theta_{x+\hat{s}} - \theta_x + A_{x,\hat{s}}), \end{aligned} \tag{2.6}$$

where it is clear that the chemical potential is a constant imaginary gauge field in the time direction. We can do a gauge transformation to eliminate the Nambu-Goldstone fields θ_x

$$A_{x,\hat{\nu}} \to A_{x,\hat{\nu}} - \theta_{x+\hat{\nu}} + \theta_x, \tag{2.7}$$

which does not change the plaquette terms. Note that in the limit $g^2 \to \infty, \lambda \to \infty$, the radial length of the matter fields is fixed to 1 and all gauge fields are constant which we set to zero. Then the action only contains the hopping term which is the classical O(2) model.

To represent the partition function (2.5) in terms of discrete variables, we apply the duality method and integrate out the continuous field. Note that the Boltzman weights can be Fourier expanded in terms of the modified Bessel functions I_n, for instance,

$$\begin{aligned} & \exp[2\kappa_\tau |\phi_x||\phi_{x+\hat{\tau}}| \cos(\theta_{x+\hat{\tau}} - \theta_x + A_{x,\hat{\tau}} - i\mu)] \\ = & \sum_{n=-\infty}^{\infty} I_{n_{x,\hat{\tau}}}(2\kappa_\tau |\phi_x||\phi_{x+\hat{\tau}}|) \exp[in_{x,\hat{\tau}}(\theta_{x+\hat{\tau}} - \theta_x + A_{x,\hat{\tau}} - i\mu)]. \end{aligned} \tag{2.8}$$

We can find similar expressions for the space hopping and the plaquette interactions. After integration over $A_{x,\hat{\nu}}, \theta_x$, we find the effective action

$$e^{-S_{eff}} = \sum_{\{m_\square\}} \left[\prod_\square I_{m_\square}(\beta_{pl}) \prod_x \left(I_{n_{x,\hat{s}}}(2\kappa_s |\phi_x||\phi_{x+\hat{s}}|) \right.\right.$$
$$\left.\left. \times I_{n_{x,\hat{\tau}}}(2\kappa_\tau |\phi_x||\phi_{x+\hat{\tau}}|) \exp(\mu n_{x,\hat{\tau}}) \right) \right], \tag{2.9}$$

where the Fourier modes, plaquette indices $m_\square$ come from Fourier expansion of the plaquette terms and link indices $n_{x,\hat{\nu}}$ come from the hopping terms. We attach these indices to plaquettes and links which form a dual lattice of our model. The integration over the continuous angular variables results in Kronecker deltas relating the various Fourier modes,

$$\int_0^{2\pi} \frac{d\theta_x}{2\pi} e^{i\theta_x \left(n_{x,\hat{\tau}} + n_{x,\hat{s}} - n_{x-\hat{\tau},\hat{\tau}} - n_{x-\hat{s},\hat{s}} \right)} = \delta^{(x)}_{n_{x,\hat{\tau}} + n_{x,\hat{s}}, n_{x-\hat{\tau},\hat{\tau}} + n_{x-\hat{s},\hat{s}}} \tag{2.10}$$

$$\int_0^{2\pi} \frac{dA_{x,\hat{\tau}}}{2\pi} e^{iA_{x,\hat{\tau}} \left(-m_x + m_{x-\hat{s}} + n_{x,\hat{\tau}} \right)} = \delta^{(x,\hat{\tau})}_{m_x - m_{x-\hat{s}}, n_{x,\hat{\tau}}} \tag{2.11}$$

$$\int_0^{2\pi} \frac{dA_{x,\hat{s}}}{2\pi} e^{iA_{x,\hat{s}} \left(m_x - m_{x-\hat{\tau}} + n_{x,\hat{s}} \right)} = \delta^{(x,\hat{s})}_{m_{x-\hat{\tau}} - m_x, n_{x,\hat{s}}} \tag{2.12}$$

which defines rules

$$n_{x,\hat{s}} = m_{below} - m_{above} \tag{2.13}$$

$$n_{x,\hat{\tau}} = m_{right} - m_{left} \tag{2.14}$$

where the subscripts such as "below" refers to the plaquette location with respect to the link. Then the link indices are completely determined by the plaquette indices. The $m_\square$ are the dual variables [193]. If we interpret $n_{x,\hat{\tau}}$ as a charge and m_x as an electric field in the spatial direction, Eq. (2.14) enforces Gauss's law. Eq. (2.13) is then the time derivative of electric field resulting in a current in spatial dimension. On the other hand, $n_{x,\hat{\nu}}$ can also be interpreted as a two-dimensional current and m_x as a magnetic field normal to the two-

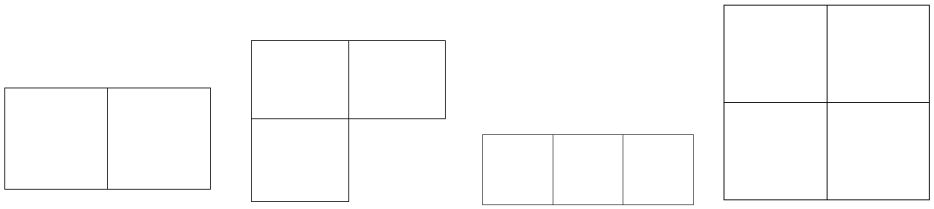

Figure 2.1: The configurations of 2-connected plaquettes, 3-connected plaquettes and 4-connected plaquettes in Eq. (2.18).

dimensional plane. In this Euclidean interpretation, Eqs. (2.13-2.14) express the current as the curl of the magnetic field. From Eqs. (2.13-2.14), we also have

$$n_{x,\hat{\tau}} - n_{x-\hat{\tau},\hat{\tau}} + n_{x,\hat{s}} - n_{x-\hat{s},\hat{s}} = 0, \tag{2.15}$$

$$\sum_{i=0}^{N_s+1} n_{i,\hat{\tau}} = m_{N_s+1} - m_0, \tag{2.16}$$

$$m_x = n_{x,\hat{\tau}} + n_{x-\hat{\tau},\hat{\tau}} + n_{x-2\hat{\tau},\hat{\tau}} + ... \tag{2.17}$$

Eq. (2.15) is the charge or current conservation. Eq. (2.16) shows that the total charge in the single time slice is the difference between the fields on the boundary. If PBC is applied, the total charge is zero. Eq. (2.17) represents the electric field as a sum of all charges to the left.

The strong coupling expansion can be easily done with Eq. (2.9). When $\beta_{pl} \ll 1$, the lowest order terms are those with all $m_\Box = 0$. We can perturbatively restore the effect of the plaquette. Consider the isotropic case $\kappa_s = \kappa_\tau = \kappa$, the expansion in the hopping

parameter κ gives:

$$
\begin{aligned}
-S_{eff} &= N\ln I_0(\beta)+\sum_{<xy>}\ln I_0\left(2\kappa\sqrt{M_xM_y}\right)+\kappa^4\left(2\frac{I_1(\beta)}{I_0(\beta)}\sum_{pl}M_1M_2M_3M_4\right)\\
&+\kappa^6\Bigg\{-\frac{I_1(\beta)}{I_0(\beta)}\sum_{pl}M_1M_2M_3M_4\left(M_1M_2+M_2M_3+M_3M_4+M_4M_1\right)\\
&+2\frac{I_1^2(\beta)}{I_0^2(\beta)}\sum_{2-\text{connected }pl}M_1M_2M_3M_4M_5M_6\Bigg\}\\
&+\kappa^8\Bigg\{\frac{2}{3}\frac{I_1(\beta)}{I_0(\beta)}\sum_{pl}M_1M_2M_3M_4\left(M_1^2M_2^2+M_2^2M_3^2+M_3^2M_4^2+M_4^2M_1^2\right)\\
&+\frac{1}{2}\frac{I_1(\beta)}{I_0(\beta)}\sum_{pl}M_1M_2M_3M_4\left(M_1M_2^2M_3+M_2M_3^2M_4+M_3M_4^2M_1+M_4M_1^2M_2\right)\\
&+\left(\frac{I_1(\beta)}{I_0(\beta)}+\frac{I_2(\beta)}{8I_0(\beta)}-\frac{2I_1^2(\beta)}{I_0^2(\beta)}\right)\sum_{pl}M_1^2M_2^2M_3^2M_4^2\\
&-\frac{I_1^2(\beta)}{I_0^2(\beta)}\sum_{2-\text{connected }pl}M_1M_2M_3M_4\\
&M_5M_6\left(M_1M_2+M_2M_3+M_3M_4+M_4M_5+M_5M_6+M_6M_1+3M_2M_5\right)\\
&+2\frac{I_1^3(\beta)}{I_0^3(\beta)}\sum_{3-\text{connected }pl}M_1M_2M_3M_4M_5M_6M_7M_8\\
&+2\frac{I_1^4(\beta)}{I_0^4(\beta)}\sum_{4-\text{connected }pl}M_1M_2M_3M_4M_5M_6M_7M_8\Bigg\}+O(\kappa^{10}),
\end{aligned}
\tag{2.18}
$$

where $M_k=\phi_k^\dagger\phi_k$, k labels the vertices on the connected plaquettes, "pl" means plaquette. The configurations of connected plaquettes are shown in Fig. 2.18. Notice that the summations are over these configurations in all different directions. The range of validity of the expansion can be checked by Monte Carlo simulation [12].

2.2.2 The large λ limit and the transfer matrix

When $\lambda\to\infty$, M_x is frozen to 1, or in other words, the Brout-Englert-Higgs mode becomes infinitely massive. Because the compact variables (θ_x and $A_{x,\hat{\nu}}$) have been

integrated out, the partition function can be expressed in terms of discrete sums. These sums can be formulated in a compact way using tensorial notations [142]. Before doing that, we define the normalized Bessel functions

$$t_n(z) = \frac{I_n(z)}{I_0(z)}. \tag{2.19}$$

These functions have useful properties. For instance $t_n(0) = \delta_{n,0}$. For z non-zero and finite, we have

$$1 = t_0(z) > t_1(z) > t_2(z) > \cdots > 0. \tag{2.20}$$

In addition, for sufficiently large z,

$$t_n(z) \approx 1 - \frac{n^2}{2z}. \tag{2.21}$$

And for small z,

$$t_n(z) \simeq z^n/(2^n n!). \tag{2.22}$$

Following the general principles of the construction [142], we attach a $B^{(\square)}$ tensor to every plaquette

$$B^{(\square)}_{m_1 m_2 m_3 m_4} = \begin{cases} t_{m_\square}(\beta_{pl}), & \text{if } m_1 = m_2 = m_3 = m_4 = m_\square \\ 0, & \text{otherwise,} \end{cases} \tag{2.23}$$

a $A^{(s)}$ tensor to the horizontal links

$$A^{(s)}_{m_{above} m_{below}} = t_{|m_{below} - m_{above}|}(2\kappa_s), \tag{2.24}$$

and a $A^{(\tau)}$ tensor to the vertical links

$$A^{(\tau)}_{m_{left} m_{right}} = t_{|m_{left} - m_{right}|}(2\kappa_\tau)\ \mathrm{e}^{(m_{right} - m_{left})\mu}. \tag{2.25}$$

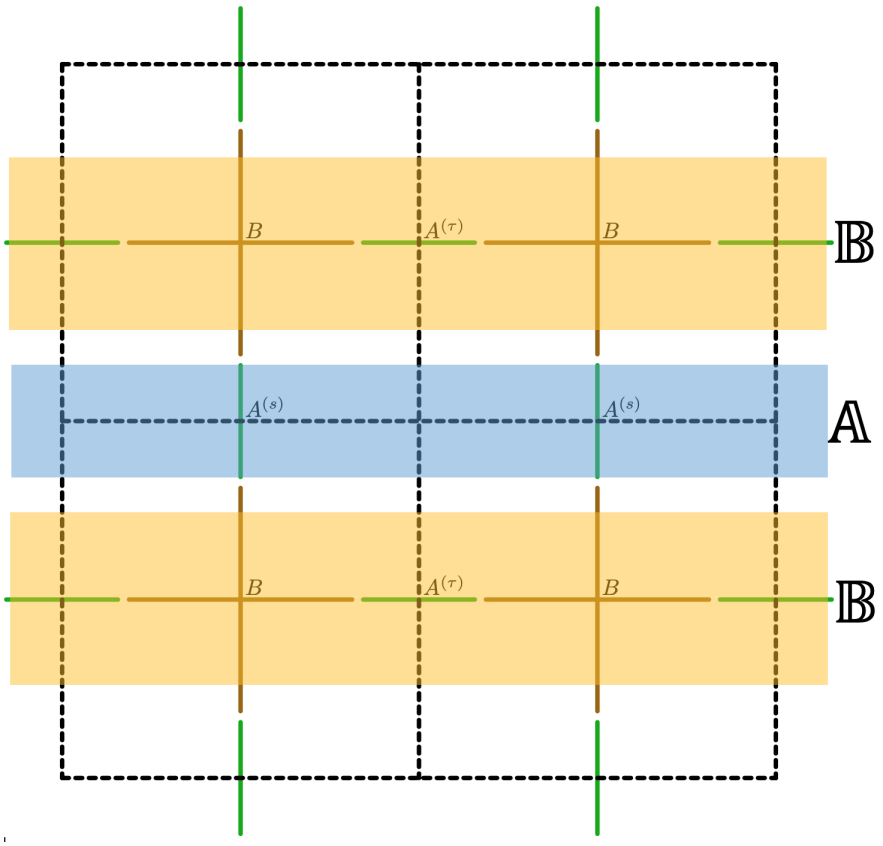

Figure 2.2: The basic B and A tensors (in brown and green, respectively, colors online). The $A^{(s)}$ are attached to the horizontal (spatial) links of the lattice. The $A^{(\tau)}$ are attached the vertical (temporal) links. The product of the tensors in yellow shaded area form a $\mathbb{B}$ tensor. The product of the tensors in blue shaded area form a $\mathbb{A}$ tensor. [12]

The partition function can now be written as

$$Z = (I_0(\beta_{pl})I_0(2\kappa_s)I_0(2\kappa_\tau))^V \times \mathrm{Tr}\left[\prod_{h,v,\square} A^{(s)}_{m_{above}m_{below}} A^{(\tau)}_{m_{left}m_{right}} B^{(\square)}_{m_1m_2m_3m_4}\right]. \quad (2.26)$$

The traces are performed by contracting the vertical and horizontal indices as shown in Fig. 2.2.

To construct the transfer matrix $\mathbb{T}$, we first define a matrix $\mathbb{B}$ as the product of the plaquette tensors on a time slice alternating with the vertical link tensor in between the

plaquettes

$$\mathbb{B}_{(m_1,m_2,\ldots m_{N_s})(m_1',m_2'\ldots m_{N_s}')} = t_{m_1}(2\kappa_\tau)\delta_{m_1,m_1'}t_{m_1}(\beta_{pl}) \times$$

$$t_{|m_1-m_2|}(2\kappa_\tau)\delta_{m_2,m_2'}t_{m_2}(\beta_{pl})t_{|m_2-m_3|}(2\kappa_\tau)\ldots$$

$$t_{m_{N_s}}(\beta_{pl})t_{m_{N_s}}(2\kappa_\tau)e^{\mu Q}, \tag{2.27}$$

where Q is the total charge, see Eq. (2.16). We next define a matrix $\mathbb{A}$ as the product

$$\mathbb{A}_{(m_1,m_2,\ldots m_{N_s})(m_1',m_2'\ldots m_{N_s}')} = \tag{2.28}$$

$$t_{|m_1-m_1'|}(2\kappa_s)t_{|m_2-m_2'|}(2\kappa_s)\ldots t_{|m_{N_s}-m_{N_s}'|}(2\kappa_s).$$

The $\mathbb{B}$ and $\mathbb{A}$ tensors are shown in Fig. 2.2. With these notations we can construct a symmetric transfer matrix $\mathbb{T}$. Since $\mathbb{B}$ is diagonal, real and positive, we can define its square root in an obvious way and write the transfer matrix as

$$\mathbb{T} = \sqrt{\mathbb{B}}\mathbb{A}\sqrt{\mathbb{B}}. \tag{2.29}$$

Then the partition function can be written as

$$Z = (I_0(\beta_{pl})I_0(2\kappa_s)I_0(2\kappa_\tau))^V \mathrm{Tr}\left[\mathbb{T}^{N_\tau}\right]. \tag{2.30}$$

Alternatively, we could diagonalize the symmetric matrix $\mathbb{A}$ and define the (dual) transfer matrix

$$\tilde{\mathbb{T}} = \sqrt{\mathbb{A}}\mathbb{B}\sqrt{\mathbb{A}}. \tag{2.31}$$

2.2.3 The Polyakov loop

The Polyakov loop, P, is a specific instance of the Wilson loop. The latter is defined by closed loops built out of gauge fields, and is gauge invariant. The Polyakov

loop is a Wilson loop which wraps around the temporal direction (with PBC) making it non-contractible. The Polyakov loop is an order parameter for confinement/deconfinement transitions in pure gauge theories. In particular it monitors the center symmetry of the gauge group, and the screening of a static test charge by the gauge field. As defined above, the Polyakov loop has the form

$$P = \prod_{n=0}^{N_\tau - 1} U_{x^* + n\hat{\tau}, \hat{\tau}} \tag{2.32}$$

in the Abelian Higgs model considered here, which is a loop along a single space-slice. The expectation value of the Polyakov loop is,

$$\langle P \rangle = \frac{1}{Z} \int \mathcal{D}[\phi^\dagger] \mathcal{D}[\phi] \mathcal{D}[U] \left(\prod_{n=0}^{N_\tau - 1} U_{x^* + n\hat{\tau}, \hat{\tau}} \right) e^{-S}, \tag{2.33}$$

with x^* a single specific spatial site where the Polyakov loop passes through. In QFT of complex matter field, the gauge field is coupled to the current. So the gauge field in time direction is coupled to the charge density. Then the insertion of the Polyakov loop adds a "1" to the charge density. The free energy induced by the inclusion of a static charge is related to the expectation value of the Polyakov loop by [161]

$$\exp[-F/T] \propto \langle P \rangle, \tag{2.34}$$

where F is the free energy, and T is the temperature. The insertion of the Polyakov loop into the system forces a scalar current in the opposite direction in order to lower the system energy. This is illustrated in Fig. 2.3, where 00BC means fields on the boundary are zero, equivalent to OBC we mention before, 10BC means the field quantum number is 1 on the left boundary and 0 on the right boundary. We will discuss the 10BC in Sec. 2.5. However, the cost for the current to run the length of N_τ is controlled by the hopping parameter coupling

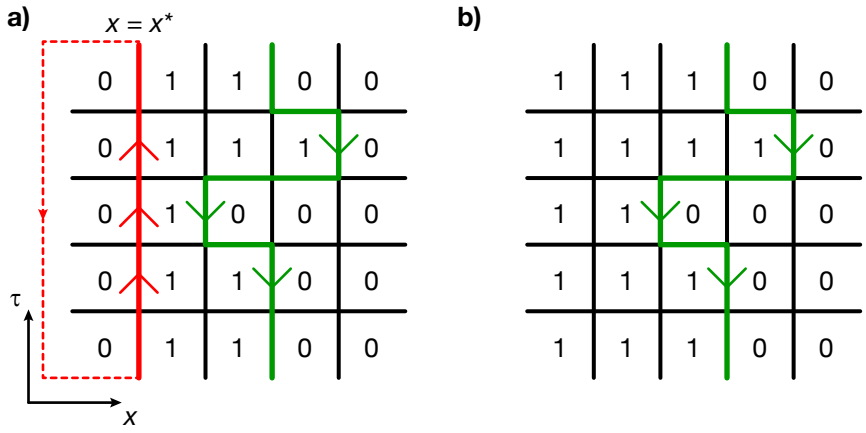

Figure 2.3: (color online) The Polyakov loop (arrows pointing up) and the matter loop (arrows pointing down) composed of matter charges and plaquette quantum numbers for a) 00BC and b) 10BC without the Polyakov loop. Additional columns of zeros or ones are implicit. The dotted line indicates the wrapping in the Euclidean time direction. [241]

and the length of N_τ, and this cost must be overcome for the Polaykov loop expectation value to be nonzero.

By repeating the derivations in Sec. 2.2.1, we can also re-write $\langle P \rangle$ in terms of discrete field-quantum-number variables. Note that the only difference in the derivation is the integrals on the links which contain the additional $U_{x,\hat{\tau}}$ variables from the Polyakov loop,

$$\int \frac{dA_{x^*,\hat{\tau}}}{2\pi} e^{i(n_{x^*,\hat{\tau}} - m_{x^*} + m_{x^*-\hat{s}} + 1)A_{x^*,\hat{\tau}}} = \delta_{n,m_r - m_l - 1}. \tag{2.35}$$

Here the subscripts l and r denote the "left" and "right" plaquette quantum numbers, respectively, to the vertical (temporal) link in question. This shifts the difference in ms by one at the links which contain the Polyakov loop, but all the other links remain the same.

Now we can write the expectation value as,

$$\langle P\rangle = \frac{1}{Z}\sum_{\{m\}}\left[\prod_{x,\nu<\mu} t_m(\beta_{pl})\right]\left[\prod_{x,\nu} t_{m-m'}(2\kappa)\right]\times \left[\prod_{n=0}^{N_\tau-1}\frac{t_{m-m'-1}(2\kappa)}{t_{m-m'}(2\kappa)}\right]. \tag{2.36}$$

Here the last product is over those links from Eq. (2.33) that are included in the Polyakov loop. This allows us to identify the Polyakov loop in terms of the new variables as,

$$P = \prod_{n=0}^{N_\tau-1}\frac{t_{m-m'-1}(2\kappa)}{t_{m-m'}(2\kappa)}. \tag{2.37}$$

2.2.4 The energy gap and the conjectured finite size scaling

By re-writing the partition function as a trace over products of transfer matrices, we can expose the dependence on N_τ,

$$\langle P\rangle = \frac{\tilde{Z}}{Z} = \frac{\mathrm{Tr}\left[\tilde{\mathbb{T}}^{N_\tau}\right]}{\mathrm{Tr}[\mathbb{T}^{N_\tau}]} = \frac{\sum_{i=0}^{N}\tilde{\lambda}_i^{N_\tau}}{\sum_{i=0}^{N}\lambda_i^{N_\tau}}, \tag{2.38}$$

where in the last step we have diagonalized the transfer matrices. This makes it clear that in the large N_τ limit the Polyakov loop expectation value is dominated by the largest eigenvalues $\tilde{\lambda}_0$ and λ_0. Thus, we find,

$$\log\langle P\rangle \simeq N_\tau \log\left(\tilde{\lambda}_0/\lambda_0\right) \tag{2.39}$$

$$= -N_\tau \Delta E, \tag{2.40}$$

with ΔE the energy gap between the ground state of the system with the static charge, and that without, for sufficiently large N_τ. Then

$$\langle P\rangle \simeq e^{-N_\tau \Delta E} \tag{2.41}$$

for sufficiently large N_τ (or low temperatures). This provides us a way to find the energy gap, first calculate the expectation value with HOTRG at large N_τ, then plot $\ln \langle P \rangle$ as a function of N_τ, finally we obtain the energy gap by extracting the slopes of the log-plot. Conventional Monte Carlo simulations and TRG calculations with a typical bond dimension of $D_{\text{bond}} \approx 40$ provide consistent evidence for the scheme [213].

In the limit where g^2 becomes zero, our model is the classical O(2) model, which has phase transition from the gapped to the gapless phase. This kind of transition is called the Berezinskii-Kosterlitz-Thouless (BKT) transition. For κ large enough, *i.e.* greater than the BKT transition value, and $g^2 N_s$ small enough, we expect that

$$\Delta E \simeq \frac{a}{N_s} + b\, g^2 N_s, \tag{2.42}$$

where a and b are still functions of κ. The first term is the leading behavior of the scaling of the energy gap in the gapless BKT phase at finite volume. It seems that the next order of logarithmic corrections are suppressed with OBC, which is our future study. If it is true, our conjecture could be good even for moderate system sizes. The guessed correction corresponds to a linear potential, which comes from the first order perturbation theory at small g^2. If we multiply Eq. (2.42) by N_s, then the right hand side depends only on $g^2 N^2$. We conjecture that this feature persists beyond the lowest order approximation, namely,

$$\Delta E N_s = f(g^2 N_s^2). \tag{2.43}$$

In addition, we can observe from numerical results that for larger $g^2 N_s^2$, $f(g^2 N_s^2) \sim g N_s$, which means that in this intermediate regime, ΔE become approximately independent of N_s and is proportional to g [213].

However, the data collapse will eventually break down if we increase g to large values while keeping N_s constant. For very large g (small β_{pl}), the lowest energy state corresponds to having all plaquette quantum numbers set to zero. This is accomplished when the matter loop follows exactly the Polyakov loop in the opposite direction. This state contributes $(t_1(2\kappa))^{N_\tau}$ to the partition function with a corresponding energy difference, ΔE, of $-\ln(t_1(2\kappa))$ in the large N_τ limit. Thus, for large values of g, we expect

$$\Delta E \to -\ln(t_1(2\kappa)), \tag{2.44}$$

independent of N_s. In particular, in the anisotropic case, when $2\kappa_\tau$ is big,

$$\Delta E \to \frac{1}{4\kappa_\tau}. \tag{2.45}$$

2.3 The time coninuum limit

In this section, we obtain the Hamiltonian of Abelian Higgs model by taking the time continuum limit of the transfer matrix $\mathbb{T}$ defined by Eq. (2.29). According to the discussions in Sec. 1.3, both β_{pl} and κ_τ go to infinity, and κ_s goes to zero, as the lattice spacing in time direction goes to zero. This is consistent with the fact that the transfer matrix should be close to 1 when two consecutive times are very close. In the limit $\kappa_s = 0$, the inside matrix $\mathbb{A}$ becomes the identity and the transfer matrix $\mathbb{T} = \sqrt{\mathbb{B}}\mathbb{A}\sqrt{\mathbb{B}}$ becomes $\mathbb{B}$ which is diagonal. From Eq. (2.21), we see that the only way to have $\mathbb{T}$ close to the identity is to require that *both* κ_τ and β_{pl} become large, which confirms our previous discussion in Chapter 1. At leading order in the inverse of these large parameters, the eigenvalues of $\mathbb{T}$

are

$$\begin{aligned}\lambda_{(m_1,m_2,\ldots m_{N_s})} &= 1-\frac{1}{2}\Bigg[\frac{1}{\beta_{pl}}(m_1^2+m_2^2+\cdots+m_{N_s}^2)\\ &+ \frac{1}{2\kappa_\tau}(m_1^2+(m_2-m_1)^2+\cdots+(m_{N_s}-m_{N_s-1})^2+m_{N_s}^2\Bigg]. \quad (2.46)\end{aligned}$$

Then consider the leading order in κ_s. From the definition of $\mathbb{A}$ in Eq. (2.28), we see that the leading order in κ_s is obtained by letting just one $m_i - m_i' = \pm 1$. Note that $t_1(2\kappa_s) \approx \kappa_s$ for small κ_s. We have

$$\mathbb{A} = \prod_i \delta_{m_i,m_i'} + \kappa_s \sum_j \left(\delta_{m_j,m_j'+1}\prod_{i\neq j}\delta_{m_i,m_i'}\right) + \kappa_s\left(\sum_j \delta_{m_j,m_j'-1}\prod_{i\neq j}\delta_{m_i,m_i'}\right). \quad (2.47)$$

Finally we can write the transfer matrix at leading order in all small quantities

$$\begin{aligned}\mathbb{T} &= \prod_i \delta_{m_i,m_i'} - \prod_i \delta_{m_i,m_i'}\frac{1}{2}\Bigg[\frac{1}{\beta_{pl}}(m_1^2+m_2^2+\cdots+m_{N_s}^2)\\ &+ \frac{1}{2\kappa_\tau}(m_1^2+(m_2-m_1)^2+\cdots+(m_{N_s}-m_{N_s-1})^2+m_{N_s}^2\Bigg]\\ &+ \kappa_s \sum_j \left(\delta_{m_j,m_j'+1}\prod_{i\neq j}\delta_{m_i,m_i'}\right) + \kappa_s\left(\sum_j \delta_{m_j,m_j'-1}\prod_{i\neq j}\delta_{m_i,m_i'}\right). \quad (2.48)\end{aligned}$$

2.3.1 The spin-S Hamiltonian

We already know the matrix elements of the transfer matrix from Eq. (2.48). The Hamiltonian can be easily obtianed by noting that $\mathbb{T} = e^{-aH} \approx 1 - aH$ for small temporal lattice spacing a. We define local operators on each spatial site

$$L_i^z |m_i\rangle = m_i |m_i\rangle, \quad (2.49)$$

$$U_i^{\pm} |m_i\rangle = |m_i \pm 1\rangle, \quad (2.50)$$

where $m_i = 0, \pm 1, \pm 2, \ldots$. $U_i^{\pm}$ are special types of raising and lowering operators for field quantum numbers. They are different from the ladder operators in the angular momentum

algebra. In the basis of eigenvectors of L^z, applying U^+ (U^-) to them also raises (lowers) the electric field quantum number by 1 but with all coefficients 1. Now the quantum Hamiltonian for the Abelian Higgs model for infinite spin is written,

$$H = \frac{U}{2}\sum_{i=1}^{N_s}(L_i^z)^2 + \frac{Y}{2}{\sum_i}'(L_{i+1}^z - L_i^z)^2 - X\sum_{i=1}^{N_s}U_i^x \ , \tag{2.51}$$

where the sum, $\sum_i'$, takes the OBC into account and includes $(L_1^z)^2 + (L_{N_s}^z)^2$. The parameters are

$$U \equiv \frac{1}{\beta_{pl}a} = \frac{g^2}{a}, \quad Y \equiv \frac{1}{2\kappa_\tau a}, \quad X \equiv \frac{2\kappa_s}{a}, \tag{2.52}$$

a is the temporal lattice spacing. $U^x = (U^+ + U^-)/2$ is similar in spirit to L^x, the x component of angular momentum, but with different matrix elements. In the Hamiltonian Eq. (2.51), the first term represents the plaquette interactions, which is the energy of the electric field (there is no magnetic field in (1+1) dimensions). The second term is associated with the integration of the time links. They can be interpreted as charges determined by Gauss's law, in other words the difference between the two field quantum numbers on each side of the link. Finally, the third term represents the spatial hopping term and reveals the equivalence between the spatial hopping of charge and the local spin-flip of the electric field. Notice that this Hamiltonian is consistent with Eq. (1.20) which is obtained by canonical quantization. If we truncate the values of m at $|m_{max}| = S$, we call it the "spin-S" truncation for convenience, even though we no longer are using the angular momentum algebra.

2.3.2 H with the Polyakov loop

Using the reformulation from Sec. 2.2.3, we can follow the same prescription for taking the continuous-time limit and apply it to the Polaykov loop. This implies taking the same limit for the P operator. We find,

$$P \to 1 + \frac{1}{2(2\kappa_\tau)} \left(2(m_r - m_l) - 1\right) + \mathcal{O}((2\kappa_\tau)^{-2}) \,. \tag{2.53}$$

This corresponds to an additional term in the quantum Hamiltonian which is located at a single specific site, and allows us to write,

$$\tilde{H} = H - \frac{Y}{2}(2(L^z_{i^*+1} - L^z_{i^*}) - 1) \tag{2.54}$$

where $\tilde{H}$ is the quantum Hamiltonian corresponding to the addition of a static charge at a specific site, i^*, and H is the original quantum Hamiltonian of the Abelian Higgs model from Eq. (2.51).

After taking this limit, it's clear that the energy gap, ΔE, between the ground states of $\tilde{H}$ and H is due to the additional term and the inserted static charge. This energy gap, when calculated in the low-temperature limit, is the same quantity that is calculated in the isotropic coupling case at large N_τ from Sec. 2.2.4.

In numerical calculations, and to avoid the effects of boundary conditions as much as possible, we put the Polyakov loop on the middle link of the square lattice (in the isotropic coupling picture), or equivalently, we remove the $(N_s/2)^{\text{th}}$ term from the Y sum in Hamiltonian (2.51) and shift it by one. Then the Hamiltonian with the Polyakov loop

included reads,

$$\tilde{H} = \frac{U}{2}\sum_{i=1}^{N_s}(L_i^z)^2 + \frac{Y}{2}{\sum_{i\neq\frac{N_s}{2}}}'(L_{i+1}^z - L_i^z)^2$$
$$+ \frac{Y}{2}(L_{\frac{N_s}{2}+1}^z - L_{\frac{N_s}{2}}^z - 1)^2 - X\sum_{i=1}^{N_s} U_i^x. \tag{2.55}$$

By a simple rearranging of terms this can be cast into the form from Eq. (2.54). So adding a Polyakov loop creates a single charge in the neutral system (*i.e.* Eq. (2.51)).

To conclude this section, we empasize that the process outlined in this chapter can in principle be generalized for other models such as non-Abelian gauge groups in $(1+1)$ or higher spatial dimensions. See Appendix D for a derivation for the Abelian Higgs model with a topological term. Tensor formulations and exact blocking procedures have already been worked out for non-Abelian gauge groups in Ref. [142]. These questions are under active consideration and readers can refer to [216, 215, 13].

2.3.3 The charge representation

By Gauss's Law, the charge (link) quantum numbers are defined as $\bar{L}_{i+\frac{1}{2}}^z = L_{i+1}^z - L_i^z$. This allows one to use the charge representation. The corresponding $\bar{U}^{\pm}$ have the same form. If we increase the field (plaquette) quantum number at site i by 1, the charge quantum number $\bar{L}_{i+\frac{1}{2}}^z$ will be decreased by 1, but $\bar{L}_{i-\frac{1}{2}}^z$ will be increased by 1. So the ladder operators in the field representation are related with the ones in charge representation by

$$U_i^+ = \bar{U}_{i-\frac{1}{2}}^+ \bar{U}_{i+\frac{1}{2}}^-. \tag{2.56}$$

With OBC, $\bar{L}^z_{\frac{1}{2}} = L^z_1$, $\bar{L}^z_{N_s+\frac{1}{2}} = -L^z_{N_s}$, and we can solve for field quantum numbers in terms of charge quantum numbers

$$L^z_i = \sum_{j=0}^{i-1} \bar{L}^z_{j+\frac{1}{2}}. \tag{2.57}$$

Then Eq. (2.51) reads

$$\begin{aligned}\bar{H} = &\frac{U}{2} \sum_{0\le j,k<N_s} c_{jk} \bar{L}^z_{j+\frac{1}{2}} \bar{L}^z_{k+\frac{1}{2}} + \frac{Y}{2} \sum_{i=0}^{N_s} (\bar{L}^z_{i+\frac{1}{2}})^2 \\ &- \frac{X}{2} \sum_{i=1}^{N_s} (\bar{U}^+_{i-\frac{1}{2}} \bar{U}^-_{i+\frac{1}{2}} + \bar{U}^-_{i-\frac{1}{2}} \bar{U}^+_{i+\frac{1}{2}}) - \tilde{\mu} \sum_{i=1}^{N_s} \bar{L}^z_{i+\frac{1}{2}} \ ,\end{aligned} \tag{2.58}$$

where $c_{jk} = N_s - \max\{j,k\}$, $\tilde{\mu} = \mu/a$ is the chemical potential. Note that Hamiltonian (2.51) has N_s sites, while there are N_s+1 sites in Hamiltonian (2.58). The former has total charge zero, while the latter has charge conservation symmetry and can represent all charge sectors probed by adjusting the external field on the right boundary. For other boundary conditions or insertions of Polyakov loops, Eq. (2.57) changes, so the U term in Eq. (2.58) is different. Although Hamiltonian (2.58) has long range interactions in the first term, a similar form has been used to study the real-time dynamics of the Schwinger model with qubits by coarse graining in time [150]. In our case, we focus on Hamiltonians (2.51) and (2.55) as they have only nearest-neighbor interactions which allows easy implementations on optical lattices.

We emphasize that without any truncation, Eq. (2.58) and Eq. (2.51) are exactly mapping term by term. However, they are quite different with small truncation, where the Hilbert space cannot be mapped with Gauss's Law. An important feature of Eq. (2.58) is that the X term is gapless for any spin truncation in the thermodynamic limit, which may drive a quantum phase transition from a gapped to a gapless phase. As the O(2) limit

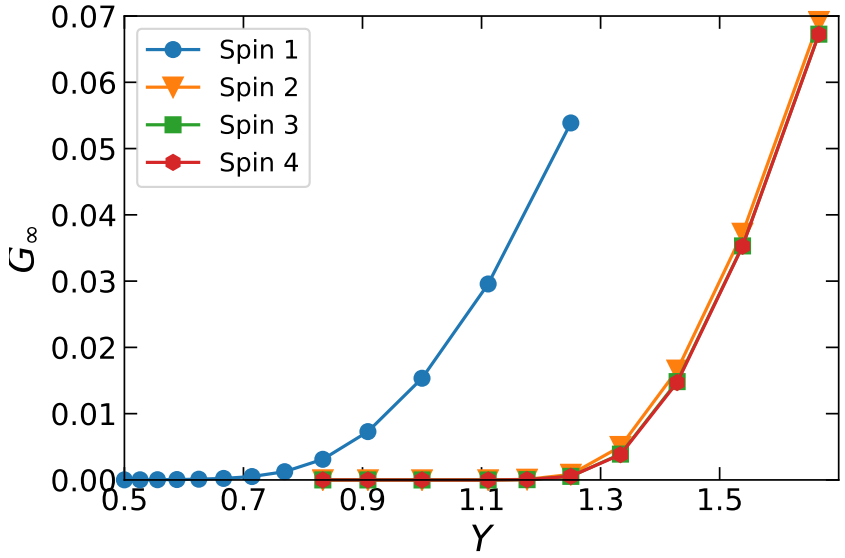

Figure 2.4: (Color online) Energy gaps of O(2) Hamiltonian with spin truncations 1 - 4 in the thermodynamic limit, as a function of Y.

($g^2 \to \infty$) of the Abelian Higgs model has a BKT transition, it is remarkable that the BKT universality class survives the time continuum limit and small spin truncation in charge representation. This is a big advantage of Eq. (2.58). The extrapolated energy gap in the thermodynamic limit is shown in Fig. 2.4, where we see the BKT transition happens for all spin truncations. In addition, the gap closes much slower for spin-1 truncation than bigger spin truncation. And the gaps for $S \geq 3$ are almost the same. While in Eq. (2.51), the X term is always gapped for any finite truncation even in the thermodynamic limit, so only a gapped to gapped quantum phase transition may happen. The following numerical results would show that there is no quantum phase transition in Eq. (2.51) with any finite spin truncation. A direct calculation of eigenvalues of U^x gives the energy spectrum $E_k = \cos(\pi k/(2S+2))$, which is indeed gapless for infinite S. For finite systems, we can gradually

increase spin truncation until the spectrum of Eq. (2.58) and Eq. (2.51) match within a given precision. So the finite size scalling of BKT transition can still be studied in Eq. (2.51) with bigger spin truncation. But the advantage of Eq. (2.51) is that it is always short range in the presence of gauge coupling, which allows us to easily design quantum simulators with cold atoms in optical lattices.

2.4 Spin truncation and finite-size scaling

In this section, we use the density matrix renormalization group (DMRG) [226, 197] for our studies in the continuous-time limit. The finite DMRG algorithm with matrix-product-state (MPS) [169] optimization was performed using the ITensor C++ library [1]. Note that the quantum entanglement comes from the nearest-neighbor interaction in the field representation, while it comes from the nearest-neighbor hopping in the charge representation. In the gapless phase where X is relatively larger than Y, the bipartite entanglement entropy for the field representation is much smaller than that of the charge representation, so a much smaller bond dimension is needed for the former case using MPS.

2.4.1 The O(2) limit

In our previous work [12], we discussed the O(2) limit where $U \to 0$ ($g^2 \to 0$), and the $\kappa_\tau \gg \beta_{pl} \gg \kappa_s$ limit separately, where we used the charge representation and field representation with a three state truncation respectively. Because the O(2) model has a gapless phase where high quantum number states are easily excited, a three-state

[1] Version 2.1.1, http://itensor.org/

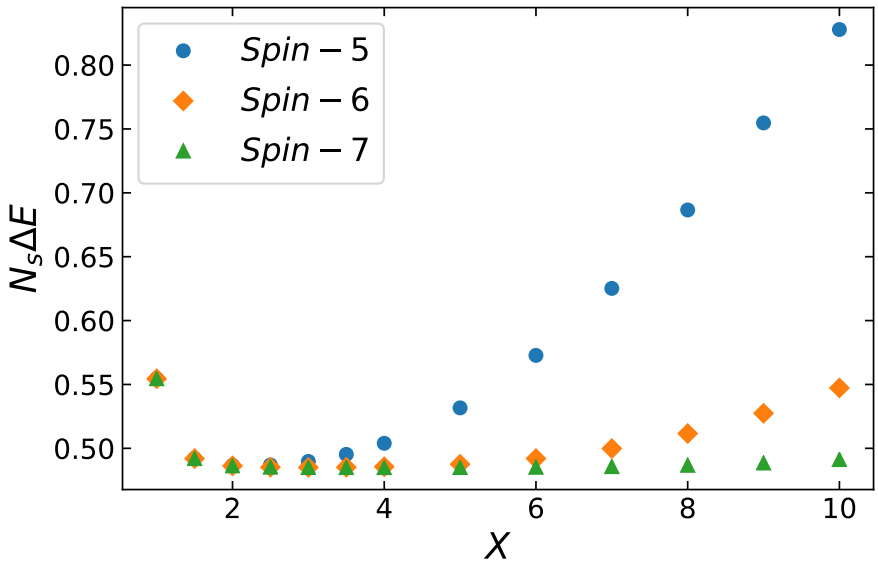

Figure 2.5: The enegy gap in the O(2) limit with $N_s = 32$ in field representation as a function of X. [213]

truncation is far from enough for Hamiltonian (2.51). Here we want to connect these two limits continuously by keeping more states in the truncation.

To test how many states we should keep to simulate the O(2) model using Eq. (2.51) with $U = 0$, we gradually increase the number of states and calculate the energy gap between the ground states of Hamiltonians (2.51) and (2.55). In these calculations we used units of $Y = 1$ in the Hamiltonian. Studying the data collapse requires precise values of $N_s\Delta E$ in the O(2) limit. The energy gap of the O(2) model in the BKT region scales like $1/N_s$ in a polynomial form, with the coefficient of $1/N_s$ constant, which is verified in Fig. 2.5 where $N_s\Delta E$ is almost constant for a large range of $X \in [2, 10]$ with $N_s = 32$. We also see that a spin-5 truncation is good enough for $X \approx 2$, and a spin-6 truncation is essentially perfect for $X \in [2, 4]$.

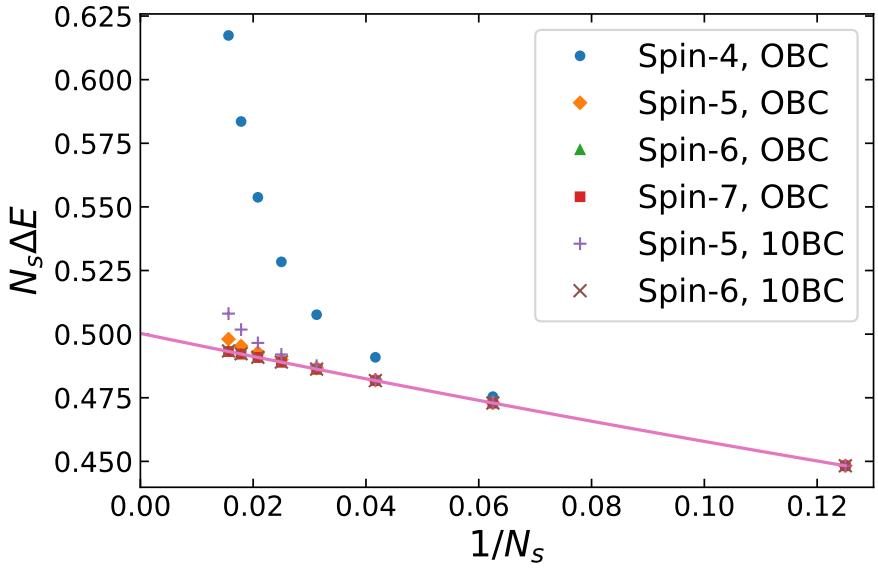

Figure 2.6: The enegy gap in the O(2) limit with $X = 2$ in plaquette quantum number representation as a function of $1/N_s$ for different spin-truncations. [213]

Finite-size effects also play a role. As shown in Fig. 2.6, at $X = 2$, a spin-5 truncation breaks down after $N_s = 40$, but a spin-6 truncation works perfectly well for $N_s \leq 64$. The extrapolation of $N_s\Delta E$ to the thermodynamic limit gives $N_s\Delta E = 0.50029(8)$, which is consistent with $Y/2 = 0.5$ in units of Y in the continuous-time limit. By calculating the energy gap between the charge-0 and charge-1 sectors with Hamiltonian (2.58), we show that the energy gaps for the two representations of O(2) converge to the same values with a spin-6 truncation. This can be seen in Fig. 2.7.

2.4.2 Finite size scaling of energy gap

As discussed in the previous section, a spin-6 truncation is good enough to probe the finite-size scaling of the energy gap in the O(2) limit for $2 \leq X \leq 5$ up to $N_s = 32$. As a

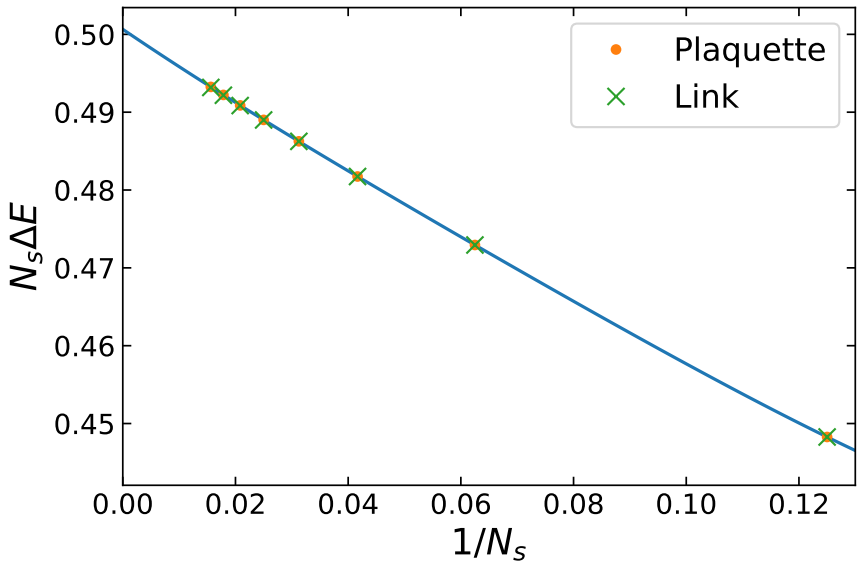

Figure 2.7: The enegy gap in the O(2) limit with a spin-6 truncation in the plaquette quantum number representation and link quantum number representation as a function of $1/N_s$. Here $N_s = 8, 16, ..., 64$ with $X = 2$ fixed. [213]

finite gauge coupling g will suppress the contribution of high plaquette quantum numbers, a spin-6 truncation should work well for any finite g and is used for all DMRG calculations in the following discussion.

As explained before, arguments regarding the behavior at small and large gN_s led us to conjecture that $N_s\Delta E$ is solely a function of the product $(gN_s)^2$. Fig. 2.8 supports this idea. Note that for the discrete-time (Lagrangian) calculations at various κ, ΔE was rescaled by 2κ while for the continuous time (Hamiltonian) calculations, a similar rescaling of $2\kappa_\tau a$ was introduced by setting $Y = 1$. The remarkable FSS properties of the Polyakov loop in the Abelian Higgs model are illustrated by the collapse of 24 datasets in Fig. 2.8. There are four different spatial sizes N_s represented in the figure (N_s = 4, 8, 16, and 32) and it is possible to probe the critical behavior with systems of modest spatial sizes.

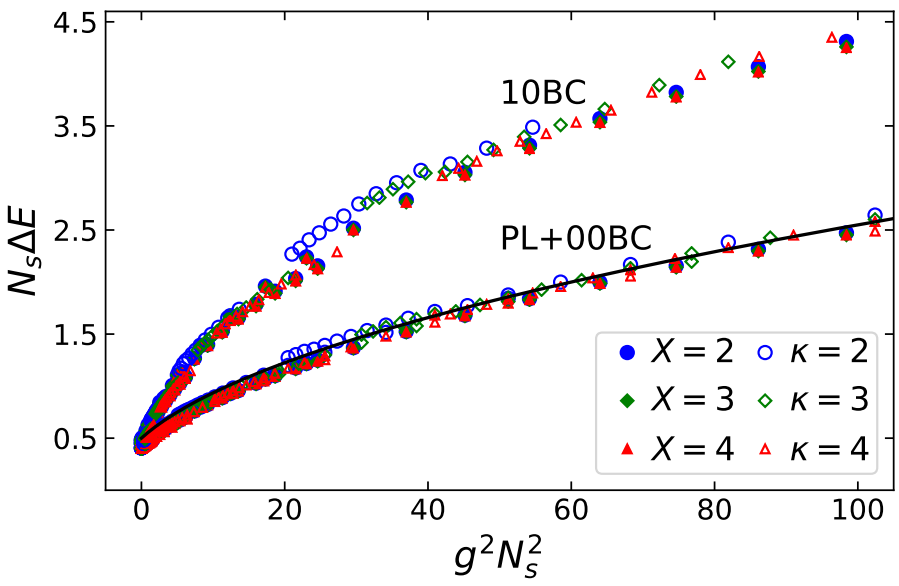

Figure 2.8: (color online) $N_s\Delta E$ versus $g^2N_s^2$ for the gap ΔE created by the insertion of the Polaykov loop (lower set) or an external electric field (10 boundary conditions, upper set). Open (filled) markers represent Lagrangian (Hamiltonian) data. The choices of parameters, units and methods for both of the 24 datasets are explained in the text. The black line represents the function $\Delta E N_s = \sqrt{(gN_s/4)^2 + 0.25}$. [241]

Checking this data collapse is an important test for possible quantum simulations. The FSS is related to the energy gap ΔE created by inserting a Polyakov loop or by applying an external electric field (explained in Sec. 2.5). When the gauge coupling g approaches zero, we have an O(2) model whose universal properties are of the BKT type. The data collapse can be interpreted as originating from a relevant renormalization-group direction coming from the BKT conformal fixed point. When the hopping parameters exceed their critical value at the BKT transition, we have infinite correlation length at infinite volume and $\Delta E \propto 1/N_s$ at finite N_s. Fig. 2.8 indicates that when we turn on g, $N_s\Delta E$ is a linear function of $(gN_s)^2$ at small argument and then a linear function of gN_s at larger argument. The latter behavior is more clear in the top graph of Fig. 2.9, where $N_s\Delta E$ as a function

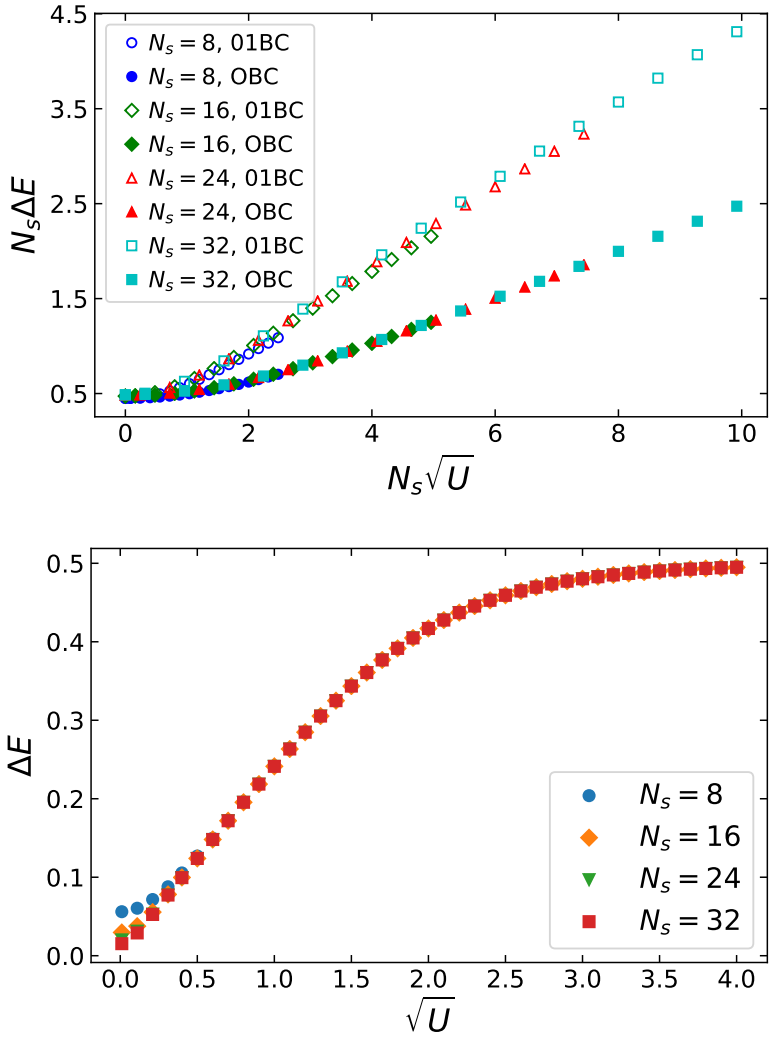

Figure 2.9: (color online) The same as Fig. 2.8, but plot $N_s\Delta E$ versus gN_s, only with Hamiltonian data for $X = 2$ (top). The same data as top figure, but plot ΔE versus g only for OBC (bottom).

of gN_s is plotted. Note that the former behavior is in a limited range of gN_s, which means as long as we turn on g, no matter how small it is, it will open a gap which is proportional to g. This can be seen in the bottom graph of Fig. 2.9, where we see that the range of g in which $\Delta E \sim g^2$ shrinks quickly as we increase the size of the system. A linear fit for the

linear part gives $\Delta E \approx g/4$. We emphasize that this is nontrivial, the perturbation theory only gives us terms in powers of g^2. The results tell us that $\Delta E N_s = \sqrt{(gN_s/4)^2 + 0.25}$ for not too big g, see the black line in Fig. 2.8. For very big g^2, the energy gap saturate to 0.5 because the ground states for both Hamiltonian (2.51) and Hamiltonian (2.55) have $m_i = 0$ everywhere, which is also consistent with Eq. (2.45) when we set $Y = 1/2a\kappa_\tau = 1$.

The two parts of Fig. 2.8 each contain 24 data sets with 12 from a discrete Euclidean time Lagrangian, while the other 12 are from the continuous-time Hamiltonian limit. It is remarkable that the two calculations provide the same universal functions. That is, in an appropriate regime, up to a rescaling by κ, the ΔE calculated in the continuous-time limit is equal to the ΔE calculated in the isotropic-coupling discrete case. It is also interesting that $N_s \Delta E$ in the $g^2 \to 0$ limit have the same value 0.5 as ΔE in the $g^2 \to \infty$ limit. Ultimately, it is this equivalence between the two formulations which enables the transfer of results from the experimentally accessible Hamiltonian dynamics to the Lagrangian formulation. Moreover, the FSS properties of the Polyakov loop allow for a well controlled benchmark of an experimental implementation by transiting from small to large system sizes.

We emphasize that the collapse is by no means automatic. It breaks down for κ not large enough, if we increase g to large values while keeping N_s constant (there are hints of this in Fig. 2.8 for the small N_s data), or if the truncation value is smaller than $m_{max} = 2$.

2.5 Replacing the Polyakov loop by special boundary conditions

2.5.1 Isotropic coupling

By inserting the Polyakov loop, one probes the response of the system to the addition of a single static charge. For a total charge, Q, the $Q \neq 0$ sectors of the theory can be probed by changing the boundary conditions of the system, this is like subjecting the system to an external electric field. One can consider the pure Abelian Higgs model with a boundary of zeros on one side, and a boundary of ones on the other in the field-quantum-number representation. With the conventions used in this text, to put the system in the $Q = -1$ sector amounts to setting a boundary of ones on the left side of the system, and a boundary of zeros on the right side (10BC). With these boundary conditions (and the now absent Polyakov loop) Gauss's law tells us that there is a total charge of -1 across a time slice. In the tensor language the boundary tensors, in this case the B tensors, are assigned the state $m = 1$ on one side, and $m = 0$ on the other.

The relationship between the situation with the Polyakov loop inserted, and the system with special boundary conditions can be made more clear by a simple example. It consists of sliding the Polyakov loop all the way to the boundary of a system with OBC. We will relate the $Q = -1$ sector (which is identical to the $Q = 1$ sector) to the Polyakov loop. Take a system where, along a time slice, charge is defined at a link as the difference of the electric field as $n = m_{\text{right}} - m_{\text{left}}$, with $Q = \sum n$. Then at the link with the Polyakov loop one has $n = m_{\text{right}} - m_{\text{left}} - 1$. If one slides this all the way to the left-most boundary

link, it becomes $n = m_{\text{right}} - 0 - 1 = m_{\text{right}} - 1$. This is precisely the charge one would find by setting the left boundary quantum numbers to one and removing the Polaykov loop entirely. By Gauss's law the charge of this system would be -1. Thus, a system with skewed boundary conditions of zeros on one side and ones on the other is equal to a system with OBC with a Polaykov loop pushed to the boundary link.

Since the Polyakov loop is related to a special circumstance of boundary conditions, we would expect the energy gap from the inclusion of the Polyakov loop to be qualitatively similar to the energy gap between the $Q = -1$ and $Q = 0$ sectors. Indeed, a collapse can be found for the energy gap from Lagrangian data in Fig. 2.8. Again, there is collapse for sufficiently small g, and collapse breaking at large enough g. In addition, $\Delta E_{10} \to -\ln(t_1(2\kappa))$ for large g regardless of N_s, which is in agreement with the Polyakov loop result.

2.5.2 Continuous-time limit

Similar to the isotropic coupling case, in the continuous-time limit special boundary conditions can be imposed to probe the $Q \neq 0$ sectors of the theory. Whereas before, in Sec. 2.3.1 & 2.3.2, OBC were used (zeros on both spatial ends) and the Polyakov loop was inserted in the center, one can consider the pure model in the absence of the Polyakov loop, and change the left spatial-boundary end-point to one. By Gauss's law, one can see that this leaves the system with total charge $Q = -1$.

To implement these boundary conditions in DMRG, one has to imagine there are two additional sites on the chain, one to the left, and one to the right. The right-side site, say, has quantum number zero (the same as in the typical OBC case), however on the left-

side site we assign value one. To include the effect of the boundary conditions we re-write the Hamiltonian accordingly:

$$H_{10} = \frac{U}{2}\sum_{i=1}^{N_s}(L_i^z)^2 + \frac{Y}{2}\sum_{i=1}^{N_s-1}(L_{i+1}^z - L_i^z)^2 + \frac{Y}{2}(L_{N_s}^z)^2 + \frac{Y}{2}(L_1^z - 1)^2 - X\sum_{i=1}^{N_s} U_i^x. \tag{2.59}$$

This is the form of the Hamiltonian in the $Q = -1$ sector, in contrast to (2.51) which is the Hamiltonian with zeros on the boundaries (the $Q = 0$ sector). In Fig. 2.8 and Fig. 2.9, one can see the data collapse of the energy gap between systems with 10BC and OBC across a range of spatial sizes and gauge couplings. Notice that in all cases, $N_s\Delta E \simeq 0.5$ when $g^2 \simeq 0$, which corresponds to the gapless BKT phase in the O(2) limit. We also notice that the energy gap at finite g^2 for 10BC is bigger than the gap for PL-00BC. Because 10BC breaks the inversion symmetry of the system, creating a charge on the right costs more energy than that on the left. We can understand this by doing the transformation $L_i'^z = L_i^z - 1$ for $i \leq N_s/2$. Then the Hamiltonian with 10BC is related to the Hamiltonian with the Polyakov loop by $H_{10} \to \tilde{H} + U\sum_{i=1}^{N_s/2} L_i'^z + N_sU/4$, which is simply adding a linear potential on the left half of the system. But the data collapse is still present, indicating the same universality class.

2.6 Conclusions

In this chapter we show that the duality method with TRG formulation can be used to re-write the partition function of Abelian Higgs lattice gauge theory as a traced product of local tensors with discrete indices. We can directly perform numerical TRG

calculations to this reformulation. This reformulation also help us to find the Hamiltonian formulation in the continuous time limit. The Hamiltonian formulation is consistent with the one we obtained with canonical quantization in Chapter 1. The path integral with the insertion of a Polyakov loop can also be tackled with the same procedure.

We have studied the expectation value of the Polyakov loop in the compact Abelian Higgs model in 1+1 dimension. In our study we compared the TRG, MC, and the DMRG method and found excellent agreement between them. It was found that the Polaykov loop is related to the energy gap between charge-sectors of the Abelian Higgs model and that this energy gap exhibits universal finite-size scaling behavior. The scaling of the energy gap was studied in both the fully discrete lattice system and the continuous-time quantum limit of this model, and it was found that the universal behavior of the energy gap survives this limit. In addition, special boundary conditions were able to reproduce similar features of the data collapse found from the Polyakov loop which provides an alternate method to study this energy gap.

The results in this chapter give support to Chapter 3 where it is proposed to use the 2D Abelian Higgs model as a proof of principle model for the case of quantum simulation using cold atoms in optical lattices. In that chapter the energy gap associated with the Polyakov loop and its FSS collapse are suggested as observables for the simulation. This work shows, in detail, the passage from the discrete Lagrangian lattice model to the continuous-time quantum Hamiltonian model. This is done in a way such that gauge invariance is maintained exactly and the result is suitable for quantum simulation. That is,

configurations in the quantum simulation are those of the physical state-space of the model (up to spin truncations).

Chapter 3

Quantum simulation of Abelian Higgs model in optical lattices

3.1 Introduction

LGT are fundamental to our understanding of strongly interacting particles in high energy physics. Translating the success of quantum simulations with cold atoms in optical lattices [92] of systems relevant to condensed matter physics, such as the Bose-Hubbard model, to the quantum simulation of LGT would open the door to real-time and finite-density calculations which are beyond the realm of classical computations. An important first step is to achieve this goal for models in one space and one time (1+1) dimensions in a well controlled setting. While the dynamics of the Schwinger model, quantum electrodynamics in 1+1 dimensions, has been explored using a few qubit digital quantum simulation in a system of trapped ions [150] or classical-quantum algorithms on IBM quantum com-

puters [123], the analog quantum simulation of gauge theories with cold atoms requires complex experimental settings. Existing efforts involve mixtures of bosonic and fermionic atoms [9, 117] or dipolar interactions of cold molecules [80] and are still in progress.

Based on the theoretical preparation in Chapter 2, we are in a position to find appropriate quantum simulators to quantum simulate the $(1 + 1)$-d Abelian Higgs model. In this chapter, I will introduce two kinds of quantum simulators engineered with ultra-cold atoms in optical lattices in our proposals. The first one is the two-species Bose-Hubbard model, and the second one is a multi-leg ladder of atoms interacting with Rydberg dressed interactions. As I mentioned in Sec. 1.5, these models are not difficult to realize within current experimental techniques. In particular, we envision probing the universal features of this model via a "Polyakov loop" in the second proposal. In gauge theories, the expectation values of Wilson loops play a fundamental role, serving, for example, as order parameters to discriminate confined and deconfined phases of quarks and gluons in QCD. The Polyakov loop itself is relevant in finite-temperature studies [79], however its calculation at finite density with classical computing methods is often plagued by sign problems.

In contrast to other approaches [247, 243, 207, 244, 116, 229, 245, 134, 135, 87, 9, 117, 80] and similar to [150], we use a manifestly gauge-invariant formulation [12] where Gauss's law is inherently fulfilled. In addition, we consider the limit [12] where the scalar self-coupling becomes large and the Higgs mode decouples from the low energy theory. We are then left with a gauged O(2) spin model with *compact* field integration. Fourier analysis provides a *discrete* reformulation in agreement with Pontryagin duality [175] and suitable for an analog quantum simulation. See Chapter 2 for details.

3.2 The two-species Bose-Hubbard model

The general form of a two-species Bose-Hubbard model that can be realized in optical lattices is

$$\begin{aligned}\mathcal{H} = &-\sum_{\langle ij\rangle}(t_a a_i^\dagger a_j + t_b b_i^\dagger b_j + h.c.) - \frac{t_{ab}}{2}\sum_i (a_i^\dagger b_i + b_i^\dagger a_i) \\ &- \sum_{i,\alpha}(\mu_{a+b} + \Delta_\alpha) n_i^\alpha + \sum_{i,\alpha}\frac{U_\alpha}{2} n_i^\alpha (n_i^\alpha - 1) + W\sum_i n_i^a n_i^b \\ &+ \sum_{\langle ij\rangle,\alpha} V_\alpha n_i^\alpha n_j^\alpha + \sum_{\langle ij\rangle} V_{ab} n_i^a n_j^b\end{aligned} \tag{3.1}$$

with $\alpha = a, b$ indicating the two different species, t_α the hopping amplitude for each species, t_{ab} the amplitude of interchanging two species, $\mu_{a+b} + \Delta_\alpha$ the chemical potential, U_α the intra-species onsite interaction, W the inter-species onsite interaction, V_α the intra-species nearest neighbor interaction, V_{ab} the inter-species nearest neighbor interaction, $n_i^a = a_i^\dagger a_i$ and $n_i^b = b_i^\dagger b_i$ the number operators, and $|n_i^a, n_i^b\rangle$ the corresponding on-site basis. In this expression, the chemical potential μ_{a+b} is associated with the conservation of total number of bosons $n_a + n_b$. Some similar and related two-species Bose-Hubbard have been studied previously[132, 133, 44, 50]. We have shown[248, 12] that in different limits, this model can be used to quantum simulate the effective Hamiltonian for the O(2) model or for the Abelian Higgs model.

It is possible to adjust the chemical potentials in Eq. (3.1) in order to set $\langle n_i\rangle = \langle n_i^a + n_i^b\rangle = 2S$. Then, in the limit where $U_a = U_b = W$ are very large and positive, the on-site Hilbert space can then be restricted to the states satisfying $n_i = 2S$. All the other states (with $n_i \neq 2S$) belong to high-energy sectors that are separated from this one by energies of order the on-site interaction energy. Writing $U_{a(b)} = U_0 \pm \delta$ and working in the

limit $U_0 \gg \delta, (U_0 - W), V_{ab}, V_\alpha, t_\alpha, \Delta_\alpha$, the effective Hamiltonian , up to second order in degenerate perturbation theory, corresponds to the spin-S Hamiltonian (see Appendix B for the derivation)

$$\begin{aligned}
\mathcal{H}_{eff} &= (\frac{V_a}{2} - \frac{t_a^2}{U_0} + \frac{V_b}{2} - \frac{t_b^2}{U_0} - V_{ab}) \sum_{<ij>} L_i^z L_j^z \\
&\quad -\frac{t_a t_b}{U_0} \sum_{<ij>} (L_i^+ L_j^- + L_i^- L_j^+) \\
&\quad + \Big[(n-1)\delta + (\frac{pn}{2} V_a + \Delta_a - p(n+1)\frac{t_a^2}{U_0}) \\
&\quad -(\frac{pn}{2} V_b + \Delta_b - p(n+1)\frac{t_b^2}{U_0}) \Big] \sum_i L_i^z \\
&\quad -t_{ab} \sum_i L_i^x + (U_0 - W) \sum_i (L_i^z)^2 \ . \qquad (3.2)
\end{aligned}$$

where p is the number of neighbors, $n = 2S$ is the filling number of particles on each site and $\hat{L}$ is the angular momentum in the representation spin-S. Note that the $t_\alpha^2 (\alpha = a, b)$ terms come from the second order perturbation expansion, while other terms are exact mapping. In Appendix A, we discuss a few immature proposals for the practical experimental implementations for the two-species Bose-Hubbard model. It contains questions we we still need to confirm, so I put it into the appendix.

3.2.1 The O(2) model

In the O(2) limit, the Hamiltonian of Abelian Higgs model in the charge representation becomes

$$\bar{H} = \frac{Y}{2} \sum_{i=0}^{N_s} (\bar{L}_{i+\frac{1}{2}}^z)^2 - \frac{X}{2} \sum_{i=1}^{N_s} (\bar{U}_{i-\frac{1}{2}}^+ \bar{U}_{i+\frac{1}{2}}^- + \bar{U}_{i-\frac{1}{2}}^- \bar{U}_{i+\frac{1}{2}}^+) - \tilde{\mu} \sum_{i=1}^{N_s} \bar{L}_{i+\frac{1}{2}}^z \ , \qquad (3.3)$$

Comparing it to the effective Hamiltonian (3.2), we find that when the hopping amplitude is tuned to be $t_\alpha = \sqrt{(V_\alpha + V_{ab}) U_0 / 2}$ and the on-site interspecies conversion term $t_{ab} = 0$,

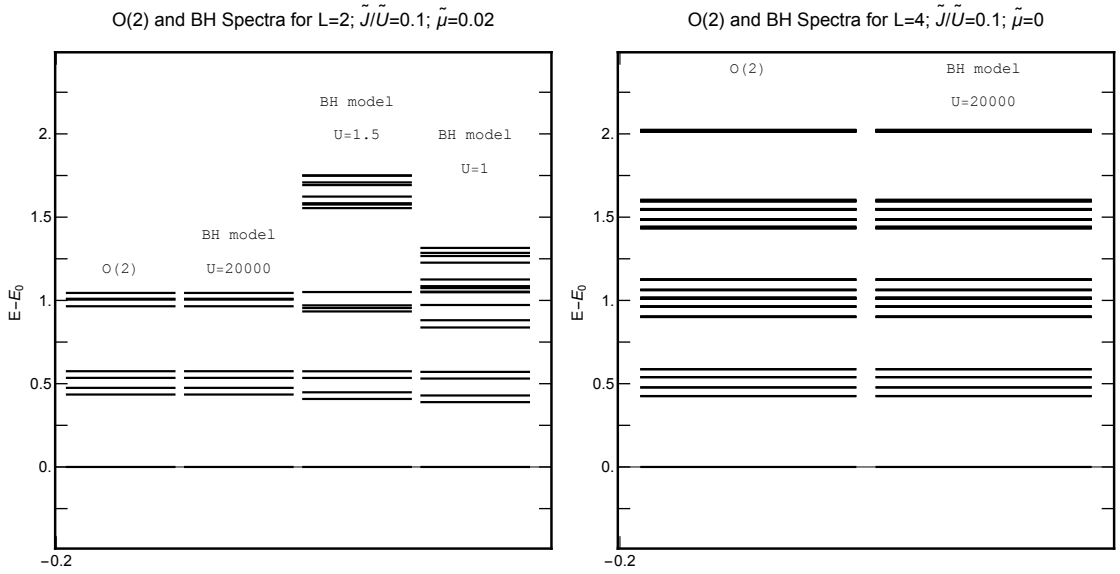

Figure 3.1: $O(2)$ with $\tilde{J}/\tilde{U} = 0.1$ and Bose-Hubbard spectra for $L = 2$ with $\tilde{\mu} = 0.02$ (left) and $L = 4$ with $\tilde{\mu} = 0$ (right). [12]

the effetive Hamiltonian is mapped to Eq. (3.3) with spin-1 truncation. The parameters are related as $Y = 2(U_0 - W)$, $\tilde{\mu} = -\delta - (\Delta_a - V_a) + (\Delta_b - V_b)$, and $X = 2\sqrt{(V_a + V_{ab})(V_b + V_{ab})}$. The three states $|2, 0\rangle$, $|1, 1\rangle$ and $|0, 2\rangle$ correspond to the three states of the spin-1 projection. To check the mapping, we compare the energy spectrum of O(2) Hamiltonian and that of two-species Bose-Hubbard Hamiltonian in Fig. 3.1. We can see they matches perfect. Note that the O(2) Hamiltonian with spin-1 truncation only reflects the physics for $Y \gg X$, when the $(\bar{L}^z_{i+1/2})^2$ term limit the spin excitation. Higher truncaiton is needed for X not small. But spin-1 truncation survives the BKT universality class, it is still interesting to explore it experimentally.

Similarly, by increasing the chemical potentials, it is possible to restrict the Hilbert space to $n_i^a + n_i^b = 2S$ which corresponds to a spin-S ($S > 1$) projection in the $O(2)$ model. However, the ladder operators in the O(2) Hamiltonian (3.3) is different from the ones in

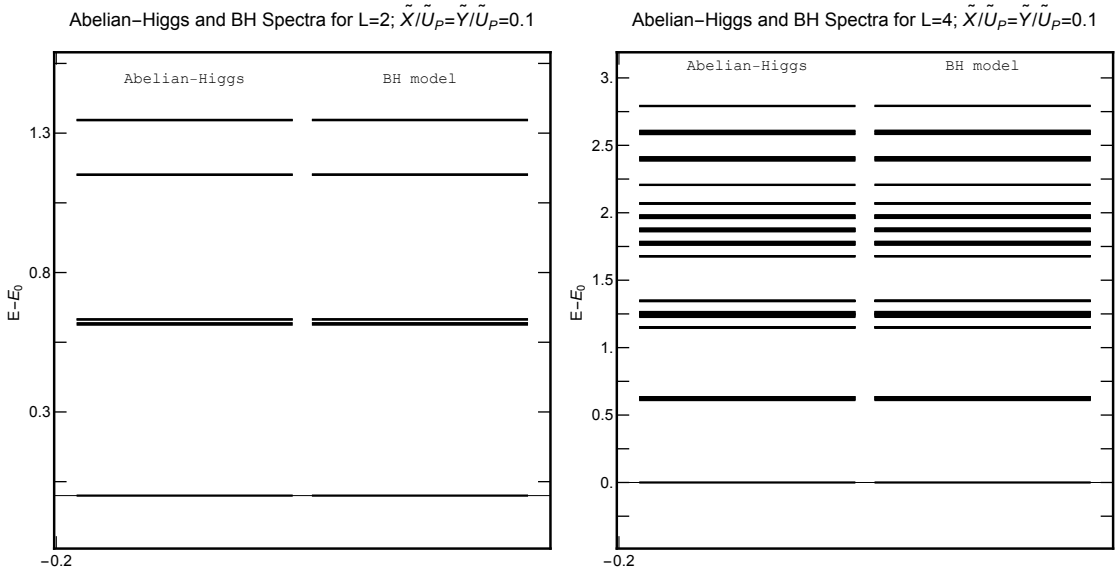

Figure 3.2: Abelian-Higgs model with $\tilde{X}/\tilde{U} = 0.1$, $\tilde{Y}/\tilde{U} = 0.1$ and the corresponding Bose-Hubbard spectra for $L = 2$ (left) and $L = 4$ (right). [12]

the angular momentum algebra. But the mapping still works for large S. Because the matrix elements

$$\sqrt{S(S+1) - m(m+1)} = \sqrt{S(S+1)}\sqrt{1 - \frac{m(m+1)}{S(S+1)}}. \tag{3.4}$$

For large S, the matrix elements are almost constant for those $m \ll S$. In finite systems, the contributions from big spin excitation are small, then the ladder operators can be used to approximate the $\bar{U}^{\pm}$ if we rescale them by $\sqrt{S(S+1)}$. The disadvantage is that we waste a lot of experimental resources by doing this.

3.2.2 The $1 \ll \beta_{pl} \ll \kappa_\tau$ limit of the Abelian Higgs model

We already see that the mapping between the two kinds of ladder operators only works for spin-1 truncation and large spin truncation. For spin-1 truncation, the Hamilto-

nian in the field representation (2.51) only describes the physics at $1 \ll \beta_{pl} \ll \kappa_\tau$. In this limit, $U \gg Y$, $(L_i^z)^2$ term dominate the energy bands, so spin-1 truncation is good enough. The two-species Bose-Hubbard Hamiltonian of Eq. (3.1) is mapped onto the Abelian Higgs Hamiltonian of Eq. (2.51) by setting $t_a = t_b = 0$, $Y = -(V_a + V_b - 2V_{ab})$, $X = \sqrt{2}t_{ab}$, $U = 2(U - W - Y)$, $\Delta_{a(b)} = -2V_{a(b)}$. The mapping is exact, no perturbation calculations. We can see the spectra match very well in Fig. 3.2. As we discussed in Sec. 2.4, higher spin truncation is required for Hamiltonian (2.51) to study the critical behavior of the Abelian Higgs model. But again, using the scheme described in Sec. 3.2.1 will waste a lot of resources.

3.3 The multi-leg ladder with a single atom along a rung

In this section, we invoke a single atomic species in an optical lattice on a multi-leg ladder and recently explored Rydberg-dressed interactions in this platform [239], aiming at maximal simplicity both on the theoretical and experimental side.

An important feature of the Hamiltonians considered above is that L_i^z has positive and negative eigenvalues and cannot be realized as the number operator of a Bose-Hubbard model unless a large chemical potential [248, 214, 11] or two atomic species are introduced [248]. For a similar reason, a 2-leg ladder with $2s$ atoms per rung for a spin-s truncation was suggested in Ref. [12], however the hopping along a rung can only emulate the L^x operator in the rotation group representation instead of the U^x operator in Eq. (2.51) and (2.55). Here, we propose a simpler experimental realization to overcome this difficulty, namely an asymmetric ladder of N_s rungs of length $2s+1$ each with a single atom per rung.

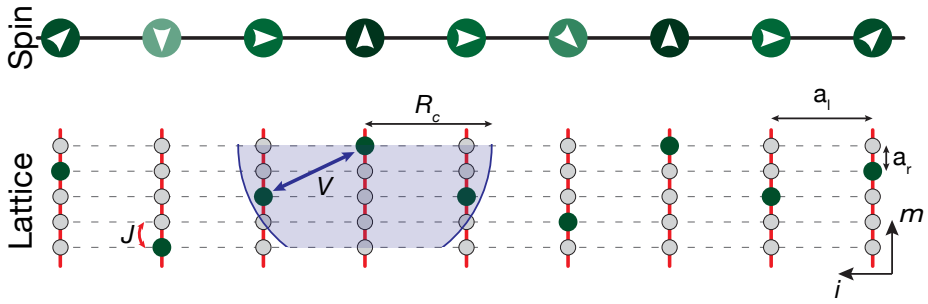

Figure 3.3: (color online) Multi-leg ladder implementation for spin-2. The upper part shows the possible m_z-projections. Below, we show the corresponding realization in a ladder within an optical lattice. The atoms (green disks) are allowed to hop within a rung with a strength J, while no hopping is allowed along the legs. The lattice constants along rungs and legs are a_r and a_l respectively. Coupling between atoms in different rungs is implemented via an isotropic Rydberg-dressed interaction V with a cutoff distance R_c (marked by blue shading). [241]

The lattice constants are a_l and a_r along legs and rungs respectively, see Fig. 3.3, and the tunnel coupling along the legs is vanishing while it has a strength J along the rungs. In this case, the L^z-projection of the spin is encoded in the position m of the atom within a given rung and can be read out with near-unity fidelity in a quantum gas microscope [92]. The initialization of the system can be achieved in such a setup by preparing an atomic Mott insulator and employing site-resolved optical potentials [225].

We now aim at establishing a quantitative connection between the spin Hamiltonians (2.51) and (2.55) and the Hamiltonian of such a ladder system. The latter reads

$$\hat{H} = -\frac{J}{2}\sum_{i=1}^{N_s}\sum_{m=-s}^{s-1}\left(\hat{a}^\dagger_{m,i}\hat{a}_{m+1,i} + h.c\right) - \sum_{i=1}^{N_s}\sum_{m=-s}^{s}\epsilon_{m,i}\hat{n}_{m,i} + \sum_{i,i'=1}^{N_s}\sum_{m,m'=-s}^{s} V_{m,m',i,i'}\,\hat{n}_{m,i}\hat{n}_{m',i'}. \tag{3.5}$$

Here, we have introduced an interaction $V_{m,m',i,i'}$ between two particles at positions (m,i) and (m',i') as well as an on-site potential $\epsilon_{m,i}$. The term $X\sum_i U_i^x$ in Eq. (2.51) and (2.55) directly maps to the tunneling term in Hamiltonian (3.5) for $J = X$. Realizing the other two

terms requires fine-tuned values $V_{m,m',i,i'} = V_{m,m'}\,\delta_{i',i+1}$ with $V_{m,m'} = -|V_0| + Y(m-m')^2/2$ for the interaction potential between two particles constrained by the Kronecker-symbol $\delta_{i',i+1}$ to be located in two neighboring rungs. Furthermore, the on-site potentials have to be tuned to $\epsilon_{m,i} = -Um^2/2$ for the rungs with $i \neq 1, N_s$ and $\epsilon_{m,1} = \epsilon_{m,N_s} = -(U+Y)m^2/2$ for two rungs at the boundaries, up to an irrelevant constant energy offset $-(N_s-1)|V_0|/N_s$ implied for all on-site potentials.

Introducing a Polyakov loop amounts to changing the on-site potentials on the two central rungs $N_s/2$ and $N_s/2+1$ to $\epsilon_{m,N_s/2} = -Um^2/2 - Ym$ and $\epsilon_{m,N_s/2+1} = -Um^2/2 + Y(m-1/2)$, respectively. The boundary condition 10BC can be realized by tuning the on-site potential at one end of the ladder to $\epsilon_{m,1} = -Um^2/2 - Y(m-1)^2/2$.

While the tailored on-site potentials $\epsilon_{m,i}$ can be generated using optical potentials controlled at the single-site level [78], realizing the quadratic distance dependence of the interaction between two particles is challenging in cold atomic gases. However, they can still be realized approximately using off-resonant optical coupling of the atoms to Rydberg states. The resulting isotropic Rydberg-dressed interactions [100, 176] in cold atoms have recently begun to be explored in a many-body setting [239] and exhibit a characteristic distance dependence $V(R) = U_0/(1 + (R/R_c)^6)$ for two atoms separated by a distance R. The saturation value U_0 can be tuned to be positive or negative, and the interaction range R_c is set by the interactions of the coupled Rydberg states and typically reaches up to several sites in an optical lattice, see Sec. 3.4.

The key idea in implementing quadratic interactions in the ladder model consists in utilizing an asymmetric ladder with different lattice constants along legs and rungs

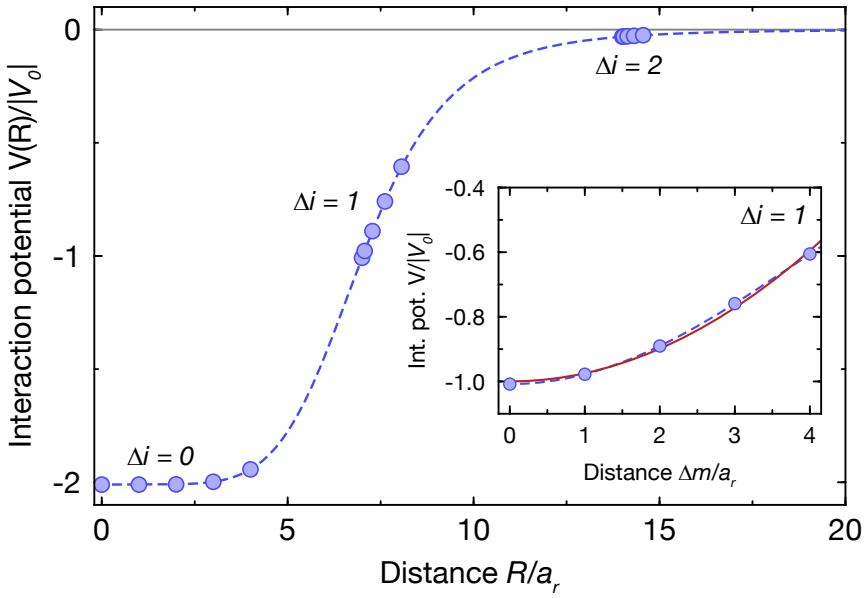

Figure 3.4: (color online) Quadratic interactions on an asymmetric ladder for $s = 2$. The isotropic Rydberg-dressed potential (dashed blue line) is sampled at different distances occurring in the ladder (blue points). Interactions between atoms in different rungs separated by $\Delta i = |i - i'|$ occur in groups. The inset shows the approximate quadratic dependence for $\Delta i = 1$ versus distance $\Delta m = |m - m'|$ within a rung compared to a true quadratic interaction (red solid line). The parameters used are $R_c = a_l = 7\, a_r$. [241]

respectively. In the limit of large a_l/a_r, the interaction potential along the rung approximately acquires the desired quadratic distance dependence for neighboring rungs with $|V_0| = |U_0|/(1+(a_l/R_c)^6)$ and $Y = 6|U_0|(a_l/R_c)^6(a_r/a_l)^2/(1+(a_l/R_c)^6)^2$. At the same time, interactions between next-nearest-neighbor rungs can be minimized, see Fig. 3.4, making them irrelevant for the predicted collapse shown in Fig. 2.8. This and other imperfections as well as concrete experimental numbers are further discussed in Sec. 3.4.

A strength of the presented ladder implementation is the simple realization of models with different spin. A natural first step would be to check the experimental feasibility of the proposal with just two legs, i.e. $s = 1/2$ in Eq. (3.5). The emerging spin model

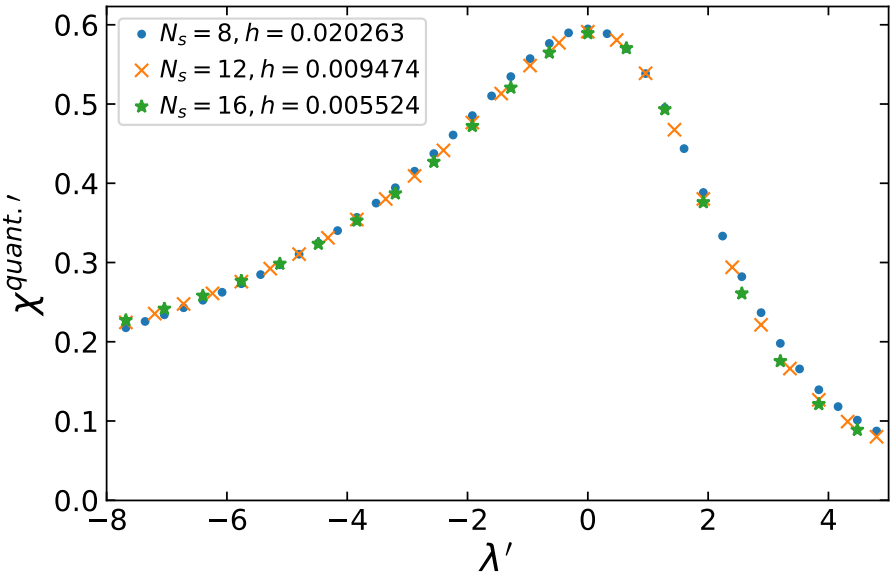

Figure 3.5: (color online) Data collapse for the quantum magnetic susceptibility of the quantum Ising chain with the known rescaling $\chi^{quant.\prime} = \chi^{quant.} N_s^{-(1-\eta)}$ versus $\lambda' = N_s^{1/\nu}(\lambda - 1)$. The reduced magnetic field $h' = hN_s^{15/8} = 1$ for all three system sizes. [241]

corresponds to the well studied spin-1/2 quantum Ising chain in a transverse field with the Hamiltonian

$$\hat{H} = -\lambda \sum_{i=1}^{N_s} \hat{\sigma}_i^z \hat{\sigma}_{i+1}^z - h_x \sum_{i=1}^{N_s} \hat{\sigma}_i^x - h \sum_{i=1}^{N_s} \hat{\sigma}_i^z. \tag{3.6}$$

The transverse field is realized by the tunneling of the atoms and has a strength $h_x = J/2$. Tuning $\epsilon_{\pm 1/2} = \pm h - (N_s - 1)(|V_0| - \lambda)/N_s$, $V_{1/2,1/2} = -|V_0|$, $V_{-1/2,1/2} = -|V_0| + 2\lambda$ is required to realize the other two terms.

Expressing all energies in units of the transverse field ($h_x = 1$), this model has a second order phase transition at $\lambda = 1$ with known exponents [171]. As quantum simulations are still made on relatively small lattices, it is convenient to study the finite-size scaling dictated by the Renormalization Group (RG) analysis of the second-order phase transition.

The zero temperature magnetic susceptibility reads

$$\chi^{quant.} = \frac{1}{N_s} \sum_{<i,j>} \langle (\hat{\sigma}_i^z - \langle \hat{\sigma}_i^z \rangle)(\hat{\sigma}_j^z - \langle \hat{\sigma}_j^z \rangle) \rangle \tag{3.7}$$

where $\langle ... \rangle$ are short notations for $\langle \Omega | ... | \Omega \rangle$ with $|\Omega\rangle$ the lowest energy state of $\hat{H}$. The data collapse obtained with the standard RG rescalings is illustrated in Fig. 3.5.

The quantum Ising model has for example been quantum simulated in systems of ultra-cold ions [21] and with atoms in tilted optical lattices [200]. New generations of D-wave machines have more versatile time-dependent capabilities. It seems possible to maintain a transverse field [122] but there are temperature effects that need to be better understood. Multi-mode cavity photon-mediated interactions [217] can also be used to simulate the quantum Ising model. The possibility of extending these setups or related ones to reproduce a multi-leg ladder is being investigated.

3.4 Experimental implementation for the multi-leg ladder

3.4.1 Quadratic interactions in a ladder

For the quantum simulation of the Abelian Higgs model in spin-s truncation, we aim to implement a ladder system with quadratic interactions between particles in neighboring rungs of the ladder. The starting point is an isotropic Rydberg-dressed potential $V(R) = U_0/(1 + (R/R_c)^6)$ with a cutoff distance $R_c = (C_6/2\Delta)^{1/6}$ and a saturation value $U_0 = \Omega^4/8\Delta^3$ given by the laser coupling Ω, detuning Δ and van-der Waals coefficient C_6 for the interaction between the coupled Rydberg states [100, 176]. Quadratic interactions can be realized in a ladder with different lattice constant a_l along the legs and a_r along the

rungs. To see this, we express the distance between two particles in terms of the rung and leg lattice constants and indices as

$$R = \sqrt{(\Delta m\, a_r)^2 + (\Delta i\, a_l)^2}, \tag{3.8}$$

where we have abbreviated the separations along the legs and rungs with $\Delta i \equiv |i - i'|$ and $\Delta m \equiv |m - m'|$. Inserting this in the interaction potential $V(R)$, we obtain for the nearest-neighbor rung with $\Delta i = 1$

$$\begin{aligned} V(R) &= \frac{U_0}{1 + (\sqrt{(\Delta m a_r)^2 + (a_l)^2}/R_c)^6} \\ &\approx \frac{U_0}{1 + (a_l/R_c)^6} - \frac{1}{2}\frac{6U_0(a_l/R_c)^6(a_r/a_l)^2}{(1 + (a_l/R_c)^6)^2}\ \Delta m^2 \\ &+ O\left((a_r/a_l)^4 \Delta m^4\right). \end{aligned} \tag{3.9}$$

For the expansion, we have assumed $(\Delta m\, a_r)/a_l \ll 1$ This allows us to express the potential

$$V = -|V_0| + \frac{Y}{2}\Delta m^2 \tag{3.10}$$

given in the main text in terms of the experimentally relevant parameters U_0, a_l, a_r and R_c by identifying

$$Y = \frac{6|U_0|(a_l/R_c)^6(a_r/a_l)^2}{(1 + (a_l/R_c)^6)^2} \tag{3.11}$$

$$|V_0| = \frac{|U_0|}{1 + (a_l/R_c)^6}. \tag{3.12}$$

For simplicity, we have hereby assumed attractive interactions and written $U_0 = -|U_0|$.

As the interactions between next-nearest-neighbor rungs are assumed to be vanishing in the desired spin model in Eq. (2.51), it is important to check that they are small enough in this approximation. The next-nearest-neighbor-rung interactions (NNNRI) are

obtained by just setting $a_l \to 2a_l$ in the above parameters, yielding

$$Y^{(2)} = \frac{6|U_0|(2a_l/R_c)^6(a_r/2a_l)^2}{(1+(2a_l/R_c)^6)^2} \tag{3.13}$$

$$|V_0^{(2)}| = \frac{|U_0|}{1+(2a_l/R_c)^6} \tag{3.14}$$

$$H_{NNNRI} = \sum_{i=1}^{N_s-2} \sum_{m,m'=-s}^{s} \left(-|V_0^{(2)}| + \frac{Y^{(2)}}{2}\Delta m^2 \right) \hat{n}_{m,i}\hat{n}_{m',i+2}. \tag{3.15}$$

In order to continue the discussion, it is now helpful to gain some intuition for where the quadratic dependence is a good approximation to the Rydberg-dressed potential. One exemplary Rydberg-dressed potential is depicted in the main text in Fig. 3.4. As one can see in this example, the points for the different Δi are grouped. This is generally necessary to achieve a large ratio between $\Delta i = 1$ and $\Delta i = 2$, i.e. a suppression of NNNRI. Furthermore, the $\Delta i = 1$ points should be located close to the most linear part of the potential $R \approx R_c$. This can be understood from the geometric argument that in the limit $a_r/a_l \to 0$, where the quadratic approximation of R in Δm works best, we sample a linear potential with approximately quadratically spaced points. At the same time, however, pushing a_r/a_l towards zero squeezes the points closer together, effectively reducing the interaction Y. This is also directly obvious from the quadratic dependence of Y on a_r/a_l shown in Eq. (3.11). To summarize, one has to compromise between maximizing Y, minimizing $Y^{(2)}$ and optimal quadratic dependence within a rung.

Qualitatively, Fig. 3.4 and our previous discussion indicate to work close to the regime $R_c \approx a_l$. Setting for simplicity $R_c = a_l$, we can estimate the ratio between nearest-

neighbor and next-nearest-neighbor rung interactions as (approximating $2^6 + 1 \approx 2^6$)

$$|V_0| = \frac{1}{2}|U_0| \tag{3.16}$$

$$|V_0^{(2)}| = \frac{1}{64}|U_0| \tag{3.17}$$

$$Y = \frac{3}{2}|U_0|\left(a_r/a_l\right)^2 \tag{3.18}$$

$$Y^{(2)} = \frac{3}{128}|U_0|\left(a_r/a_l\right)^2. \tag{3.19}$$

This shows that NNNRI are suppressed by approximately $|Y|/|Y^{(2)}| = 2^6 = 64$ in this regime and hence only reach up to 1.5% of the nearest-neighbor-rung interactions (NNRI). Furthermore, it should be noted that already small changes in a_l/R_c influence the exact numbers due to the strong scaling with $(a_l/R_c)^6$, which allows for considerable flexibility in fine-tuning the implementation. For example, increasing a_l/R_c slightly above unity suppresses the NNNRI to values below 1%, such that they can easily be tuned to be irrelevant for the collapse displayed in Fig. 2.8.

Fig. 3.6 shows $N_s\Delta E$ obtained from the Hamiltonian of the ladder system with NNNRI 1.5% of NNRI by DMRG. The data collapse is robust to NNNRI for the ladder systems which are mapped to the spin Hamiltonians with 10BC, while it is broken dramatically by such a small NNNRI in the ladder systems which are mapped from the spin Hamiltonians with a Polyakov loop. In the O(2) limit, NNNRI doesn't change the critical property for the former, while it would open a gap to the gapless phase for the latter, which has been confirmed numerically (not shown here). However, based on 1st order perturbation theory, we can correct the ground state energy by subtracting the expectation value of NNNRI, $\langle H_{NNNRI}\rangle$, from it. The corrected data sets collapse perfectly onto the same lines of collapse in Fig. 2.8. Experimentally, we can measure the density-density correlations

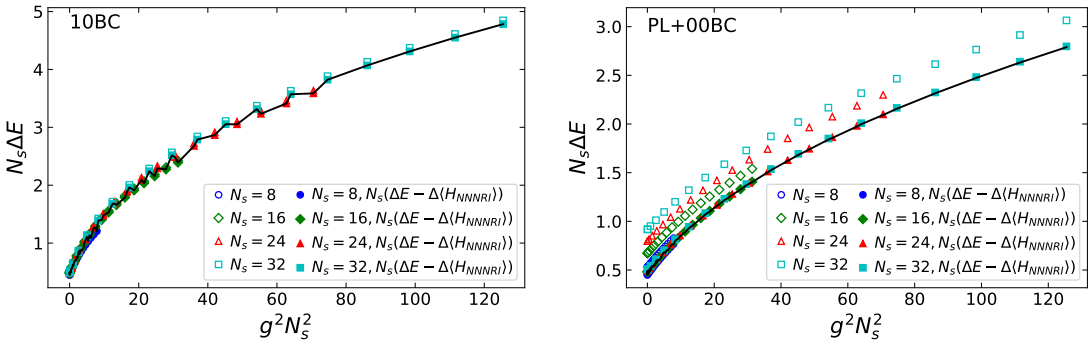

Figure 3.6: (color online) $N_s\Delta E$ obtained from the ladder Hamiltonians with NNNRI 1.5% of NNRI (open markers). When mapping from the spin Hamiltonians to the ladder systems, the energy gap between 10BC and 00BC systems (left) is more robust to NNNRI than the energy gap between PL+00BC and 00BC systems (right). We can correct the ground state energy by subtracting the ground state expectation value of NNNRI from it (filled markers). The solid lines are the collapse lines from the spin Hamiltonians. [241]

between next-nearest-neighbor rungs $\langle \hat{n}_{m,i}\hat{n}_{m',i+2}\rangle$ and extract $\langle H_{NNNRI}\rangle$ to do the same correction.

3.4.2 Imperfections due to decoherence

Experimentally, the achievable Rydberg-dressed interaction strength U_0 is limited via the effective decay rate γ_{eff} of the dressed state due to the coupling to a Rydberg state with a limited lifetime [100, 239]. This leads to decoherence in the time evolution of the system not captured by purely Hamiltonian dynamics described by Eq. (3.5). Generally, both the Rydberg-dressed interaction strength as well as the effective decay rate increase with larger Rydberg-state admixture. One can quantify the coherence in terms of a "figure of merit" $Q = |U_0|/\gamma_{\text{eff}}$, which expresses the average number of coherent cycles per decay event.

For simulating the Abelian Higgs model in the spin representation, the additional constraint of realizing quadratic interactions effectively reduces the usable interactions. Considering Fig. 3.4, this is directly obvious as the strongest interactions ($\Delta\, i = 0$) are not sampled for a single atom per rung. A useful figure of merit is given by comparing the quadratic part of the interaction Eq. (3.11) with the effective decoherence,

$$\begin{aligned} Y/\gamma_{\text{eff}} &= 6\frac{(a_l/R_c)^6}{(1+(a_l/R_c)^6)^2}(a_r/a_l)^2|U_0|/\gamma_{\text{eff}} \\ &= 6\frac{(a_l/R_c)^6}{(1+(a_l/R_c)^6)^2}\,(a_r/a_l)^2\,Q. \end{aligned} \tag{3.20}$$

This shows that realizing an optimal quadratic dependence, which requires ideally $a_r/a_l \to 0$, as well as maximally suppressing the NNNRI, which requires $R_c/a_l \to 0$, conflicts with the interaction-to-decoherence ratio. Below, we outline a parameter regime showing that the experimental implementation still seems feasible.

3.4.3 Measurement of the energy gap

In order to experimentally measure the energy gap displaying the universal scaling (see Fig. 2.8), it is necessary to first prepare the ground states of the respective models. Their mean energy $\langle E\rangle$, with $\langle\ldots\rangle$ denoting the quantum average, can then be reconstructed by two sets of measurements. In a first set of measurements, the atomic distributions are immediately frozen by switching off interactions and tunneling at the same time. The contributions of on-site potentials, $\sum_{i=1}^{N_s}\sum_{m=-s}^{s}\epsilon_{m,i}\langle\hat{n}_{m,i}\rangle$, and interactions, $\sum_{i,i'=1}^{N_s}\sum_{m,m'=-s}^{s}V_{m,m',i,i'}\,\langle\hat{n}_{m,i}\hat{n}_{m',i'}\rangle$, to the mean energy can then be extracted from the measured atomic distribution by measuring the mean local density $\langle\hat{n}_{m,i}\rangle$ and density-density correlations $\langle\hat{n}_{m,i}\hat{n}_{m',i'}\rangle$ respectively. Both are accessible in a quantum gas

microscope with local detection [70]. In a second set of measurements, the contribution of the tunneling term to the mean energy has to be determined. This amounts to extracting first-order correlations of the form $\langle \hat{a}^\dagger_{m,i} \hat{a}_{m+1,i} \rangle$, which has recently been demonstrated for atoms in optical lattices employing Talbot interferometry [192]. The reconstruction of the energy relies on knowledge of the on-site potentials, interactions and tunnel coupling along the rungs, each of which can be calibrated in independent measurements.

3.4.4 Experimental numbers

In the following, we give some concrete experimental figures to underline the feasibility of realizing the desired spin models. Hereby, we assume tunneling along the rungs with strength $J/h = 100\,\mathrm{Hz}$, which is e.g. readily achieved for rubidium in optical lattices [225].

Spin-s model with quadratic interactions

First, we focus on the feasibility of reaching the parameter regime for the ladder implementation of the spin-s truncation of the Abelian Higgs model to study the collapse displayed in Fig. 2.8. Aiming at $J = Y$ ($X = 1$ in Fig. 2.8), the required interaction strength for $R_c = a_l \approx 7\, a_r$ is $|U_0|/\hbar \approx 2\pi \times 3.3\,\mathrm{kHz}$ (using Eq. (3.18)). Assuming a coupling strength of $\Omega/\hbar = 2\pi \times 100\,\mathrm{MHz}$ to the Rydberg state, which is within reach in future, specialized experiments, the desired interaction $|U_0|$ and hence Y can be achieved with a detuning of $\Delta/\hbar \approx 2\pi \times 1560\,\mathrm{MHz}$. The interaction strength between two Rydberg atoms with $80P_{3/2}$, measured by the van der Waals dispersion coefficient, is $C_6 \approx 5500\,\mathrm{GHz}\,\mu\mathrm{m}^6$. As a result, for the chosen detuning, the cutoff distance is $R_c = (C_6/2\Delta)^{1/6} \approx 3.5\,\mu\mathrm{m}$ and hence an experimentally realistic lattice spacing of $a_r \approx 500\,\mathrm{nm}$ would lead to $R_c/a_r \approx 7$. For the

lifetime $\tau = 250\,\mu$s of the admixed Rydberg state $80P_{3/2}$, the dressed state acquires an effective decay rate of $\gamma_{\text{eff}} \approx 4\,\text{s}^{-1}$, resulting in $J/\gamma_{\text{eff}} \approx 25$. Tuning to larger values of J/Y by reducing Y to study the collapse shown in Fig. 2.8 improves this ratio by a factor $\sqrt{J/Y}$ for constant Δ due to smaller Rydberg-state admixture.

A direct increase in the figure of merit should be possible by using lighter elements like potassium or lithium, for which larger tunneling rates are feasible. This allows for working at a larger Rydberg-state admixture, which is favorable to increase the quality factor. Furthermore, improvements are possible by increasing Rabi couplings to Rydberg states, by implementing more advanced dressing schemes [19] or in future experiments in a cryogenic environment, where the Rydberg lifetime is expected to increase (to 1.2 ms for $80P$) due to suppression of black-body-radiation-induced decay. Combining these steps, we estimate a possible increase in the figure of merit by well above one order of magnitude.

Spin-$1/2$ Ising model

The spin-1/2 Ising model (Eq. (3.6)) discussed in the main text constitutes a first, easier step for implementing the described ladder systems. Contrary to the more complex spin-models, in this case no asymmetric ladder is required, i.e. $a_r = a_l$. Keeping the condition $R_c = a_l$, in this case $\lambda \approx U_0/4$ using the same definition as in Eq. (3.6). For a Rabi-coupling of $\Omega/\hbar = 2\pi \times 100\,\text{MHz}$ and a detuning of $\Delta/\hbar \approx 2\pi \times 1560\,\text{MHz}$, the accessible spin interaction strength is $\lambda/\hbar = 2\pi \times 825\,\text{Hz}$. A tunneling strength of $J/\hbar = 2\pi \times 100\,\text{Hz}$ along the rungs translates to a transverse field of $h_x/\hbar = 2\pi \times 50\,\text{Hz}$, such that $\lambda/h_x \approx 16.5$. For a coupling to the Rydberg state $80P_{3/2}$ with an effective decay

rate of $\gamma_{\text{eff}} \approx 4\,\text{s}^{-1}$ for the above admixture parameters, the figure of merit in this regime becomes $h_x/\gamma_{\text{eff}} \approx 12.5$. Towards stronger transverse fields, the figure of merit increases proportional to $\sqrt{h_x/\lambda}$, such that it reaches up to 50 in the critical region $\lambda/h_x = 1$. Furthermore, it can be improved by the same means quoted above for the more complex spin model.

3.5 Conclusions

We have presented an experimental platform for the quantum simulation of the Abelian Higgs model in 1+1 dimension and outlined a strategy for an initial benchmark of the quantum simulator. An interesting perspective is the experimental simulation of out-of-equilibrium dynamics following a quantum quench, which promises insight into dynamics described by the LGT when inaccessible with classical computing.

Chapter 4

Probing the conformal Calabrese-Cardy scaling with cold atoms

4.1 Introduction

The concept of universality provides a unified approach to the critical behavior of lattice models studied in condensed matter, lattice gauge theory (LGT) and experimentally accessible systems of cold atoms trapped in optical lattices. Conformal field theory (CFT) [174, 62] offers many interesting examples of universal behavior that can be observed for lattice models in two [14, 75, 63], three [69], and four [59, 136] dimensions. Practical simulations for these models unavoidably involve a finite volume that breaks explicitly the conformal invariance. However, this symmetry breaking follows definite patterns dictated by

the restoration of the symmetry at infinite volume and allows us to identify the universality class. In view of the rich collection of interesting CFTs, it would be highly desirable to study their universality classes using quantum simulations. In order to start this ambitious program, one needs a simple concrete example to demonstrate the feasibility of the idea.

In this chapter, we propose to use the setup of ongoing cold atom experiments to quantum simulate the $O(2)$ model with a chemical potential and check the predictions of CFT for the growth of the entanglement entropy with the size of the system corresponding to the universality class of the superfluid (SF) phase. The $O(2)$ model is an extension of the Ising model where the spin is allowed to move on a circle, making an angle θ with respect to a direction of reference. This model can be used to describe easy plane ferromagnetism and the compactness of θ leads to topological configurations called vortices. Their unbinding provides a prime example of a BKT transition [16, 130] in a way that has also been advocated to apply for gauge theories near the boundary of the conformal window [115]. When space and Euclidean time are treated isotropically, this model has important common features with models studied numerically in LGT to describe relativistic systems in the continuum limit. Quantum simulating this model and studying experimentally the CFT predictions would be a crucial first step towards applying similar methods for LGT models.

In the following, we show that these goals can be achieved by measuring the entanglement entropy of a simple Bose-Hubbard (BH) model in a very specific region for the adjustable couplings. The entanglement entropy measures the correlations between degrees of freedom in different regions of a system, is an important tool [218] in assessing the phase structure and the finite-size scaling. For a CFT in one space and one time (1+1)

dimension, the ground state entanglement entropy increases logarithmically with the spatial volume of the system and its subsystems [218, 129, 30, 35, 29, 39]. Using basic CFT results, Calabrese and Cardy [30] established that the coefficient of proportionality is in general the central charge multiplied by a rational number depending on the type of entropy and the boundary conditions (CC scaling). The central charge, denoted c, is of primordial importance in CFT. It characterizes the universality class and is present in a variety of physical observables [62, 30].

It has been proposed to use a quantum gas microscope to study the second-order Rényi entropy S_2 of one-dimensional fermionic Hubbard chains [172, 25] at half(quarter)-filling which seem consistent with $c = 1(2)$. Recently, manipulations of small one-dimensional chains of cold bosonic ^{87}Rb atoms trapped in optical lattices have allowed experimental measurements of S_2 [106, 118] using a beam splitter method [164, 57]. In these experiments, the SF phase is reached by increasing the hopping parameter J to values having the same order of magnitude as the onsite energy U. It is important to realize that in order to see a clear correspondence between the BH and $O(2)$ model, one needs $J/U \ll 1$. Some examples are given below. However, the feasibility of the measurements is restricted by the fact that very small values of J can be problematic because of disorder or finite-temperature effects. We argue that a reasonable compromise is to take $J/U \simeq 0.1$. In this regime, a detailed study [11] shows that the finite size scaling is easier to resolve near half-filling [1].

Experimental measurements have been performed for small chains of four [106] and six [118] atoms and only slightly larger sizes are expected to be within experimental

[1]For bosons, *half-filling* means twice more sites than particles, while for spin-1/2 fermions it means one particle per site.

reach in the near future [2]. An important feature of S_2 with open boundary conditions [11] is that the subleading corrections are large and decay slowly with N_s (see Eq. (4.3) below). Knowing these corrections is essential to extract the leading CC scaling using N_s accessible in experiments.

4.2 The model and the quantum simulator

The Hamiltonian of O(2) model has been obtianed in Sec. 3.2.1, see Eq. (3.3). In the following, we use the spin-1 truncation for numerical calculations, which is enough for $Y \gg X$. We will use $U = Y, J = X/2$ in this chapter. This notation is often used in the Bose-Hubbard model. Quantum simulators involving two species of bosonic atoms have been proposed for the spin-1 approximation [248, 12], also see Chapter 3. This effort is directly related to recent attempts (for recent reviews see Refs. [207, 229, 245]) to develop quantum simulators for models studied in LGT.

If the chemical potential in Eq. (3.3) is large and positive, the states in O(2) model with negative eigenvalues play a minor role in numerical calculations. If we omit these states, we can replace $\bar{L}_x^z$ by the occupation number n_x and $\bar{U}_x^+$ by the creation operator $a_x^\dagger$ in Eq. (3.3). We then obtain the simple Bose-Hubbard Hamiltonian:

$$\hat{H} = \frac{U}{2} \sum_x n_x(n_x - 1) - J \sum_x (a_x^\dagger a_{x+1} + h.c.). \tag{4.1}$$

This approximate correspondence already discussed in the literature [73, 187] is supported by results presented below. In the following, we focus on the region of the phase diagram where $\tilde{\mu} \simeq U/2 \gg J$ illustrated in Fig. 4.1. In this regime, where the system has half-

[2] In the discussion we focus on experiments with 16 sites or less.

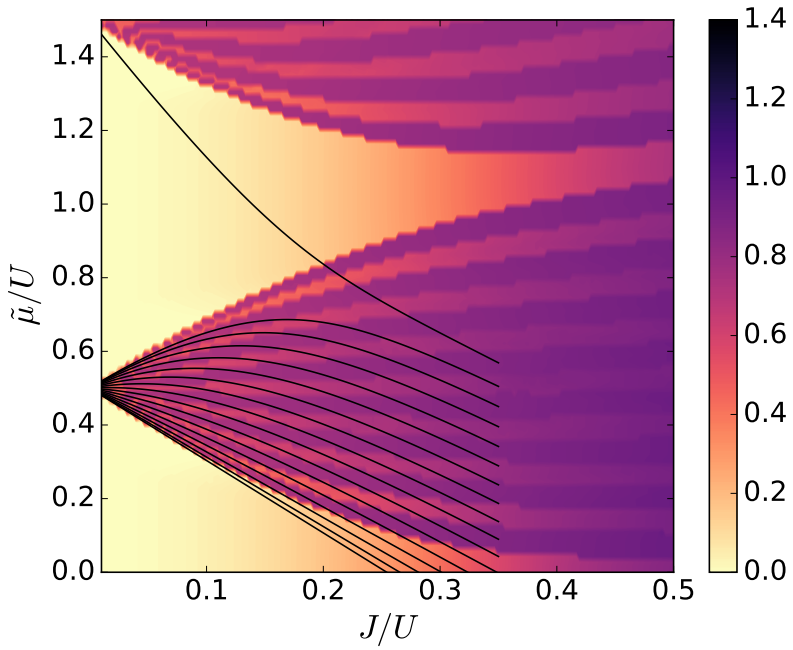

Figure 4.1: S_2 for $O(2)$ with $N_s = 16$ and OBC. Laid over top are the BH boundaries between particle number sectors. [214]

filling, the particle occupancies 0 and 1 dominate for BH (hard core limit) and there is an *approximate* correspondence with the spin-1/2 XX model which is integrable and has a central charge $c = 1$ [218, 129].

4.3 The second order Rényi entropy

Recent cold atom experiments [106, 118] have measured the second-order Rényi entropy

$$S_2(\mathcal{A}) \equiv -\ln\big(\mathrm{Tr}\big(\rho_{\mathcal{A}}^2\big)\big) \ , \tag{4.2}$$

for a variety of subsystems $\mathcal{A}$ and open boundary conditions (OBC). The reduced density matrix $\hat{\rho}_{\mathcal{A}}$ is obtained by tracing over the complement of $\mathcal{A}$. CFT provides severe restrictions

on the dependence of S_2 on the size of the system and the subsystem [30, 35, 39, 29, 71]. In the following, we restrict ourselves to systems with an even number of sites and a subsystem $\mathcal{A}$ of size $N_s/2$. Fig. 4.1 displays S_2 for $N_s = 16$ as a function of J/U and the chemical potential. The lower (upper) light part is the Mott phase with particle density $\lambda = 0$ (1), and the 15 plateaus corresponding to the particle number sectors 1, 2, ..., $N_s - 1$ in the SF phase in between are visible. Its boundaries $\tilde{\mu}/U = 1/2 \pm 2J/U$ at small J follow from a perturbative calculation and are consistent with Refs. [10, 131] for BH at larger J . In the following, we focus on the half-filling region which is more or less horizontal in the SF region and can be reached numerically at arbitrarily small J/U. The choice for half-filling was made because of the following: Near the boundaries of the Mott insulator lobes with the superfluid phase the Rényi entropy takes on a constant value of ln(2). Between each lobe there are $N_s - 2$ boundaries denoting the particle number in the chain, with an approximate symmetry around $N_s/2$ particles (i.e. half-filling for bosons). This number has the clearest signal for the entanglement entropy (see Ref. [11]) and therefore all work here. In addition, all work here was done with open boundary conditions. However, while this is more easily realized in experiment, the second order Rényi entropy with open boundary conditions has much larger fluctuations than the von Neumann entropy (See Ref. [11]).

Since existing experiments only allow a very limited number of sites, it is crucial to take into account subleading corrections. Using existing results [30, 35, 39, 29, 71] for subsystems of size $N_s/2$, we consider the form:

$$S_2(N_s) = K + A \ln(N_s) + \frac{B \cos\left(\frac{\pi N_s}{2}\right)}{(N_s)^p} + \frac{D}{\ln^2(N_s)}, \tag{4.3}$$

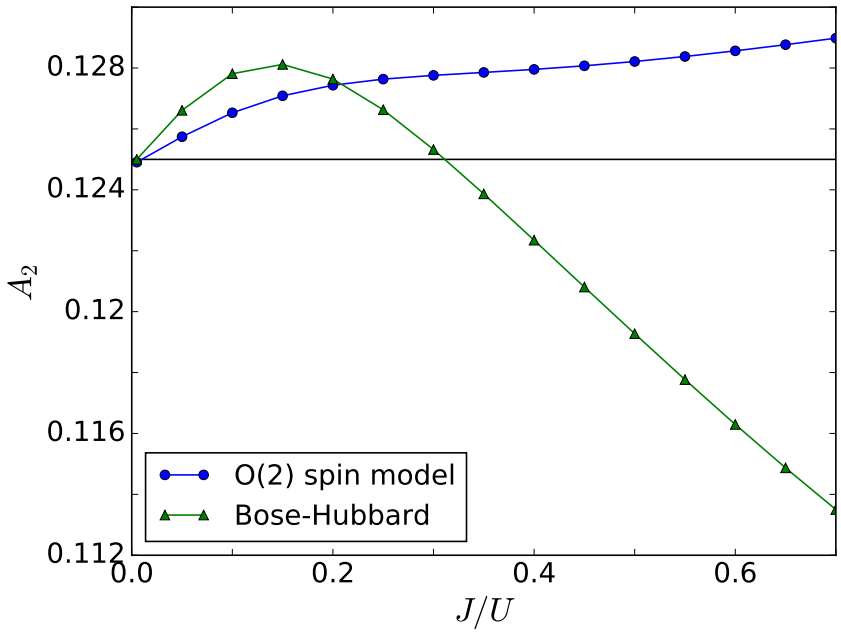

Figure 4.2: The A values from fits to S_2 with open boundary conditions for Bose-Hubbard data (green triangles online) and $O(2)$ spin model data with a spin-1 truncation (blue circles online) at half-filling. The horizontal line is the conformal field theory prediction. The A values were extracted from a fit to Eq. (4.3) with a correction term proportional to $1/\ln^2(N_s)$. The farthest point to the left is at $J = 0.005$, and the lines through the data are meant to guide the eye. [214]

where K, A, p, B, and D are fitting parameters. For OBC, the CC scaling predicts $A = c/8$.

4.3.1 The dependence of fitting parameters on J/U

Here we consider fits to the second order Rényi entanglement entropy, S_2, across a range of J/U values to better understand the dependence on J/U. These fits were done with DMRG data for $N_s = 4$ up to $N_s = 64$. We fit the second order Rényi entanglement entropy with a subsystem size of $l = N_s/2$ and compared the coefficient of logarithmic

scaling, A, between the BH and $O(2)$ models for various finite-size correction terms. The A values as a function of J/U can be found in Fig. 4.2 with a correction term proportional to $1/\ln^2(N_s)$ which is predicted by conformal field theory (CFT) [39]. We considered additional corrections like $1/N_s$, $1/\ln(N_s)$, etc ... We found some features were robust across different functional forms for the corrections. For larger J/U the BH A values tended to decrease monotonically, while the $O(2)$ A values seem to increase. There appears to be a crossing between the BH data and the CFT prediction around $J/U \approx 0.35$. However at small J/U, only the correction $\propto 1/\ln^2(N_s)$ showed a tendency towards $A_2 \approx 1/8$ as $J/U \to 0$, a soluble limit where $c = 1$.

4.3.2 Finite temperature effects

We considered the effects of a finite temperature for a few cases on the Rényi entropy. An example of the finite temperature effects on the scaling with the system size is shown in Fig. 4.3. As one can see the finite temperature effects are much more pronounced for smaller J/U. To take the finite temperature effects into account it is enough to add a term linear in l or N_s, for the subsystem or system scaling respectively. The fits in Fig. 4.3 and those used in the main text were done similarly, using Eq. (4.3) with an additional linear term. For a discussion for the thermal correction term derived from CFT, see Appendix C.

In conclusion, in order to verify the prediction $A = c/8$, the choice for $J/U = 0.1$ for quantum simulation is a nice compromise since ideally the smaller the J/U the better for the mapping between BH and $O(2)$, however, for experimental purposes too small a value of

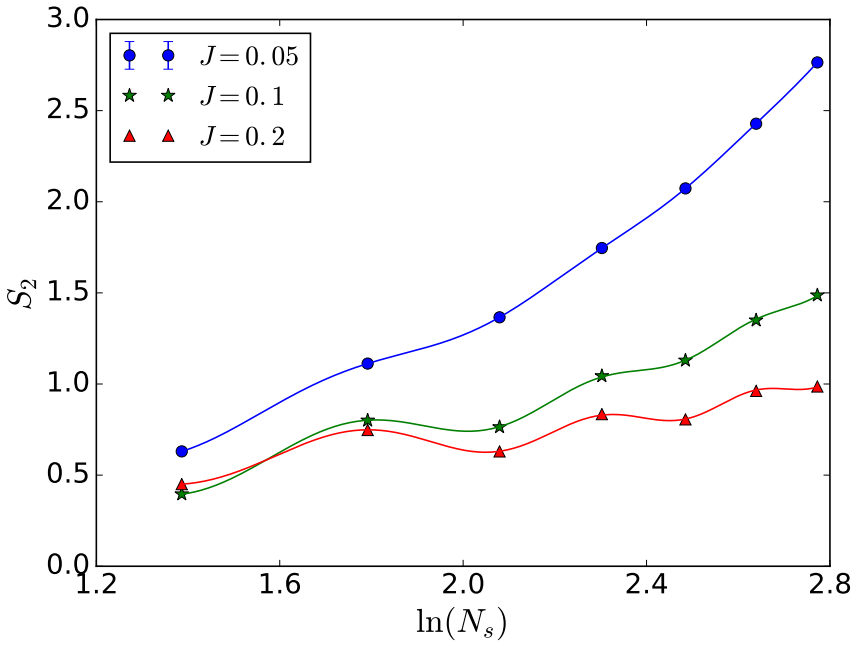

Figure 4.3: The second order Rényi entropy, S_2, as a function of the logarithm of system size with a finite temperature and $l = N_s/2$. Here $U = 1$ and $T = 0.04$ is shown. The lines through the data points are fits using Eq. (4.3) with one addition term linear in the system size. The $J = 0.05$ data used sampling methods however the errors are smaller than the markers. [214]

J is inconvenient because of the associated long time scales and sensitivity to uncontrolled disorder, and finite temperature effects are larger at smaller J/U.

4.3.3 J/U = 0.1

We have calculated S_2 at half-filling for $J/U = 0.1$ for the two models considered with DMRG using the ITensor C++ library. For the $O(2)$ model, the results were cross-checked [11] with TRG methods [142, 248, 236].

If we use the numerical data for N_s up to 64, we obtain $A = 0.1263$ for $O(2)$ and 0.1278 for BH which is close to the CC prediction 0.125 for $c = 1$. The difference between

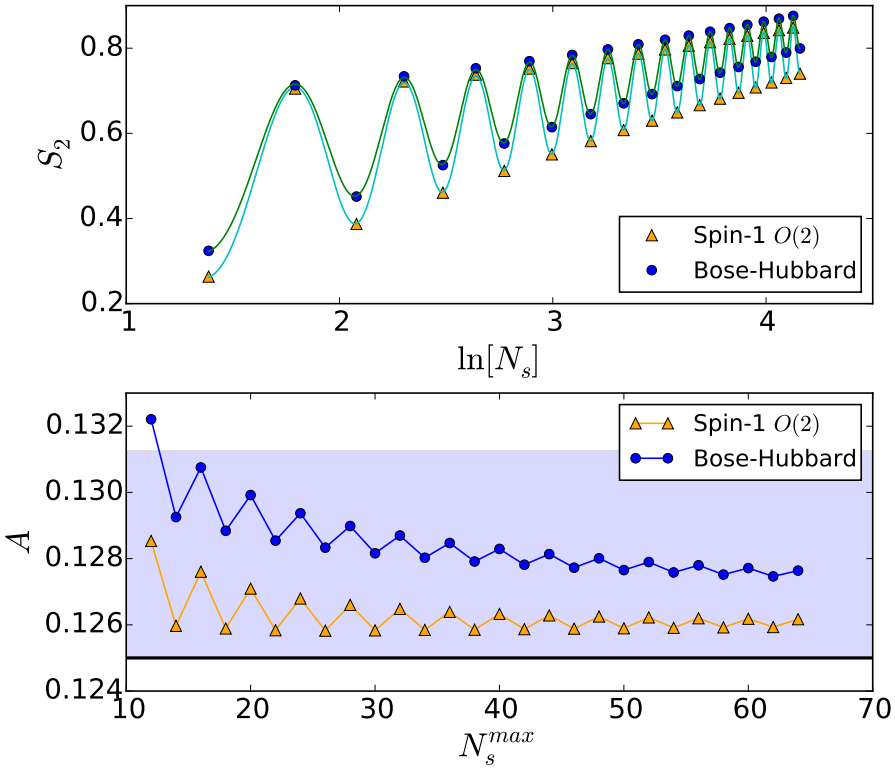

Figure 4.4: (top) S_2 at half-filling with OBC for $O(2)$ and BH with $J/U = 0.1$. The solid lines are the fits for BH and $O(2)$. (bottom) Values of A as a function of the maximal value of N_s used in the fit, the band represents a positive departure of 5 percent from the expected value 0.125. [214]

the two models can be reduced significantly by decreasing J/U, which also brings A closer to 0.125 [11]. In order to test the predictive ability of the fit for smaller spatial sizes we have reduced the maximal value N_s^{max} of N_s from 64 to smaller values, down to 12. The results for S_2 and A are shown in Fig. 4.4 which suggests that the estimates converge slowly to the CFT value as N_s^{max} increases. It has also been noticed that if J/U is increased to $J/U \simeq 0.3$ for BH, the sign of D changes in a way that seems almost independent of the other subleading corrections used. In this region of parameters, the periodic corrections are

smaller which may facilitate the estimate of c, however the close connection with the $O(2)$ model is lost.

4.4 Experimental setup

We now proceed to explain the proposed experimental setup. We consider an optical lattice experiment with single-particle resolved readout and local manipulation of the optical potential, similar to Ref. [106]. In the experiment, two copies of the one-dimensional many-body state of interest are prepared in adjacent rows of an optical lattice, and global and local Rényi entropies can be measured by a beamsplitter operation implemented via a controlled tunneling operation between the two copies (Fig. 4.5a). The parity of the atom number in one copy after the beamsplitter operation gives access to the quantum mechanical purity [57].

BH systems with tunable parameters U and J and well-defined particle number are realized in current experiments with one particle per site. Fig. 4.5b shows a proposed scheme to achieve half-filling at $J/U \approx 0.1$: N_p bosons are initialized in the Mott regime $J \ll U$, as in current experiments. A superimposed harmonic confinement as well as two sharp, confining walls separated by N_s sites ensure that the system remains in its ground state as the optical lattice depth is adiabatically reduced to achieve the desired J/U. The harmonic confinement is then removed to realize a homogeneous system with hard wall boundary conditions at half-filling. For system sizes considered here, this scheme should allow adiabatic preparation of the ground state with available experimental tools. Alter-

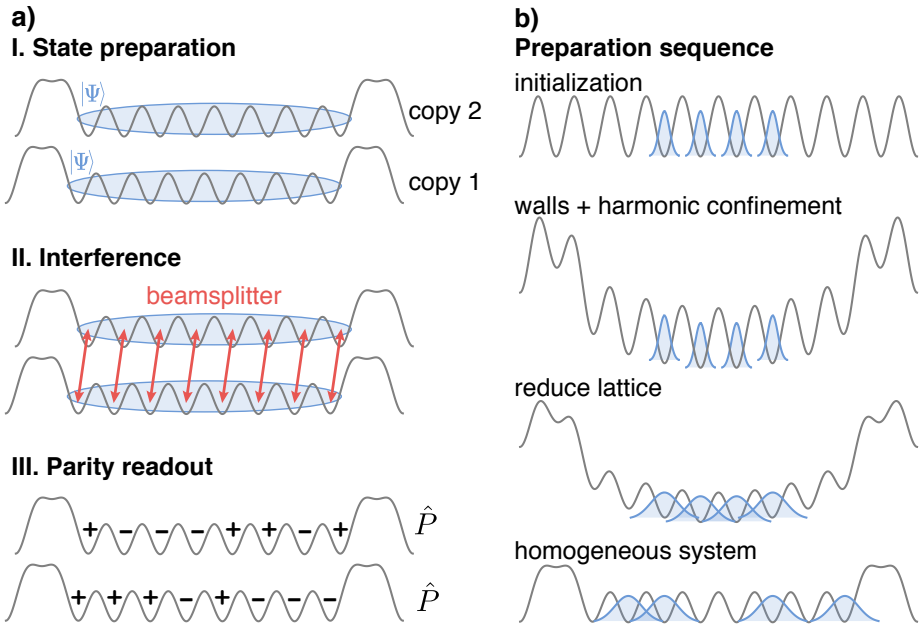

Figure 4.5: Measuring entanglement entropy in optical lattices. a) Two copies of a quantum state $|\Psi\rangle$ interfere under a beamsplitter operation, and site-resolved number measurements reveal the local parity $\hat{P}$ and entanglement entropy. b) Proposed state preparation for BH systems at half-filling, here for 4 atoms on 8 sites. Particles indicated by wavefunctions (blue online) are initialized in a deep optical lattice, where the local environment can be shaped via harmonic confinement and sharp features projected with a spatial light modulator. As the lattice depth is reduced, the particles delocalize but are confined by repulsive walls. [214]

natively, techniques based on optical superlattices may be able to prepare lattice ground states at half-filling [211].

After preparing twin tubes with half-filling in their ground state and applying the beamsplitter operation, one can measure the number of particles modulo 2 at each site x of a given copy (n_x^{copy}) [106], and use the result [57]:

$$\exp(-S_2) = \mathrm{Tr}\left(\rho_{\mathcal{A}}^2\right) = \langle (-1)^{\sum_{x\in\mathcal{A}} n_x^{copy}} \rangle \ , \tag{4.4}$$

to calculate S_2.

The probability for parity $(-1)^{n_x} = \pm 1$ is $(1 \pm \exp(-S_2))/2$. As S_2 increases, more cancellations occur and one needs on the order of $\exp(2S_2)$ measurements to overcome the fluctuations. From Fig. 4.4, and assuming N_s to be less than 16 (i. e., less than 8 particles at half-filling with an entropy per particle of order 0.05), the maximal measured S_2 is less than 1.1. For $\mathcal{N}$ independent measurements, we find that the statistical error is

$$\sigma_{S_2} = \sqrt{(e^{2S_2} - 1)/\mathcal{N}} \, . \tag{4.5}$$

For the maximal value $S_2 = 1.1$, it takes about 800 measurements to reach $\sigma_{S_2} \simeq 0.1$. Due to the logarithmic growth of S_2, the number of measurements only needs to increase like $N_s^{1/4}$ to maintain a desired accuracy, which is not a prohibitive growth.

In addition to the statistical errors, one needs to take into account that finite temperature as well as preparation and manipulation errors contribute a classical entropy $S^{class.}$. Assuming that this classical entropy is linear in the number of particles in the system, it can be estimated by making use of an approximate particle-hole symmetry: near half-filling, $S_2(N_s)$ of the ground state is in good approximation symmetric in the particle number about $N_p = N_s/2$. By measuring $S_2^{exp.}(N_s)$ for a range of particle numbers in the vicinity of $N_s/2$, the excess classical entropy per particle in the experiment can be determined. Subtracting this estimate of the classical entropy from the experimentally measured $S_2^{exp.}$ gives a corrected estimate of the ground state entanglement entropy $S_2^{corr.}$, which we compare to CFT via Eq. (4.3). For the system sizes considered here, deviations from an exact particle-hole symmetry are small and exhibit a regular behavior at zero and finite temperature [40]. Understanding and fitting these effects is important to get estimates of $S_2^{corr.}$ with errors less than 0.02.

In order to give an idea of possible experimental outcomes, we have numerically studied the sensitivity of the fit results of Eq. (4.3) to statistical errors in the measured values of S_2. By repeatedly fitting synthetically generated data (SGD) with Gaussian noise on S_2 of magnitude σ_{S_2} as illustrated in Fig. 4.6 (left), we find that it translates into errors of the fit approximately as $\sigma_A = 3.1\sigma_{S_2}$ (see supplemental materials in [214] for details) for a global fit of the central charge involving data up to $N_s = 16$. To reach a statistical uncertainty in A comparable to systematic errors of the order 0.02, the statistical error on σ_{S_2} has to be on the order of 0.005.

Alternatively, we can try to fit $S^{class.}$. For this purpose, we have considered the finite temperature (T) effects for $T = 0.2J$ and $0.4J$ in Fig. 4.6 (left). Remarkably, these effects can be fitted by adding only one term linear in N_s. If $S^{class.}$ generated during the experiment follows this linear behavior, it may be used to determine some effective temperature. Note that the finite temperature effects become more important as we decrease J.

So far we have only used the values of S_2 corresponding to a subsystem of size $N_s/2$. CFT also provides prediction for arbitrary subsystem sizes ℓ with $1 \leq \ell \leq N_s - 1$. The large oscillations when ℓ is changed for $N_s = 8$ are shown in Fig. 4.6 (right). Finite-T effects can be fitted with a single additional term linear in ℓ. Importantly, the experimental measurements of the parities at each site shown in Eq. (4.4) allow us to calculate S_2 for *all* possible subsystems without extra measurements. Estimates of c from numerical calculations at fixed N_s fits in other models have up to 20 percent errors [151,

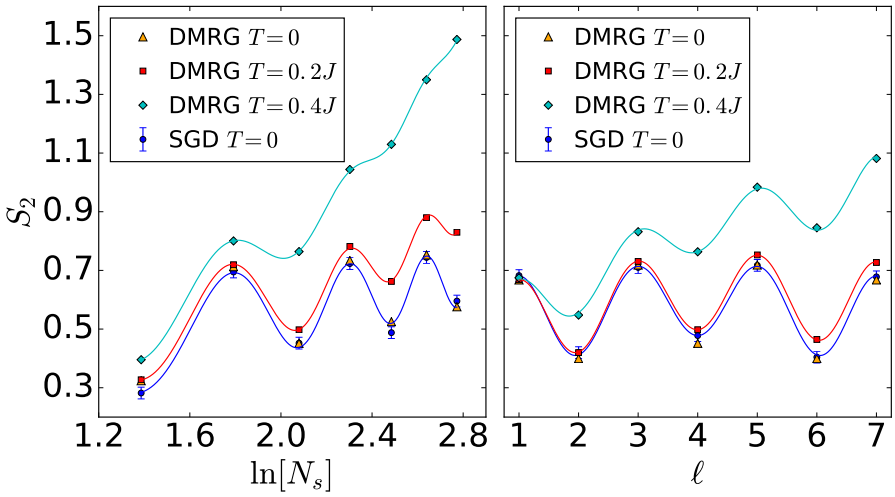

Figure 4.6: S_2 at half-filling for BH with $J/U = 0.1$ (triangles, orange online) and SGD with random Gaussian fluctuations with $\sigma_{S_2} = 0.02$ (circles, blue online). (left): vs. $\ln(N_s)$ for a subsystem of size $N_s/2$ with the solid line corresponding to a fit of the SGD from Eq. (4.3). (right): vs. the subsystem size ℓ for $N_s = 8$; the solid line corresponds to a fit of the SGD using the formulas of Ref. [232]. Same quantities for $T = 0.2J$ (squares, red online) and $T = 0.4J$ (diamonds, cyan online). [214]

11]. Knowing S_2 for all the subsystems also allows us to calculate the mutual information [172, 106], where the $S^{class.}$ contributions cancel.

4.5 Conclusion

In conclusion, we have shown that the simple BH model which is implemented in current experimental measurements of S_2 can be used as a quantum simulator for the classical $O(2)$ model with a chemical potential. We showed that the region of the phase diagram near half-filling and small J/U offers rich possibilities that complement the existing experiments at unity-filling and larger J/U [106, 118]. The changes in S_2 due to the size of the system or the subsystem show strong periodic oscillations which are of the same order of magnitude as the average S_2 for $N_s \leq 16$. We provided complementary methods to

estimate and subtract $S^{class.}$ from $S_2^{exp.}$. Existing experiments could immediately confirm the periodic patterns found in the numerical calculations and fits. Accurate determination of c would require larger statistics or a suitable use of the complete information about the subsystems. Conformal symmetry connects disparate physical systems from condensed matter and LGT. While this equivalence is usually apparent in theory in the thermodynamic limit, we have shown that the basic equivalence between the BH model and the classical $O(2)$ model can already be identified in present cold-atom experiments. Our proposed method could enable the first direct verification of conformal scaling in an experimentally accessible system.

New directions should be pursued. Half-filling initial states can also be obtained by a sudden expansion. The presence of additional approximate conserved charges makes the thermalization non-trivial and interesting [173, 56, 195, 219]. The possibility of revivals in the time-dependent $S_2(t)$ for time scales of the order of 200 ms for $J/U = 0.1$, a duration about 10 times longer than current experiments [118], is under study. The techniques discussed here for the bosonic case can also be applied to Fermi-Hubbard systems [172], for which optical lattice experiments with single-site resolution are rapidly becoming available [95, 168, 47, 170]. It would be desirable to develop specific procedures to study models with other values of c (Ising, Z_N clock, Potts) or with $O(3)$ symmetry with a chemical potential, which have a similar phase diagram [27], and could be quantum simulated [137]. More insight on conformal symmetry could be gained by studying particle number fluctuations [104, 177, 77]. The entanglement entropy can also be calculated in pure gauge theories using standard Monte Carlo methods [28]. Methods for calculating the entanglement entropy in

the presence of fermion determinants have been designed on the lattice [64] and in the continuum [124].

Chapter 5

Quantum Joule Expansion of One-dimensional Systems

5.1 Introduction

A celebrated experiment in the context of classical statistical mechanics is the Joule expansion. The free expansion of an ideal gas from an initial volume V to a final volume $2V$ does not change the temperature of the gas and the increase in entropy is $nR\ln 2$. For interacting gases, the temperature decreases for attractive interactions, such as for the van der Waals gas, and increases for repulsive interactions. But what happens for quantum systems? The Joule expansion of an isolated perfect quantum gas is discussed in [36], where the time evolution of the particle number density displays periodicity with period proportional to the square of the size of the system, consistent with the recurrence time for free bosons and free fermions obtained in [114], and much smaller than the classical Poincaré

recurrence time, which scales exponentially with the size of the system. For generic quantum systems, the recurrence time [23] is much longer, typically scaling as a double exponential of the system size [114, 163].

Sudden expansion of an initially confined thermal state for hard-core bosons was studied in Ref. [235], where the dynamical fermionization and the quasi-condensation during the expansion are observed. These studies focus on integrable systems where analytic tools can be used. But discussions of the question of thermalization at long times are still missing, which is a prerequisite to answer the Joule question in the quantum regime. In this article, we discuss the sudden expansion of bosons and spinless fermions in one-dimensional lattice system, from initially confined thermal states. As integrable quantum systems do not thermalize, we focus on nonintegrable quantum systems and discuss their time evolution and thermalization.

The paper is arranged as follows. In Section 5.2 we introduce the boson and spinless fermion models that we study and discuss the time evolution following the removal of the barrier (expansion from size $L/2$ to size L), the diagonal and the canonical ensemble descriptions for observables in the equilibrated regime, and the Rényi entropy. In Section 5.3, the weights of the eigenstates for the diagonal ensemble (DE) and the canonical ensemble (CE) descriptions are calculated and compared. We find that, above a certain initial temperature, the final effective temperature obtained from the canonical ensemble description is negative. Results for the von Neumann entropy and the second order Rényi entropy are presented in Section 5.4. In Section 5.5 we investigate the full long-time evolved solution, the diagonal ensemble description and the canonical ensemble with an effective final tem-

perature at the level of the reduced density matrices and their eigenvalues and eigenstates in these three cases. In Section 5.6, we calculate the momentum distribution function, which at long times shows the expected population inversion for the negative effective temperature cases. In Section 5.7 we present the answer to the Joule question, that is, the final effective temperature after expansion from $L/2$ to L as function of the temperature of the thermal state at $t = 0$. Finite-size analysis shows that effective negative temperatures survive in the thermodynamic limit for the case of spinless fermions, suggesting that Joule expansion can be used as a way to dynamically create negative temperature fermionic states. Finally, Section 2.6 contains a summary and conclusions.

5.2 The Models

We consider two models: the one-dimensional Bose-Hubbard model and one-dimensional spinless fermions with nearest-neighbor (NN) and next-nearest-neighbor (NNN) hopping and interaction. Open boundary conditions are used for both models. The Hamiltonian for the Bose Hubbard model is:

$$\hat{H}^b = -J \sum_{l=1}^{L-1} (a_l^\dagger a_{l+1} + H.c.) + \frac{U}{2} \sum_{l=1}^{L} n_l^b (n_l^b - 1) \ , \tag{5.1}$$

and the Hamiltonian for spinless fermions is:

$$\begin{aligned} \hat{H}^f \ = \ & -J_1 \sum_{l=1}^{L-1} (c_l^\dagger c_{l+1} + H.c.) + V_1 \sum_{l=1}^{L-1} n_l^f n_{l+1}^f \\ & -J_2 \sum_{l=1}^{L-2} (c_l^\dagger c_{l+2} + H.c.) + V_2 \sum_{l=1}^{L-2} n_l^f n_{l+2}^f \ , \end{aligned} \tag{5.2}$$

where L is the total number of sites, $a_l^\dagger$ (a_l) is the creation (annihilation) operator of bosons at site l, satisfying the commutation relations $[a_l, a_{l'}^\dagger] = \delta_{ll'}$, and $c_l^\dagger$ (c_l) is the

creation (annihilation) operator of spinless fermions at site l, satisfying the anitcommutation relations $\{c_l, c_{l'}^\dagger\} = \delta_{ll'}$. $n_l^b = a_l^\dagger a_l$ ($n_l^f = c_l^\dagger c_l$) is the particle number operators for bosons (fermions) at site l. Repulsive interactions $U, V_1, V_2 > 0$ are considered for both systems. For nonintegrable systems, the energy levels are repulsive and the level spacing distribution is given by the Wigner-Dyson distribution, which has been found for both $\hat{H}^b$ [128] and $\hat{H}^f$ [191]. The fermionic model $\hat{H}^f$ contains next-nearest-neighbor terms J_2 and V_2 that may seem prohibitively difficult to achieve experimentally. We note, however, that this model can also be realized with a zigzag ladder, with one leg containing the odd sites of Eq. (5.2) and the other leg containing the even sites. The J_1 and V_1 in Eq. (5.2) are terms connecting odd and even sites, and therefore are the inter-leg zig-zag terms in the ladder system. In the ladder system, the J_2 and V_2 terms then become the intra-leg nearest-neighbor terms. We set $\hbar = k_B = 1$ in the following and fix the hopping energy $J_1 = V_1 = J = 1$ in our calculations. The results we present are for spinless fermions with $J_2 = V_2 = 1$ and bosons with $U = 3$, unless otherwise specified.

In the Joule expansion, a volume of gas is initially prepared with a thermal state inside one half of a container via a partition, with the other half of the container empty. The partition is then suddenly removed and the gas is let to expand freely to occupy the whole volume. For particles on a lattice, a similar initial setup can be achieved by adding a high potential throughout the right half of the lattice, $\hat{H}_W = W \sum_{l=L/2+1}^{L} n_l$, where $W \gg J, U, J_1, J_2, V_1, V_2$. In the numerical calculations presented here, we set $W = 10^6$ to make sure that $\beta W \gg 1$ in all calculations, so particles won't hop to the right half due to high temperatures. At time $t = 0$, the high potential is suddenly removed (W is quenched

to zero) and particles can then move on a twice bigger lattice. For fermions (bosons), we consider the initial state to be a $N_p = L/4$-particle ($L = 20$ unless otherwise specified) thermal state $\hat{\rho}_0^f$ ($\hat{\rho}_0^b$) at a finite temperature $T_0^f = 1/\beta_0^f$ ($T_0^b = 1/\beta_0^b$) in the left half of the lattice. Using the method described in section 1.6, we can find the time-evolved state $\hat{\rho}^t$, the DE density matrix $\hat{\rho}^d$ and the corresponding CE density matrix $\hat{\rho}^c$ with an effective inverse temperature β_{eff}, and discuss their properties.

Like in a classical gas, the average energy of the initial Hamiltonian H_0 (particles confined to $L/2$) with *repulsive* interactions at a certain temperature is higher than that of the final Hamiltonian H_F (system size L) with the same temperature. So a higher effective temperature is needed for Eq. (1.30) to be satisfied. Conversely, for attractive interactions (such as in the classical van der Waals gas), the system is expected to cool down upon expansion. For repulsive interactions, such as the systems studied here, an interesting possibility can occur. If the initial average energy is higher than the infinite-temperature energy for the final Hamiltonian, a negative temperature is needed to compensate for the difference. It is convenient to describe this in terms of inverse temperature: the system is prepared in some positive inverse temperature that decreases upon expansion for repulsive interactions. There will be some initial positive inverse temperature for which it decreases to zero (infinite temperature) after expansion. Any positive initial inverse temperature that is smaller than that will then lead to even smaller final inverse temperatures, leading to negative values.

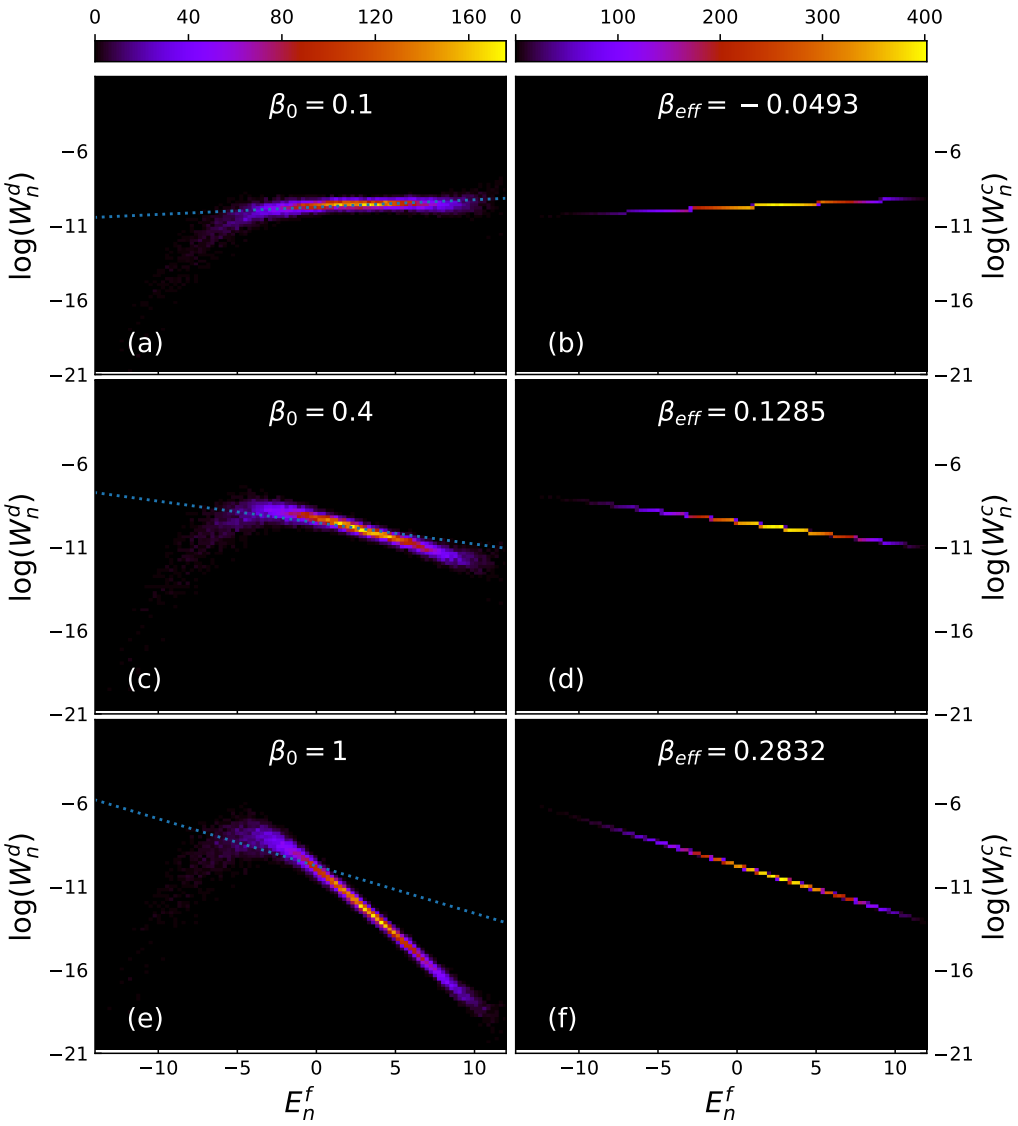

Figure 5.1: (Color online) Two-dimensional histograms for the weights of eigenstates in the DE, W_n^d (a,c,e) and those in the corresponding CE, W_n^c (b,d,f). Results are for spinless fermions with initial inverse temperatures $\beta_0 = 0.1$ (a), $\beta_0 = 0.4$ (c) and $\beta_0 = 1$ (e). The corresponding CE with effective inverse temperatures are shown in (b,d,f). The color scale represents the number of states per unit area. The dashed lines in the left column are translations of the lines from the right column, indicating the slopes in the right column.

5.3 Weights in Ensembles

In global quench protocols, the energy uncertainty $\Delta E/\bar{E}$, which only depends on the DE, is algebraically small with the system size $(1/\sqrt{L})$ for pure initial states [179],

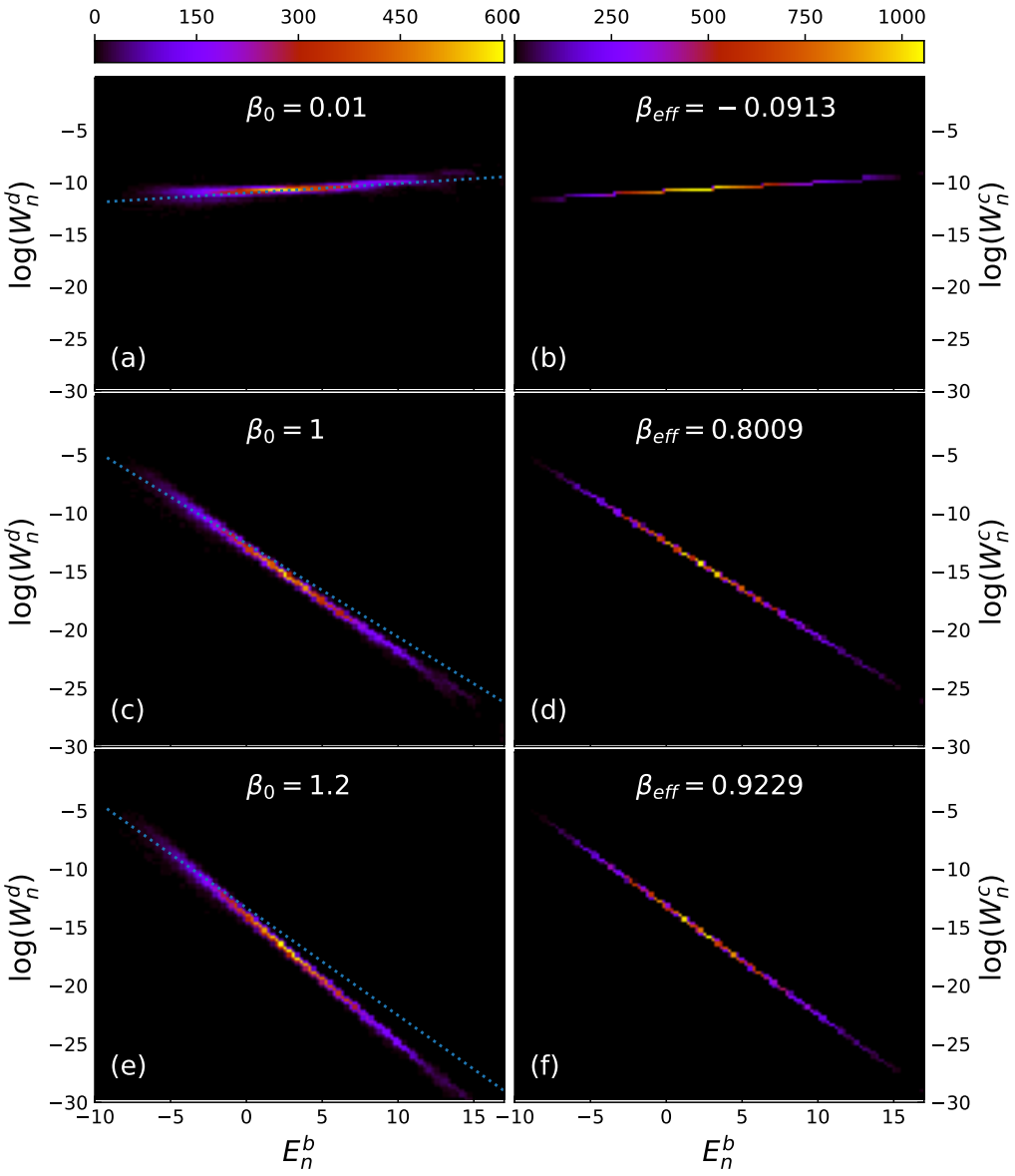

Figure 5.2: (Color online) Same as Fig. 5.1, but for bosons with 20 sites, 5 particles and $U = 3$.

which is also numerically verified for our case. The small energy window $[\bar{E} - \Delta E, \bar{E} + \Delta E]$ defines a microcanonical ensemble which is equivalent to the CE in the thermodynamic limit. As our initial states already have the Boltzmann weights, it is interesting to explore and compare the weights in the whole spectrum in the DE, W_n^d, and those in the corresponding

CE, W_n^c. Similar comparisons have been conducted in studies of global quantum quenches from pure states [203] and thermal states [240, 96].

In Fig. 5.1, we show the 2-d histograms for logarithms of these weights in the DE [Figs. 5.1(a), 5.1(c) and 5.1(e)] and the CE [Figs. 5.1(b), 5.1(d) and 5.1(f)]. We choose 100×100 bins, and the color scale on each bin represents the number of states inside it. The results are for spinless fermions expanding from thermal states with three different initial temperatures. We see that in the DE, the weights lie in a narrow band for all temperatures. There is a tail bending down for the spectrum at low energies, but with a much smaller density of states. The weights in the CE are all straight lines as should be the case by definition. We have included these as dashed lines in the left column of Fig. 5.1 to compare the slopes. At low initial temperature, e.g. $\beta_0 = 1$, the slopes of the narrow straight band in the DE and the line for the CE are very different. As we increase the initial temperature, they match better and better. It can be understood in the following way. Note that the summation in Eq. (1.30), $\sum_m E_m W_m^d$, can be divided into two parts: one is the summation in the bending tail of the weights in the DE which is close to the bottom of the energy spectrum, the other one is the summation in the remaining narrow straight band. Although the tail has small density of states, it can still dominate the summation at very low initial temperatures, because the weight in the DE, $W_m^d = \sum_i \rho_i^0 \langle m|i\rangle \langle i|m\rangle$, contains the Boltzmann weight $\rho_i^0 = e^{-\beta_0 e_i}/Z_0(\beta_0)$ given by the initial temperature. As the tail is bending down, the line of the CE must rotate anticlockwise from the straight narrow band of the DE to fit the data in it at low initial temperatures [see Fig. 5.1(e)]. For higher initial temperatures, the narrow straight band dominates the summation, and Eq. (1.30) is

effectively a linear fit for this band. Note that for the highest initial temperature $\beta_0 = 0.1$, the effective temperature is negative, and the weights in the DE and the CE match perfectly in the densest part of the spectrum [see Fig. 5.1(a)]. This match between the DE and the CE weights results in agreements for expectations of almost all equithermal operators [81] in the two ensembles and the model has strong thermalization [7] in the negative temperature regime.

The results for bosons are depicted in Fig. 5.2. The weights in the DE also lie in a straight narrow band. The tail in the low energy spectrum only bends down slightly. So the difference in slopes for the DE and the CE is much smaller than in the case of fermions. We still see that the higher the temperature, the better is the match between the DE and the CE. The slopes also agree accurately at very high initial temperature $\beta_0 = 0.01$. Note that a much higher initial temperature is needed for the effective temperature to be negative. We will see that the negative effective temperature actually does not exist in the thermodynamic limit for bosons, but it does for fermions. This is discussed in Section 5.7.

5.4 Entropy For Ensembles

In this section we investigate the entropy profiles for the initial state, the state after long-time expansion, the DE density matrix and the CE density matrix. We calculate the quantity in Eq. (1.34) for $n = 1$ (the von Neumann entropy) and $n = 2$ (the second order Rényi entropy), and subsystems containing left $l_A = 1, 2, ..., 20$ sites. We choose the time evolved density matrix to be at a long time after expansion, $tJ = 6000$, where thermalization

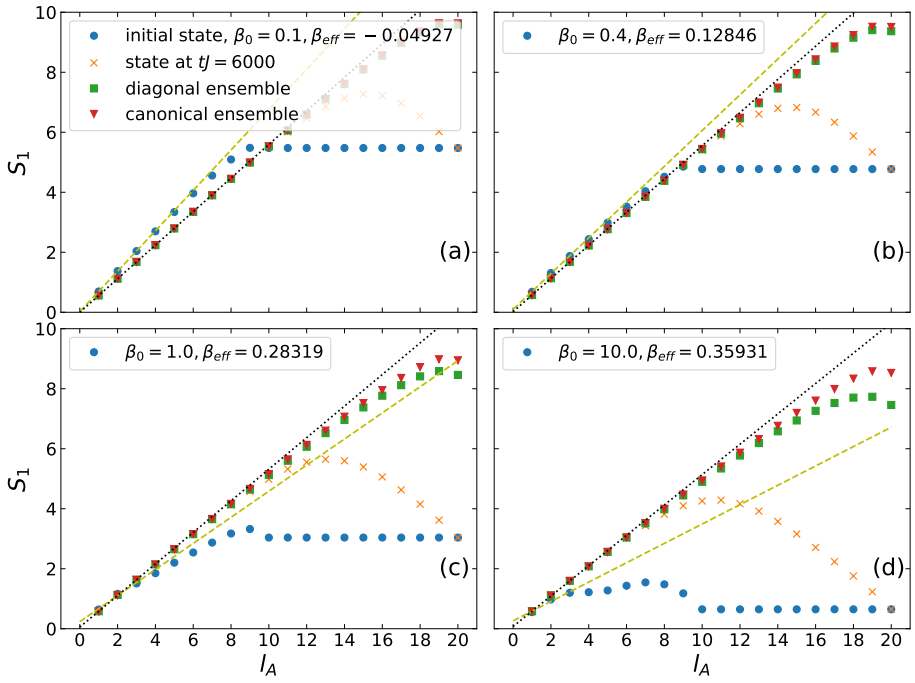

Figure 5.3: (Color online) The von Neumann entropy of the reduced density matrix containing left l_A sites for the initial thermal state (blue circle), the state at long time $tJ = 6000$ (orange cross), the diagonal ensemble (green square) and the canonical ensemble (red inverted triangle). Results are for spinless fermions with initial inverse temperatures $\beta_0 = 0.1$ (a), $\beta_0 = 0.4$ (b), $\beta_0 = 1$ (c) and $\beta_0 = 10$ (d). The green dashed lines are linear fits of the first 3 subsystems for the initial states. The black dotted lines are linear fits of the first 3 subsystems for the canonical ensemble density matrices.

has occured for a long time. Numeric results show the equilibration of entropy after $tJ = 50$ for all cases considered here. We compare the results for different temperatures for both spinless fermions and bosons.

5.4.1 Von Neumann Entropy

Fig. 5.3 shows the von Neumann entropy of the reduced density matrix for the subsystem containing left l_A sites. The results are for spinless fermions expanding from thermal states with four different initial temperatures. For initial thermal states, the par-

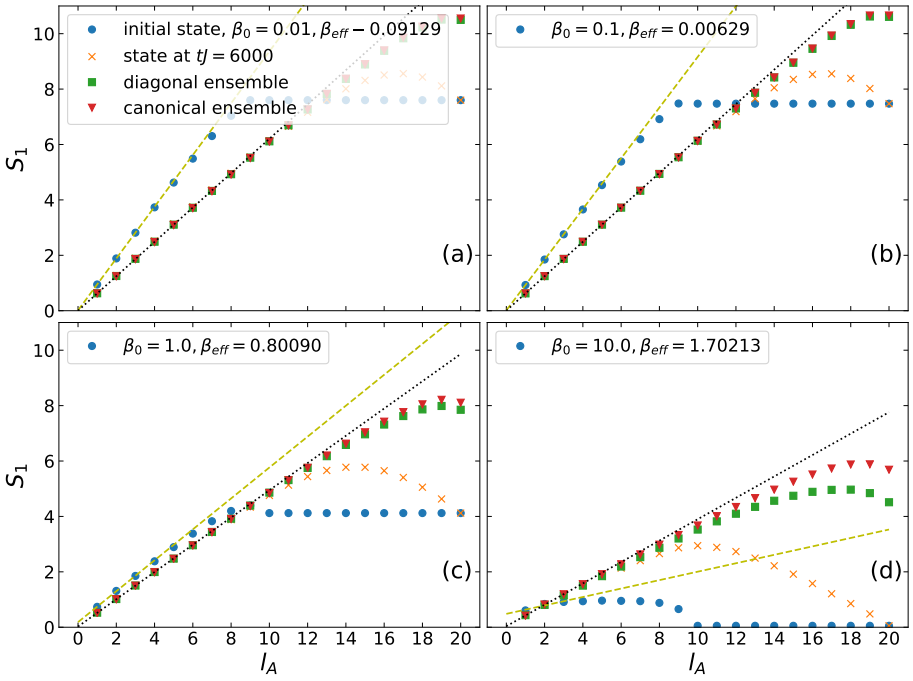

Figure 5.4: (Color online) Same as Fig. 5.3 but for bosons with initial inverse temperatures $\beta_0 = 0.01$ (a), $\beta_0 = 0.1$ (b), $\beta_0 = 1$ (c) and $\beta_0 = 10$ (d).

ticles are initially confined in the left half part, so the Rényi entropy is identical for all subsystems bigger than half. We can clearly see from Fig. 5.3(a) the volume law in S_1 for up to six subsystems at high temperature $\beta_0 = 0.1$, which is consistent with Eq. (1.36). In Fig. 5.3(b) a lower temperature $\beta_0 = 0.4$ results in five subsystems satisfying the volume law. As we decrease the initial temperature further, there are only three subsystems satisfying volume law in Fig. 5.3(c) for $\beta_0 = 1$ and no sign of volume law in Fig. 5.3(d) for $\beta_0 = 10$. These results show the crossover from the volume law for subsystems at high temperatures to the logarithmic scaling in the ground state. The CE density matrices all show volume law for many subsystems. Because the effective temperature is always high even for very low initial temperature (see Fig. 5.3(d)). Still, the higher the effective temperature is, the more subsystems satisfying the volume law. The von Neumann entropy increases

linearly up to 11 sites in Fig. 5.3(a) where the negative effective temperature should be considered to be "larger" than the infinite temperature. And it increases linearly up to 6 sites in Fig. 5.3(d). Note that the deviation from the volume law for larger subsystems at high temperatures does not contradict Eq. (1.36) because Eq. (1.36) is derived under the condition that the system is infinitely long. Intuitively, as the Rényi entropy has contributions from both entanglement and thermal mixture, the former increases at first with increasing subsystem size, but decreases for subsystem sizes bigger than half of the whole system. So it is reasonable that the entropy bends down from the linearly increasing line. For a detailed study of properties of thermal Rényi entropy, see [25].

In Fig. 5.1 we have shown that the weights in the DE are very similar to the weights in the CE for high initial temperatures. So the diagonal entropy and thermal entropy should be very close. This is confirmed in Fig. 5.3(a), (b) and Fig. 5.5(a), (b), where the Rényi entropy of reduced density matrices for $\hat{\rho}_d$ and $\hat{\rho}_c$ agrees for almost all subsystems. In Fig. 5.3(c) $\beta_0 = 1$, S_{1A} in the DE deviates from that for the CE for subsystems bigger than 15. On one hand, the deviation for the full systems is consistent with the results in Fig. 5.1(e)(f) where it shows that the distribution of weights is very different for the DE and the CE. On the other hand, S_{1A} still agrees for most subsystems even if the distribution of weights is very different for the whole system. In Fig. 5.3(d) $\beta_0 = 10$, the deviation between the S_{1A} in the DE and that in the CE is much bigger, but there are still 12 subsystems that have the same von Neumann entropy. Note that it can be proved that S_1 of the DE for the whole system only has non-extensive difference from that of the microcanonical ensemble,

no matter whether the initial state is pure or mixed [55]. And this non-extensive difference can be decreased by increasing the initial temperature in our case.

Finally, we check the reduced von Neumann entropy for the time-evolved density matrix in Fig. 5.3. We see that at the high temperature $\beta_0 = 0.1$, the time-evolved density matrix has the same S_1 as the CE and the DE density matrices for subsystems up to eleven sites. And ten-, eight- and six-site subsystems have the same von Neumann entropy for temperatures $\beta_0 = 0.4$, $\beta_0 = 1$ and $\beta_0 = 10$, respectively. So it is concluded that when the temperature is higher, the maximum subsystem size that has the same von Neumann entropy in $\hat{\rho}_t$, $\hat{\rho}_d$ and $\hat{\rho}_c$ is bigger. Note that the reduced S_1 increases first to the highest point and then bends down until the full von Neumann entropy goes back to the initial full von Neumann entropy. This is because the full von Neumann entropy is invariant under the unitary change of basis, which is the unitary time evolution here.

The results for bosons depicted in Fig. 5.4 are similar to those for spinless fermions. They are summarized as follows. For initial thermal state, there are six, six, five and three sites having volume law von Neumann entropy at initial inverse temperature $\beta_0 = 0.01$ [Fig. 5.4(a)], $\beta_0 = 0.1$ [Fig. 5.4(b)], $\beta_0 = 1$ [Fig. 5.4(c)] and $\beta_0 = 10$ [Fig. 5.4(d)] respectively. And for the canonical ensemble density matrix, the von Neumann entropy in the left eleven, eleven, ten and seven sites show volume law at these four initial temperatures. The DE von Neumann entropy is identical to the CE von Neumann entropy for all subsystems at initial inverse temperatures $\beta_0 = 0.01, 0.1$. They are equal in the left fifteen sites and left eight sites at initial inverse temperatures $\beta_0 = 1$ and $\beta_0 = 10$, respectively. These results are also consistent with those in Fig. 5.2. The time-evolved density matrix at $tJ = 6000$

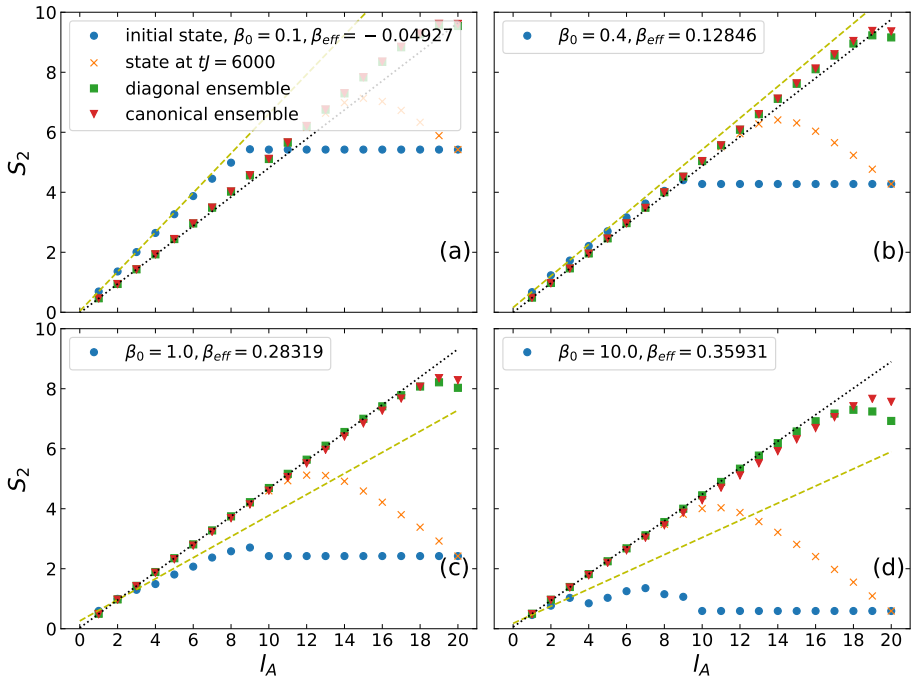

Figure 5.5: (Color online) Same as Fig. 5.3, but for the second order Rényi entropy.

has the same von Neumann entropy with both $\hat{\rho}^d$ and $\hat{\rho}^c$ in the left eleven, eleven, nine and six sites in the four graphs respectively.

5.4.2 The second order Rényi entropy

Since the results for the two models are very similar, we only consider spinless fermions in this section. As shown in Fig. 5.5, the second order Rényi entropy also has high agreement for the CE and the DE, that is, nineteen, eighteen, eleven and eight sites have the same value for $\beta_0 = 0.1, 0.4, 1, 10$, respectively. And the time-evolved state has twelve, eleven, ten and eight sites with S^t_{2A} equal to them. The main difference from Fig. 5.3 and Fig. 5.4 is that, unlike the von Neumann entropy where the higher the initial temperature

is, the bigger the subsystems having linearly increasing entropy are, there are five, six, twelve (sixteen for the DE) and six sites having linearly increasing $S_{2A}^{d(c)}$, respectively. We find that the entropy bends up for high initial temperatures [the data of the DE and the CE lie on or above the black dotted linear fit in Fig. 5.5(a)]. This convexity is weakened by decreasing the initial temperature and finally the entropy becomes concave again [the data of the DE and the CE lie on or below the black dotted linear fit in Fig. 5.5(d)]. In Ref. [146], it is argued that S_{pA} ($p > 1$) are convex functions of the subsystem size for finite-energy density eigenstates of chaotic many-body Hamiltonians, linear at $\beta = 0$ and more convex at bigger $|\beta|$. For our models with twenty sites and quarter filling, we verify the above argument but just in a small energy window around the infinite temperature eigenstate. Moreover, more obvious convexity is observed in high energy levels near the top of the spectrum while the levels near the bottom of the spectrum are all concave, which explains why $S_{2A}^{c(d)}$ with negative effective temperature is more convex in Fig. 5.5 even if $|\beta_{eff}|$ is smaller. Note that at low temperatures, the second order Rényi entropy of the DE can be bigger than that of the CE for big subsystems, while the von Neumann entropy of the DE is always no greater than that of the CE.

As the second order Rényi entropy can be measured experimentally by a beam-splitter operation implemented via a controlled tunneling operation between the two copies of a many-body state [57, 106], we investigate the details of time evolution of S_{2A}^{t} in this section. Note that for twenty sites and quarter filling, the numerical results show small time fluctuations in Rényi entropy for all subsystems at long times, even for the lowest temperature considered here $\beta_0 = 10$, which indicates that the time-dependent terms are

cancelled out due to dephasing. In Eq. (1.37), the only time-independent terms are those with $m = n, m' = n'$ or $m = n', m' = n$. So for long times,

$$\begin{aligned} S_{2A}^t &\approx -\ln\Bigg(\sum_{m,m'} \rho^0_{mm}\rho^0_{m'm'} \langle m|i_B\rangle \langle i'_B|m'\rangle \langle m'|i'_B\rangle \langle i_B|m\rangle \\ &\quad + \sum_{m\neq m'} \rho^0_{mm'}\rho^0_{m'm} \langle m'|i_B\rangle \langle i'_B|m'\rangle \langle m|i'_B\rangle \langle i_B|m\rangle \Bigg) \\ &= -\ln\Bigg(\sum_{m,m'} \rho^0_{mm}\rho^0_{m'm'} T_{AB}^{mm'} + \sum_{m\neq m'} \rho^0_{mm'}\rho^0_{m'm} T_{BA}^{m'm} \Bigg) \end{aligned} \tag{5.3}$$

where $T_{AB}^{mm'} = \mathrm{Tr}_A\left[(\mathrm{Tr}_B |m\rangle \langle m|)(\mathrm{Tr}_B |m'\rangle \langle m'|)\right]$ and $T_{BA}^{m'm} = \mathrm{Tr}_B\left[(\mathrm{Tr}_A |m'\rangle \langle m'|)(\mathrm{Tr}_A |m\rangle \langle m|)\right]$. The second summation contributes to the difference between the equilibrated S_{2A} and the S_{2A} for the DE. If it is negligible compared to the first summation, the time-evolved Rényi entropy equilibrates to the value for the DE which agrees with the value for the CE. For small subsystem sizes $l_A \ll l_B$, consider any $m \neq m'$, $T_{AB}^{mm'}$ traces out much more degrees of freedom (exponentially more with the volume difference between A and B) of two orthogonal eigenstates than $T_{BA}^{m'm}$ does, resulting in more reduction of orthogonality. So we expect $T_{AB}^{mm'} \gg T_{BA}^{m'm}$ and $S_{2A}^t \approx S_{2A}^d$ for $l_A/L \ll 1$. Furthermore, as $\sum_{m,m'} \rho^0_{mm}\rho^0_{m'm'} = 1$, the first summation is equal to some typical value of $T_{AB}^{mm'}$, denoted as T_{AB}^0, while the second summation can be written as

$$T_{BA}^o \sum_{m\neq m'} \rho^0_{mm'}\rho^0_{m'm} = T_{BA}^o \left(e^{-S_2^{\beta_0}} - e^{-S_2^d}\right) \tag{5.4}$$

where T_{BA}^o is some typical value of $T_{BA}^{m'm}$, $S_2^{\beta_0}$ is the second order Rényi entropy for the initial state, S_2^d is the second order Rényi entropy for the DE. S_2^d is extensive with L because it is close to S_2^c (see Fig. 5.5), while $S_2^{\beta_0}$ is extensive with $L/2$. Because the average entropy per site for quarter filling is bigger than that for half filling and the effective temperature is higher than the initial temperature after the expansion, the second term in Eq. (5.4)

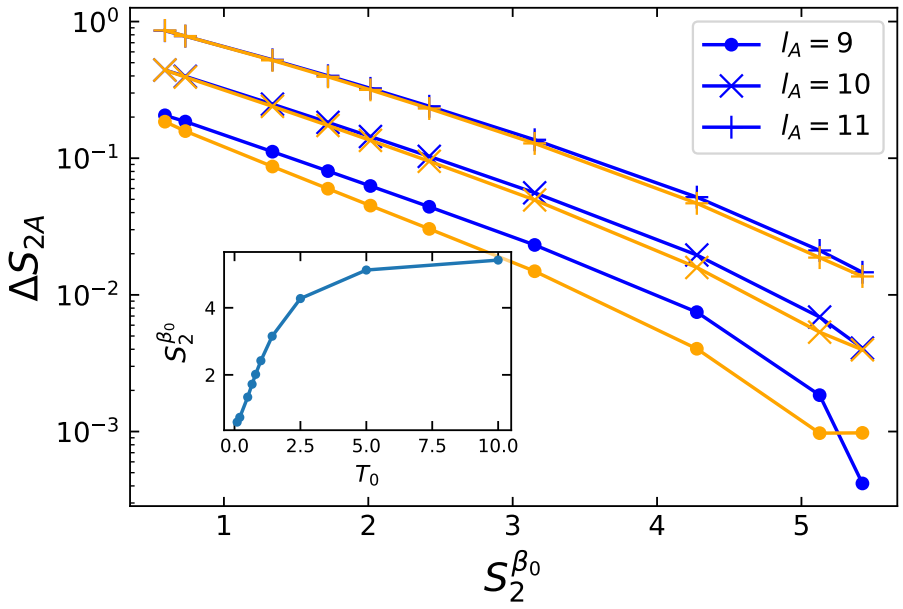

Figure 5.6: (Color online) The difference between time-averaged Rényi entropy $\bar{S}_{2A}$ and the DE Rényi entropy S^d_{2A} as a function of initial second order Rényi entropy. The results are for spinless fermions, three subsystems with $l_A = 9, 10, 11$. The inset shows the initial second order Rényi entropy as a function of initial temperature T_0. The yellow markers depict the results for $tJ = 6000$.

is negligible for large L. So as long as the initial state is thermal, Eq. (5.4) is at least exponentially small with $L/2$.

Note that the dependence of $T^{mm'}_{AB}$ and $T^{m'm}_{BA}$ on the initial temperature and the system size also contributes to the difference between the time-evolved Rényi entropy and the DE Rényi entropy. If Eq. (5.4) is small,

$$S^t_{2A} \approx S^d_{2A} - T^o_{BA}\, e^{S^d_{2A} - S_2^{\beta_0}} \tag{5.5}$$

where $T^o_{BA} < \mathrm{Tr}_B \left[\left(\mathrm{Tr}_A \left| m_o \right\rangle \left\langle m_o \right| \right)^2 \right]$ is also exponentially small with the subsystem size for $|m_o\rangle$ being a finite-energy density eigenstate of a chaotic system [146]. We plot Figs. 5.6 and 5.7 to quantitatively investigate the second term in Eq. (5.5). To plot Fig. 5.6, we calculate

the time evolution of S_{2A}^t for subsystems containing the left $9, 10, 11$ sites respectively to $tJ = 200$, with time step size $\tau J = 1$. To avoid large deviations due to the fluctuations in time and the short-time far-from-equilibrium states, we average S_{2A}^t using only the last 120 steps of the time evolution data. In Fig. 5.6, we plot the difference between S_{2A}^d for the DE and the time-averaged value $\Delta S_{2A} = S_{2A}^d - \bar{S}_{2A}$ as a function of the second order Rényi entropy for the initial thermal state $S_2^{\beta_0}$. Varying the number of long-time data points in the time-average calculation does not change the plot. The exponential decay of ΔS_{2A} with the initial thermal entropy can be clearly seen from these numerical results. The decay rates are almost the same for three subsystems at least for $\beta_0 > 0.2$. The results at $tJ = 6000$ are also plotted, which are very close to the results for time-averaged entropy. The inset of Fig. 5.6 shows $S_2^{\beta_0}$ as a function of initial temperature T_0, where we see $S_2^{\beta_0}$ is firstly linear with T_0 at low initial temperature and saturates at high initial temperature. So ΔS_{2A} also exponentially decays with the initial temperature when $T_0 < 1$. In Fig. 5.7, the same quantity for $l_A/L = 1/2$ is plotted as a function of the system size, where we see that ΔS_{2A} is exponentially small with the system size. The decay rate is higher for higher initial temperatures. The inset (a) confirms that $S_{2A}^{\beta_0}$ is proportional to the size of the system. So ΔS_{2A} also exponentially decays with $S_{2A}^{\beta_0}$ across different system sizes. The inset (b) shows the linearity of S_2^d with the system size, where the weak convexity is due to the increase of effective temperature for larger system sizes. The two insets also confirm that $e^{-S_2^d}$ is negligible in Eq. (5.4), at least for $L \geq 12$ where the data of S_2^d is more linear with L. The results at $tJ = 6000$ are not close to the time-averaged ones due to the large time fluctuations for small systems.

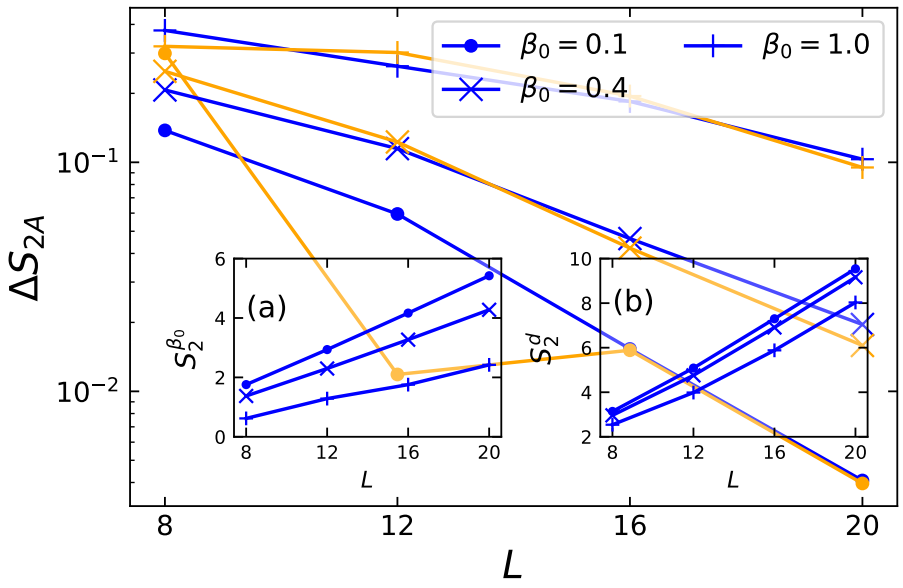

Figure 5.7: (Color online) The difference between time-averaged Rényi entropy $\bar{S}_{2A}$ and the DE Rényi entropy S^d_{2A} for $l_A/L = 1/2$ as a function of the system size. The results are for spinless fermions, three initial inverse temperatures $\beta_0 = 0.1, 0.4, 1.0$. The insets show the initial second order Rényi entropy (a) and the diagonal second order Rényi entropy (b) as a function of the system size. The yellow markers depict the results for $tJ = 6000$.

Finally, we investigate the time fluctuations of the Rényi entropy. We calculate the variance of S^t_{2A} in time,

$$\begin{aligned} Var(S^t_{2A}) &= \lim_{\tau\to\infty} \frac{1}{\tau}\int_0^\tau d\tau \left(S^\tau_{2A} - \bar{S}_{2A}\right)^2 \\ &\approx \frac{1}{N_\tau}\sum_{i=1}^{N_\tau} \left(S^{\tau_i}_{2A} - \bar{S}_{2A}\right)^2, \end{aligned} \tag{5.6}$$

where we take $N_\tau = 120$ and $\{\tau_i\} = \{81, 82, ..., 200\}$. The variance as a function of $S_2^{\beta_0}$ is depicted in Fig. 5.8, where we see that the fluctuations also exponentially decay with $S_2^{\beta_0}$, at least for not very high temperatures ($\beta_0 = 0.1$ for the largest $S_2^{\beta_0}$ in the figure). The inset also shows that the variance is exponentially small with the system size, with a bigger decay rate for higher temperatures.

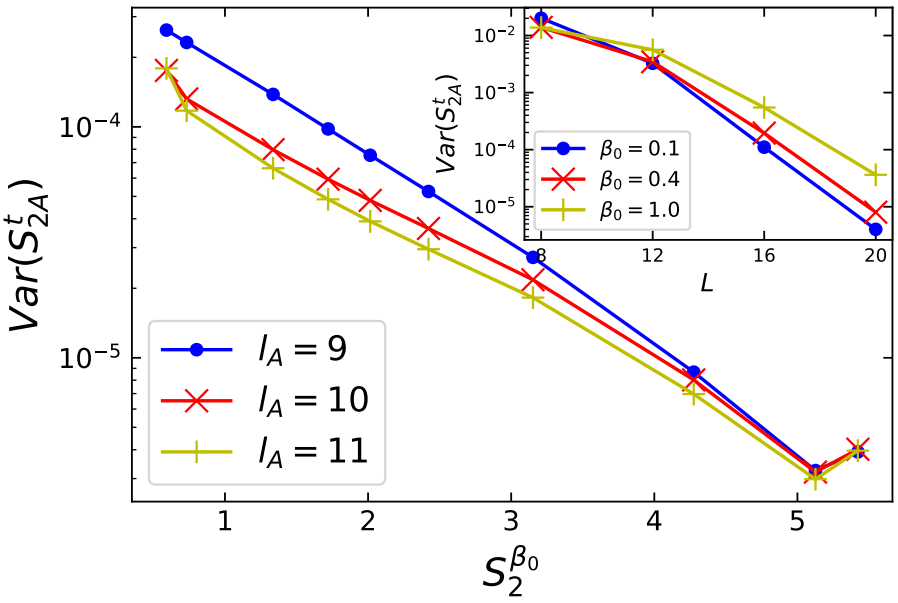

Figure 5.8: (Color online) Variance of S^t_{2A} in time for $tJ = 81, 82, ..., 200$, as a function of $S_2^{\beta_0}$. The results are for spinless fermions, subsystems with $l_A = 9, 10, 11$. The inset shows the same quantity with $l_A = 10$ but as a function of system size at temperatures $\beta_0 = 0.1, 0.4, 1.0$.

5.5 Reduced Density Matrices

The above observations indicate that the reduced density matrices of $\hat{\rho}^t$ at long time, $\hat{\rho}^d$ and $\hat{\rho}^c$ may be very similar, for not too large subsystems. In order to check this, we calculate the eigenvalues of the reduced density matrices λ_A and plot $\log(\lambda_A)$ as a function of the eigenenergy E^m_A of the Hamiltonian associated with the subsystem $\hat{H}_A$. Another important question is to decide if these eigenvalues λ_A are equal to the weights in thermal density matrix of the subsystem $\hat{\rho}^c(A) = e^{-\beta_{eff}\hat{H}_A}/Z_A$. In order to answer this question, we consider subsystems containing more than five sites, for which the reduced density matrix

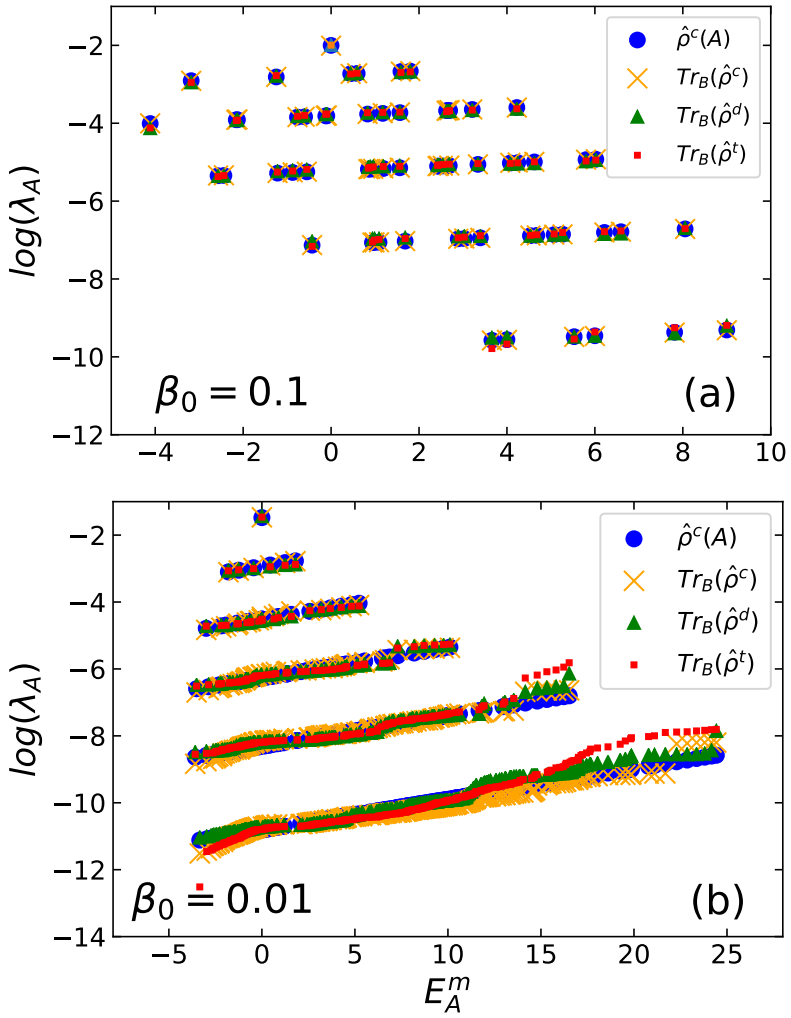

Figure 5.9: (Color online) Logarithm of eigenvalues of reduced density matrices for the canonical ensemble, the diagonal ensemble and the time-evolved state at $tJ = 6000$, compared with the weights in the canonical ensemble constructed by the Hamiltonian for the subsystem $\hat{H}_A$. The subsystem contains the left six sites of the lattice. The results are for spinless fermions with the initial temperature $\beta_0 = 0.1$ (a) and bosons with the initial temperature $\beta_0 = 0.01$ (b). In each subplot, from top to bottom, the linearly arranged points represent zero, one, two, three, four and five particle states respectively.

can be divided into six sub-sectors which have zero, one, two, three, four and five particles respectively. If the sub-sector contains p particles, the bath of the subsystem should have $5 - p$ particles. To compare the weights with correct normalization factor Z_A in each sub-

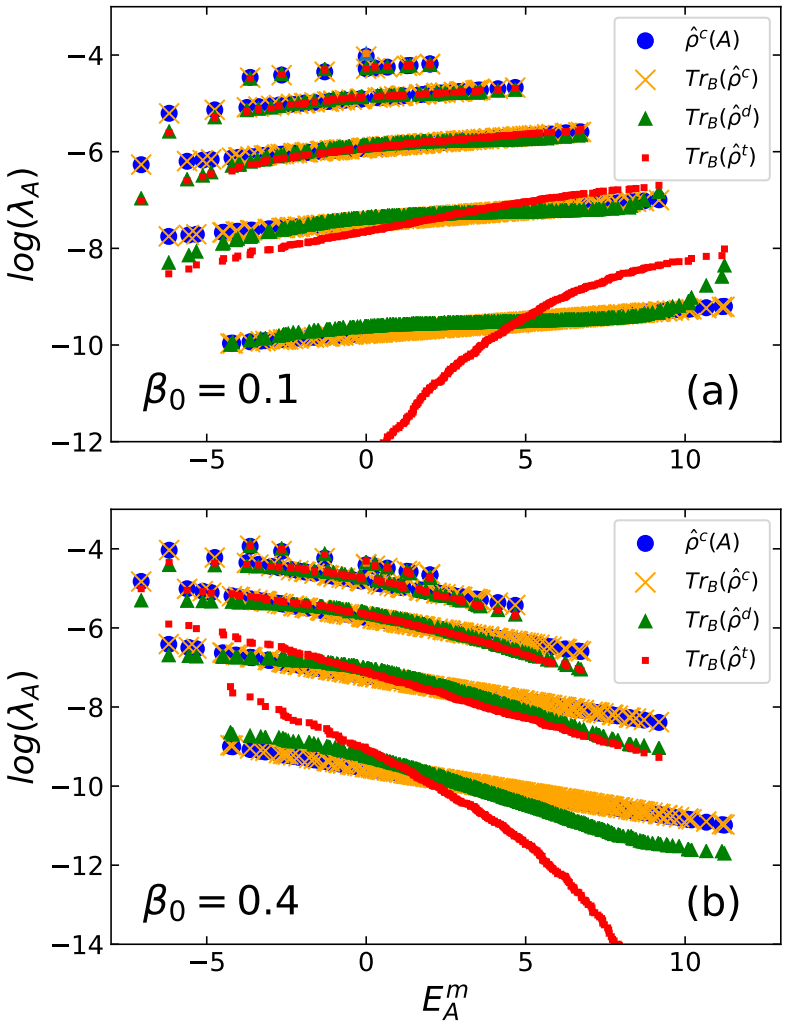

Figure 5.10: (Color online) The same with Fig. 5.9 but only for spinless fermions. The subsystem contains the left ten sites of the lattice. The initial temperatures are $\beta_0 = 0.1$ (a) and $\beta_0 = 0.4$ (b). Note that in (b), the point for the zero-particle state is very close to the one-particle states line.

sector, the correct thermal density matrix of the subsystem A should be chosen as the reduced density matrix of a thermal density matrix that contains two uncorrelated thermal states with total particle number conservation of the whole system. To be specific, let $\{|E_A^{m_p}\rangle\}$ be the eigenstates of H_A^p with p particles, $\{|E_B^{m_{5-p}}\rangle\}$ be the eigenstates of H_B^{5-p}

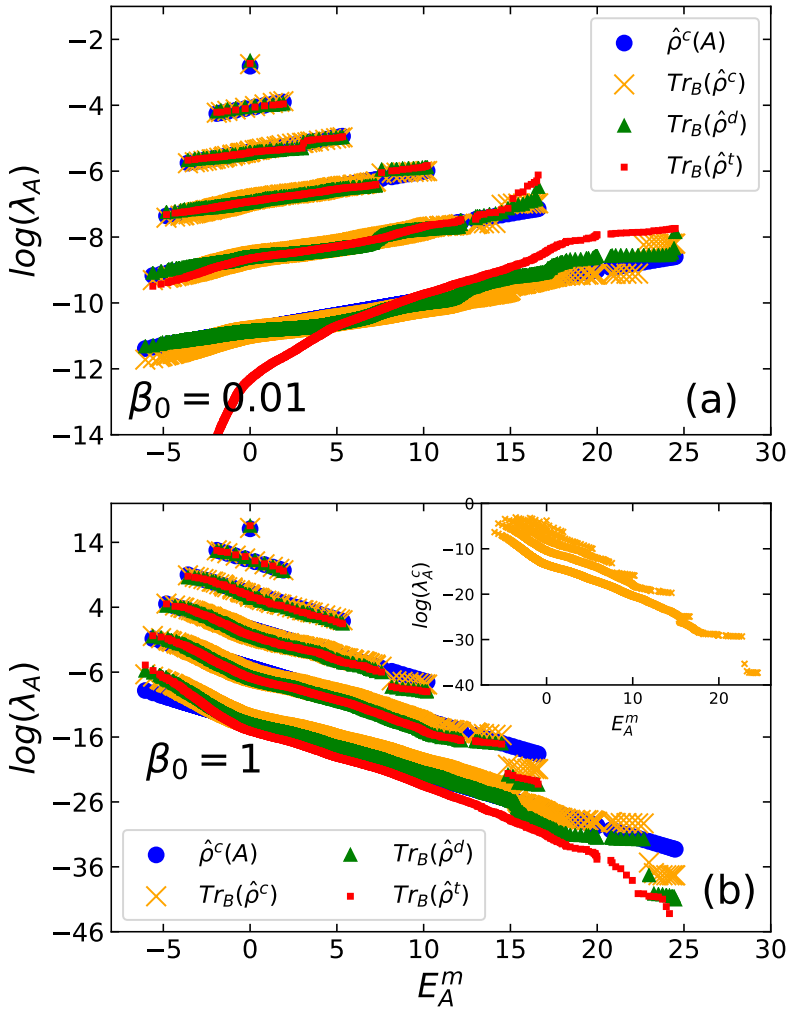

Figure 5.11: (Color online) The same with Fig. 5.10, but for bosons with initial temperatures $\beta_0 = 0.01$ (a), $\beta_0 = 1$ (b). In (b), those points for zero, one, two, three and four particle states are shifted up by constants for better view. The inset shows the actual eigenvalues for the reduced density matrix of canonical ensemble without shift.

with $5-p$ particles, the whole thermal density matrix at temperature β_{eff} is

$$\hat{\rho}^c(AB) = \sum_{p=0}^{5} \frac{e^{-\beta_{eff}(E_A^{m_p}+E_B^{m_{5-p}})}}{Z_{AB}} \left|E_A^{m_p}\right\rangle \otimes \left|E_B^{m_{5-p}}\right\rangle \left\langle E_B^{m_{5-p}}\right| \otimes \left\langle E_A^{m_p}\right|, \qquad (5.7)$$

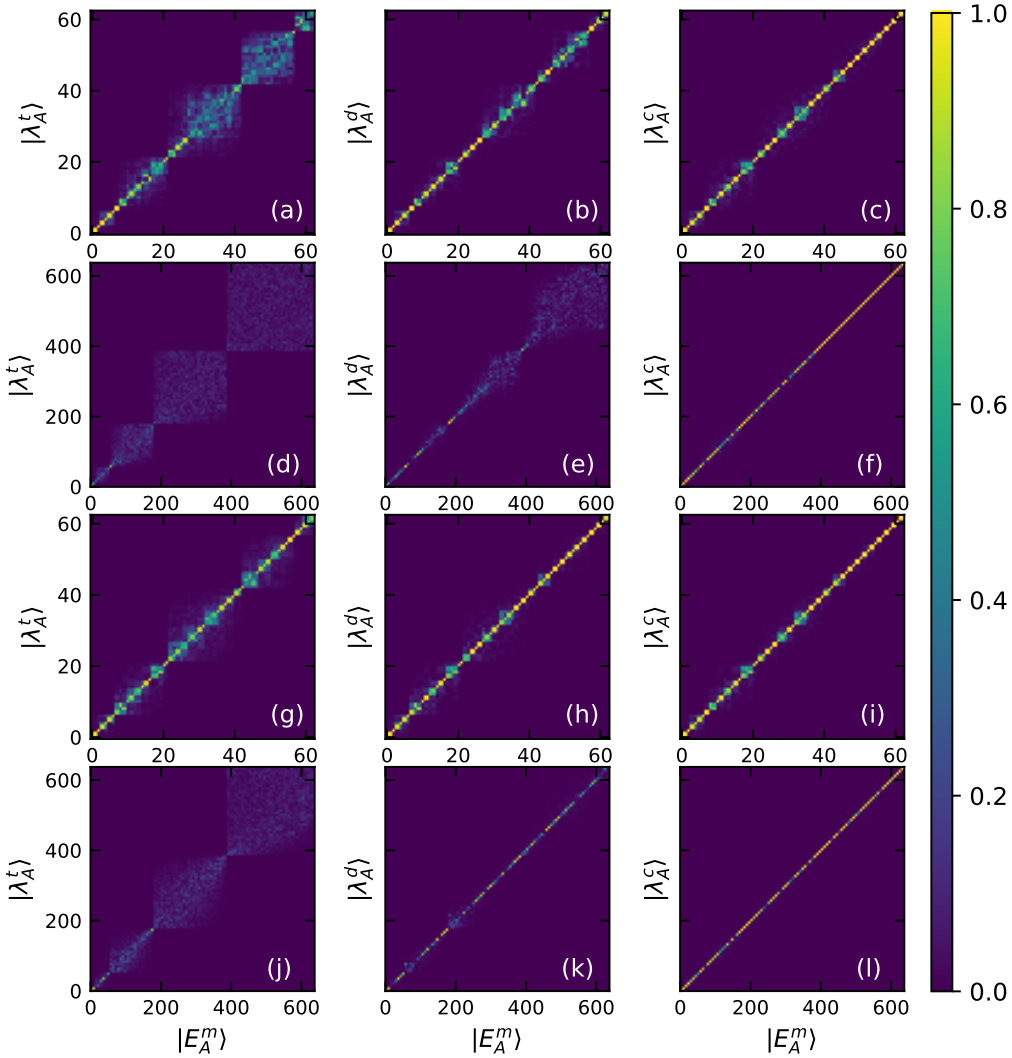

Figure 5.12: (Color online) Overlaps between eigenstates of reduced density matrices of $\hat{\rho}^t$ (a, d, g, j), $\hat{\rho}^d$ (b, e, h, k), $\hat{\rho}^c$ (c, f, i, l) and those of $\hat{H}_A$. The subsystem contains the left six sites in (a-c, g-i) and ten sites in (d-f, j-l). The results are for spinless fermions with initial inverse temperature $\beta_0 = 0.1$ (a-f) and $\beta_0 = 0.4$ (g-l).

where $Z_{AB} = \sum_{p=0}^{5} Z_A^p Z_B^{5-p}$ is the partition function of the whole system. So the thermal density matrix of A satisfying the total particle number conservation is

$$\begin{aligned} \hat{\rho}^c(A) &= \mathrm{Tr}_B\, \hat{\rho}^c(AB) \\ &= \sum_{p=0}^{5} \frac{e^{-\beta_{eff} E_A^{m_p}} Z_B^{5-p}}{Z_{AB}} \left|E_A^{m_p}\right\rangle \left\langle E_A^{m_p}\right|. \end{aligned} \tag{5.8}$$

Fig. 5.9 shows the results for the subsystem containing left six sites. Fig. 5.9(a) is for spinless fermions with $\beta_0 = 0.1$ and Fig. 5.9(b) is for bosons with $\beta_0 = 0.01$. Fig. 5.10 depicts the results for spinless fermions with $\beta_0 = 0.1$ [Fig. 5.10(a)] and $\beta_0 = 0.4$ [Fig. 5.10(b)], where the subsystem contains left ten sites. And Fig. 5.11 shows the results for bosons with $\beta_0 = 0.01$ [Fig. 5.11(a)] and $\beta_0 = 1$ [Fig. 5.11(b)], where the subsystem also contains left ten sites. Fig. 5.9, Fig. 5.10(a) and Fig. 5.11(a) have negative effective temperatures, so the slopes of the lines are positive, while the effective temperatures are positive for Fig. 5.10(b) and Fig. 5.11(b), the slopes are negative. The points linearly arranged belong to the same sub-sector with a certain particle number. From top to bottom, they are zero, one, two, three, four, five particle states, respectively. First note that for spinless fermions the spectrum of reduced CE, $\mathrm{Tr}_B\left(\hat{\rho}^c\right)$, match perfectly with that of $\hat{\rho}^c(A)$ for all cases shown here. However, there are two main deviations for bosons. First, there are some ripples in the spectra of reduced CE around that of $\hat{\rho}^c(A)$ for sub-sectors containing more than two particles. This effect is more obvious for the lower temperature $\beta_0 = 1$ than for the higher temperature $\beta_0 = 0.01$ in the same subsystem, see Fig. 5.11. Second, there are discontinuities near the top of the spectrum for sub-sectors containing more than two particles. The states near the top of the spectrum in those sub-sectors jump higher from the lines for the negative effective temperature but jump lower from the lines for the case of positive effective temperature. But overall they still match well.

For spinless fermions, it can be seen that in Fig. 5.9(a), the four density matrices have almost the same spectra, except that the line of the five-particle sector in the time-evolved state rotates anti-clockwise a little. In Fig. 5.10(a), the initial temperature is

the same, but the subsystem is bigger, then only the first two sub-sectors containing zero and one particle have perfect match for all four density matrices. While for the sub-sector containing two particles, the eigenvalues of $\mathrm{Tr}_B\,\hat{\rho}^d$ and $\mathrm{Tr}_B\,\hat{\rho}^t$ become smaller near the bottom of the spectra, similar to Fig. 5.1 where the DE also has lower weights near the bottom of the spectra. For sub-sectors with more particles, the reduced DE can always stay around the reduced CE because the similarity of weights between DE and CE as shown in Fig. 5.1, while $\mathrm{Tr}_B\,\hat{\rho}^t$ has bigger and bigger deviations. In Fig. 5.10(b) where the initial temperature is lower, the spectra in the first two sectors still match well. For the sub-sector with two particles, the eigenvalues for $\mathrm{Tr}_B\,\hat{\rho}^d$ and $\mathrm{Tr}_B\,\hat{\rho}^t$ are smaller near both the top and the bottom of the spectrum, also similar to the behavior of weights in Fig. 5.1. The fact that the reduced DE have bigger deviations at lower initial temperature is also consistent with the result in Fig. 5.1 that the DE has bigger difference from the CE at lower initial temperature. The spectrum of $\mathrm{Tr}_B\,\hat{\rho}^t$ is also very different from the other three for the five-particle states. Note that the big deviations in the time evolved state is not due to time fluctuations. We have checked the results for other ten different times and they behave almost the same. So the eigenvalues of $\mathrm{Tr}_B\,\hat{\rho}^t$ still equilibrate but not to those of reduced DE.

For bosons, as shown in Fig. 5.11, we can still see the ripples and discontinuities in $\mathrm{Tr}_B\,(\hat{\rho}^d)$ and $\mathrm{Tr}_B\,(\hat{\rho}^t)$ for the sub-sectors containing more than two particles. The spectrum for reduced DE match well to the reduced CE for all three cases considered here, because the DE and the CE for bosons are very similar for initial inverse temperature smaller than 1, as shown in Fig. 5.2. For $\beta_0 = 1$, Fig. 5.2(c) shows that most of the weights in DE

are a little smaller than those in CE, which also happens here for the reduced DE and the reduced CE. $\mathrm{Tr}_B\left(\hat{\rho}^t\right)$ have eigenvalues matching well to the other three for sub-sectors containing no more than four particles, but big differences appear for five-particle states in the subsystem with ten sites.

For all the cases considered here, most of the eigenvalues of all four density matrices in at least the first four sub-sectors with no more than three particles agree with each other. The contribution from these eigenvalues dominate the value of Rényi entropy, so the entropy of the subsystem containing the left ten sites or fewer all have indiscernible difference in Sec. 5.4. Another question is if the corresponding eigenstates, $|\lambda_A\rangle$, are the same with the eigenstates of the Hamiltonian associated with the subsystem, $|E_A^m\rangle$. If it is, then any observables residing in this subsystem are expected to thermalize as long as they depend little on the high energy eigenstates belonging to the sub-sectors with large number of particles. To check this, we plot the overlaps between eigenstates of the three density matrices and those of $\hat{H}_A$ in Fig. 5.12. The results are for spinless fermions with $\beta_0 = 0.1$ [Fig. 5.12(a-f)] and $\beta_0 = 0.4$ [Fig. 5.12(g-l)]. Fig. 5.12(a-c)(g-i) are for the subsystem containing the left six sites and Fig. 5.12(d-f)(j-l) are for the subsystem containing the left ten sites. Fig. 5.12(a,d,g,j) are for the reduced time-evolved states, Fig. 5.12(b,e,h,k) for the reduced DE and Fig. 5.12(c,f,i,l) for the reduced CE. For $\beta_0 = 0.1$, we see from Fig. 5.12(c)(f) that most of the eigenstates of the reduced CE are the same with those of $\hat{H}_A$ (referred as "good" eigenstates here). And we have shown that the eigenvalues are very close. So the reduced density matrix of a thermal state is still thermal with the same temperature. This is the intensive property of temperature in quantum mechanics. The reduced DE for

the subsystem containing six sites still have many good eigenstates, most of which are in the sub-sectors with no more than two particles, while for the subsystem containing ten sites it has only a small portion of eigenstates that are good. As the expectation value of an observable depend on the diagonal ensemble, we conclude that nearly all obervables thermalize as long as they reside in small subsystems and few-particle sub-sectors. The reduced time-evolved state has much fewer good eigenstates. But it can be seen that for the subsystem containing six sites, the first two sub-sectors containing no more than one particle (first 7 states) still have good resutls. So for small subsystems and few-particle sub-sectors, the time-evolved states becomes thermal at long enough time. The results for the lower initial temperature $\beta_0 = 0.4$ are better than those for $\beta_0 = 0.1$, where it is clear that there are more good eigenstates in both the reduced time-evolved state and the reduced DE. Note that for the six-site subsystem, unlike the case with $\beta_0 = 0.1$ where most of the good eigenstates are in low particle number sub-sectors, $\beta_0 = 0.4$ has most of the good eigenstates in high particle number sub-sectors, which may due to the different signs of effective temeprature. We also investigate the results for $\beta_0 = 1$, which have similar behaviors to $\beta_0 = 0.4$ but are a little worse than $\beta_0 = 0.4$. Note that more good eigenstates does not mean that the density matrix is closer to thermal. As high particle number eigenstates have much lower weights, the reduced time-evolved states for higher initial temperatures may be still closer to the thermal states.

We conclude this section with a comment on the theory of equilibration and thermalization. Intuitively, few-particle sub-sectors have more degrees of freedom serving as their bath, so they should behave more like the corresponding thermal states. For the sub-

sector containing five particles, the bath only has one degree of freedom. But there still are a large number of dephasing terms, which could result in the equilibration of eigenvalues of reduced time-evolved states but not to those of reduced DE, similar to the behaviors of Rényi entropy. In Ref. [141], a theorem states that the time averaged distance between the reduced time-evolved density matrix and the reduced DE density matrix is bounded by $1/2\sqrt{d_A/d^{eff}(\mathrm{Tr}_B\,(\hat{\rho}_d))} \leq 1/2\sqrt{d_A^2/d^{eff}(\hat{\rho}_d)}$, where d_A is the dimension of the subsystem, $d^{eff}(\mathrm{Tr}_B\,(\hat{\rho}_d))$ is the effective dimension of the reduced DE and $d^{eff}(\hat{\rho}_d)$ is the effective dimension of the DE. From the stronger bound we see that the subsystem must be smaller than half in the sense $l_A/L < 1/2$. For the weaker bound, the maximal $d^{eff}(\hat{\rho}_d)$ is the dimension of the Hilbert space for the whole system when the weights in the DE are constant. In our case, the weights in the CE and the DE are very similar at high effective temperatures, so for $l_A/L < 1/2$, the subsystem equilibrates to the reduced DE density matrix in the thermodynamic limit. When $l_A/L = 1/2$ and large L, the dimension of the whole system for spinless fermions $\ln d_w^f \approx (2\ln 2 - 3/4\ln 3)L$, and $\ln d_A^f \approx L/2\ln 2$. So $(d_A^f)^2/d_w^f \approx e^{0.131L}$ is exponentially large with the size of the system. A careful calculation shows that we need $l_A/L < 0.4175$ for the weaker bound to be exponentially small at high temperature. Similarly for bosons, $\ln d_w^b \approx (5/4\log(5) - 2\ln 2)L$, $\ln d_A^b \approx (3/4\ln 3 - 1/2\ln 2)L$, $(d_A^b)^2/d_w^b \approx e^{0.33L}$. And we need $l_A/L < 0.2045$ for the weaker bound to be exponentially small. The numeric results for $l_A/L = 1/2$ show good agreement between eigenvalues but not good agreement between eigenstates. Following the derivation in the Appendix A of Ref. [141], replacing the coefficients by the matrix elements considered here, the average distance is bounded by $1/2\sqrt{d_A e^{-S_2^{\beta_0}} T_{BA}^o}$, where again T_{BA}^o is a typical value of T_{BA}^{mn}. For

$\beta_0 = 0$, $d_A e^{-S_2^{\beta_0}}$ is at most an algebraically increasing function of system size, while T^o_{BA} is typically exponentially small. So in our case, it is possible for subsystems bigger than half of the system ($l_A/L > 1/2$) to equilibrate to the corresponding reduced DE density matrix in the thermodynamic limit.

Next, the DE is a weighted sum of eigenstate projectors. ETH in the strong sense states that every eigenstate is thermal for few-body observables [121]. And the similarity of reduced density matrices between the DE and the CE can be explained by the strong form of ETH which states that the reduced density matrix of a single finite energy density eigenstate of chaotic many-body quantum systems is equivalent to the thermal density matrix of the subsystem as long as the subsystem is much smaller than its complement and as long as $l_A/L < 1/2$ for many observables [81]. The subsystem ETH [66] states that the norm of the "off-diagonal" matrix $\hat{\rho}_A^{mn} = \mathrm{Tr}_B\left(|m\rangle\langle n|\right)$ $(m \neq n)$ is exponentially small for subsystems with $l_A/L < 1/2$, which explains the similarity between reduced $\hat{\rho}^t$ and reduced DE. Inside the small window where the energy density is peaked, all the reduced density matrix of eigenstates give the same thermal states for the subsystem. We show that even the full density matrix of the DE is close to the CE at high temperatures for the models we study here. So at high temperatures, the size of the subsystem that thermalizes just depends on the size of the subsystem that equilibrates to the reduced DE.

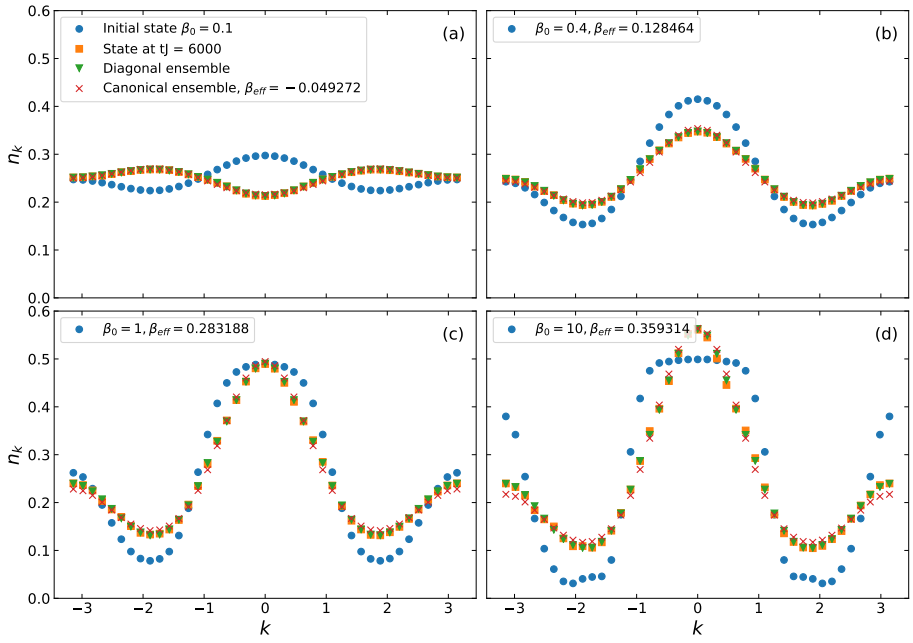

Figure 5.13: (Color online) MDFs of the initial state, the time-evolved state at $tJ = 6000$, the DE and the corresponding CE as a function of momentum $k \in (-\pi, \pi)$. The results are for spinless fermions, with different initial inverse temperatures $\beta_0 = 0.1$ (a), $\beta_0 = 0.4$ (b), $\beta_0 = 1$ (c) and $\beta_0 = 10$ (d).

5.6 Momentum Distribution Function

In this section, we use the momentum distribution function (MDF) to test the above conclusions. The MDF for fermions is

$$n_k^f = \frac{1}{L} \sum_{p,q} e^{-ik(p-q)} \langle c_p^\dagger c_q \rangle, \tag{5.9}$$

where $p, q = 1, 2, ..., L$ are the real-space locations. And the MDF for bosons is

$$n_k^b = \frac{1}{L} \sum_{p,q} e^{-ik(p-q)} \langle a_p^\dagger a_q \rangle. \tag{5.10}$$

The MDF is a few-body observable because it contains a summation of two-body observables, so it is expected to thermalize according to the above results. Regardless, we calculate the MDF for the initial state $\hat{\rho}^0$, the time-evolved state $\hat{\rho}^t$ at long time $tJ = 6000$, the DE

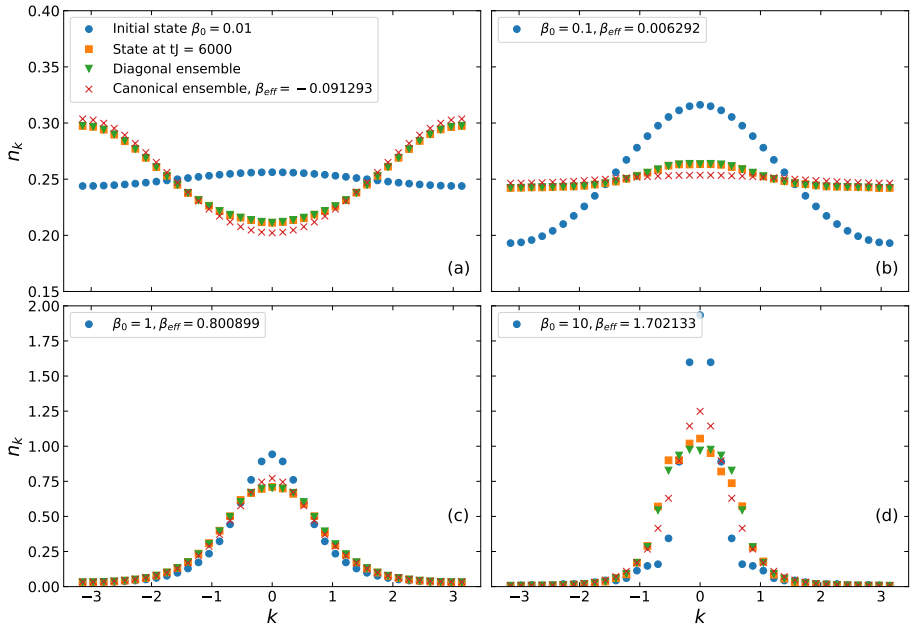

Figure 5.14: The same with Fig. 5.13 but for bosons. The initial inverse temperatures are $\beta_0 = 0.01$ (a), $\beta_0 = 0.1$ (b), $\beta_0 = 1$ (c) and $\beta_0 = 10$ (d).

density matrix $\hat{\rho}^d$ and the CE density matrix $\hat{\rho}^c$. If the MDF equilibrates, its expectation value using $\hat{\rho}^t$ should be the same as that using $\hat{\rho}^d$. And if the MDF thermalizes, all the expectation values, using $\hat{\rho}^t$, $\hat{\rho}^d$ and $\hat{\rho}^c$ should be the same.

Fig. 5.13 shows the results for spinless fermions with the same four initial temperatures as those in Fig. 5.3. Let's first briefly describe the MDF in the initial state. At low initial temperature $\beta_0 = 10$ [Fig. 5.13(d)], there are plateaus around $k = 0, \pm 1.8$. The momenta around $k = 0, \pm\pi$ have the highest population, while the momenta around $k = \pm 1.8$ have the lowest population. These behaviors can be understood by Fourier transforming the kinetic terms in Hamiltonian Eq. (5.2), $-2(\cos k + \cos 2k)$, which has one global minima $k = 0$, two local minima $k = \pm\pi$ and two global maxima $k \approx \pm 1.8$. At low temperature, the global minimum $k = 0$ is occupied first, then the nearby levels, one particle per level, due

to the Pauli exclusion principle. The height of the plateau is 0.5 because of normalization by the full volume. If the surrounding levels have higher energy than the other two local minima $k = \pm\pi$ do, particles start to occupy $k = \pm\pi$ and their surrounding levels. Very few particles will occupy the two maxima $k = \pm 1.8$ and their surroundings. At higher temperatures (Fig. 5.13(a)(b)(c)), the plateaus are smoothed out by thermal fluctuations. Close to the infinite temperature limit, more and more particles occupy the high energy levels, and eventually the MDF becomes flat.

The equilibration and thermalization of the MDF in Fig. 5.13 are very clear. In Fig. 5.13(a), $\beta_0 = 0.1$, the MDFs for $\hat{\rho}_t$, $\hat{\rho}_d$ and $\hat{\rho}_c$ do not have a visible difference, indicating strong thermalization of the MDF. The inversion of occupation is very interesting, and is a result of the changing of sign of the temperature. The effective final temperature we calculated for this case is indeed negative. The difference in three MDFs is still extremely small in Fig. 5.13(b) where the initial temperature is lower $\beta_0 = 0.4$. Further decreasing the initial temperature results in bigger difference between the MDF for $\hat{\rho}_c$ and the other two MDFs. This difference is clear in Fig. 5.13(d), where the MDF for $\hat{\rho}_c$ has lower occupation around $k = \pm\pi$, higher occupation around $k = \pm 1.8$, lower occupation for $k \in (-1.1, -0.7)$ and higher occupation for $k \in (-0.7, 0)$. These differences are probably finite size effects because they are much smaller than those in smaller systems with the same particle filling. Since these differences are overall relatively small, the MDF in the CE is still a good approximation for the real MDF at long times. It should be emphasized that although there are three slightly asymmetric points for $k \in (0, 0.5)$ in Fig. 5.13(d), which

is due to time fluctuations, the MDFs for DE and time-evolved state are the same for all four initial temperatures.

Fig. 5.14 shows the results for bosons. As the model we consider for bosons only has nearest-neighbor hopping, the hopping energy only have a single minimum at $k = 0$ and maxima at $k = \pm\pi$. So for positive effective temperatures [Fig. 5.14(b)(c)(d)], the occupation is peaked at $k = 0$, while for negative effective temperatures [Fig. 5.14(a)], the occupation is the lowest at $k = 0$. Note that the MDF for $\hat{\rho}^t$ and $\hat{\rho}^d$ has little difference in Fig. 5.14(a)(b)(c), and the small difference around $k = 0$ in Fig. 5.14(d) comes from time fluctuations. While they have obvious deviations from that of the CE for all cases, we can see that the MDF of the CE is more peaked at $k = 0$ for positive effective temperatures in Fig. 5.14(c)(d), while its value around $k = 0$ is smaller than that of the DE for negative effective temperature in Fig. 5.14(a). In Fig. 5.14(b), the effective temperature is close to infinity, MDF of the CE is flatter than that of the DE. Again these deviations are much smaller than those in smaller systems, so we believe they are finite-size effects.

From the above results we conclude that equilibration is much easier than thermalization. The intuitive reason is that the time-dependent terms are expected to cancel out due to dephasing. And it can also be partially understood from the similarity of $\mathrm{Tr}_B\left(\hat{\rho}^d\right)$ and $\mathrm{Tr}_B\left(\hat{\rho}^t\right)$ discussed in the last section. To see it more rigorously, we follow the derivation in Ref. [55, 240] and calculate the variance of an observable in time

$$\triangle^2 O \;=\; \sum_{m\neq n} |\rho_{0,mn}|^2 |O_{mn}|^2 < M \sum_{m\neq n} |\rho_{0,mn}|^2, \tag{5.11}$$

where M is the maximal off-diagonal matrix element of $\hat{O}$, then similar to Eq. (5.4),

$$\triangle^2 O < M\left(e^{-S_2^{\beta_0}} - e^{-S_2^d}\right) \tag{5.12}$$

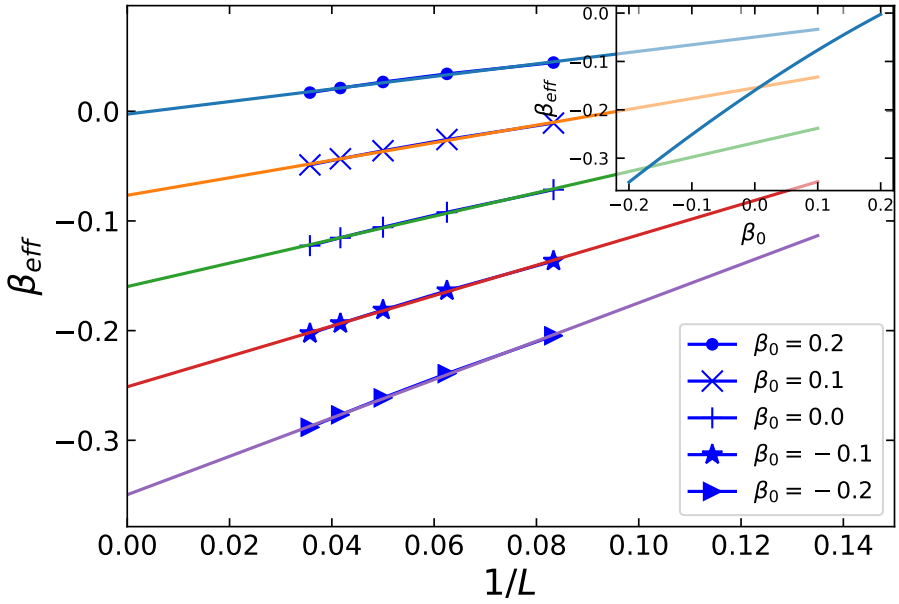

Figure 5.15: The finite size scaling of the effective inverse temperature for spinless fermions. The lines from top to bottom, the initial inverse temperatures are $\beta_0 = 0.2, 0.1, 0, -0.1, -0.2$ respectively. The system sizes used are $L = 12, 16, 20, 24, 28$. The inset shows the effective inverse temperature as a function of the initial inverse temperature extrapolated to the thermodynamic limit.

From the same arguments for Eq. (5.4) we conclude that as long as the initial state is at a finite temperature, the variance exponentially decays with the volume of the system, as long as the off diagonal elements are not exponentially large as $e^{S_2^{\beta_0}}$. Moreover, even at $T = 0$, ETH asserts that the off diagonal elements of few-body observables are exponentially small with the size of the system. So initial thermal states substantially decrease the fluctuations in time.

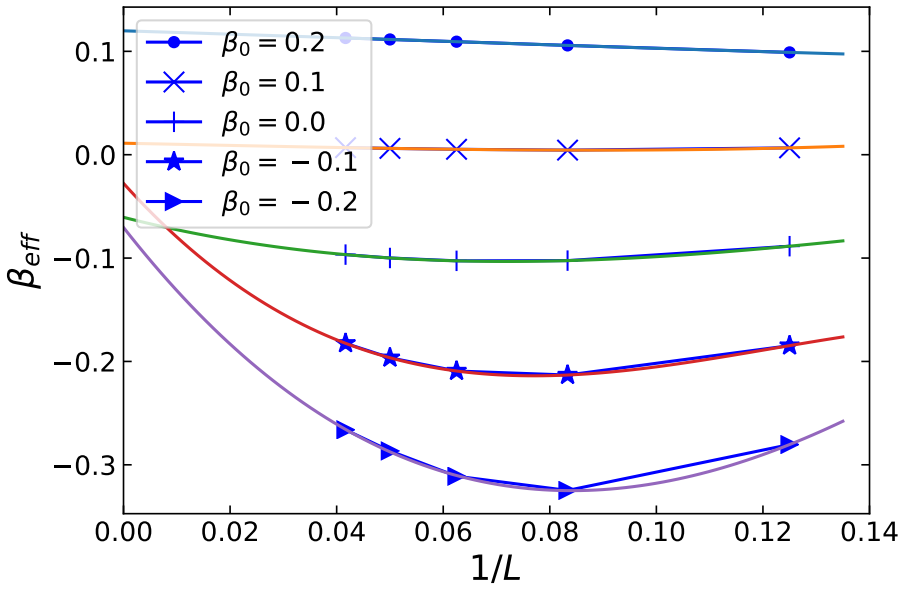

Figure 5.16: The same plot with Fig. 5.15 for bosons. The system sizes used are $L = 8, 12, 16, 20, 24$.

5.7 The Effective Temperature

We have seen that the effective temperature obtained by Eq. (1.30) can be negative. It is interesting that the negative temperature state can be created simply by sudden expansion to a larger volume. The numerical results presented in the previous sections are for finite system sizes. An important question is whether this negative temperature survives in the thermodynamic limit. To answer this question, we do a finite size analysis of the effective inverse temperature β_{eff}. In order to go to larger system sizes, we consider a configuration where $L/4$ particles expand inside a ring of L sites. Making use of the translation invariance [189], we can then calculate the spectrum of the final Hamiltonian up to 28 sites with 7 particles for spinless fermions (the dimension of Hilbert space is $1,184,040$) and 24 sites with 6 particles for bosons (the dimension of Hilbert space is $475,020$).

The results for spinless fermions are depicted in Fig. 5.15. We see for all initial temperatures shown in the figure, the effective inverse temperature β_{eff} is a linear function of $1/L$. Linear fits can be extrapolated and the value of β_{eff} in the thermodynamic limit can be extracted. Note that for spinless fermions, β_{eff} decreases as we increase the size of the system. For $L \to \infty$, an initial inverse temperature $\beta_0 = 0.2$ results in an infinite temperature state, and higher initial temperatures result in negative temperature states after expansion. The inset of Fig. 5.15 shows β_{eff} as a function of β_0 in the thermodynamic limit, which exhibits slight concavity. The same plot for bosons is shown in Fig. 5.16. We see that for bosons, β_{eff} increases with the system size at initial inverse temperature $\beta_0 = 0.2, 0.1$. For smaller initial inverse temperatures, β_{eff} decreases at first and then increases rapidly for larger systems. The linear fits are not convincing there. In fact, as the highest eigenenergy density diverges, for any positive initial temperature which has extensive total energy, we expect that the negative temperature should not survive in the thermodynamic limit for bosons with repulsive interactions.

5.8 Conclusion

We studied the Joule expansion for one-dimensional nonintegrable quantum lattice systems containing bosons or spinless fermions. We calculated and compared the weights of the eigenstates in the DE and the CE, for different initial temperatures, for the two models. The effective final temperature for the CE is obtained by matching the total energy of the system before and after the expansion. The effective temperature can be negative when the initial temperature is high enough, where the weights of the DE and the CE can match very

well. As the DE determines the equilibrated expectation values of observables, it is expected that extensive observables can thermalize at high initial temperatures. We analyzed the von Neumann and second order Rényi entropies in the DE, the CE and for the exact numerical time-evolved state at long times. The agreement between the DE and the CE can extend to the whole system for high initial temperatures because of the similarity in weights. And the agreement between the time-evolved states and the other two can extend beyond $l_A = L/2$ at high temperatures. We provided analytical arguments and numerical confirmation that ΔS_{2A}, the difference between the second-order Renyi entropy calculated in the DE and the fully time-evolved time-averaged one at long times, around $l_A = L/2$ is exponentially small in system size L (Fig. 5.7). We examined the eigenvalues and the eigenstates of the reduced density matrices directly and found that the reduced time-evolved density matrix at long times can be thermal for small subsystems. The momentum distribution functions have strong thermalizations at high initial temperature, and show population inversion after the expansion if the effective temperature is negative.

Note again that for initial temperatures larger than a certain value, the system thermalizes in a negative-temperature state. Negative temperature states have been created in cold atoms in spin systems[155] and for motional degrees of freedom of a fermionic system[26], and are of interest for a number of exotic phenomena that can be realized with them[149]. We propose that negative temperature states can be created by sudden expansion to a larger system size. In this paper we only considered repulsive interactions. For fermions, the negative temperature is a feature that remains in the thermodynamic limit. For bosons with repulsive interactions, there can be no negative temperature state in the

thermodynamic limit since the energy spectrum is unbounded. For finite, experimentally realistic system sizes, there can be negative-temperature states and these can also be obtained through Joule expansion.

There are still a number of unanswered questions. For example, what is the maximal size of the subsystem whose Rényi entropy can equilibrate to those of the reduced DE and the reduced CE for a certain initial temperature? And what is the biggest subsystem whose reduced time-evolved density matrix is thermal for a given initial temperature? Why do the eigenvalues of reduced time-evolved states in high-particle-number sub-sectors equilibrate to different values than the reduced DE? Answering these questions needs further detailed study of the diagonal and off-diagonal matrix elements of initial states in the basis of final Hamiltonian and the reduced density matrix of projector operators $|m\rangle\langle m|$ and "off-diagonal" operators $|m\rangle\langle n|$ $(m \neq n)$, which can be the subject of future work.

In terms of experimental realization of the models studied, the bosonic model is a simple Bose Hubbard model that can be created with cold atoms on optical lattices. Creating the wall that initially confines the particles to the left half of the system requires local manipulation of the optical potential and may be realized using holographic techniques [106]. The spinless fermions model we studied contains nearest-neighbor and next-nearest-neighbor hoppings and interactions. As discussed in Sec. 5.2, it is equivalent to a zig-zag two-leg ladder with only nearest-neighbor terms (inter and intra-leg). Nearest-neighbor interactions may be created and tuned via Rydberg-dressed potentials[100, 176, 239]. The inter and intra-leg nearest-neighbor interactions and hopping can be tuned to different values by varying the lattice spacing on the rung and along the legs to different values

and exploiting the range and shape of the Rydberg-dressed potential, as was done in Ref. [241]. Multi-mode cavity photon-mediated interactions [217] may also be used to create the needed interactions.

Chapter 6

Conclusions

In this thesis, we obtain the Hamiltonian formulation of the Abelian Higgs lattice gauge theory by using the duality method with TRG reformulation in Chapter 2. The method can be applied to observables like the Polyakov loop and other lattice gauge models. We found universal finite size scaling behavior of the energy gap between the ground states with and without an insertion of the Polyakov loop. The scaling function does not change by deforming the lattice to time continuum limit.

An interesting feature (not included in the thesis, see [213]) found in our study is that at finite space-time volume and weak gauge coupling, there is a sudden increase of the Polyakov loop when we increase κ beyond the critical value corresponding to the BKT transition. Since the primary scope of this work is to explore results at finite volume and finite lattice spacing in order to move the prospect of quantum simulating gauge theories using cold atoms in optical lattices forward, understanding this sudden increase in the context of the continuum limit and the infinite volume limit is left for future work.

In Chapter 3, we propose two schemes to quantum simulate the Abelian Higgs model. One is to use the two-species Bose-Hubbard model which can be mapped to an effective spin Hamiltonian. By tuning the parameters, we can realize the Abelian Higgs model. But this only works for spin-1 truncation which only reflects some limiting cases of the Abelian Higgs model, or very large spin truncation which would waste a lot of experimental resources. The other one is to use a multi-leg ladder of atoms trapped in optical lattices interacting with Rydberg dressed interactions. This method can mimic any spin truncation, and the positive quadratic interactions can be realized approximately in a squeezed multi-leg ladder where the lattice spacing along the rung is much smaller than that along the leg. The results measured in the multi-leg ladder are stable to experimental defects or can be easily corrected by measuring the density-density correlations. The feasibility of this experimental proposal for the quantum simulation of the Abelian Higgs model in 1+1 dimension provides a proof of principle that High Energy physics can be simulated in low energy cold atom systems. Experimental study of the phase diagram and the out-of-equilibrium dynamics following a quantum quench for the LGT is also possible as long as the quantum simulator has been realized in optical lattices.

In Chapter 4, we show that, taking the large sub-leading corrections into account, the Calabrese-Cardy conformal field theory (CFT) predictions for the leading logarithmic scaling of these entropies are consistent with a central charge $c = 1$ and this scaling survives the time-continuum limit and truncation of the microscopic degrees of freedom, modifications which allow us to connect the Lagrangian formulation to quantum Hamiltonian. In the limit where the product of the spatial and temporal couplings is close to zero, the

model with half-filled charges has the same phase diagram as the half-filled single-species Bose Hubbard model in the corresponding parameter region, where they also have the same entanglement entropy. This paves the way for using current experimental techniques of cold bosonic atoms trapped in one-dimensional optical lattices and designed to measure the second-order Rényi entanglement entropy S_2 between two partitions to verify detailed predictions of CFT and estimate the central charge c. We show that the ground state of Bose Hubbard systems at half-filling can be prepared by adiabatically removing the initial harmonic confinement. The S_2 can be measured by preparing two copies of a quantum state, letting them interfere under a beam-splitter operation, and measuring the local parity [57, 106]. We show that the measurement of central charge can have accuracy better than 5% for up to 16 sites and the number of measurements needed within a statistical error is estimated.

Finally in Chapter 5, we discuss the sudden expansion of bosons and spinless fermions initially prepared in thermal states. To answer the question of the Joule expansion in quantum systems, we compare the density matrices of all subsystems at long times to those in a canonical ensemble with an effective temperature found by total energy conservation. There are good agreements for density matrices in small subsystems and all observables in these subsystems are expected to thermalize. A negative temperature state can be prepared by the sudden expansion of a high temperature thermal state of fermions. Future work in this direction could be the study of different expansion rates of singlons and doublons, where doublons going through the early thermalized singlons is possible. Sudden expansion of coupled heavy and light particles are still interesting to study.

Bibliography

[1] K. Aikawa, A. Frisch, M. Mark, S. Baier, R. Grimm, and F. Ferlaino. Reaching Fermi Degeneracy via Universal Dipolar Scattering. *Physical Review Letters*, 112(1):010404, January 2014.

[2] K. Aikawa, A. Frisch, M. Mark, S. Baier, A. Rietzler, R. Grimm, and F. Ferlaino. Bose-einstein condensation of erbium. *Phys. Rev. Lett.*, 108:210401, May 2012.

[3] Marco Anderlini, Patricia J Lee, Benjamin L Brown, Jennifer Sebby-Strabley, William D Phillips, and J Porto. Controlled exchange interaction between pairs of neutral atoms in an optical lattice. *Nature*, 448(7152):452–456, July 2007.

[4] S Ashhab and A J Leggett. Bose-einstein condensation of spin-1/2 atoms with conserved total spin. *Phys. Rev. A*, 68:063612, 2003.

[5] M. Atala, M. Aidelsburger, M. Lohse, J. T. Barreiro, B. Paredes, and I. Bloch. Observation of chiral currents with ultracold atoms in bosonic ladders. *Nature Physics*, 10:588–593, August 2014.

[6] Marcos Atala, Monika Aidelsburger, Michael Lohse, Julio T Barreiro, Belén Paredes, and Immanuel Bloch. Observation of chiral currents with ultracold atoms in bosonic ladders. *Nature Physics*, 10:588, jul 2014.

[7] M. C. Bañuls, J. I. Cirac, and M. B. Hastings. Strong and weak thermalization of infinite nonintegrable quantum systems. *Phys. Rev. Lett.*, 106:050405, Feb 2011.

[8] S. Baier, M. J. Mark, D. Petter, K. Aikawa, L. Chomaz, Z. Cai, M. Baranov, P. Zoller, and F. Ferlaino. Extended bose-hubbard models with ultracold magnetic atoms. *Science*, 352(6282):201–205, 2016.

[9] D. Banerjee, M. Dalmonte, M. Müller, E. Rico, P. Stebler, U.-J. Wiese, and P. Zoller. Atomic quantum simulation of dynamical gauge fields coupled to fermionic matter: From string breaking to evolution after a quench. *Phys. Rev. Lett.*, 109:175302, Oct 2012.

[10] Ghassan George Batrouni and Richard T. Scalettar. World-line quantum monte carlo algorithm for a one-dimensional bose model. *Phys. Rev. B*, 46:9051–9062, Oct 1992.

[11] A. Bazavov, Y. Meurice, S.-W. Tsai, J. Unmuth-Yockey, Li-Ping Yang, and Jin Zhang. Estimating the central charge from the rényi entanglement entropy. *Phys. Rev. D*, 96:034514, Aug 2017.

[12] A. Bazavov, Y. Meurice, S.-W. Tsai, J. Unmuth-Yockey, and Jin Zhang. Gauge-invariant implementation of the abelian-higgs model on optical lattices. *Phys. Rev. D*, 92:076003, Oct 2015.

[13] Alexei Bazavov, Simon Catterall, Raghav G Jha, and Judah Unmuth-Yockey. Tensor renormalization group study of the non-abelian higgs model in two dimensions. *arXiv preprint arXiv:1901.11443*, 2019.

[14] A. A. Belavin, Alexander M. Polyakov, and A. B. Zamolodchikov. Infinite Conformal Symmetry in Two-Dimensional Quantum Field Theory. *Nucl. Phys.*, B241:333–380, 1984.

[15] Noomen Belmechri, Leonid Förster, Wolfgang Alt, Artur Widera, Dieter Meschede, and Andrea Alberti. Microwave control of atomic motional states in a spin-dependent optical lattice. *J. Phys. B: At. Mol. Opt. Phys.*, 46(10):104006, May 2013.

[16] V. L. Berezinskiĭ. Destruction of Long-range Order in One-dimensional and Two-dimensional Systems Possessing a Continuous Symmetry Group. II. Quantum Systems. *Soviet Journal of Experimental and Theoretical Physics*, 34:610, 1972.

[17] W. Beugeling, R. Moessner, and Masudul Haque. Finite-size scaling of eigenstate thermalization. *Phys. Rev. E*, 89:042112, Apr 2014.

[18] Wouter Beugeling, Roderich Moessner, and Masudul Haque. Off-diagonal matrix elements of local operators in many-body quantum systems. *Phys. Rev. E*, 91:012144, Jan 2015.

[19] R. M. W. van Bijnen and T. Pohl. Quantum magnetism and topological ordering via rydberg dressing near förster resonances. *Phys. Rev. Lett.*, 114(24):243002, 2015.

[20] Giulio Biroli, Corinna Kollath, and Andreas M. Läuchli. Effect of rare fluctuations on the thermalization of isolated quantum systems. *Phys. Rev. Lett.*, 105:250401, Dec 2010.

[21] R. Blatt and C. F. Roos. Quantum simulations with trapped ions. *Nat. Phys.*, 8(4):277–284, 2012.

[22] Immanuel Bloch, Jean Dalibard, and Wilhelm Zwerger. Many-body physics with ultracold gases. *Rev. Mod. Phys.*, 80:885–964, Jul 2008.

[23] P. Bocchieri and A. Loinger. Quantum recurrence theorem. *Phys. Rev.*, 107:337–338, Jul 1957.

[24] O. Bohigas, M. J. Giannoni, and C. Schmit. Characterization of chaotic quantum spectra and universality of level fluctuation laws. *Phys. Rev. Lett.*, 52:1–4, Jan 1984.

[25] Lars Bonnes, Hannes Pichler, and Andreas M. Läuchli. Entropy perspective on the thermal crossover in a fermionic hubbard chain. *Phys. Rev. B*, 88:155103, Oct 2013.

[26] S. Braun, J. P. Ronzheimer, M. Schreiber, S. S. Hodgman, T. Rom, I. Bloch, and U. Schneider. Negative absolute temperature for motional degrees of freedom. *Science*, 339(6115):52–55, 2013.

[27] Falk Bruckmann, Christof Gattringer, Thomas Kloiber, and Tin Sulejmanpasic. Two-dimensional o(3) model at nonzero density: From dual lattice simulations to repulsive bosons. *Phys. Rev. D*, 94:114503, Dec 2016.

[28] P. V. Buividovich and M. I. Polikarpov. Numerical study of entanglement entropy in SU(2) lattice gauge theory. *Nucl. Phys.*, B802:458–474, 2008.

[29] Pasquale Calabrese, Massimo Campostrini, Fabian Essler, and Bernard Nienhuis. Parity effects in the scaling of block entanglement in gapless spin chains. *Phys. Rev. Lett.*, 104:095701, Mar 2010.

[30] Pasquale Calabrese and John Cardy. Entanglement entropy and quantum field theory. *Journal of Statistical Mechanics: Theory and Experiment*, 2004(06):P06002, jun 2004.

[31] Pasquale Calabrese and John Cardy. Time dependence of correlation functions following a quantum quench. *Phys. Rev. Lett.*, 96:136801, Apr 2006.

[32] Pasquale Calabrese and John Cardy. Entanglement and correlation functions following a local quench: a conformal field theory approach. *Journal of Statistical Mechanics: Theory and Experiment*, 2007(10):P10004–P10004, oct 2007.

[33] Pasquale Calabrese and John Cardy. Quantum quenches in extended systems. *Journal of Statistical Mechanics: Theory and Experiment*, 2007(06):P06008–P06008, jun 2007.

[34] Pasquale Calabrese and John Cardy. Entanglement entropy and conformal field theory. *Journal of Physics A: Mathematical and Theoretical*, 42(50):504005, dec 2009.

[35] Pasquale Calabrese and John L. Cardy. Entanglement entropy and quantum field theory: A Non-technical introduction. *Int.J.Quant.Inf.*, 4:429, 2006.

[36] S. Camalet. Joule expansion of a pure many-body state. *Phys. Rev. Lett.*, 100:180401, May 2008.

[37] A. S. Campbell, D. M. Gangardt, and K. V. Kheruntsyan. Sudden expansion of a one-dimensional bose gas from power-law traps. *Phys. Rev. Lett.*, 114:125302, Mar 2015.

[38] John Cardy. Quantum quenches to a critical point in one dimension: some further results. *Journal of Statistical Mechanics: Theory and Experiment*, 2016(2):023103, feb 2016.

[39] John Cardy and Pasquale Calabrese. Unusual corrections to scaling in entanglement entropy. *Journal of Statistical Mechanics: Theory and Experiment*, 2010(04):P04023, 2010.

[40] John Cardy and Christopher P. Herzog. Universal Thermal Corrections to Single Interval Entanglement Entropy for Two Dimensional Conformal Field Theories. *Phys.Rev.Lett.*, 112(17):171603, 2014.

[41] J. Catani, L. De Sarlo, G. Barontini, F. Minardi, and M. Inguscio. Degenerate bose-bose mixture in a three-dimensional optical lattice. *Phys. Rev. A*, 77:011603, Jan 2008.

[42] J. Catani, G. Lamporesi, D. Naik, M. Gring, M. Inguscio, F. Minardi, A. Kantian, and T. Giamarchi. Quantum dynamics of impurities in a one-dimensional bose gas. *Phys. Rev. A*, 85:023623, Feb 2012.

[43] A Celi, P Massignan, J Ruseckas, N Goldman, I?B Spielman, G Juzeli?nas, and M Lewenstein. *Phys. Rev. Lett.*, 112:043001, 2014.

[44] Pochung Chen and Min-Fong Yang. Quantum phase transitions in a two-species hard-core boson Hubbard model in two dimensions. *Phys. Rev. B*, 82(18):180510, November 2010.

[45] Y.-A. Chen, S. D. Huber, S. Trotzky, I. Bloch, and E. Altman. Many-body Landau-Zener dynamics in coupled one-dimensional Bose liquids. *Nature Physics*, 7:61–67, January 2011.

[46] Yu-Ao Chen, Sebastian D Huber, Stefan Trotzky, Immanuel Bloch, and Ehud Altman. Many-body LandauZener dynamics in coupled one-dimensional Bose liquids. *Nature Physics*, 7:61, oct 2010.

[47] Lawrence W. Cheuk, Matthew A. Nichols, Melih Okan, Thomas Gersdorf, Vinay V. Ramasesh, Waseem S. Bakr, Thomas Lompe, and Martin W. Zwierlein. Quantum-gas microscope for fermionic atoms. *Phys. Rev. Lett.*, 114:193001, May 2015.

[48] Cheng Chin, Rudolf Grimm, Paul Julienne, and Eite Tiesinga. Feshbach resonances in ultracold gases. *Rev. Mod. Phys.*, 82:1225–1286, Apr 2010.

[49] A. Chotia, B. Neyenhuis, S. A. Moses, B. Yan, J. P. Covey, M. Foss-Feig, A. M. Rey, D. S. Jin, and J. Ye. Long-Lived Dipolar Molecules and Feshbach Molecules in a 3D Optical Lattice. *Physical Review Letters*, 108(8):080405, February 2012.

[50] Chia-Min Chung, Shiang Fang, and Pochung Chen. Quantum and thermal transitions out of the pair-supersolid phase of two-species bosons on a square lattice. *Phys. Rev. B*, 85(21):214513, June 2012.

[51] S. Coleman. *Aspects of Symmetry*. Cambridge University Press, Cambridge, 1985.

[52] N. R. Cooper, J. Dalibard, and I. B. Spielman. Topological bands for ultracold atoms. *Rev. Mod. Phys.*, 91:015005, Mar 2019.

[53] Michael Creutz. *Quarks, gluons and lattices*, volume 8. Cambridge University Press, 1985.

[54] Gregory M. Crosswhite, A. C. Doherty, and Guifré Vidal. Applying matrix product operators to model systems with long-range interactions. *Phys. Rev. B*, 78:035116, Jul 2008.

[55] Luca D'Alessio, Yariv Kafri, Anatoli Polkovnikov, and Marcos Rigol. From quantum chaos and eigenstate thermalization to statistical mechanics and thermodynamics. *Advances in Physics*, 65(3):239–362, 2016.

[56] A. J. Daley. Quantum trajectories and open many-body quantum systems. *Advances in Physics*, 63:77–149, March 2014.

[57] A. J. Daley, H. Pichler, J. Schachenmayer, and P. Zoller. Measuring entanglement growth in quench dynamics of bosons in an optical lattice. *Phys. Rev. Lett.*, 109:020505, Jul 2012.

[58] L. De Lathauwer, B. De Moor, and J. Vandewalle. A multilinear singular value decomposition. *SIAM Journal on Matrix Analysis and Applications*, 21(4):1253–1278, 2000.

[59] Thomas DeGrand. Lattice studies of QCD-like theories with many fermionic degrees of freedom. *Phil. Trans. R. Soc. A*, 369:2701–2717, 2011.

[60] Alan Denbleyker, Yuzhi Liu, Y. Meurice, M. P. Qin, T. Xiang, Z. Y. Xie, J. F. Yu, and Haiyuan Zou. Controlling sign problems in spin models using tensor renormalization. *Phys. Rev. D*, 89:016008, Jan 2014.

[61] J. M. Deutsch. Quantum statistical mechanics in a closed system. *Phys. Rev. A*, 43:2046–2049, Feb 1991.

[62] Philippe Di Francesco, Pierre Mathieu, and David Sénéchal. *Conformal field theory*. Graduate texts in contemporary physics. Springer, New York, NY, 1997.

[63] V. S. Dotsenko. Critical Behavior and Associated Conformal Algebra of the Z(3) Potts Model. *Nucl. Phys.*, B235:54–74, 1984.

[64] Joaquín E. Drut and William J. Porter. Hybrid monte carlo approach to the entanglement entropy of interacting fermions. *Phys. Rev. B*, 92:125126, Sep 2015.

[65] J Dukelsky, M. A Martín-Delgado, T Nishino, and G Sierra. Equivalence of the variational matrix product method and the density matrix renormalization group applied to spin chains. *Europhysics Letters (EPL)*, 43(4):457–462, aug 1998.

[66] Anatoly Dymarsky, Nima Lashkari, and Hong Liu. Subsystem eigenstate thermalization hypothesis. *Phys. Rev. E*, 97:012140, Jan 2018.

[67] J. Eisert, M. Cramer, and M. B. Plenio. Colloquium: Area laws for the entanglement entropy. *Rev. Mod. Phys.*, 82:277–306, Feb 2010.

[68] Viktor Eisler and Ingo Peschel. Evolution of entanglement after a local quench. *Journal of Statistical Mechanics: Theory and Experiment*, 2007(06):P06005–P06005, jun 2007.

[69] Sheer El-Showk, Miguel F. Paulos, David Poland, Slava Rychkov, David Simmons-Duffin, and Alessandro Vichi. Solving the 3d ising model with the conformal bootstrap. *Phys. Rev. D*, 86:025022, Jul 2012.

[70] M. Endres, M. Cheneau, T. Fukuhara, C. Weitenberg, P. Schauß, C. Gross, L. Mazza, M. C. Bañuls, L. Pollet, I. Bloch, and S. Kuhr. Single-site- and single-atom-resolved measurement of correlation functions. *Appl. Phys. B*, 113(1):27–39, 2013.

[71] Maurizio Fagotti and Pasquale Calabrese. Universal parity effects in the entanglement entropy of xx chains with open boundary conditions. *Journal of Statistical Mechanics: Theory and Experiment*, 2011(01):P01017, 2011.

[72] Richard P. Feynman. Simulating physics with computers. *International Journal of Theoretical Physics*, 21(6):467–488, Jun 1982.

[73] Matthew P. A. Fisher. *Strong Interaction in Low Dimensions*. Kluwer Academic, 2004.

[74] S Fölling, S Trotzky, P Cheinet, M Feld, R Saers, A Widera, T Müller, and I Bloch. Direct observation of second-order atom tunnelling. *Nature*, 448:1029, aug 2007.

[75] Daniel Friedan, Zong-an Qiu, and Stephen H. Shenker. Conformal Invariance, Unitarity and Two-Dimensional Critical Exponents. *Phys. Rev. Lett.*, 52:1575–1578, 1984.

[76] F. Fröwis, V. Nebendahl, and W. Dür. Tensor operators: Constructions and applications for long-range interaction systems. *Phys. Rev. A*, 81:062337, Jun 2010.

[77] Takeshi Fukuhara, Sebastian Hild, Johannes Zeiher, Peter Schauß, Immanuel Bloch, Manuel Endres, and Christian Gross. Spatially resolved detection of a spin-entanglement wave in a bose-hubbard chain. *Phys. Rev. Lett.*, 115:035302, Jul 2015.

[78] Takeshi Fukuhara, Adrian Kantian, Manuel Endres, Marc Cheneau, Peter Schauß, Sebastian Hild, David Bellem, Ulrich Schollwöck, Thierry Giamarchi, Christian Gross, Immanuel Bloch, and Stefan Kuhr. Quantum dynamics of a mobile spin impurity. *Nat. Phys.*, 9(4):235–241, 2013.

[79] Kenji Fukushima and Vladimir Skokov. Polyakov loop modeling for hot qcd. *Progress in Particle and Nuclear Physics*, 96:154 – 199, 2017.

[80] B. Gadway. talk given at the NPQI meeting, Argonne, March 29, 2018.

[81] James R. Garrison and Tarun Grover. Does a single eigenstate encode the full hamiltonian? *Phys. Rev. X*, 8:021026, Apr 2018.

[82] Christof Gattringer, Thomas Kloiber, and Michael Müller-Preussker. Dual simulation of the two-dimensional lattice u(1) gauge-higgs model with a topological term. *Phys. Rev. D*, 92:114508, Dec 2015.

[83] S. Genway, A. F. Ho, and D. K. K. Lee. Thermalization of local observables in small hubbard lattices. *Phys. Rev. A*, 86:023609, Aug 2012.

[84] Alexander W. Glaetzle, Marcello Dalmonte, Rejish Nath, Christian Gross, Immanuel Bloch, and Peter Zoller. Designing frustrated quantum magnets with laser-dressed rydberg atoms. *Phys. Rev. Lett.*, 114:173002, Apr 2015.

[85] Christian Gogolin, Markus P. Müller, and Jens Eisert. Absence of thermalization in nonintegrable systems. *Phys. Rev. Lett.*, 106:040401, Jan 2011.

[86] S. Goldstein, J. L. Lebowitz, R. Tumulka, and N. Zanghì. Long-time behavior of macroscopic quantum systems. *The European Physical Journal H*, 35(2):173–200, Nov 2010.

[87] Daniel González-Cuadra, Erez Zohar, and J Ignacio Cirac. Quantum simulation of the abelian-higgs lattice gauge theory with ultracold atoms. *New Journal of Physics*, 19(6):063038, jun 2017.

[88] D. Greif, T. Uehlinger, G. Jotzu, L. Tarruell, and T. Esslinger. Short-Range Quantum Magnetism of Ultracold Fermions in an Optical Lattice. *Science*, 340:1307–1310, June 2013.

[89] Daniel Greif, Thomas Uehlinger, Gregor Jotzu, Leticia Tarruell, and Tilman Esslinger. Short-range quantum magnetism of ultracold fermions in an optical lattice. *Science*, 340(6138):1307–1310, 2013.

[90] Markus Greiner, Olaf Mandel, Tilman Esslinger, Theodor W Hänsch, and Immanuel Bloch. Quantum phase transition from a superfluid to a Mott insulator in a gas of ultracold atoms. *Nature*, 415(6867):39–44, 2002.

[91] A. Griesmaier, J. Werner, S. Hensler, J. Stuhler, and T. Pfau. Bose-Einstein Condensation of Chromium. *Physical Review Letters*, 94(16):160401, April 2005.

[92] Christian Gross and Immanuel Bloch. Quantum simulations with ultracold atoms in optical lattices. *Science*, 357(6355):995–1001, 2017.

[93] Thomas Guhr, Axel MllerGroeling, and Hans A. Weidenmller. Random-matrix theories in quantum physics: common concepts. *Physics Reports*, 299(4):189 – 425, 1998.

[94] D. S. Hall, M. R. Matthews, J. R. Ensher, C. E. Wieman, and E. A. Cornell. Dynamics of component separation in a binary mixture of bose-einstein condensates. *Phys. Rev. Lett.*, 81:1539–1542, Aug 1998.

[95] Elmar Haller, James Hudson, Andrew Kelly, Dylan A. Cotta, Bruno Peaudecerf, Graham D. Bruce, and Stefan Kuhr. Single-atom imaging of fermions in a quantum-gas microscope. *Nat. Phys.*, 11:738, 2015.

[96] Kai He and Marcos Rigol. Initial-state dependence of the quench dynamics in integrable quantum systems. ii. thermal states. *Phys. Rev. A*, 85:063609, Jun 2012.

[97] Kai He and Marcos Rigol. Initial-state dependence of the quench dynamics in integrable quantum systems. iii. chaotic states. *Phys. Rev. A*, 87:043615, Apr 2013.

[98] F. Heidrich-Meisner, S. R. Manmana, M. Rigol, A. Muramatsu, A. E. Feiguin, and E. Dagotto. Quantum distillation: Dynamical generation of low-entropy states of strongly correlated fermions in an optical lattice. *Phys. Rev. A*, 80:041603(R), Oct 2009.

[99] Jochen Heitgers. *Numerical simulations of gauge-Higgs models on the lattice.* PhD thesis, Verlag nicht ermittelbar, 1997.

[100] N. Henkel, R. Nath, and T. Pohl. Three-dimensional roton excitations and supersolid formation in rydberg-excited bose-einstein condensates. *Phys. Rev. Lett.*, 104:195302, May 2010.

[101] J. Herbrych, A. E. Feiguin, E. Dagotto, and F. Heidrich-Meisner. Efficiency of fermionic quantum distillation. *Phys. Rev. A*, 96:033617, Sep 2017.

[102] Yasuaki Hikida, Yuya Kusuki, and Tadashi Takayanagi. Eigenstate thermalization hypothesis and modular invariance of two-dimensional conformal field theories. *Phys. Rev. D*, 98:026003, Jul 2018.

[103] Christoph Holzhey, Finn Larsen, and Frank Wilczek. Geometric and renormalized entropy in conformal field theory. *Nuclear Physics B*, 424(3):443 – 467, 1994.

[104] Chen-Lung Hung, Xibo Zhang, Nathan Gemelke, and Cheng Chin. Observation of scale invariance and universality in two-dimensional Bose gases. *Nature*, 470:236, jan 2011.

[105] Tatsuhiko N. Ikeda, Yu Watanabe, and Masahito Ueda. Finite-size scaling analysis of the eigenstate thermalization hypothesis in a one-dimensional interacting bose gas. *Phys. Rev. E*, 87:012125, Jan 2013.

[106] Rajibul Islam, Ruichao Ma, Philipp M Preiss, M Eric Tai, Alexander Lukin, Matthew Rispoli, and Markus Greiner. Measuring entanglement entropy in a quantum many-body system. *Nature*, 528:77, dec 2015.

[107] D. Jaksch, C. Bruder, J. I. Cirac, C. W. Gardiner, and P. Zoller. Cold bosonic atoms in optical lattices. *Phys. Rev. Lett.*, 81:3108–3111, Oct 1998.

[108] K. Jansen, J. Jersk, C.B. Lang, T. Neuhaus, and G. Vones. Phase structure of scalar compact qed. *Nuclear Physics B*, 265(1):129 – 144, 1986.

[109] R. V. Jensen and R. Shankar. Statistical behavior in deterministic quantum systems with few degrees of freedom. *Phys. Rev. Lett.*, 54:1879–1882, Apr 1985.

[110] B.-Q. Jin and V. E. Korepin. Quantum spin chain, toeplitz determinants and the fisher—hartwig conjecture. *Journal of Statistical Physics*, 116(1):79–95, Aug 2004.

[111] J. E. Johnson and S. L. Rolston. Interactions between rydberg-dressed atoms. *Phys. Rev. A*, 82:033412, Sep 2010.

[112] D. R. T. Jones, John Kogut, and D. K. Sinclair. Electrodynamics of the planar model: Its phase diagram, continuum limit, and mass spectrum. *Phys. Rev. D*, 19:1882–1905, Mar 1979.

[113] J. Kajala, F. Massel, and P. Törmä. Expansion dynamics in the one-dimensional fermi-hubbard model. *Phys. Rev. Lett.*, 106:206401, May 2011.

[114] Eriko Kaminishi, Jun Sato, and Tetsuo Deguchi. Recurrence time in the quantum dynamics of the 1d bose gas. *Journal of the Physical Society of Japan*, 84(6):064002, 2015.

[115] David B. Kaplan, Jong-Wan Lee, Dam T. Son, and Mikhail A. Stephanov. Conformality Lost. *Phys. Rev.*, D80:125005, 2009.

[116] Kenichi Kasamatsu, Ikuo Ichinose, and Tetsuo Matsui. Atomic quantum simulation of the lattice gauge-higgs model: Higgs couplings and emergence of exact local gauge symmetry. *Phys. Rev. Lett.*, 111:115303, Sep 2013.

[117] V Kasper, F Hebenstreit, F Jendrzejewski, M K Oberthaler, and J Berges. Implementing quantum electrodynamics with ultracold atomic systems. *New Journal of Physics*, 19(2):023030, 2017.

[118] Adam M. Kaufman, M. Eric Tai, Alexander Lukin, Matthew Rispoli, Robert Schittko, Philipp M. Preiss, and Markus Greiner. Quantum thermalization through entanglement in an isolated many-body system. *Science*, 353(6301):794–800, 2016.

[119] Ehsan Khatami, Guido Pupillo, Mark Srednicki, and Marcos Rigol. Fluctuation-dissipation theorem in an isolated system of quantum dipolar bosons after a quench. *Phys. Rev. Lett.*, 111:050403, Jul 2013.

[120] Ehsan Khatami, Marcos Rigol, Armando Relaño, and Antonio M. García-García. Quantum quenches in disordered systems: Approach to thermal equilibrium without a typical relaxation time. *Phys. Rev. E*, 85:050102(R), May 2012.

[121] Hyungwon Kim, Tatsuhiko N. Ikeda, and David A. Huse. Testing whether all eigenstates obey the eigenstate thermalization hypothesis. *Phys. Rev. E*, 90:052105, Nov 2014.

[122] Andrew D. King, Juan Carrasquilla, Jack Raymond, Isil Ozfidan, Evgeny Andriyash, Andrew Berkley, Mauricio Reis, Trevor Lanting, Richard Harris, Fabio Altomare, Kelly Boothby, Paul I. Bunyk, Colin Enderud, Alexandre Frchette, Emile Hoskinson, Nicolas Ladizinsky, Travis Oh, Gabriel Poulin-Lamarre, Christopher Rich, Yuki Sato, Anatoly Yu Smirnov, Loren J. Swenson, Mark H. Volkmann, Jed Whittaker, Jason

Yao, Eric Ladizinsky, Mark W. Johnson, Jeremy Hilton, and Mohammad H. Amin. Observation of topological phenomena in a programmable lattice of 1,800 qubits. *Nature*, 560(7719):456–460, 2018.

[123] N. Klco, E. F. Dumitrescu, A. J. McCaskey, T. D. Morris, R. C. Pooser, M. Sanz, E. Solano, P. Lougovski, and M. J. Savage. Quantum-classical computation of schwinger model dynamics using quantum computers. *Phys. Rev. A*, 98:032331, Sep 2018.

[124] Igor R. Klebanov, Silviu S. Pufu, Subir Sachdev, and Benjamin R. Safdi. Entanglement Entropy of 3-d Conformal Gauge Theories with Many Flavors. *JHEP*, 05:036, 2012.

[125] John Kogut and Leonard Susskind. Hamiltonian formulation of wilson's lattice gauge theories. *Phys. Rev. D*, 11:395–408, Jan 1975.

[126] John B. Kogut. An introduction to lattice gauge theory and spin systems. *Rev. Mod. Phys.*, 51:659–713, Oct 1979.

[127] John B. Kogut. The lattice gauge theory approach to quantum chromodynamics. *Rev. Mod. Phys.*, 55:775–836, Jul 1983.

[128] Corinna Kollath, Guillaume Roux, Giulio Biroli, and Andreas M Luchli. Statistical properties of the spectrum of the extended bose–hubbard model. *Journal of Statistical Mechanics: Theory and Experiment*, 2010(08):P08011, aug 2010.

[129] V. E. Korepin. Universality of entropy scaling in one dimensional gapless models. *Phys. Rev. Lett.*, 92:096402, Mar 2004.

[130] J. M. Kosterlitz and D. J. Thouless. Ordering, metastability and phase transitions in two-dimensional systems. *Journal of Physics C Solid State Physics*, 6:1181–1203, April 1973.

[131] T. D. Kühner and H. Monien. Phases of the one-dimensional bose-hubbard model. *Phys. Rev. B*, 58:R14741–R14744, Dec 1998.

[132] A. B. Kuklov and B. V. Svistunov. Counterflow superfluidity of two-species ultracold atoms in a commensurate optical lattice. *Phys. Rev. Lett.*, 90:100401, Mar 2003.

[133] Anatoly Kuklov, Nikolay Prokof'ev, and Boris Svistunov. Commensurate Two-Component Bosons in an Optical Lattice: Ground State Phase Diagram. *Phys. Rev. Lett.*, 92(5):050402, February 2004.

[134] Yoshihito Kuno, Kenichi Kasamatsu, Yoshiro Takahashi, Ikuo Ichinose, and Tetsuo Matsui. Real-time dynamics and proposal for feasible experiments of lattice gauge–higgs model simulated by cold atoms. *New Journal of Physics*, 17(6):063005, jun 2015.

[135] Yoshihito Kuno, Shinya Sakane, Kenichi Kasamatsu, Ikuo Ichinose, and Tetsuo Matsui. Quantum simulation of $(1+1)$-dimensional u(1) gauge-higgs model on a lattice by cold bose gases. *Phys. Rev. D*, 95:094507, May 2017.

[136] Julius Kuti. The Higgs particle and the lattice. *PoS*, KMI2013:002, 2015.

[137] C. Laflamme, W. Evans, M. Dalmonte, U. Gerber, H. Mej??a-D??az, W. Bietenholz, U. J. Wiese, and P. Zoller. $\mathbb{C}$P(N???1) quantum field theories with alkaline-earth atoms in optical lattices. *Annals Phys.*, 370:117–127, 2016.

[138] J. I. Latorre, E. Rico, and G. Vidal. Ground state entanglement in quantum spin chains. *Quantum Info. Comput.*, 4(1):48–92, January 2004.

[139] P Lee, M Anderlini, B Brown, J Sebby-Strabley, W Phillips, and J Porto. Sublattice Addressing and Spin-Dependent Motion of Atoms in a Double-Well Lattice. *Phys. Rev. Lett.*, 99(2):020402, July 2007.

[140] Maciej Lewenstein, Anna Sanpera, Veronica Ahufinger, Bogdan Damski, Aditi Sen(De), and Ujjwal Sen. Ultracold atomic gases in optical lattices: mimicking condensed matter physics and beyond. *Advances in Physics*, 56(2):243–379, 2007.

[141] Noah Linden, Sandu Popescu, Anthony J. Short, and Andreas Winter. Quantum mechanical evolution towards thermal equilibrium. *Phys. Rev. E*, 79:061103, Jun 2009.

[142] Yuzhi Liu, Y. Meurice, M. P. Qin, J. Unmuth-Yockey, T. Xiang, Z. Y. Xie, J. F. Yu, and Haiyuan Zou. Exact blocking formulas for spin and gauge models. *Phys. Rev. D*, 88:056005, Sep 2013.

[143] E. Y. Loh, J. E. Gubernatis, R. T. Scalettar, S. R. White, D. J. Scalapino, and R. L. Sugar. Sign problem in the numerical simulation of many-electron systems. *Phys. Rev. B*, 41:9301–9307, May 1990.

[144] M. Lu, N. Q. Burdick, and B. L. Lev. Quantum Degenerate Dipolar Fermi Gas. *Physical Review Letters*, 108(21):215301, May 2012.

[145] M. Lu, N. Q. Burdick, S. H. Youn, and B. L. Lev. Strongly Dipolar Bose-Einstein Condensate of Dysprosium. *Physical Review Letters*, 107(19):190401, November 2011.

[146] Tsung-Cheng Lu and Tarun Grover. Renyi entropy of chaotic eigenstates. *Phys. Rev. E*, 99:032111, Mar 2019.

[147] David J. Luitz and Yevgeny Bar Lev. Anomalous thermalization in ergodic systems. *Phys. Rev. Lett.*, 117:170404, Oct 2016.

[148] Michele Maggiore. *A modern introduction to quantum field theory*, volume 12. Oxford university press, 2005.

[149] Stephan Mandt, Akos Rapp, and Achim Rosch. Interacting fermionic atoms in optical lattices diffuse symmetrically upwards and downwards in a gravitational potential. *Physical Review Letters*, 106:250602, Jun 2011.

[150] Esteban A Martinez, Christine A Muschik, Philipp Schindler, Daniel Nigg, Alexander Erhard, Markus Heyl, Philipp Hauke, Marcello Dalmonte, Thomas Monz, Peter Zoller, and Rainer Blatt. Real-time dynamics of lattice gauge theories with a few-qubit quantum computer. *Nature*, 534:516, jun 2016.

[151] Leonardo Mazza, Davide Rossini, Rosario Fazio, and Manuel Endres. Detecting two-site spin-entanglement in many-body systems with local particle-number fluctuations. *New Journal of Physics*, 17(1):013015, 2015.

[152] G. Mazzarella, S. M. Giampaolo, and F. Illuminati. Extended bose hubbard model of interacting bosonic atoms in optical lattices: From superfluidity to density waves. *Phys. Rev. A*, 73:013625, Jan 2006.

[153] Ian P McCulloch. From density-matrix renormalization group to matrix product states. *Journal of Statistical Mechanics: Theory and Experiment*, 2007(10):P10014–P10014, oct 2007.

[154] D McKay and B DeMarco. Thermometry with spin-dependent lattices. *New J. Phys.*, 12(5):055013, May 2010.

[155] Patrick Medley, David M. Weld, Hirokazu Miyake, David E. Pritchard, and Wolfgang Ketterle. Spin gradient demagnetization cooling of ultracold atoms. *Phys. Rev. Lett.*, 106:195301, May 2011.

[156] Madan Lal Mehta. *Random matrices*, volume 142. Elsevier, 2004.

[157] Y. Meurice. Accurate exponents from approximate tensor renormalizations. *Phys. Rev. B*, 87:064422, Feb 2013.

[158] A. Minguzzi and D. M. Gangardt. Exact coherent states of a harmonically confined tonks-girardeau gas. *Phys. Rev. Lett.*, 94:240404, Jun 2005.

[159] Rubem Mondaini, Keith R. Fratus, Mark Srednicki, and Marcos Rigol. Eigenstate thermalization in the two-dimensional transverse field ising model. *Phys. Rev. E*, 93:032104, Mar 2016.

[160] Rubem Mondaini and Marcos Rigol. Eigenstate thermalization in the two-dimensional transverse field ising model. ii. off-diagonal matrix elements of observables. *Phys. Rev. E*, 96:012157, Jul 2017.

[161] I. Montvay and G. Munster. *Quantum fields on a lattice*. Cambridge Monographs on Mathematical Physics. Cambridge University Press, 1997.

[162] István Montvay and Gernot Münster. *Quantum fields on a lattice*. Cambridge University Press, 1997.

[163] Takashi Mori, Tatsuhiko N Ikeda, Eriko Kaminishi, and Masahito Ueda. Thermalization and prethermalization in isolated quantum systems: a theoretical overview. *Journal of Physics B: Atomic, Molecular and Optical Physics*, 51(11):112001, may 2018.

[164] C. Moura Alves and D. Jaksch. Multipartite entanglement detection in bosons. *Phys. Rev. Lett.*, 93:110501, Sep 2004.

[165] Clemens Neuenhahn and Florian Marquardt. Thermalization of interacting fermions and delocalization in fock space. *Phys. Rev. E*, 85:060101(R), Jun 2012.

[166] K.-K. Ni, S. Ospelkaus, M. H. G. de Miranda, A. Pe'er, B. Neyenhuis, J. J. Zirbel, S. Kotochigova, P. S. Julienne, D. S. Jin, and J. Ye. A High Phase-Space-Density Gas of Polar Molecules. *Science*, 322:231–, October 2008.

[167] Jae Dong Noh, Eiki Iyoda, and Takahiro Sagawa. Heating and Cooling of Quantum Gas by Eigenstate Joule Expansion. *arXiv e-prints*, page arXiv:1811.10051, Nov 2018.

[168] Ahmed Omran, Martin Boll, Timon A. Hilker, Katharina Kleinlein, Guillaume Salomon, Immanuel Bloch, and Christian Gross. Microscopic observation of pauli blocking in degenerate fermionic lattice gases. *Phys. Rev. Lett.*, 115:263001, Dec 2015.

[169] Stellan Östlund and Stefan Rommer. Thermodynamic limit of density matrix renormalization. *Phys. Rev. Lett.*, 75:3537–3540, Nov 1995.

[170] Maxwell F. Parsons, Florian Huber, Anton Mazurenko, Christie S. Chiu, Widagdo Setiawan, Katherine Wooley-Brown, Sebastian Blatt, and Markus Greiner. Site-resolved imaging of fermionic ^{6}Li in an optical lattice. *Phys. Rev. Lett.*, 114:213002, May 2015.

[171] Pierre Pfeuty. The one-dimensional ising model with a transverse field. *Ann. Phys.*, 57(1):79–90, 1970.

[172] H. Pichler, L. Bonnes, A. J. Daley, A. M. Läuchli, and P. Zoller. Thermal versus entanglement entropy: a measurement protocol for fermionic atoms with a quantum gas microscope. *New Journal of Physics*, 15(6):063003, June 2013.

[173] H. Pichler, A. J. Daley, and P. Zoller. Nonequilibrium dynamics of bosonic atoms in optical lattices: Decoherence of many-body states due to spontaneous emission. *Phys. Rev. A*, 82:063605, Dec 2010.

[174] A. M. Polyakov. *Gauge Fields and Strings*. Contemporary concepts in physics. Taylor & Francis, 1987.

[175] Lev Semenovich Pontryagin. Topological groups. 1946.

[176] G. Pupillo, A. Micheli, M. Boninsegni, I. Lesanovsky, and P. Zoller. Strongly correlated gases of rydberg-dressed atoms: Quantum and classical dynamics. *Phys. Rev. Lett.*, 104:223002, Jun 2010.

[177] Stephan Rachel, Nicolas Laflorencie, H. Francis Song, and Karyn Le Hur. Detecting quantum critical points using bipartite fluctuations. *Phys. Rev. Lett.*, 108:116401, Mar 2012.

[178] Marcos Rigol. Quantum quenches and thermalization in one-dimensional fermionic systems. *Phys. Rev. A*, 80:053607, Nov 2009.

[179] Marcos Rigol, Vanja Dunjko, and Maxim Olshanii. Thermalization and its mechanism for generic isolated quantum systems. *Nature*, 452:854, apr 2008.

[180] Marcos Rigol and Mattias Fitzpatrick. Initial-state dependence of the quench dynamics in integrable quantum systems. *Phys. Rev. A*, 84:033640, Sep 2011.

[181] Marcos Rigol and Alejandro Muramatsu. Emergence of quasicondensates of hard-core bosons at finite momentum. *Phys. Rev. Lett.*, 93:230404, Dec 2004.

[182] Marcos Rigol and Alejandro Muramatsu. Fermionization in an expanding 1d gas of hard-core bosons. *Phys. Rev. Lett.*, 94:240403, Jun 2005.

[183] MARCOS RIGOL and ALEJANDRO MURAMATSU. Free expansion of impenetrable bosons on one-dimensional optical lattices. *Modern Physics Letters B*, 19(18):861–881, 2005.

[184] Marcos Rigol and Mark Srednicki. Alternatives to eigenstate thermalization. *Phys. Rev. Lett.*, 108:110601, Mar 2012.

[185] J. P. Ronzheimer, M. Schreiber, S. Braun, S. S. Hodgman, S. Langer, I. P. McCulloch, F. Heidrich-Meisner, I. Bloch, and U. Schneider. Expansion dynamics of interacting bosons in homogeneous lattices in one and two dimensions. *Phys. Rev. Lett.*, 110:205301, May 2013.

[186] Heinz J Rothe. *Lattice Gauge Theories: An Introduction Third Edition*, volume 74. World Scientific Publishing Company, 2005.

[187] S. Sachdev. *Quantum phase transitions*. Cambridge University Press, second ed. edition, 2011.

[188] M. Saffman, T. G. Walker, and K. Mølmer. Quantum information with rydberg atoms. *Rev. Mod. Phys.*, 82:2313–2363, Aug 2010.

[189] Anders W. Sandvik. Computational studies of quantum spin systems. *AIP Conference Proceedings*, 1297(1):135–338, 2010.

[190] Lea F. Santos and Marcos Rigol. Localization and the effects of symmetries in the thermalization properties of one-dimensional quantum systems. *Phys. Rev. E*, 82:031130, Sep 2010.

[191] Lea F. Santos and Marcos Rigol. Onset of quantum chaos in one-dimensional bosonic and fermionic systems and its relation to thermalization. *Phys. Rev. E*, 81:036206, Mar 2010.

[192] Bodhaditya Santra, Christian Baals, Ralf Labouvie, Aranya B. Bhattacherjee, Axel Pelster, and Herwig Ott. Measuring finite-range phase coherence in an optical lattice using Talbot interferometry. *Nat. Commun.*, 8:15601, 2017.

[193] Robert Savit. Duality in field theory and statistical systems. *Rev. Mod. Phys.*, 52:453–487, Apr 1980.

[194] V W Scarola and S D Sarma. Quantum phases of the extended Bose-Hubbard Hamiltonian: Possibility of a supersolid state of cold atoms in optical lattices. *Phys. Rev. Lett.*, 95(3):033003, 2005.

[195] Johannes Schachenmayer, Lode Pollet, Matthias Troyer, and Andrew J. Daley. Thermalization of strongly interacting bosons after spontaneous emissions in optical lattices. *EPJ Quantum Technology*, 2(1):1, Jan 2015.

[196] S. Scherg, T. Kohlert, J. Herbrych, J. Stolpp, P. Bordia, U. Schneider, F. Heidrich-Meisner, I. Bloch, and M. Aidelsburger. Nonequilibrium mass transport in the 1d fermi-hubbard model. *Phys. Rev. Lett.*, 121:130402, Sep 2018.

[197] Ulrich Schollwck. The density-matrix renormalization group in the age of matrix product states. *Annals of Physics*, 326(1):96 – 192, 2011. January 2011 Special Issue.

[198] J. Sebby-Strabley, M. Anderlini, P. S. Jessen, and J. V. Porto. Lattice of double wells for manipulating pairs of cold atoms. *Phys. Rev. A*, 73:033605, Mar 2006.

[199] Daniel Shanks. Non-linear transformations of divergent and slowly convergent sequences. *Journal of Mathematics and Physics*, 34(1-4):1–42, 1955.

[200] Jonathan Simon, Waseem S. Bakr, Ruichao Ma, M. Eric Tai, Philipp M. Preiss, and Markus Greiner. Quantum simulation of antiferromagnetic spin chains in an optical lattice. *Nature*, 472(7343):307–312, 2011.

[201] Jan Smit. *Introduction to quantum fields on a lattice.* Cambridge University Press, 2002.

[202] P Soltan-Panahi, J Struck, P Hauke, A Bick, W Plenkers, G Meineke, C Becker, P Windpassinger, M Lewenstein, and K Sengstock. Multi-component quantum gases in spin-dependent hexagonal lattices. *Nat Phys*, 7(5):434–440, May 2011.

[203] S. Sorg, L. Vidmar, L. Pollet, and F. Heidrich-Meisner. Relaxation and thermalization in the one-dimensional bose-hubbard model: A case study for the interaction quantum quench from the atomic limit. *Phys. Rev. A*, 90:033606, Sep 2014.

[204] S. Sotiriadis, P. Calabrese, and J. Cardy. Quantum quench from a thermal initial state. *EPL (Europhysics Letters)*, 87(2):20002, jul 2009.

[205] Tomasz Sowiński and Miguel Á. García-March. One-dimensional mixtures of several ultracold atoms: a review. *arXiv e-prints*, page arXiv:1903.12189, Mar 2019.

[206] Mark Srednicki. The approach to thermal equilibrium in quantized chaotic systems. *Journal of Physics A: Mathematical and General*, 32(7):1163–1175, jan 1999.

[207] L. Tagliacozzo, A. Celi, A. Zamora, and M. Lewenstein. Optical abelian lattice gauge theories. *Annals of Physics*, 330:160 – 191, 2013.

[208] Yijun Tang, Nathaniel Q Burdick, Kristian Baumann, and Benjamin L Lev. Bose–einstein condensation of162dy and160dy. *New Journal of Physics*, 17(4):045006, apr 2015.

[209] G. Thalhammer, G. Barontini, L. De Sarlo, J. Catani, F. Minardi, and M. Inguscio. Double species bose-einstein condensate with tunable interspecies interactions. *Phys. Rev. Lett.*, 100:210402, May 2008.

[210] C Trefzger, C Menotti, and M Lewenstein. Pair-Supersolid Phase in a Bilayer System of Dipolar Lattice Bosons. *Phys. Rev. Lett.*, 103(3):035304, July 2009.

[211] S. Trotzky, Y-A. Chen, I. P. McCulloch, U. Schollwöck, J. Eisert, and I. Bloch. Probing the relaxation towards equilibrium in an isolated strongly correlated one-dimensional bose gas. *Nat. Phys.*, 8:325–330, 2012.

[212] S. Trotzky, L. Pollet, F. Gerbier, U. Schnorrberger, I. Bloch, N. V. Prokof'ev, B. Svistunov, and M. Troyer. Suppression of the critical temperature for superfluidity near the mott transition. *Nature Physics*, 6:998 EP –, 10 2010.

[213] J. Unmuth-Yockey, Jin Zhang, A. Bazavov, Y. Meurice, and S.-W. Tsai. Universal features of the abelian polyakov loop in $1+1$ dimensions. *Phys. Rev. D*, 98:094511, Nov 2018.

[214] J. Unmuth-Yockey, Jin Zhang, P. M. Preiss, Li-Ping Yang, S.-W. Tsai, and Y. Meurice. Probing the conformal calabrese-cardy scaling with cold atoms. *Phys. Rev. A*, 96:023603, Aug 2017.

[215] Judah F. Unmuth-Yockey. Gauge-invariant rotor hamiltonian from dual variables of 3d $u(1)$ gauge theory. *Phys. Rev. D*, 99:074502, Apr 2019.

[216] Judah Francis Unmuth-Yockey. Duality methods and the tensor renormalization group: applications to quantum simulation. 2017.

[217] Varun D. Vaidya, Yudan Guo, Ronen M. Kroeze, Kyle E. Ballantine, Alicia J. Kollár, Jonathan Keeling, and Benjamin L. Lev. Tunable-range, photon-mediated atomic interactions in multimode cavity qed. *Phys. Rev. X*, 8:011002, Jan 2018.

[218] G. Vidal, J. I. Latorre, E. Rico, and A. Kitaev. Entanglement in quantum critical phenomena. *Phys. Rev. Lett.*, 90:227902, Jun 2003.

[219] L. Vidmar, S. Langer, I. P. McCulloch, U. Schneider, U. Schollwöck, and F. Heidrich-Meisner. Sudden expansion of mott insulators in one dimension. *Phys. Rev. B*, 88:235117, Dec 2013.

[220] L. Vidmar, J. P. Ronzheimer, M. Schreiber, S. Braun, S. S. Hodgman, S. Langer, F. Heidrich-Meisner, I. Bloch, and U. Schneider. Dynamical quasicondensation of hard-core bosons at finite momenta. *Phys. Rev. Lett.*, 115:175301, Oct 2015.

[221] Lev Vidmar, Deepak Iyer, and Marcos Rigol. Emergent eigenstate solution to quantum dynamics far from equilibrium. *Phys. Rev. X*, 7:021012, Apr 2017.

[222] Lev Vidmar, Wei Xu, and Marcos Rigol. Emergent eigenstate solution and emergent gibbs ensemble for expansion dynamics in optical lattices. *Phys. Rev. A*, 96:013608, Jul 2017.

[223] J. von Neumann. Proof of the ergodic theorem and the h-theorem in quantum mechanics. *The European Physical Journal H*, 35(2):201–237, Nov 2010.

[224] Hendrik Weimer, Markus Müller, Igor Lesanovsky, Peter Zoller, and Hans Peter Büchler. A Rydberg quantum simulator. *Nature Physics*, 6:382, mar 2010.

[225] Christof Weitenberg, Manuel Endres, Jacob F. Sherson, Marc Cheneau, Peter Schauß, Takeshi Fukuhara, Immanuel Bloch, and Stefan Kuhr. Single-spin addressing in an atomic mott insulator. *Nature*, 471(7338):319–324, 2011.

[226] Steven R. White. Density matrix formulation for quantum renormalization groups. *Phys. Rev. Lett.*, 69:2863–2866, Nov 1992.

[227] Steven R. White. Density-matrix algorithms for quantum renormalization groups. *Phys. Rev. B*, 48:10345–10356, Oct 1993.

[228] Steven R. White. Density matrix renormalization group algorithms with a single center site. *Phys. Rev. B*, 72:180403, Nov 2005.

[229] U.-J. Wiese. Ultracold quantum gases and lattice systems: quantum simulation of lattice gauge theories. *Annalen der Physik*, 525(10-11):777–796, 2013.

[230] Kenneth G. Wilson. Confinement of quarks. *Phys. Rev. D*, 10:2445–2459, Oct 1974.

[231] C.-H. Wu, J. W. Park, P. Ahmadi, S. Will, and M. W. Zwierlein. Ultracold Fermionic Feshbach Molecules of Na23K40. *Physical Review Letters*, 109(8):085301, August 2012.

[232] J. C. Xavier and F. C. Alcaraz. Rényi entropy and parity oscillations of anisotropic spin-s heisenberg chains in a magnetic field. *Phys. Rev. B*, 83:214425, Jun 2011.

[233] Lin Xia, Laura A Zundel, Juan Carrasquilla, Aaron Reinhard, Joshua M Wilson, Marcos Rigol, and David S Weiss. Quantum distillation and confinement of vacancies in a doublon sea. *Nature Physics*, 11:316, feb 2015.

[234] Z. Y. Xie, J. Chen, M. P. Qin, J. W. Zhu, L. P. Yang, and T. Xiang. Coarse-graining renormalization by higher-order singular value decomposition. *Phys. Rev. B*, 86:045139, Jul 2012.

[235] Wei Xu and Marcos Rigol. Expansion of one-dimensional lattice hard-core bosons at finite temperature. *Phys. Rev. A*, 95:033617, Mar 2017.

[236] Li-Ping Yang, Yuzhi Liu, Haiyuan Zou, Z. Y. Xie, and Y. Meurice. Fine structure of the entanglement entropy in the o(2) model. *Phys. Rev. E*, 93:012138, Jan 2016.

[237] Toru Yoshizawa, Eiki Iyoda, and Takahiro Sagawa. Numerical large deviation analysis of the eigenstate thermalization hypothesis. *Phys. Rev. Lett.*, 120:200604, May 2018.

[238] J. F. Yu, Z. Y. Xie, Y. Meurice, Yuzhi Liu, A. Denbleyker, Haiyuan Zou, M. P. Qin, J. Chen, and T. Xiang. Tensor renormalization group study of classical xy model on the square lattice. *Phys. Rev. E*, 89:013308, Jan 2014.

[239] Johannes Zeiher, Rick van Bijnen, Peter Schauß, Sebastian Hild, Jae-yoon Choi, Thomas Pohl, Immanuel Bloch, and Christian Gross. Many-body interferometry of a rydberg-dressed spin lattice. *Nat. Phys.*, 12(12):1095–1099, 2016.

[240] J. M. Zhang, C. Shen, and W. M. Liu. Quantum quench dynamics of the bose-hubbard model at finite temperatures. *Phys. Rev. A*, 83:063622, Jun 2011.

[241] Jin Zhang, J. Unmuth-Yockey, J. Zeiher, A. Bazavov, S.-W. Tsai, and Y. Meurice. Quantum simulation of the universal features of the polyakov loop. *Phys. Rev. Lett.*, 121:223201, Nov 2018.

[242] Erez Zohar and Michele Burrello. Formulation of lattice gauge theories for quantum simulations. *Phys. Rev. D*, 91:054506, Mar 2015.

[243] Erez Zohar, J. Ignacio Cirac, and Benni Reznik. Simulating compact quantum electrodynamics with ultracold atoms: Probing confinement and nonperturbative effects. *Phys. Rev. Lett.*, 109:125302, Sep 2012.

[244] Erez Zohar, J. Ignacio Cirac, and Benni Reznik. Cold-atom quantum simulator for su(2) yang-mills lattice gauge theory. *Phys. Rev. Lett.*, 110:125304, Mar 2013.

[245] Erez Zohar, J Ignacio Cirac, and Benni Reznik. Quantum simulations of lattice gauge theories using ultracold atoms in optical lattices. *Reports on Progress in Physics*, 79(1):014401, dec 2015.

[246] Erez Zohar, J. Ignacio Cirac, and Benni Reznik. Quantum Simulations of Lattice Gauge Theories using Ultracold Atoms in Optical Lattices. *Rep. Prog. Phys.*, 79(1):014401, 2016.

[247] Erez Zohar and Benni Reznik. Confinement and lattice quantum-electrodynamic electric flux tubes simulated with ultracold atoms. *Phys. Rev. Lett.*, 107:275301, Dec 2011.

[248] Haiyuan Zou, Yuzhi Liu, Chen-Yen Lai, J. Unmuth-Yockey, Li-Ping Yang, A. Bazavov, Z. Y. Xie, T. Xiang, S. Chandrasekharan, S.-W. Tsai, and Y. Meurice. Progress towards quantum simulating the classical O(2) model. *Phys. Rev. A*, 90:063603, Dec 2014.

Appendix A

Experimental implementations for the two-species Bose-Hubbard model

In this appendix, we discuss a few not fully developed proposals for the practical experimental implementations for the two-species Bose-Hubbard model. It contains questions we we still need to confirm. We consider $V_{ab} = 0$ in the following discussion. We propose to use three candidate systems for realizing the effective Hamiltonians: (A) two different atomic species, such as ^{87}Rb and ^{41}K, (B) a single atomic species in two different hyperfine states, and (C) a ladder system, so that the two species of bosons correspond to a single boson species being in either of the two legs of the ladder. We conclude this section with a discussion of the best option for each case (O(2) and Abelian Higgs).

A.1 ^{87}Rb - ^{41}K mixtures on an optical lattice

For quantum simulating the O(2) model, a ^{87}Rb and ^{41}K Bose-Bose mixture can be used. Due to the physical nature of the different atoms, the hopping amplitudes (t_a, t_b) are different to begin with, as well as the intraspecies interactions (U_a, U_b). In addition, species-dependent optical lattices [139, 3, 154, 202, 15] are widely used in boson systems, which allows the hopping amplitudes of each individual species to be further tuned to some extent. An interspecies Feshbach resonance is accessible [41, 209] and can be used to vary the interspecies interaction (W). The most difficult parameter to achieve may be the extended repulsion, V_α. A nearest-neighbor repulsion is however present, albeit small, when we consider Wannier Gaussian wave functions centered on nearby lattice sites according to previous study [152]. Other proposals may be explored, such as by using dipolar bosons [210], or by pumping bosons to higher Bloch bands [194] in order to engineer the nearest neighbor interaction. An schematic of this set-up is illustrated in Fig. A.1. It is important to have the on-site interactions U_α significantly larger than the temperature. For the mixture considered here the temperature and recoil energies are of the order of 100nK and values of U 10-20 times larger can typically be reached [209, 42, 22]. This implementation can not be used to quantum simulate the Abelian Higgs model since the on-site species conversion term t_{ab} can not be created.

The requirement of small repulsive nearest-neighbor intra-species repulsions V_a and V_b seems to be the main challenge for implementing the effective Bose-Hubbard Hamiltonian. Ref. [152] considers atoms with contact interactions in the presence of the lattice and the overall trap potentials and the Wannier functions, and calculates that the nearest-neighbor

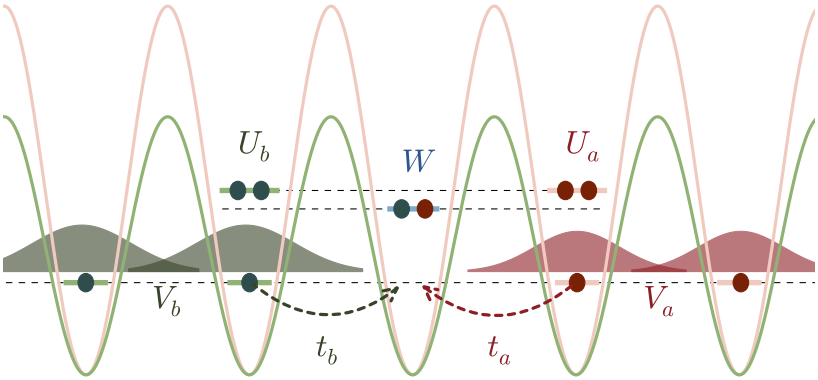

Figure A.1: (Color Online) Two-species (green and red) of bosons on species-dependent optical lattices (with the same color), taken from [248].

interaction strength goes as $\epsilon^2 U$, where U is the on-site interaction and ϵ is called lattice attenuation factor, also referred to as direct exchange or overlap.

For our mapping from the Bose-Hubbard Hamiltonian to the spin-1 Hamiltonian to work, we need to be in the strong coupling limit. It seems an 8 recoil-energy lattice (about the point insulator physics starts), $\epsilon = 10^{-3}$, and therefore $V \simeq \epsilon^2 U \simeq 10^{-6} U$. Now, for O(2), we need $t_\alpha = \sqrt{V_\alpha U/2}$, so this would give $t \simeq 10^{-3} U$, or $U \simeq 1000t$. This is probably problematic: It seems like once one fixes the depth of the lattice, all parameters (U, V, and t) are already fixed, so one may not be able to additionally tune things so that $t_\alpha = \sqrt{V_\alpha U/2}$. If we had only one species of bosons, then one could maybe additionally tune U via a Feshbach resonance, but we can not tune it for both species at the same time. If we want larger V, then we would need to have shallower lattices. It seems a 3.5 recoil lattice would give $\epsilon \simeq 10^{-2}$ which is so shallow that one is typically working with a superfluid. At 3.5 recoil one might even doubt the single-band approximation.

Another possible route for having a nearest-neighbor interaction V would be by using dipolar atoms or molecules. Experiments with ultra cold dipolar quantum gases have been performed with chromium [91], erbium [2, 1], and dysprosium [145, 144, 208], which have magnetic moments $6\mu_B$, $7\mu_B$ and $10\mu_B$, respectively, and with polar molecules, such as ^{40}K ^{87}Rb and ^{23}Na ^{40}K [166, 49, 231].Dipolar atoms and molecules tend to have very small dipole moments, the best case to date in K-Rb molecules in their molecular ground state. We think this is less than $0.01U$, but we would need to verify. A nearest-neighbor interaction $V = 0.01U$ would give $t = \sqrt{VU/2} = 0.07U$.

A final possible route for generating V would be to use atoms in higher orbitals[194]. Need to be looked into in more detail. Other atomic species to be considered for the two-species mixture include ^{7}Li, ^{133}Cs, ^{23}Na, and ^{39}K. This implementation, where the two species of bosons are two different types of atoms, does not allow for going between the O(2) and Abelian Higgs model within the same set-up, since it can not create the effective Hamiltonian for the Abelian Higgs.

A.2 Bosons in two hyperfine states

Mixtures of ^{87}Rb in $|F = 2, m_F = -1\rangle$ and $|F = 1, m_F = -1\rangle$ states have been produced in the quantum degenerate regime[94], and also $|F = 2, m_F = 2\rangle$ and $|F = 1, m_F = -1\rangle$ mixtures. When the Hamiltonian also possesses SU(2) symmetry, this system has been referred to as spin-half bosons[4]. Use of several hyperfine states and Raman laser couplings have been used to generate synthetic dimensions[43]. The use here of two internal states would correspond to a synthetic ladder[43].

For the **Abelian Higgs model**, the usual hopping terms t_a and t_b can be tuned to be negligibly small by increasing the optical lattice potential amplitude since the dependence is exponential. The on-site interactions (U_a, U_b, and W) are then the largest energy scales. The on-site conversion term t_{ab} can be achieved by direct microwave ("RF") coupling.

For the **O(2) model**, t_{ab} is not needed and t_a and t_b can be small and tuned to be $t_\alpha = \sqrt{V_\alpha U/2}$.

For the $|F = 2, m_F = -1\rangle$ and $|F = 1, m_F = -1\rangle$ mixture, the on-site interaction strengths are not exactly the same. They are found to be [94] U_a:W:U_b ratio equals 1.03:1:0.97. This is fine for us although having a/b symmetry in the model would have been nice. Other bosonic atoms for which mixtures of atoms in two hyperfine states can be prepared should also be considered, including particularly ^{23}Na.

A species-dependent potential can be used for each hyperfine state so that U_a and t_a can be tuned independently of U_b and t_b, and then the inter-species (W) can be further tuned by shifting the relative distance between the two lattices after the other parameters are fixed. One can imagine starting with a 3D lattice potential, with two directions (call them X and Y) very strong, to give a series of 1D lattices along Z with strong hopping strengths. Along X and Y, the hopping strength can be made negligible. Now one could allow atoms to be in two hyperfine states (e.g. for ^{87}Rb, $F = 1$, m_F=-1,+1) - to separate sites along, say, X, one can make the lattice beams along that direction have an angle between their polarizations - this makes the light have a weak modulation of its polarization along X, going back and forth between more circular with one handedness, than the other. The two internal states' light shifts are differently sensitive to the two polarizations, and

this gives a weak physical separation between the potential minima. If the separation is made comparable to the Wannier wavepacket size (harmonic oscillator length), W can be tuned. V would naturally be much smaller. This candidate system also in principle allows for simulating both models (O(2) and Abelian Higgs) with the same set-up by tuning the parameters accordingly.

Also here there is the issue of the small nearest-neighbor interaction V that is needed. Again, this seems to be the main problem. For $O(2)$ it needs to be repulsive and the hopping tuned such that $t = \sqrt{VU/2}$. For the Abelian Higgs, it needs to be attractive, but no further fine-tuning is required.

A.3 Ladder systems with double-well potentials

The two-species Bose-Hubbard model could be realized with a single type of bosonic atom loaded on a ladder structure with a and b corresponding to the two legs of the ladder. Ladder systems have been realized experimentally by using lattices of double wells [198, 74, 45, 88, 5].

For the **Abelian Higgs model**, $t_a = t_b = 0$ and $t_{ab} \neq 0$ is required. The hopping amplitudes can be tuned such that the hopping in the direction along the ladder is negligible, but finite along the rungs, thus exchanging a, b species index at the same rung.

The problem of V. An attractive intraspecies nearest-neighbor interaction ($V_a = V_b = -\tilde{Y}/2$) is also needed for the Abelian Higgs model, favoring having two atoms in neighboring sides on the same leg of the ladder. This acts as a nearest-neighbor ferromagnetic coupling in the effective one-dimensional spin chain Hamiltonian. For the experimental implementation,

an attractive nearest neighbor interaction may be obtained by using cold dipolar atoms or molecules, with dipole moments aligned along the ladder and with inter-rung distance such that the rapidly decaying dipole-dipole interaction between next-nearest-neighbors can be neglected. With this alignment of the moments, the inter-species interaction in the same rung (W) is repulsive, which is also what we need for our perturbation expansion.

For the **O(2) model**, the requirement is $t_\alpha = \sqrt{V_\alpha U/2} \ll U$ and $t_{ab} = 0$. Experimentally, this corresponds to increasing the barrier of the individual double well potential, but allowing weak hopping along the ladder. The nearest-neighbor interaction V would be either from small contribution from expansion in terms of Wannier functions as claimed in Ref. [152], or using a dipolar gas with the dipole moments all aligned perpendicular to the direction of the ladder so that the interaction is repulsive. The spatial separations would have to be such that dipole-dipole interaction does not give significant next-nearest-neighbor interactions, which are not present in our study. There may be a major challenge here which is that in our perturbation expansion we consider also a strong inter-species on-site interaction W, besides the strong intra-species on-site interaction U. In this set-up, W corresponds to interaction of particles sitting in different minima of the same double well potential, so their interaction is going to be much weaker than the intra-species on-site interaction U for particles in the same minimum.

The rung length (distance between the two minima in the same double well potential) may be tuned to be much smaller than the inter-site distance (distance between two sites along the ladder) to minimize this problem but W would still be much smaller than U. Since the species index simply corresponds to the atoms being in one leg of the ladder

versus the other, some mapping techniques would be needed to make species-sensitive measurements, for example, the left well could be resonantly transferred to a separate internal state, and then a Stern-Gerlach field applied during time-of-flight. This candidate system also in principle allows for simulating both models (O(2) and Abelian Higgs) with the same set-up by tuning the parameters accordingly.

Appendix B

Perturbation theory for the two-species Bose-Hubbard model

In this appendix, we derive the effective spin Hamiltonian (3.2) from the original two-species Bose-Hubbard Hamiltonian (3.1) by the second order degenerate perturbation theory. A portion of these notes was initially written by Chen-Yen Lai, then our collaborators and I checked and generalized the results.

B.1 Some preliminaries

Here we collect some definitions to avoid confusion on summation notation, operator definitions, etc.

- A sum over nearest neighbors $\sum_{\langle ij \rangle}$ is understood as the first index, i, running over all sites and the second index, j, running over *all* neighbors (*i.e.* in the forward and backward directions) of the site i (here we consider a cubic lattice). Let d be the

number of dimensions and $\hat{\mu}_k$ is a unit vector in direction k, then

$$\sum_{\langle ij \rangle} \hat{O}_{ij} \equiv \sum_i \sum_{k=1}^{d} \sum_{j=i-\hat{\mu}_k}^{j=i+\hat{\mu}_k} \hat{O}_{ij}, \tag{B.1}$$

where $\hat{O}_{ij}$ is some object associated with a link, for instance, $\hat{O}_{ij} = a_i^\dagger a_j$ or a gauge field, living directly on the link. With such a convention each link enters in the sum twice, in positive and negative direction. For example, for sites 1 and 2 the sum contains $\hat{O}_{12} + \hat{O}_{21}$.

In the lattice gauge theory community it is customary to sum over links only in the forward direction, so the summation is typically:

$$\sum_i \sum_{k=1}^{d} O_{i,i+\hat{\mu}_k}. \tag{B.2}$$

- Let L_x, L_y, L_z be the components of the angular momentum operator. We define the raising and lowering operators as:

$$L^\pm = L_x \pm i L_y \tag{B.3}$$

Then the matrix element of the raising operator is defined as

$$\langle l, m | L^+ | l, m-1 \rangle = \sqrt{(l+m)(l-m+1)}. \tag{B.4}$$

This matches the convention of, for instance, Landau, Lifshitz, "Quantum Mechanics". Then

$$L^+ L^- = L_x^2 + L_y^2, \quad L^2 = L^+ L^- + L_z^2. \tag{B.5}$$

Also

$$L_i^+ L_j^- + L_i^- L_j^+ = 2(L_i^x L_j^x + L_i^y L_j^y). \tag{B.6}$$

B.2 Two-species Bose-Hubbard model under strong coupling expansion

In order to simulate a rotor model with positive and negative eigenvalue states, we consider a two-species Bose-Hubbard model with commensurate filling fraction $\sum_\alpha n^\alpha = n$ on each lattice site. The two-species Bose-Hubbard Hamiltonian ($\alpha = a, b$ indicates two different species, respectively) on square optical lattice reads

$$\begin{aligned} \mathcal{H} &= -\sum_{\langle ij\rangle}(t_a a_i^\dagger a_j + t_b b_i^\dagger b_j + h.c.) + \sum_{i,\alpha}\Delta_\alpha n_i^\alpha \\ &+ \frac{U_0}{2}\sum_i n_i^\alpha(n_i^\alpha - 1) + W\sum_i n_i^a n_i^b + \sum_{\langle ij\rangle\alpha} V_\alpha n_i^\alpha n_i^\alpha, \end{aligned} \tag{B.7}$$

with the number operator $n_i^a = a_i^\dagger a_i$ and $n_i^b = b_i^\dagger b_i$. The first term represents the kinetic energy (hopping). The second term is chemical potential and energy off-set of each species. The $U_0(W)$ is the on-site intra-species (inter-species) interaction, and V term is nearest neighbor interaction.

In the strong coupling limit, $|U_0|, |W| \gg t_\alpha$, the local interaction $U_0(W)$ allows us to choose the basis $|n_i^a, n_i^b\rangle$ with $n_i^a + n_i^b = n$, and treat the hopping terms as perturbation. Therefore, only a virtual process by exchanging particles between neighboring sites is allowed at second order.

$$\mathcal{H}_0 = \sum_{i,\alpha}\Delta_\alpha n_i^\alpha + \frac{U_0}{2}\sum_i n_i^\alpha(n_i^\alpha - 1) + W\sum_i n_i^a n_i^b + \sum_{\langle ij\rangle\alpha} V_\alpha n_i^\alpha n_i^\alpha, \tag{B.8}$$

$$\mathcal{H}_I = -\sum_{\langle ij\rangle}(t_a a_i^\dagger a_j + t_b b_i^\dagger b_j + h.c.). \tag{B.9}$$

Our vacuum on a pair is defined as $|n_i^a, n_i^b, n_j^a, n_j^b\rangle$ under constraint $n_i^a + n_i^b = n_j^a + n_j^b = n$. Therefore, we have $[2(\frac{n}{2}) + 1]^2$ basis states on a single link. We are going to show that this can be mapped onto a spin-$n/2$ model.

For simplicity, we use $n = 2$ in the following calculation. Of course, it can be generalized for arbitrary n. The nearly degenerate basis states are the following:

$$|2,0;2,0\rangle, |2,0;1,1\rangle, |2,0;0,2\rangle, |1,1;2,0\rangle, |1,1;1,1\rangle, |1,1;0,2\rangle, |0,2;2,0\rangle, |0,2;1,1\rangle, |0,2;0,2\rangle. \tag{B.10}$$

Later we will map these states onto the eigenstates of the angular momentum $L = 1$, respectively:

$$\begin{pmatrix} |l_1 = 1, m_1 = 1; l_2 = 1, m_2 = 1\rangle \\ |l_1 = 1, m_1 = 1; l_2 = 1, m_2 = 0\rangle \\ |l_1 = 1, m_1 = 1; l_2 = 1, m_2 = -1\rangle \\ |l_1 = 1, m_1 = 0; l_2 = 1, m_2 = 1\rangle \\ |l_1 = 1, m_1 = 0; l_2 = 1, m_2 = 0\rangle \\ |l_1 = 1, m_1 = 0; l_2 = 1, m_2 = -1\rangle \\ |l_1 = 1, m_1 = -1; l_2 = 1, m_2 = 1\rangle \\ |l_1 = 1, m_1 = -1; l_2 = 1, m_2 = 0\rangle \\ |l_1 = 1, m_1 = -1; l_2 = 1, m_2 = -1\rangle \end{pmatrix} \tag{B.11}$$

At the leading order, the energy spectrum is, $\mathcal{H}_0|vac_{link}\rangle = E_0|vac_{link}\rangle$:

$$E_0 = Diag\begin{pmatrix} 4\Delta_a + 2U_0 + 4V_a \\ 3\Delta_a + \Delta_b + U_0 + W + 2V_a \\ 2\Delta_a + 2\Delta_b + 2U_0 \\ 3\Delta_a + \Delta_b + U_0 + W + 2V_a \\ 2\Delta_a + 2\Delta_b + 2W + V_a + V_b \\ \Delta_a + 3\Delta_b + U_0 + W + 2V_b \\ 2\Delta_a + 2\Delta_b + 2U_0 \\ \Delta_a + 3\Delta_b + U_0 + W + 2V_b \\ 4\Delta_b + 2U_0 + 4V_b \end{pmatrix}, \quad |vac_{link}\rangle = \begin{pmatrix} |2,0;2,0\rangle \\ |2,0;1,1\rangle \\ |2,0;0,2\rangle \\ |1,1;2,0\rangle \\ |1,1;1,1\rangle \\ |1,1;0,2\rangle \\ |0,2;2,0\rangle \\ |0,2;1,1\rangle \\ |0,2;0,2\rangle \end{pmatrix} \tag{B.12}$$

Let's leave it here for now, and calculate the second order part.

The effective Hamiltonian on single link can be calculated as $\langle vac_{link}|\mathcal{H}_I(E_0 - \mathcal{H}_0)^{-1}\mathcal{H}_I|vac_{link}\rangle$. Therefore, from $(E_0 - \mathcal{H}_0)^{-1}\mathcal{H}_I|vac_{link}\rangle =$

$$\begin{pmatrix} \frac{-t_a\sqrt{6}}{-U_0+V_a}|3,0;1,0\rangle + \frac{-t_a\sqrt{6}}{-U_0+V_a}|1,0;3,0\rangle \\ \frac{-t_a\sqrt{3}}{-U_0-(U_0-W)+2V_a}|3,0;0,1\rangle + \frac{-t_b}{-U_0+(U_0-W)}|2,1;1,0\rangle + \frac{-t_a}{-U_0+(U_0-W)}\sqrt{4}|1,0;2,1\rangle \\ \frac{-t_b\sqrt{2}}{-U_0+2(U_0-W)-V_b}|2,1;0,1\rangle + \frac{-t_a\sqrt{2}}{-U_0+2(U_0-W)-V_a}|1,0;1,2\rangle \\ \frac{-t_a\sqrt{4}}{-U_0+(U_0-W)}|2,1;1,0\rangle + \frac{-t_a\sqrt{3}}{-U_0+(U_0-W)+2V_a}|0,1;3,0\rangle + \frac{-t_b}{-U_0+(U_0-W)}|1,0;2,1\rangle \\ \frac{-t_a\sqrt{2}}{-U_0+V_a}|0,1;2,1\rangle + \frac{-t_b\sqrt{2}}{-U_0+V_b}|1,0;1,2\rangle + \frac{-t_a\sqrt{2}}{-U_0+V_a}|2,1;0,1\rangle + \frac{-t_b\sqrt{2}}{-U_0+V_b}|1,2;1,0\rangle \\ \frac{-t_b\sqrt{4}}{-U_0+(U_0-W)}|1,2;0,1\rangle + \frac{-t_a}{-U_0+(U_0-W)}|0,1;1,2\rangle + \frac{-t_b\sqrt{3}}{-U_0+(U_0-W)+2V_b}|1,0;0,3\rangle \\ \frac{-t_b\sqrt{2}}{-U_0+2(U_0-W)-V_b}|0,1;2,1\rangle + \frac{-t_a\sqrt{2}}{-U_0+2(U_0-W)-V_a}|1,2;1,0\rangle \\ \frac{-t_b\sqrt{4}}{-U_0+(U_0-W)}|0,1;1,2\rangle + \frac{-t_a}{-U_0+(U_0-W)}|1,2;0,1\rangle + \frac{-t_b\sqrt{3}}{-U_0+(U_0-W)+2V_b}|0,3;1,0\rangle \\ \frac{-t_b\sqrt{6}}{-U_0+V_b}|0,3;0,1\rangle + \frac{-t_b\sqrt{6}}{-U_0+V_b}|0,1;0,3\rangle \end{pmatrix} \tag{B.13}$$

Furthermore, we assume $U_0 \gg (U_0 - W), V_\alpha$ to first order, thus the virtual process has a contribution proportional to $-t_\alpha t'_\alpha / U_0$. Also, we separate the total effective Hamiltonian of single link into diagonal (Dia) and off-diagonal (Off) part. The off-diagonal part contains only 8 elements:

$$\begin{aligned}
\mathcal{H}_{eff}^{Off} &= -4\frac{t_a t_b}{U_0}
\begin{pmatrix}
0 & 0 & 0 & 0 & 0 & 0 & 0 & 0 & 0 \\
0 & 0 & 0 & 1 & 0 & 0 & 0 & 0 & 0 \\
0 & 0 & 0 & 0 & 1 & 0 & 0 & 0 & 0 \\
0 & 1 & 0 & 0 & 0 & 0 & 0 & 0 & 0 \\
0 & 0 & 1 & 0 & 0 & 0 & 1 & 0 & 0 \\
0 & 0 & 0 & 0 & 0 & 0 & 0 & 1 & 0 \\
0 & 0 & 0 & 0 & 1 & 0 & 0 & 0 & 0 \\
0 & 0 & 0 & 0 & 0 & 1 & 0 & 0 & 0 \\
0 & 0 & 0 & 0 & 0 & 0 & 0 & 0 & 0
\end{pmatrix} \\
&= -2\frac{t_a t_b}{U_0}
\begin{pmatrix}
0 & 0 & 0 & 0 & 0 & 0 & 0 & 0 & 0 \\
0 & 0 & 0 & 2 & 0 & 0 & 0 & 0 & 0 \\
0 & 0 & 0 & 0 & 2 & 0 & 0 & 0 & 0 \\
0 & 2 & 0 & 0 & 0 & 0 & 0 & 0 & 0 \\
0 & 0 & 2 & 0 & 0 & 0 & 2 & 0 & 0 \\
0 & 0 & 0 & 0 & 0 & 0 & 0 & 2 & 0 \\
0 & 0 & 0 & 0 & 2 & 0 & 0 & 0 & 0 \\
0 & 0 & 0 & 0 & 0 & 2 & 0 & 0 & 0 \\
0 & 0 & 0 & 0 & 0 & 0 & 0 & 0 & 0
\end{pmatrix}
\end{aligned} \tag{B.14}$$

and the diagonal part results in, up to a constant $-4\frac{t_a^2}{U_0} - 4\frac{t_b^2}{U_0}$, $\mathcal{H}_{eff}^{Dia} =$

$$Diag\begin{pmatrix} -8\frac{|t_a|^2}{U} + 4\frac{|t_b|^2}{U} \\ -3\frac{|t_a|^2}{U} + 3\frac{|t_b|^2}{U} \\ 2\frac{|t_a|^2}{U} + 2\frac{|t_b|^2}{U} \\ -3\frac{|t_a|^2}{U} + 3\frac{|t_b|^2}{U} \\ 0 \\ 3\frac{|t_a|^2}{U} - 3\frac{|t_b|^2}{U} \\ 2\frac{|t_a|^2}{U} + 2\frac{|t_b|^2}{U} \\ 3\frac{|t_a|^2}{U} - 3\frac{|t_b|^2}{U} \\ 4\frac{|t_a|^2}{U} - 8\frac{|t_b|^2}{U} \end{pmatrix} = -3\left(\frac{|t_a|^2}{U} - \frac{|t_b|^2}{U}\right)\begin{pmatrix} 2 \\ 1 \\ 0 \\ 1 \\ 0 \\ -1 \\ 0 \\ -1 \\ -2 \end{pmatrix} - 2\left(\frac{|t_a|^2}{U} + \frac{|t_b|^2}{U}\right)\begin{pmatrix} 1 \\ 0 \\ -1 \\ 0 \\ 0 \\ 0 \\ -1 \\ 0 \\ 1 \end{pmatrix} \tag{B.15}$$

The total effective Hamiltonian can be written as $\mathcal{H}_{eff}^{link} = \mathcal{H}_{eff}^{Off} + \mathcal{H}_{eff}^{Dia} + \mathcal{H}_0^{link}$. Now, we need to go back to the H_0, and check its matrix elements from Eq. (B.12). By pulling out a constant term, $2\Delta_a + 2\Delta_b + 2W + V_a + V_b$, we arrive at

$$\begin{pmatrix} 2\Delta_a - 2\Delta_b + 2U_0 - 2W + 3V_a - V_b \\ \Delta_a - \Delta_b + U_0 - W + V_a - V_b \\ 2U_0 - 2W - V_a - V_b \\ \Delta_a - \Delta_b + U_0 - W + V_a - V_b \\ 0 \\ -\Delta_a + \Delta_b + U_0 - W - V_a + V_b \\ 2U_0 - 2W - V_a - V_b \\ -\Delta_a + \Delta_b + U_0 - W - V_a + V_b \\ -2\Delta_a + 2\Delta_b + 2U_0 - 2W - V_a + 3V_b \end{pmatrix}, \tag{B.16}$$

which can de re-written as

$$(\Delta_a - \Delta_b)\begin{pmatrix} 2 \\ 1 \\ 0 \\ 1 \\ 0 \\ -1 \\ 0 \\ -1 \\ -2 \end{pmatrix} + (U_0 - W)\begin{pmatrix} 2 \\ 1 \\ 2 \\ 1 \\ 0 \\ 1 \\ 2 \\ 1 \\ 2 \end{pmatrix} + (V_a + V_b)\begin{pmatrix} 1 \\ 0 \\ -1 \\ 0 \\ 0 \\ 0 \\ -1 \\ 0 \\ 1 \end{pmatrix} + (V_a - V_b)\begin{pmatrix} 2 \\ 1 \\ 0 \\ 1 \\ 0 \\ -1 \\ 0 \\ -1 \\ -2 \end{pmatrix} \tag{B.17}$$

From the explicit forms of matrices in Eqs. (B.14) and (B.17) we can deduce the angular momentum operators we can have. First, the off-diagonal part of the Hamiltonian connects only the states that differ by one unit of m for both sites. This can be achieved by

an operator $L_1^+ L_2^- + L_1^- L_2^+$. By explicit calculation (here $l_1 = l_2 = 1$, so we do not specify the l quantum number to save space) one can check, for instance, using Eq. (B.4):

$$\begin{aligned}(\text{raw} = 2, \text{col} = 4) &= \langle m_1 = 1; m_2 = 0 | L_1^+ L_2^- + L_1^- L_2^+ | m_1 = 0; m_2 = 1 \rangle \\ &= \langle m_1 = 1 | L_1^+ | m_1 = 0 \rangle \langle m_2 = 0 | L_2^- | m_2 = 1 \rangle = 2. \end{aligned} \tag{B.18}$$

Next, the diagonal matrix $(2, 1, 2, 1, 0, 1, 2, 1, 2)$ results from acting with $L_1^2 + L_2^2$, $(2, 1, 0, 1, 0, -1, 0, -1, -2)$ with $L_1^z + L_2^z$ and $(1, 0, -1, 0, 0, 0, -1, 0, 1)$ with $L_1^z L_2^z$.

Finally, we can write the effective Hamiltonian on single link with spin-1 operators as

$$\begin{aligned}\mathcal{H}_{eff}^{link} &= (V_a - \frac{2t_a^2}{U_0} + V_b - \frac{2t_b^2}{U_0}) L_1^z L_2^z + \frac{-2t_a t_b}{U_0}(L_1^+ L_2^- + L_1^- L_2^+) \\ &+ [(V_a + \Delta_a - \frac{3t_a^2}{U_0}) - (V_b + \Delta_b - \frac{3t_b^2}{U_0})](L_1^z + L_2^z) + (U_0 - W)[(L_1^z)^2 + (L_2^z)^2]. \end{aligned} \tag{B.19}$$

Then, we extend it to a lattice

$$\begin{aligned}\mathcal{H}_{eff} &= (\frac{V_a}{2} - \frac{t_a^2}{U_0} + \frac{V_b}{2} - \frac{t_b^2}{U_0}) \sum_{\langle ij \rangle} L_i^z L_j^z + \frac{-t_a t_b}{U_0} \sum_{\langle ij \rangle} (L_i^+ L_j^- + L_i^- L_j^+) \\ &+ [(pV_a + \Delta_a - \frac{3pt_a^2}{U_0}) - (pV_b + \Delta_b - \frac{3pt_b^2}{U_0})] \sum_i L_i^z \\ &+ (U_0 - W) \sum_i (L_i^z)^2. \end{aligned} \tag{B.20}$$

where p is the number of neighbors. From here, we are also able to generalize to arbitrary n, saying

$$\begin{aligned}\mathcal{H}_{eff} &= (\frac{V_a}{2} - \frac{t_a^2}{U_0} + \frac{V_b}{2} - \frac{t_b^2}{U_0}) \sum_{\langle ij \rangle} L_i^z L_j^z + \frac{-t_a t_b}{U_0} \sum_{\langle ij \rangle} (L_i^+ L_j^- + L_i^- L_j^+) \\ &+ [(\frac{pn}{2} V_a + \Delta_a - \frac{p(n+1)t_a^2}{U_0}) - (\frac{pn}{2} V_b + \Delta_b - \frac{p(n+1)t_b^2}{U_0})] \sum_i L_i^z \\ &+ (U_0 - W) \sum_i (L_i^z)^2. \end{aligned} \tag{B.21}$$

To remove the $L_i^z L_j^z$ term, the hopping amplitude can be chosen as $t_\alpha = \sqrt{V_\alpha U_0/2}$.

Thus, the effective Hamiltonian can be written in terms of $S = n/2$ spin operators for the case $n = 2$:

$$\mathcal{H}_{eff} = \frac{U}{2}\sum_i (L_i^z)^2 - \widetilde{\mu}\sum_i L_i^z - J\sum_{\langle ij\rangle}(L_i^x L_j^x + L_i^y L_j^y), \tag{B.22}$$

where the coefficients are given by $U = 2(U_0 - W)$, $\widetilde{\mu} = -(\Delta_a - \frac{p}{2}V_a) + (\Delta_b - \frac{p}{2}V_b)$, and $J = \sqrt{V_a V_b}$.

Appendix C

Finite temperature effects in entanglement entropy of the Bose-Hubbard model

We consider the thermal entanglement entropy of Bose Hubbard at half-filling. In our published work [214, 11], we used the following equation to fit the ground state 2nd order Rényi entropy (S_2),

$$S_2(N_s) = K + A\ln(N_s) + \frac{Bcos(\frac{\pi N_s}{2})}{(N_s)^p} + \frac{D}{\ln^2(N_s)}. \tag{C.1}$$

And we added a term linear with N_s to Eq. (C.1) to fit thermal S_2.

There is another way to fit the data. As discussed in Ref. [40], the thermal corrections for entanglement entropy scale as $e^{-\beta m_{gap}}$, where m_{gap} is the mass gap of the many-body system, which generally scale as $\frac{1}{N_s}$. We conjecture that the corrections also

contain $\frac{1}{\ln^2(N_s)}$ term, and an oscillation term for systems with OBC (need analytical checking). So we have the thermal correction for S_2:

$$\delta S_2^{pbc}(N_s) = ae^{-\frac{b}{N_s}} + \frac{c}{\ln^2(N_s)} + o(e^{-\frac{2b}{N_s}}), \tag{C.2}$$

$$\delta S_2^{obc}(N_s) = ae^{-\frac{b}{N_s}}(1 + \frac{dcos(\frac{\pi N_s}{2})}{N_s^e}) + \frac{c}{\ln^2(N_s)} + o(e^{-\frac{2b}{N_s}}). \tag{C.3}$$

where $b = 2\pi\Delta\beta$, Δ is the smallest scaling dimension among the set of operators including the stress tensor and all primaries not equal to the identity. We compare the two methods in the follow discussion (See Fig. C.4 for final compare).

C.1 BH with OBC, $J/U = 0.05, 0.2, T = 0.02, 0.04$

In Fig. C.1, we fit S_2 at finite temperature with Eq. (C.1) plus a term linear with N_s. For $J/U = 0.05$ (Fig. C.1 left), the fitting results are

1. $S_2(N_s) = 0.26265 + 0.12713\ln(N_s) + \frac{0.0943}{\ln^2(N_s)} - \frac{0.43697cos(\frac{\pi N_s}{2})}{(N_s)^{0.47645}}$ $(T = 0)$,
2. $S_2(N_s) = -0.24402 + 0.09988\ln(N_s) + \frac{0.73555}{\ln^2(N_s)} - \frac{2.68511cos(\frac{\pi N_s}{2})}{(N_s)^{1.65834}} + 0.08116N_s$ $(T = 0.02)$,
3. $S_2(N_s) = 0.06195 - 0.07591\ln(N_s) + \frac{0.16775}{\ln^2(N_s)} - \frac{5.68978cos(\frac{\pi N_s}{2})}{(N_s)^{2.67739}} + 0.1812N_s$ $(T = 0.04)$.

And for $J/U = 0.2$ (Fig. C.1 right), the fitting results are

1. $S_2(N_s) = 0.3857 + 0.12932\ln(N_s) + \frac{0.04508}{\ln^2(N_s)} - \frac{0.36267cos(\frac{\pi N_s}{2})}{(N_s)^{0.67853}}$ $(T = 0)$,
2. $S_2(N_s) = 0.58531 - 0.02843\ln(N_s) - \frac{0.03437}{\ln^2(N_s)} - \frac{0.50448cos(\frac{\pi N_s}{2})}{(N_s)^{0.85452}} + 0.01816N_s$ $(T = 0.02)$,

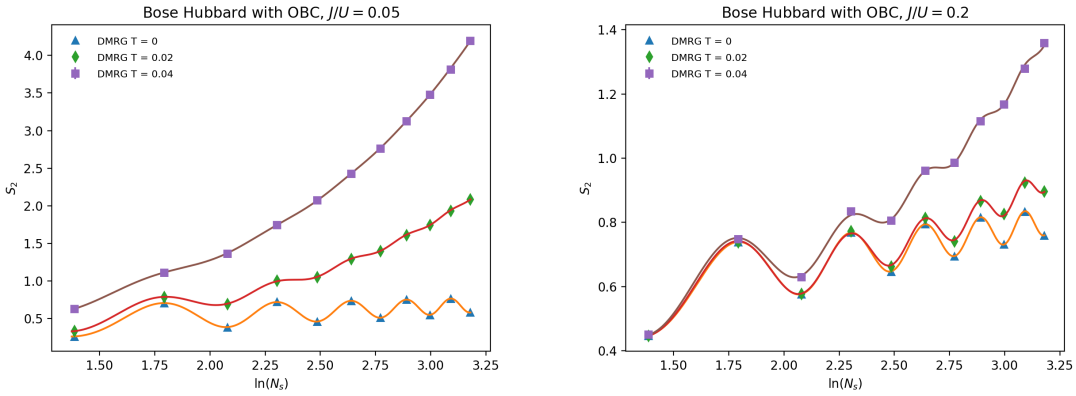

Figure C.1: S_2 at half-filling for BH with $J/U = 0.05$ (left) and $J/U = 0.2$ (right) v.s. $\ln(N_s)$. The solid lines corresponding to the fits with Eq. (C.1) plus a term linear with N_s.

3. $S_2(N_s) = 0.45968 - 0.09723\ln(N_s) + \frac{0.20719}{\ln^2(N_s)} - \frac{1.27373cos(\frac{\pi N_s}{2})}{(N_s)^{1.40295}} + 0.0497N_s$ $(T = 0.04)$.

The fits are generally good, but for thermal S_2, the coefficient of $\ln(N_s)$ term is far from the theoretical prediction (0.125).

We then subtract the ground state S_2 from finite temperature S_2 to obtain δS_2, and check Eq. (C.3) by fitting δS_2 with it. The results are shown in Fig. C.2. For $J/U = 0.05$ (left),

1. $\delta S_2^{obc}(N_s) = 3.9189232e^{-\frac{25.3303383}{N_s}}(1 + \frac{8.4209731cos(\frac{\pi N_s}{2})}{N_s^{1.5200314}}) + \frac{0.1535101}{\ln^2(N_s)}, \Delta = 0.080629$ $(T = 0.02)$,

2. $\delta S_2^{obc}(N_s) = 8.0419444e^{\frac{-21.212678}{N_s}}(1 + \frac{5.4782825cos(\frac{\pi N_s}{2})}{N_s^{1.6008824}}) + \frac{0.70218}{\ln^2(N_s)}, \Delta = 0.135044$ $(T = 0.04)$.

And for $J/U = 0.2$ (right),

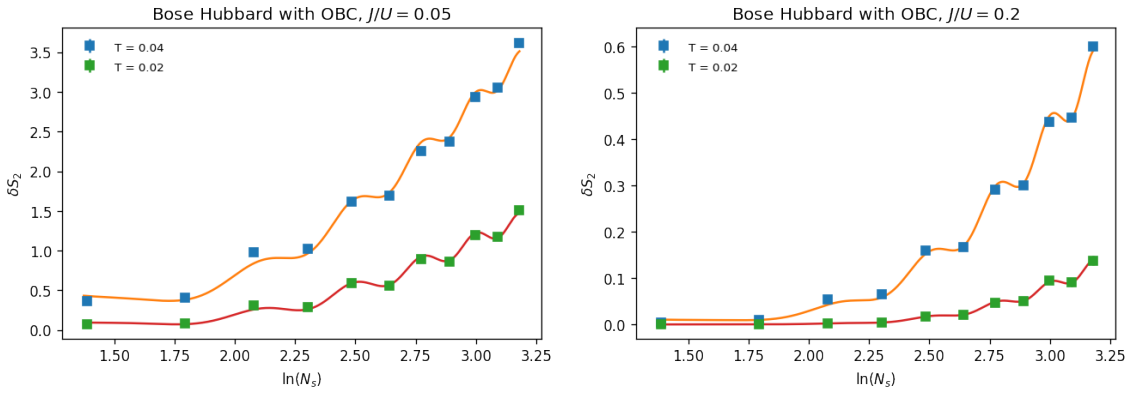

Figure C.2: δS_2 at half-filling for BH with $J/U = 0.05$ (left) and $J/U = 0.2$ (right) v.s. $\ln(N_s)$. The solid lines corresponding to the fits with Eq. (C.3).

1. $\delta S_2^{obc}(N_s) = 1.1574741e^{\frac{-53.319947}{N_s}}(1 + \frac{4.0848308cos(\frac{\pi N_s}{2})}{N_s^{1.1364486}}) - \frac{0.0003946}{\ln^2(N_s)}, \Delta = 0.169723$ ($T = 0.02$),

2. $\delta S_2^{obc}(N_s) = 2.3766018e^{\frac{-35.1676544}{N_s}}(1 + \frac{4.7709737cos(\frac{\pi N_s}{2})}{N_s^{1.3249548}}) + \frac{0.0183696}{\ln^2(N_s)}, \Delta = 0.223884$ ($T = 0.04$).

We also plot ΔS_2 v.s. N_s in Fig. C.3. We see that the thermal corrections of entanglement entropy for $J/U = 0.05$ is approximately linear with N_s, but not for $J/U = 0.2$. The second derivative of the function $f(x) = e^{-\frac{c}{x}}$, $\frac{\partial^2 f}{\partial^2 x} = e^{-\frac{c}{x}}\frac{c}{x^3}(\frac{c}{x} - 2)$. Its value for $x = 4, 6, ..., 24$ is

0.003342, 0.003941, 0.002395, 0.000985, 0.00011, -0.000361, -0.000586, -0.000673, -0.000686, -0.000661, -0.000619 for $c = 24.7215717$ ($J/U = 0.05, T = 0.02$),

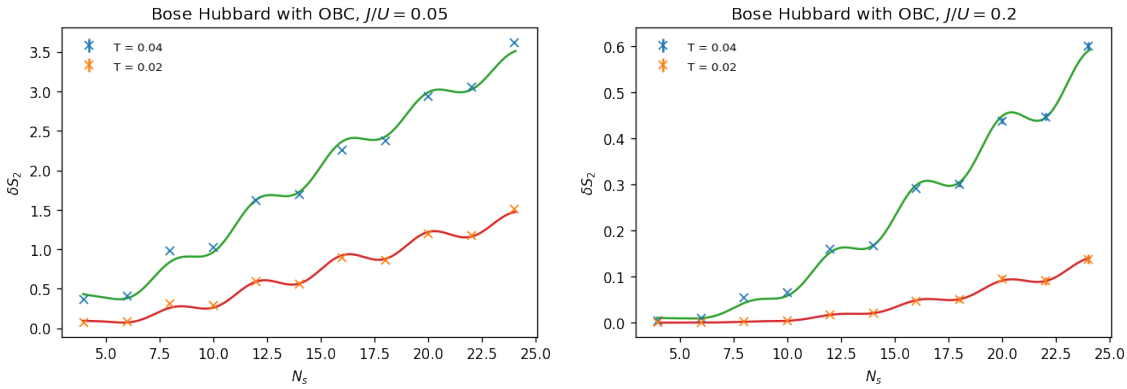

Figure C.3: δS_2 at half-filling for BH with $J/U = 0.05$ (left) and $J/U = 0.2$ (right) v.s. N_s. The thermal corrections of entanglement entropy for $J/U = 0.05$ is approximately linear with N_s, but not for $J/U = 0.2$.

0.005717, 0.004409, 0.001817, 0.000215, -0.000562, -0.000878, -0.000966, -0.000946, -0.000881, -0.000799, -0.000716 for $c = 20.8286787$ $(J/U = 0.05, T = 0.04)$,

1.7e-05, 0.000249, 0.000642, 0.000879, 0.000899, 0.000784, 0.000618, 0.00045, 0.000302, 0.000181, 8.6e-05 for $c = 52.8658659$ $(J/U = 0.2, T = 0.02)$,

0.000608, 0.001855, 0.002062, 0.001587, 0.000997, 0.000513, 0.000168, -5.8e-05, -0.000199, -0.000281, -0.000325 for $c = 34.7923985$ $(J/U = 0.2, T = 0.04)$.

We see that for $J/U = 0.05$, the function is convex for $4 \leq x \leq 12$ and concave for $14 \leq x \leq 24$. For $J/U = 0.2$, however, the function is always convex for $4 \leq x \leq 24$. This explains why δS_2 looks linear with N_s for the former case and does not for the latter case.

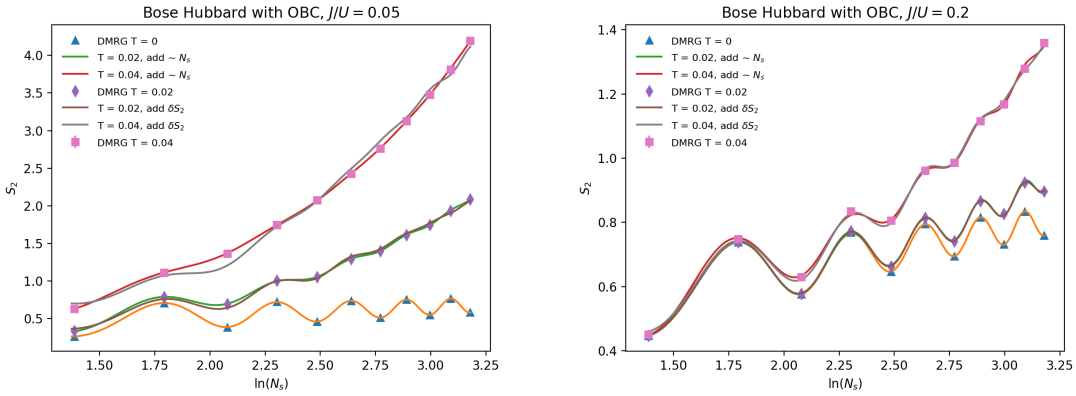

Figure C.4: $S_2(T=0)+\delta S_2$ at half-filling for BH with $J/U=0.05$ (left) and $J/U=0.2$ (right) v.s. $\ln(N_s)$. Fits with Eq. (C.1) plus a term linear with N_s are also plotted.

In Fig. C.4, we add the fitted function of δS_2 to the fitted function of ground state S_2, and compare them with the ones in Fig. C.1. We see that they both fit well.

C.2 $J/U=0.1$

For $J/U=0.1$, pbc (Fig. C.5 left), the fitting results are

1. $S_2(N_s)=0.31712+0.25428\ln(N_s)+\frac{0.06616}{\ln^2(N_s)}-\frac{0.3396cos(\frac{\pi N_s}{2})}{(N_s)^{1.20767}}$ $(T=0)$,

2. $S_2(N_s)=1.05388-0.18746\ln(N_s)-\frac{0.48539}{\ln^2(N_s)}-\frac{0.26328cos(\frac{\pi N_s}{2})}{(N_s)^{1.1161}}+0.03863N_s$ $(T=0.02)$,

3. $S_2(N_s)=0.52437-0.15052\ln(N_s)+\frac{0.03122}{\ln^2(N_s)}-\frac{0.11735cos(\frac{\pi N_s}{2})}{(N_s)^{0.60743}}+0.0907N_s$ $(T=0.04)$.

And for $J/U=0.1$, obc (Fig. C.5 right), the fitting results are

1. $S_2(N_s)=0.2987+0.12985\ln(N_s)+\frac{0.07883}{\ln^2(N_s)}-\frac{0.41286cos(\frac{\pi N_s}{2})}{(N_s)^{0.53778}}$ $(T=0)$,

2. $S_2(N_s)=0.31116-0.04517\ln(N_s)+\frac{0.2836}{\ln^2(N_s)}-\frac{0.98767cos(\frac{\pi N_s}{2})}{(N_s)^{1.03141}}+0.04159N_s$ $(T=0.02)$,

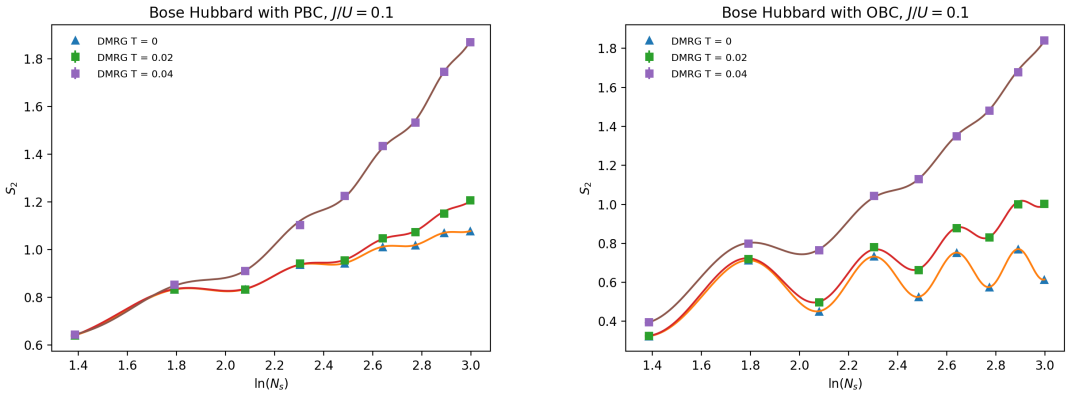

Figure C.5: S_2 at half-filling for BH with $J/U = 0.1$, pbc(left) and obc (right) v.s. $\ln(N_s)$. The solid lines corresponding to the fits with Eq. (C.1) plus a term linear with N_s.

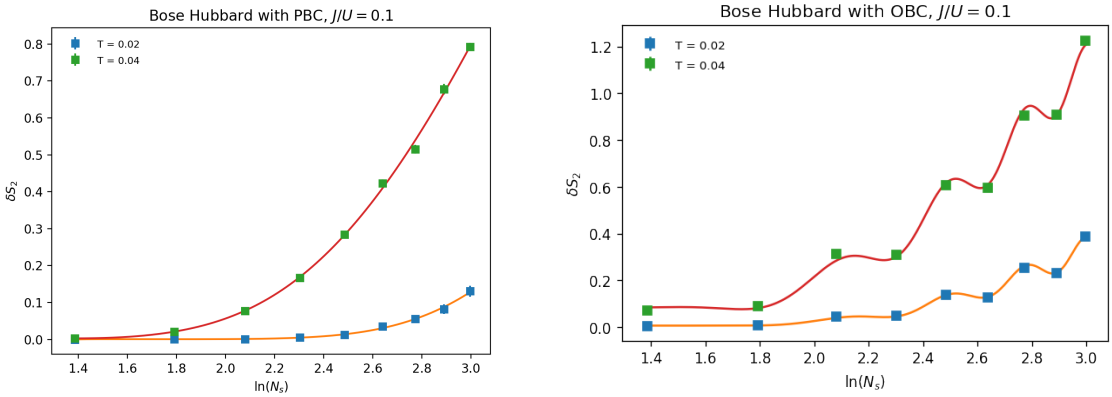

Figure C.6: δS_2 at half-filling for BH with $J/U = 0.1$, PBC (left) and OBC (right) v.s. $\ln(N_s)$.

3. $S_2(N_s) = -0.17092 + 0.08458\ln(N_s) + \frac{0.65904}{\ln^2(N_s)} - \frac{3.01774 cos(\frac{\pi N_s}{2})}{(N_s)^{1.85041}} + 0.08447 N_s$ $(T = 0.04)$.

The results of δS_2 are shown in Fig. C.6. For PBC (left),

1. $\delta S_2^{pbc}(N_s) = 3.6026959 e^{-\frac{66.825127}{N_s}} + \frac{0.0006439}{\ln^2(N_s)}, \Delta = 0.212711$ $(T = 0.02)$,

2. $\delta S_2^{pbc}(N_s) = 3.7298287 e^{\frac{-30.9684317}{N_s}} + \frac{0.0013127}{\ln^2(N_s)}, \Delta = 0.197151$ $(T = 0.04)$.

And for OBC (right),

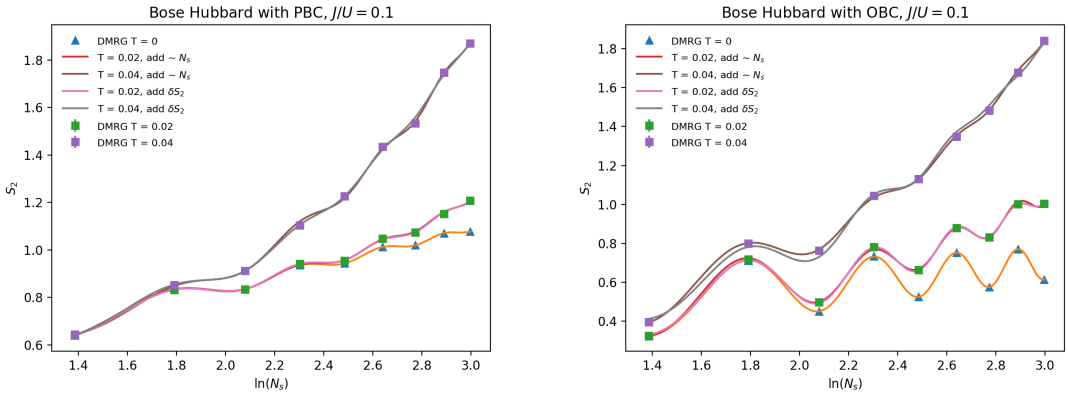

Figure C.7: $S_2(T=0)+\delta S_2$ at half-filling for BH with $J/U=0.1$, PBC (left) and OBC (right) v.s. $\ln(N_s)$. Fits with Eq. (C.1) plus a term linear with N_s are also plotted.

1. $\delta S_2^{obc}(N_s) = 1.8008392e^{\frac{-33.7040333}{N_s}}(1+\frac{2.8849524cos(\frac{\pi N_s}{2})}{N_s^{0.9874958}})+\frac{0.0104963}{\ln^2(N_s)}, \Delta = 0.107283$ $(T=0.02)$,

2. $\delta S_2^{obc}(N_s) = 3.4955867e^{\frac{-22.9785444}{N_s}}(1+\frac{6.1827109cos(\frac{\pi N_s}{2})}{N_s^{1.4742712}})+\frac{0.1228711}{\ln^2(N_s)}, \Delta = 0.146286$ $(T=0.04)$.

C.3 Scaling Dimension Δ

The formula of δS_2 also can be used to extract the smallest scaling dimension Δ of the system. We already calculate Δ each time when we fit our δS_2 data. As a comparison, we drop the high order corrections and determine Δ by linearly fitting $\ln(\delta S_2)$ v.s. $\frac{1}{N_s}$.

Also, we calculate the energy gap to extract Δ. We use the following equation to fit energy gaps,

$$\delta E = B\frac{1}{N_s^3} + C\frac{1}{N_s^2} + A_s\frac{1}{N_s} + D, \tag{C.4}$$

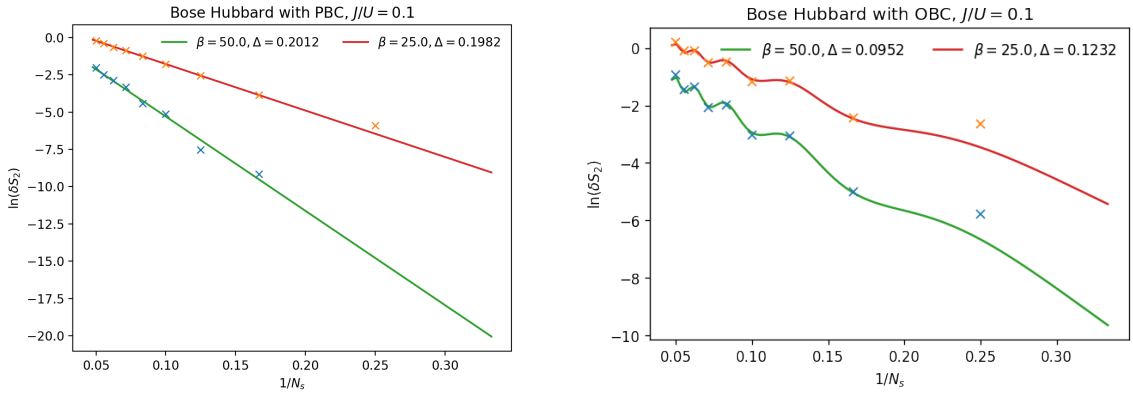

Figure C.8: Linear fit on $\ln(\delta S_2)$ at half-filling for BH with $J/U = 0.1$, PBC (left) and OBC (right) v.s. $\frac{1}{N_s}$. The results from previous sections are $\Delta = 0.212711$ $(T = 0.02, PBC)$, $\Delta = 0.197151$ $(T = 0.04, PBC)$, $\Delta = 0.105331$ $(T = 0.02, OBC)$, $\Delta = 0.141869$ $(T = 0.04, OBC)$

where $A_s = 2\pi\Delta$. We also tried equations with higher oder of $\frac{1}{N_s}$, the value of A_s changes a order of $1E-4$ for OBC, $1E-3$ for PBC.

We also use the Shanks transformation [199] to find the more accurate fitting parameter A_s, assuming it converges for infinite number of fitting systems.

We summarize all scaling dimension values in the following table. We see that the scaling dimension of OBC is half that of PBC.

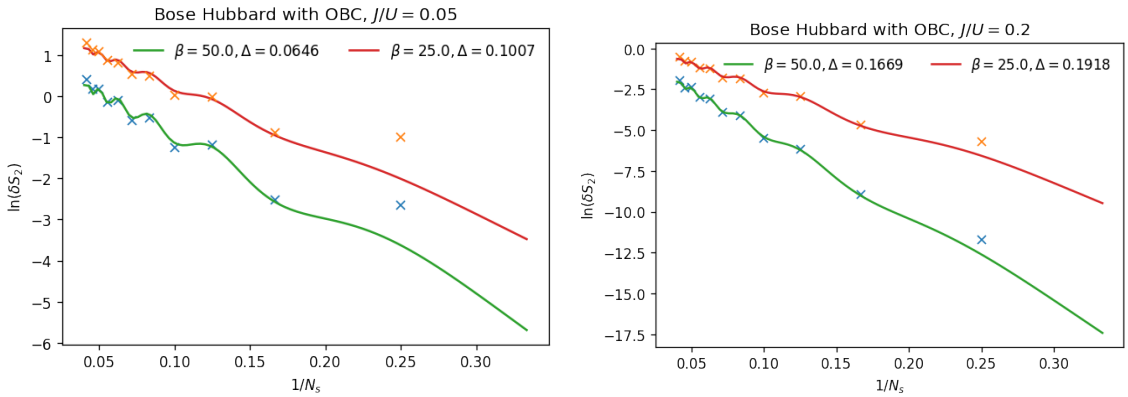

Figure C.9: Linear fit on $\ln(\delta S_2)$ at half-filling for BH with $J/U = 0.1$, PBC (left) and OBC (right) v.s. $\frac{1}{N_s}$. The results from previous sections are $\Delta = 0.078691$ $(T = 0.02, J/U = 0.05, OBC)$, $\Delta = 0.132599$ $(T = 0.04, J/U = 0.05, OBC)$, $\Delta = 0.168277$ $(T = 0.02, J/U = 0.2, OBC)$, $\Delta = 0.221495$ $(T = 0.04, J/U = 0.2, OBC)$

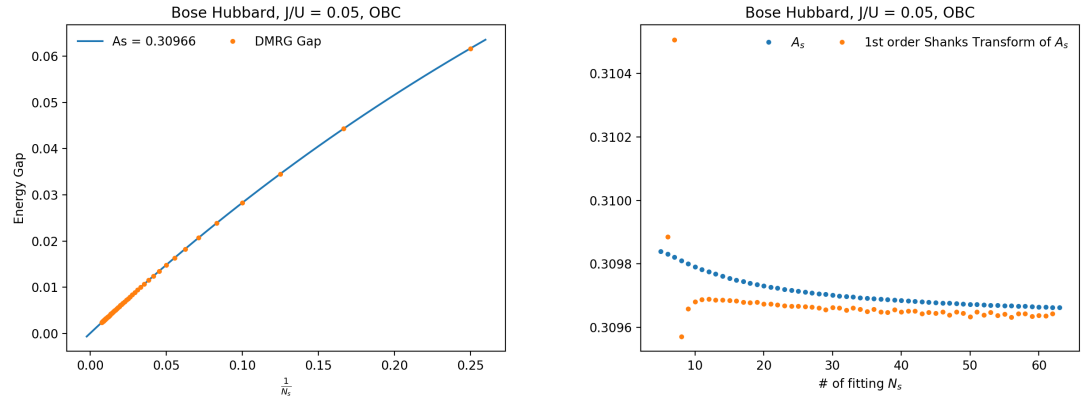

Figure C.10: (Left) Energy gaps of Bose Hubbard chain with $J/U = 0.05$, OBC. (Right) The fit parameter As as a function of the number of fitting points. The last value of A_s is 0.309644, which gives $\Delta = 0.04928$.

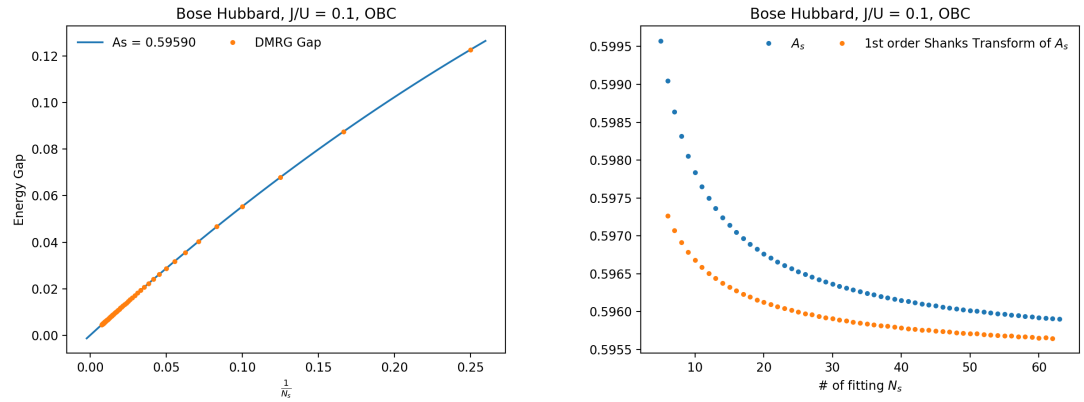

Figure C.11: (Left) Energy gaps of Bose Hubbard chain with $J/U = 0.1$, OBC. (Right) The fit parameter As as a function of the number of fitting points. The last value of A_s is 0.595647, which gives $\Delta = 0.09480$.

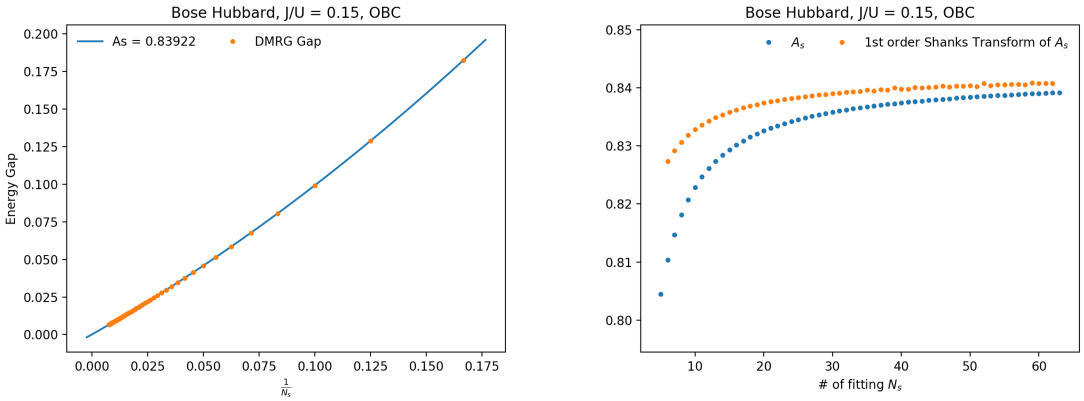

Figure C.12: (Left) Energy gaps of Bose Hubbard chain with $J/U = 0.2$, PBC. (Right) The fit parameter As as a function of the number of fitting points. The last value of A_s is 0.840813, which gives $\Delta = 0.13382$.

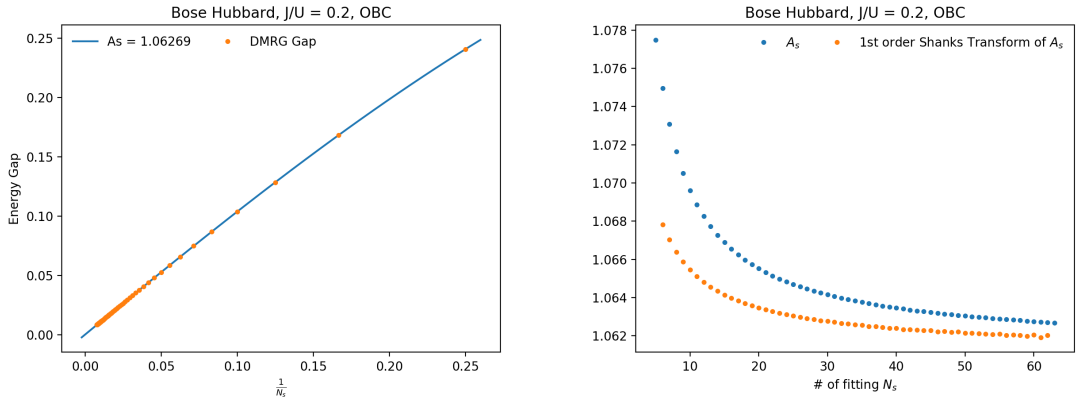

Figure C.13: (Left) Energy gaps of Bose Hubbard chain with $J/U = 0.2$, OBC. (Right) The fit parameter As as a function of the number of fitting points. The last value of A_s is 1.062028, which gives $\Delta = 0.16903$.

Item	$J/U = 0.05, obc$	$J/U = 0.05, pbc$	$J/U = 0.1, obc$	$J/U = 0.1, pbc$	$J/U = 0.15, obc$	$J/U = 0.15, pbc$	$J/U = 0.2, obc$	$J/U = 0.2, pbc$
From δS_2 v.s. $\ln(N_s)$	0.080629		0.107283	0.212711			0.169723	
From $\ln(\delta S_2)$ v.s. $\frac{1}{N_s}$	0.0646		0.0952	0.2012			0.1669	
From m_{gap} v.s. $\frac{1}{N_s}$	0.04928	0.09854	0.09480	0.18856	0.13382	0.26598	0.16903	0.33124

Table C.1: Values of scaling dimension Δ from fits of δS_2 v.s. $\ln(N_s)$, $\ln(\delta S_2)$ v.s. $1/N_s$ and m_{gap} v.s. $1/N_s$

.

Appendix D

The Abelian Higgs model with a topological term

The Abelian Higgs model with a topological term in two dimensions has been studied in Ref. [82]. The action of the model reads

$$S = S_g + S_h + S_\lambda + S_t, \tag{D.1}$$

where the first three parts are the same as Eq. (2.1). The topological part is

$$S_t = \frac{i\Theta}{2\pi} \sum_x \mathrm{Im}\left[U_{pl,x}\right], \tag{D.2}$$

The easiest way to derive the expression of the partition function in term of the dual variables is to notice that

$$\begin{aligned} e^{\beta_{pl}\cos A_x^\square - i\frac{\Theta}{2\pi}\sin A_x^\square} &= e^{2\sqrt{a^2-b^2}\cos\left(A_x^\square+\Delta\right)} \\ &= \sum_{p_x} I_{p_x}(2\sqrt{a^2-b^2}) e^{ip_x(A_x^\square+\Delta)}, \end{aligned} \tag{D.3}$$

where $a = \beta_{pl}/2, b = \Theta/4\pi, \tan\Delta = ib/a$. Moreover, $e^{-i\Delta} = \sqrt{\frac{a+b}{a-b}}$. So

$$e^{\beta_{pl}\cos A_x^{\square} - i\frac{\Theta}{2\pi}\sin A_x^{\square}} = \sum_{p_x}(\frac{\eta}{\bar{\eta}})^{p_x} I_{p_x}(2\sqrt{\eta\bar{\eta}})e^{-ip_x A_x^{\square}}, \tag{D.4}$$

where

$$\eta \equiv \frac{\beta}{2} - \frac{\theta}{4\pi}, \qquad \overline{\eta} \equiv \frac{\beta}{2} + \frac{\theta}{4\pi}. \tag{D.5}$$

Then the other derivations are the same. We can also obtain the Hamiltonian for this model and quantum simulate it in the optical lattices. This is left for a future work.